

The role of carbonate system dynamics in Southern Ocean CO₂ uptake

Oliver Legge

A thesis submitted to
the School of Environmental Sciences of the University of East Anglia
in partial fulfilment of the requirements for the degree of
Doctor of Philosophy

September 2017

This copy of the thesis has been supplied on condition that anyone who consults it is understood to recognise that its copyright rests with the author and that use of any information derived there from must be in accordance with current UK Copyright Law. In addition, any quotation or extract must include full attribution.

Abstract

Three years of carbonate system measurements from Ryder Bay on the West Antarctic Peninsula are presented. The strong, asymmetric seasonal cycle of surface water Dissolved Inorganic Carbon (DIC) is quantitatively attributed to four processes: mixing of water masses, air-sea CO₂ flux, calcium carbonate precipitation/dissolution and photosynthesis/respiration. In summer, reduced mixing with deeper water, net photosynthesis, and melting glacial ice and sea ice reduce DIC. In winter, mixing with deeper water and net heterotrophy increase DIC, resulting in aragonite saturation states close to 1. Ryder Bay is a net annual sink of atmospheric CO₂ of 0.90-1.39 mol C m⁻² yr⁻¹. The observed variability demonstrates that future climatic changes may significantly affect carbon cycling in this dynamic environment.

Carbonate system measurements from the Drake Passage and A23 sections are compared. Lower Circumpolar Deep Water (LCDW) becomes colder and fresher from Drake Passage to A23 due to mixing in the Scotia Sea. The coincident decrease in Total Alkalinity (TA) increases the fugacity of CO₂, potentially reducing CO₂ uptake in the Weddell Sea through the influence of upwelling LCDW on surface waters. Ventilation of Upper Circumpolar Deep Water (UCDW) in the south of Drake Passage suggests that this region is an important source of CO₂ to the atmosphere.

The zonal variability of the carbonate system in deep water masses around the Antarctic Circumpolar Current is assessed. Zonal variability, caused by the inflow of North Atlantic Deep Water in the Atlantic sector and UCDW in the Indian and Pacific sectors, has implications for regional air-sea CO₂ flux in the high-latitude Southern Ocean. Temporal variability in Sub-Antarctic Mode Water is investigated. Most of the observed DIC increase is attributed to rising atmospheric CO₂. There is also weak evidence for increasing remineralised organic carbon, possibly related to changes in the strength and location of ventilation.

Contents

| | | |
|----------|--|-----------|
| 1 | Introduction | 17 |
| 1.1 | Marine carbonate chemistry | 17 |
| 1.2 | Biogeochemical processes of the marine carbonate system | 21 |
| 1.2.1 | Ocean-atmosphere CO ₂ flux | 21 |
| 1.2.2 | Photosynthesis and respiration | 22 |
| 1.2.3 | Calcium carbonate precipitation and dissolution | 23 |
| 1.3 | Oceanographic context | 25 |
| 1.3.1 | The Antarctic Circumpolar Current | 25 |
| 1.3.2 | Drake Passage and the Scotia Sea | 29 |
| 1.3.3 | The West Antarctic Peninsula | 31 |
| 1.4 | The role of the Southern Ocean in carbon uptake | 34 |
| 1.4.1 | Glacial timescales | 34 |
| 1.4.2 | Contemporary Southern Ocean CO ₂ uptake | 36 |
| 1.4.3 | Sea ice and the carbonate system | 39 |
| 1.5 | Aim and objectives of this thesis | 42 |
| 2 | Methods | 45 |
| 2.1 | Methods outline | 45 |
| 2.2 | Sampling | 46 |
| 2.2.1 | RaTS sampling | 46 |
| 2.2.2 | Cruise sampling | 47 |
| 2.3 | Chemical analyses | 49 |
| 2.3.1 | DIC and TA | 50 |
| 2.3.2 | Dissolved oxygen | 51 |
| 2.3.3 | Inorganic nutrients | 54 |
| 2.4 | Datasets | 63 |

| | | |
|----------|--|-----------|
| 2.4.1 | Secondary quality control | 63 |
| 2.4.2 | Data availability | 65 |
| 3 | The seasonal cycle of ocean-atmosphere CO₂ flux in Ryder Bay | 67 |
| 3.1 | Rationale | 67 |
| 3.2 | Methods | 68 |
| 3.2.1 | Ocean and atmosphere CO ₂ concentrations | 69 |
| 3.2.2 | Ice cover and gas transfer velocity | 71 |
| 3.2.3 | Ocean-atmosphere CO ₂ flux | 73 |
| 3.2.4 | Uncertainties | 73 |
| 3.3 | Results and discussion | 75 |
| 3.3.1 | Seasonal and interannual variability | 75 |
| 3.3.2 | Unresolved complexity | 80 |
| 3.3.3 | Conclusions | 82 |
| 4 | The seasonal cycle of carbonate system processes in Ryder Bay | 83 |
| 4.1 | Rationale | 83 |
| 4.2 | Methods | 84 |
| 4.2.1 | Sampling and analysis | 84 |
| 4.2.2 | Quantifying carbonate system processes | 85 |
| 4.2.3 | Distribution of variables | 91 |
| 4.2.4 | Method limitations | 92 |
| 4.3 | Results | 95 |
| 4.3.1 | The observed carbonate system | 95 |
| 4.3.2 | Processes | 98 |
| 4.4 | Discussion | 103 |
| 4.4.1 | Saturation states | 103 |
| 4.4.2 | The seasonal cycle of carbonate processes | 104 |
| 4.4.3 | Comparison of carbon and phosphate derived net respiration | 112 |
| 4.5 | Conclusions | 113 |

| | | |
|----------|--|------------|
| 5 | Carbonate system modifications in deep waters of the Scotia Sea | 115 |
| 5.1 | Rationale | 115 |
| 5.2 | Data and methods | 116 |
| 5.2.1 | Cruise information | 116 |
| 5.2.2 | Defining vertical and horizontal boundaries | 120 |
| 5.3 | Results and discussion | 123 |
| 5.3.1 | Characterising the carbonate system on the Drake Passage and A23 sections | 123 |
| 5.3.2 | Longitudinal variation in Drake Passage | 129 |
| 5.3.3 | Water mass modifications | 132 |
| 5.3.4 | North Scotia Ridge | 145 |
| 5.4 | Conclusions | 147 |
| 6 | Circumpolar patterns in the Southern Ocean carbonate system | 149 |
| 6.1 | Rationale | 149 |
| 6.2 | Methods | 149 |
| 6.2.1 | Defining vertical and horizontal boundaries | 150 |
| 6.2.2 | Carbon partitioning | 155 |
| 6.2.3 | Pentadal trends in SAMW | 157 |
| 6.3 | Results and discussion | 158 |
| 6.3.1 | Zonal observations | 158 |
| 6.3.2 | Temporal observations in SAMW | 170 |
| 6.4 | Conclusions | 178 |
| 7 | Discussion and future work | 179 |
| 7.1 | Overview | 179 |
| 7.2 | Surface ocean processes | 181 |
| 7.2.1 | The future of the carbonate system in Ryder Bay | 181 |
| 7.2.2 | A RaTS-based carbonate system model | 184 |
| 7.2.3 | Wider applicability | 185 |
| 7.2.4 | Changes in SAMW carbon uptake | 186 |

| | | |
|-------------------|--|------------|
| 7.3 | Deep water mass variability | 187 |
| 7.3.1 | Implications of zonal carbonate system variability | 187 |
| 7.3.2 | Regional modelling challenges | 188 |
| 7.4 | Future observations | 190 |
| Appendices | | 192 |
| A | Ocean circulation and acidification demonstration | 193 |
| A.1 | Resources | 193 |
| A.2 | Part One - CO ₂ and pH | 194 |
| A.3 | Part Two - Ocean acidification | 194 |
| A.4 | Part Three - Deep water formation | 198 |
| B | The dynamic height of ACC fronts on DP and A23 sections | 201 |
| C | Scotia Sea MLR results | 203 |
| D | JR299 section plots | 207 |
| E | Pressure effect on pH and Ω | 211 |
| F | The dynamic height of ACC fronts - circumpolar | 213 |
| G | Circumpolar data distributions | 215 |
| H | Abbreviations | 219 |
| References | | 221 |

List of Figures

| | | |
|------|---|----|
| 1.1 | Schematic of the global carbon cycle | 20 |
| 1.2 | Schematic of the three ocean carbon pumps | 24 |
| 1.3 | The mean position of the ACC fronts mapped from sea surface height | 26 |
| 1.4 | Schematic of the Southern Ocean meridional overturning circulation | 29 |
| 1.5 | Map of the Scotia Sea region | 31 |
| 1.6 | A conceptual model of the effects of seasonal sea ice on the carbon- ate system | 40 |
| 2.1 | Map of the Rothera time series | 47 |
| 2.2 | Map of carbon stations on JR299 | 49 |
| 2.3 | Map of oxygen stations on JR299 | 49 |
| 2.4 | JR299 dissolved oxygen profiles | 53 |
| 2.5 | JR299 oxygen sensor calibration | 54 |
| 2.6 | Silicate defrosting tests, unfrozen vs. thawed | 57 |
| 2.7 | Silicate defrosting tests, thawing times | 59 |
| 2.8 | Comparison of unfrozen and thawed samples for nitrate, phosphate and silicate | 60 |
| 2.9 | The sensitivity of TA results to phosphate and silicate concentrations | 61 |
| 2.10 | The sensitivity of calculated carbonate system parameters to phos- phate and silicate concentrations | 63 |
| 3.1 | Atmospheric CO ₂ concentrations at Palmer Station and the South Pole | 69 |
| 3.2 | Time series of DIC and $\Delta f\text{CO}_2$ at RaTS | 76 |
| 3.3 | Time series of ocean-atmosphere CO ₂ flux at RaTS | 79 |
| 4.1 | A graphical example of process rate calculations in DIC/TA space . | 90 |
| 4.2 | Factors influencing the carbonate system in Ryder Bay | 94 |

| | | |
|------|---|-----|
| 4.3 | Time series of measured carbonate system variables at RaTS | 96 |
| 4.4 | Time series of calculated carbonate system variables at RaTS | 97 |
| 4.5 | Rates of processes affecting DIC in Ryder Bay | 99 |
| 4.6 | Monthly averages of process rates | 101 |
| 4.7 | Seasonal averages of process rates | 102 |
| 4.8 | A comparison of carbon and phosphate derived net respiration rates | 105 |
| 4.9 | Temperature at RaTS during the carbon time series | 106 |
| 4.10 | Wind direction and speed at Rothera | 108 |
| 4.11 | Salinity at RaTS during the carbon time series | 112 |
| 5.1 | Schematic of the overturning circulation in the Scotia Sea | 116 |
| 5.2 | The anatomy of a box plot | 123 |
| 5.3 | Section plots of Drake Passage temperature, salinity, oxygen and silicate | 125 |
| 5.4 | Section plots of Drake Passage carbonate system variables | 126 |
| 5.5 | Section plots of A23 temperature, salinity, oxygen and silicate | 128 |
| 5.6 | Section plots of A23 carbonate system variables | 129 |
| 5.7 | Comparison of eastern and western Drake Passage sections, JC031 . | 131 |
| 5.8 | Comparison of eastern and western Drake Passage sections, all cruises | 132 |
| 5.9 | Θ/S plot of the densest waters of the Drake Passage and A23 sections | 133 |
| 5.10 | Box plots of measured and calculated variables in WSDW | 135 |
| 5.11 | Box plots of measured and calculated variables in LCDW | 137 |
| 5.12 | Drake passage and A23 salinity, CFC12 and oxygen profiles | 139 |
| 5.13 | Drake passage and A23 potential temperature profiles | 140 |
| 5.14 | Drake passage and A23 DIC, TA and $f\text{CO}_2$ profiles | 140 |
| 5.15 | Drake passage and A23 pH, Revelle factor and Ω aragonite profiles | 141 |
| 5.16 | Box plots of measured and calculated variables in UCDW | 144 |
| 5.17 | DIC, TA, oxygen and silicate concentrations along the North Scotia Ridge | 146 |
| 5.18 | Θ/S plot of the densest waters of the Drake Passage and North Sco- tia Ridge sections | 147 |

| | | |
|------|--|-----|
| 6.1 | Validation of circumpolar dynamic height frontal definitions | 151 |
| 6.2 | A comparison of measured and averaged dynamic heights | 152 |
| 6.3 | Mean meridional circumpolar sections of salinity, $f\text{CO}_2$ and oxygen | 154 |
| 6.4 | DIC and oxygen profiles for the densest waters of the ACC | 160 |
| 6.5 | Salinity and TA profiles for the densest waters of the ACC | 161 |
| 6.6 | Ω calcite and Ω aragonite profiles for the densest waters of the ACC | 162 |
| 6.7 | Zonal plots of DIC components in the densest waters of the ACC . . | 166 |
| 6.8 | Zonal plots of $f\text{CO}_2$, pH and the Revelle factor in the densest waters of the ACC | 168 |
| 6.9 | Pentadal box plots of potential temperature, salinity, TA and DIC anomalies in SAMW | 172 |
| 6.10 | Pentadal box plots of DIC component anomalies in SAMW | 173 |
| 6.11 | Pentadal box plot of P^* anomaly in SAMW | 174 |
| 6.12 | The circumpolar distribution of SAMW data used for DIC partitioning | 176 |
| 7.1 | Schematic of a proposed model of the carbonate system in Ryder Bay | 185 |
| 7.2 | Comparison of modelled and observed air-sea CO_2 flux | 189 |
| A.1 | Bromothymol blue indicator in waters of different pH. | 194 |
| A.2 | Time series measurements of atmospheric CO_2 from Hawaii | 195 |
| A.3 | Increasing the CO_2 concentration in the model atmosphere using dry ice. | 196 |
| A.4 | The surface of the model ocean before and after increasing atmo- spheric CO_2 | 197 |
| A.5 | Observations of atmospheric CO_2 , seawater CO_2 and seawater pH from the North Pacific | 197 |
| A.6 | Examples of marine calcifiers | 198 |
| A.7 | Schematic of the global ocean conveyor belt | 199 |
| A.8 | The formation of deep water in a model ocean | 200 |
| B.1 | Validation of dynamic height frontal definitions in Drake Passage . . | 201 |
| B.2 | Validation of dynamic height frontal definitions on the A23 section . | 201 |

| | | |
|-----|---|-----|
| D.1 | DIC, TA, oxygen and silicate sections on the Drake Passage section of JR299 | 208 |
| D.2 | DIC, TA, oxygen and silicate sections on the A23 section of JR299 | 209 |
| E.1 | Drake Passage and A23 Ω aragonite | 211 |
| E.2 | The influence of pressure on pH and Ω aragonite in LCDW in Drake Passage | 212 |
| F.1 | Validation of circumpolar dynamic height frontal definitions at Drake Passage. | 213 |
| F.2 | Validation of circumpolar dynamic height frontal definitions at the prime meridian. | 213 |
| F.3 | Validation of circumpolar dynamic height frontal definitions at 115°E. | 214 |
| F.4 | Validation of circumpolar dynamic height frontal definitions at 150°W. | 214 |
| F.5 | Validation of circumpolar dynamic height frontal definitions at 103°W. | 214 |
| G.1 | The circumpolar distribution of salinity data points in SAMW | 215 |
| G.2 | The circumpolar distribution of DIC data points in SAMW | 216 |
| G.3 | The circumpolar distribution of data points in SAMW used for calculating P* | 217 |

List of Tables

| | | |
|-----|--|-----|
| 2.1 | Crossover analysis results for JR299 biogeochemical data | 66 |
| 3.1 | Ocean-atmosphere CO ₂ flux uncertainties | 74 |
| 4.1 | Distributions of endmember variables | 92 |
| 5.1 | Drake Passage cruise information | 118 |
| 5.2 | A23 cruise information | 119 |
| 5.3 | Scotia Sea frontal definitions | 120 |
| 5.4 | Scotia Sea water mass definitions | 121 |
| 6.1 | Circumpolar frontal definitions | 150 |
| 6.2 | Circumpolar water mass definitions | 153 |
| C.1 | Multiple linear regression results for WSDW | 204 |
| C.2 | Multiple linear regression results for LCDW | 205 |

Acknowledgements

I am very grateful to my supervisors Dorothee Bakker, Martin Johnson, Hugh Venables, Mike Meredith and Pete Brown, for their advice and support over the last few years - I couldn't have hoped for a better team.

I would like to thank all the people who helped to produce the RaTS and JR299 datasets used in this thesis. Without the efforts of the BAS Marine Assistants Sabrina Heiser, Mairi Fenton, Simon Reeves and Zoe Waring, the RaTS DIC and TA samples would still be water in Ryder Bay and without the technical support of the UEA technicians, especially Gareth Lee, Andy Hind, Stephen Humphrey, Steve Woodward and Andy MacDonald, that water would still be sealed in bottles in the cave. Thanks to the captain and crew of the RRS James Clark Ross for navigating safely around the Scotia Sea. Thanks also to the scientists onboard, especially Mike Boniface and Kim Pyle, and Andrew Meijers for leading two fantastic cruises.

Numerous people have influenced this work through stimulating scientific discussions at the UEA, at sea and at meetings further afield. Special thanks to Libby Jones, Bruno Delille, Brice Loose and Tim Jickells for their counsel. It has been a pleasure working among jolly, helpful and interesting colleagues in ENV and I am particularly glad for the friendship and ping pong skills of Max Thomas and Ollie Lambert.

This PhD research was funded by the Natural Environment Research Council (NERC)(NE/L50158X/1). It was also supported by British Antarctic Survey Polar Oceans funding from NERC and the UK Ocean Acidification Research Programme (NE/H017046/1) grant at the UEA, funded by NERC, the Department for Energy and Climate Change and the Department for Environment, Food and Rural Affairs. Sea ice and glacial ice DIC and TA data were part of the University of Groningen research programme 866.13.006, partly financed by the Netherlands Organisation for Scientific Research (NWO).

Chapter 1

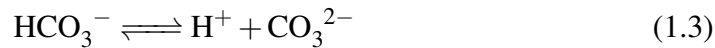
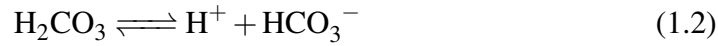
Introduction

1.1 Marine carbonate chemistry

The element carbon exists in several forms in the world's oceans. Some is present in organic molecules, as either dissolved or particulate organic carbon, but the vast majority (about 38,000 petagrams) exists as inorganic carbon (Figure 1.1). This huge pool of inorganic carbon in the ocean exchanges with the much smaller atmospheric and terrestrial carbon pools on a timescale of years to hundreds of years (Berner and Berner, 2012), making it a crucial part of the earth's climate system from a human perspective.

The flux of carbon dioxide (CO_2) between the surface ocean and the overlying atmosphere allows the exchange of inorganic carbon between these two pools. However, the ocean is able to take up far more CO_2 from the atmosphere than the amount dictated by CO_2 solubility alone, because CO_2 is only one part of the marine inorganic carbon pool, or carbonate system. When CO_2 dissolves in seawater it forms carbonic acid, which dissociates into hydrogen ions (H^+), bicarbonate ions (HCO_3^-) and carbonate ions (CO_3^{2-}) (Equations 1.1 to 1.3). The sum of the concentrations of CO_2 , H_2CO_3 , HCO_3^- and CO_3^{2-} is referred to as total dissolved inorganic carbon (TCO_2) or dissolved inorganic carbon (DIC) (Equation 1.4). At the pH of seawater (approximately 8.2) the relative contributions to DIC of CO_2 , HCO_3^- and CO_3^{2-} are 0.5%, 89% and 10.5% respectively, with a negligible amount of H_2CO_3 (Zeebe and Wolf-Gladrow, 2001). DIC can be measured analytically by acidifying

a known volume of seawater, thereby converting all species of DIC present into CO_2 and then measuring the amount of CO_2 produced (Section 2.3.1).



$$\text{DIC} = [\text{CO}_2] + [\text{H}_2\text{CO}_3] + [\text{HCO}_3^-] + [\text{CO}_3^{2-}] \quad (1.4)$$

Another important metric of the carbonate system is total alkalinity (TA) which is a measure of the charge balance in seawater and is most accurately defined as the excess of proton acceptors (bases formed from weak acids with a dissociation constant less than $10^{-4.5}$) over proton donors (acids with a dissociation constant greater than $10^{-4.5}$) (Dickson, 1981). TA is dominated by carbonate alkalinity (the sum of the charges of carbonate and bicarbonate ions) but also includes contributions from borate, water, silicate, phosphate and other weak acids and bases as shown in Equation 1.5 (Dickson, 2010). TA is usually measured by potentiometric titration (Section 2.3.1). Both DIC and TA have the analytical advantage that, when measured in gravimetric units, they are not affected by temperature or pressure.

$$\begin{aligned} \text{TA} = & [\text{HCO}_3^-] + 2[\text{CO}_3^{2-}] + [\text{B}(\text{OH})_4^-] + [\text{OH}^-] + [\text{HPO}_4^{2-}] + \\ & 2[\text{PO}_4^{3-}] + [\text{SiO}(\text{OH})_3^-] + [\text{NH}_3] + [\text{HS}^-] + \dots \\ & - [\text{H}^+] - [\text{HSO}_4^-] - [\text{HF}] - [\text{H}_3\text{PO}_4] - \dots \quad (1.5) \end{aligned}$$

The pH of water is an integral part of the carbonate system and is defined as

the negative logarithm of the hydrogen ion concentration. For seawater, it is recommended that the total hydrogen ion concentration is used to calculate pH, which includes the contribution of sulphate as well as the concentration of free hydrogen ions (Dickson et al., 2007). pH is either measured potentiometrically using an electrode or is measured using a dye and spectrophotometry (Dickson et al., 2007). The partial pressure of CO₂ (pCO₂) is usually determined by equilibrating a gas stream with a large volume of water and measuring the mole fraction of CO₂ in the gas stream (Dickson et al., 2007). The fugacity of CO₂ (*f*CO₂) is very similar to the partial pressure except that it accounts for the non-ideal nature of CO₂ gas. Given any two of these four measurable carbonate system variables (DIC, TA, pH, pCO₂), plus temperature, salinity, pressure, and phosphate and silicate concentrations, it is possible to calculate all other carbonate system variables using experimentally determined carbonate system constants (Dickson et al., 2007).

The partial pressure of CO₂ in the atmosphere has been rising, largely due to human activities, since the start of the industrial revolution (Keeling et al., 2005) and the current atmospheric CO₂ concentration is higher than any measured in ice cores over the last 800,000 years (Petit et al., 1999; Lüthi et al., 2008). As atmospheric CO₂ increases, so does the amount of CO₂ which dissolves into the ocean and this affects the balance of the carbonate system summarised in Equations 1.1 to 1.3. The net effect of dissolving more CO₂ in seawater is an increase in the concentrations of CO₂, H⁺ and HCO₃⁻ and a decrease in the concentration of CO₃²⁻. An increase in H⁺ ions means a lower pH and this process is referred to as ocean acidification (Feely et al., 2004; Orr et al., 2005). Since the start of the industrial revolution surface ocean pH has decreased by 0.1 units (Caldeira and Wickett, 2003), which corresponds to a 30% increase in H⁺ ions. See Appendix A for a description of a physical model to demonstrate ocean acidification and ocean circulation.

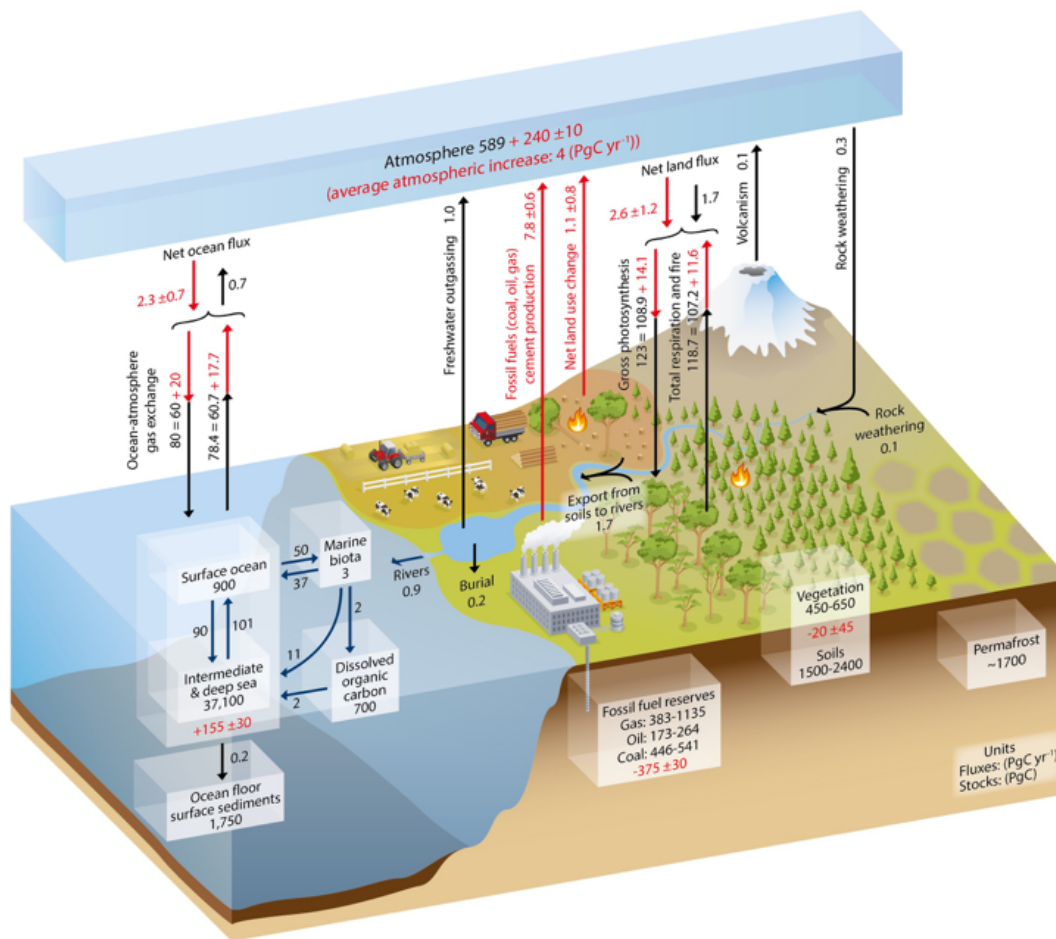


Figure 1.1: A schematic of the global carbon cycle, taken from Ciais et al. (2013). Boxes and arrows represent reservoirs and fluxes of carbon, respectively. Black numbers represent pre-industrial reservoirs and fluxes, whereas red numbers represent anthropogenic (2000 to 2009 average) reservoirs and fluxes.

The presence of CO_3^{2-} ions acts as a buffer to the increase in CO_2 and H^+ because the more CO_3^{2-} ions that are present to react with H^+ ions, the less H^+ ions are left in solution and the higher the pH. As pH and the concentration of CO_3^{2-} ions decrease, this buffering capacity decreases meaning that, for a given increase in CO_2 , more H^+ ions remain in solution. There are several ways of quantifying the oceans buffering capacity (Eggleston et al., 2010), the most common being the Revelle factor which relates the fractional change in CO_2 to the fractional change in total DIC (Revelle and Suess, 1957). The Revelle factor ranges from 8 in the tropics and subtropics to 16 in the polar oceans, with high values indicating low

buffering capacity. The polar oceans are especially sensitive to ocean acidification as their low TA to DIC ratio reduces their carbonate buffering capacity (Egleston et al., 2010; Shadwick et al., 2013).

1.2 Biogeochemical processes of the marine carbonate system

1.2.1 Ocean-atmosphere CO₂ flux

The exchange of CO₂ between the ocean and the atmosphere is an important process modulating both the concentration of CO₂ in the atmosphere and the carbonate system in seawater. Ocean-atmosphere CO₂ flux is calculated as:

$$\text{flux} = k \cdot \Delta p\text{CO}_2 \cdot K_0 \quad (1.6)$$

where k is the gas transfer velocity, K_0 is the solubility of CO₂ in seawater and $\Delta p\text{CO}_2$ is the difference in the partial pressure of CO₂ between water and air. The difference in partial pressure between the water and the air is influenced by various marine, atmospheric and terrestrial processes operating on a range of timescales. These processes include biological production and ocean circulation as well as anthropogenic influences such as fossil fuel emissions and land use changes.

While the direction of ocean-atmosphere CO₂ flux is determined by $\Delta p\text{CO}_2$, the rate of the flux is determined by the gas transfer velocity (Liss and Merlivat, 1986). Usually, k is scaled with wind speed using one of several parameterisations (Wanninkhof, 1992; Nightingale et al., 2000; Sweeney et al., 2007; Ho et al., 2011; Wanninkhof, 2014). The physical mechanisms affecting k , which underlie the empirical relationship with wind speed, include turbulence, bubble formation, surfactants and ice cover. Wind speed alone does therefore not perfectly represent the physics of gas transfer at the sea surface and the uncertainty of the parameterisations of k increases at high wind speeds where there are fewer measurements (Smith et al., 2010b). The solubility of CO₂ in seawater is strongly temperature dependent

(Weiss, 1974) with colder water being able to dissolve more gas. In some high latitude regions, cooling and sea ice formation create dense water masses, which sink, transporting this CO_2 to depth and away from contact with the atmosphere. This is known as the solubility pump (Figure 1.2). The exchange of CO_2 between the ocean and the atmosphere affects the amount of DIC in the water but does not directly affect TA.

1.2.2 Photosynthesis and respiration

The structure and function of the marine food web strongly affects the marine carbonate system. Photosynthesis by phytoplankton in the surface ocean converts DIC to organic carbon and this primary production is limited by light availability, predation and nutrient concentrations. In much of the Southern Ocean primary production is limited by iron availability (Martin, 1990). Phytoplankton are consumed by zooplankton which in turn feed larger animals, but at each trophic level some of this organic carbon is lost as faecal pellets, dead organisms and exuded dissolved organic carbon (DOC). Much of this organic carbon is remineralised back into DIC by bacteria within the upper ocean but some sinks out of the surface mixed layer, thereby removing carbon from the surface ocean and contact with the atmosphere. This is known as the organic carbon pump (Figure 1.2).

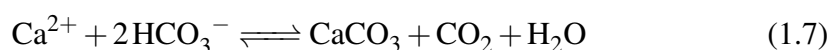
Whereas photosynthesis is limited to the upper, sunlit ocean, remineralisation continues at depth, meaning that most organic carbon is remineralised in the water column and less than 1% of particulate organic carbon (POC) is deposited on the seafloor (Lee et al., 2004). The older a water mass is (the longer it is since it was in contact with the atmosphere), the higher the DIC concentration it tends to have because more organic carbon has been remineralised. Eventually, deep water masses are upwelled and the inorganic molecules they contain are again able to fuel primary production and interact with the atmosphere.

Photosynthesis and respiration do not have a direct effect on carbonate alkalinity although they do cause a slight TA increase and decrease, respectively, due to the assimilation and remineralisation of nitrate (Brewer and Goldman, 1976).

When phytoplankton take up nitrate they also take up protons thereby increasing alkalinity. The ratio of the influence of photosynthesis and respiration on DIC and TA therefore depends on the carbon to nitrogen ratio of the organic matter being produced or respired. This ratio can be approximated as 106:16 (Redfield et al., 1963) but varies depending on the evolutionary history of the primary producer, growth rate and nutrient availability (Geider and La Roche, 2002; Quigg et al., 2003; Arrigo, 2005).

1.2.3 Calcium carbonate precipitation and dissolution

The two main forms of calcium carbonate in the ocean are calcite and its more soluble polymorph, aragonite. The precipitation of these minerals reduces TA and DIC in a 2:1 ratio (Zeebe and Wolf-Gladrow, 2001) as one mole of DIC and two negative charge equivalents are consumed to produce one mole of calcium carbonate and the reverse is true when this mineral dissolves (Equation 1.7). The precipitation of calcium carbonate causes an increase in $p\text{CO}_2$ and, potentially, a reduction in the uptake of atmospheric CO_2 . This is referred to as the CaCO_3 counter pump (Figure 1.2).



The saturation state (Ω) of calcium carbonate describes the thermodynamic potential for this mineral to precipitate or dissolve and is calculated as the product of the concentrations of dissolved calcium and carbonate ions divided by their solubility product at in-situ temperature, salinity and pressure (Zeebe and Wolf-Gladrow, 2001). Any process which decreases the concentration of CO_3^{2-} ions, such as dilution or ocean acidification, therefore causes a decrease in the saturation state of calcium carbonate. Water with a saturation state less than 1 is described as undersaturated with respect to this mineral meaning that calcium carbonate will dissolve if unprotected. Wintertime undersaturation of aragonite is predicted in the surface

waters of the Southern Ocean south of 60°S by 2030 (McNeil and Matear, 2008) and the annual mean saturation state in the Southern Ocean is predicted to be less than 1 by the end of this century (Orr et al., 2005).

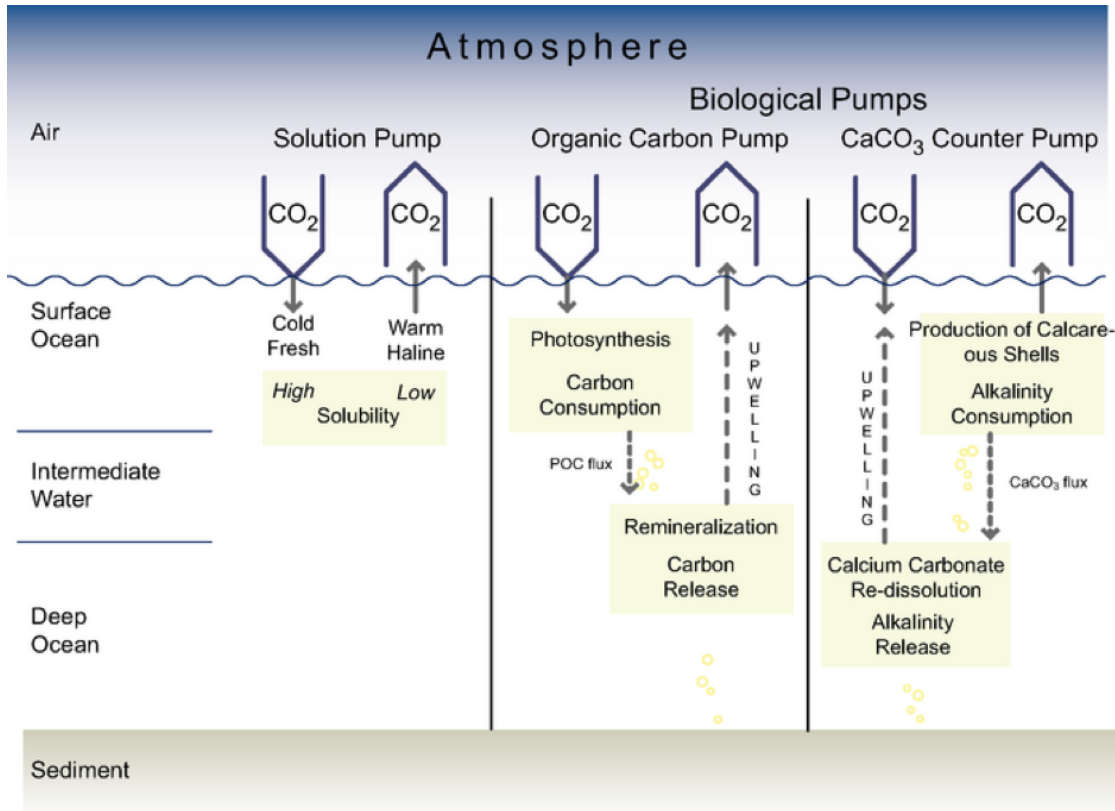


Figure 1.2: A schematic of the three ocean carbon pumps. From Heinze and Maier-Reimer (1991).

There are two significant biogeochemical consequences of a change in saturation state. Firstly, there is growing concern over how decreasing saturation states may affect the marine organisms that build calcium carbonate structures. In the Southern ocean, pteropods (Comeau et al., 2010; Bednaršek et al., 2012; Manno et al., 2012), foraminifera (Moy et al., 2009) and Antarctic krill (Kawaguchi et al., 2013) may be vulnerable to ocean acidification and resulting changes to their biomass, number and distribution could have significant ecological impacts. A reduction in the amount of CaCO₃ precipitated in surface waters may also reduce the efficiency of the organic carbon pump because CaCO₃ has been hypothesized to

act as ballast to sinking particles, increasing the vertical export of organic carbon (Klaas and Archer, 2002; Armstrong et al., 2002).

The second consequence of a changing saturation state relates to the dissolution of marine CaCO_3 sediments. The solubility of CaCO_3 increases with pressure and therefore depth in the water column. The depth at which the in situ CO_3^{2-} ion concentration crosses below the CO_3^{2-} concentration at saturation is called the saturation horizon. The aragonite saturation horizon is shallower than that of calcite due to its higher solubility. Waters of the surface ocean are supersaturated with respect to CaCO_3 minerals, whereas most of the deep ocean is undersaturated and is therefore corrosive to CaCO_3 sediments on the seafloor. If the concentration of CO_3^{2-} ions in the ocean decreases then the saturation horizon becomes shallower, exposing more of the seafloor to undersaturated water and causing more carbonate sediments to dissolve. Dissolution of carbonate sediments increases CO_3^{2-} ions which reduces pCO_2 , allowing the ocean to absorb more atmospheric CO_2 . This operates as a feedback to atmospheric CO_2 and climate over thousands to tens of thousands of years (Ridgwell and Zeebe, 2005).

1.3 Oceanographic context

1.3.1 The Antarctic Circumpolar Current

The main oceanographic feature of the Southern Ocean is the Antarctic Circumpolar Current (ACC) which flows eastwards around the Antarctic continent with a mean transport of approximately 134 Sverdrups ($1 \text{ Sv} = 10^6 \text{ m}^3 \cdot \text{s}^{-1}$) (Cunningham et al., 2003). This unbroken, zonal flow is a key part of global ocean circulation and global climate as it allows the transport of heat and chemicals between the Atlantic, Indian and Pacific basins. The ACC is driven by buoyancy forcing and strong westerly winds which cause northward Ekman transport and result in the shoaling of isopycnals towards the south (Marshall and Speer, 2012). The sloping of isopycnals across the ACC is not uniform, but occurs in several steps (Deacon, 1937) which are also associated with strong surface currents (Nowlin et al., 1977). These regions of

large horizontal density gradients and strong flow are the fronts of the ACC (Figure 1.3) which, listed from north to south, are the Sub-Antarctic Front (SAF), the Polar Front (PF) and the Southern ACC Front (SACCF) (Sievers and Nowlin, 1984; Orsi et al., 1995). A fourth front known as the Southern Boundary (SB) is often also identified and is the southernmost limit of the ACC.

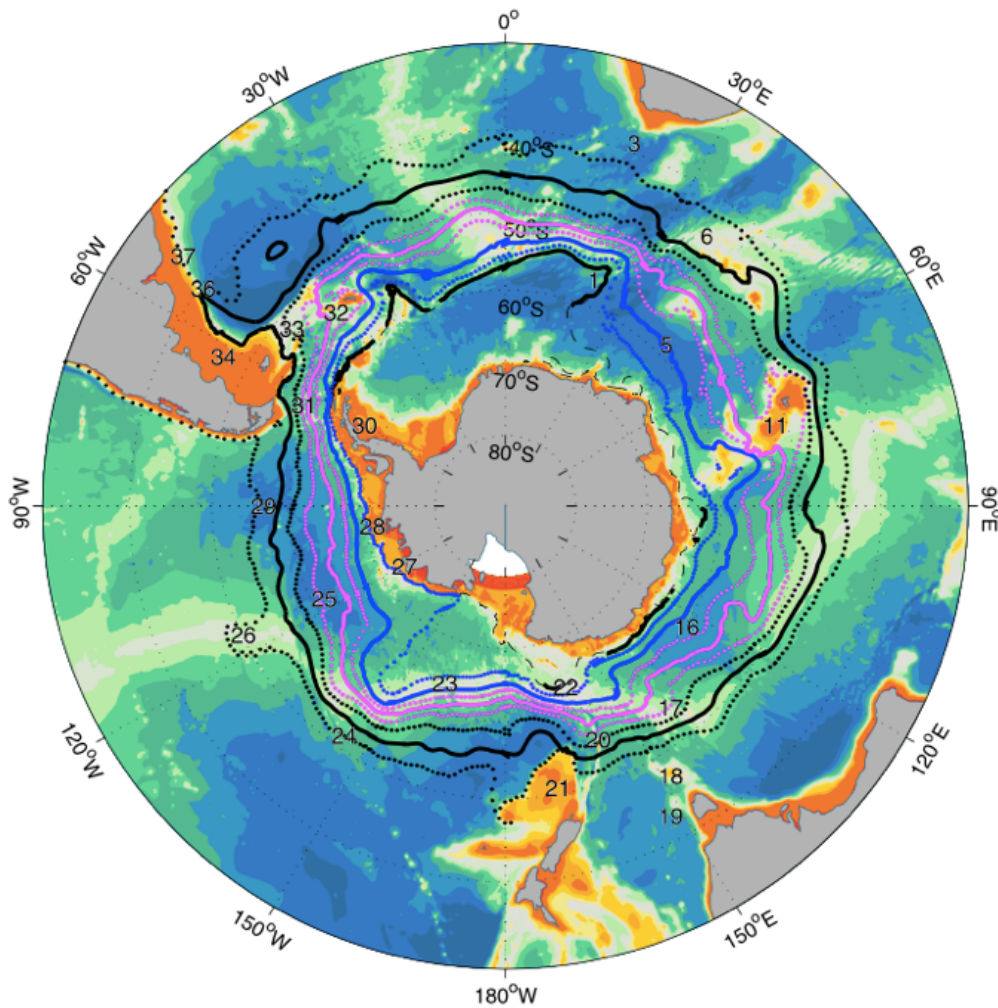


Figure 1.3: The mean position of the ACC fronts mapped from sea surface height, taken from Sokolov and Rintoul (2009). From south to north: SB (black), SACCF (blue), PF (pink), SAF (black). Main frontal jets are shown as solid lines with other branches shown as dashed lines.

The SAF separates warmer, saltier subtropical waters further north from colder, fresher waters further south. Its position is indicated by the northward sinking of the salinity minimum or the point at which the potential temperature at 400m depth

exceeds 4-5 °C (Orsi et al., 1995). The PF separates sub-Antarctic waters from cold polar surface waters and is usually identified by the northern limit of the 2 °C isotherm at 200m or the southern limit of the 2.2 °C isotherm at 800m (Orsi et al., 1995; Belkin and Gordon, 1996). The SACCF can be identified as the poleward limit of water warmer than 1.8 or 2 °C in the temperature maximum layer deeper than 500m (Orsi et al., 1995; Sokolov and Rintoul, 2002). The location of the ACC fronts can also be identified using remotely sensed sea surface height (SSH) (Gille, 1994). This allows much greater spatial and temporal resolution than ship-based data and therefore provides a more detailed picture of the fronts and their variability. Studies based on SSH and the gradient of SSH show that the three main fronts of the ACC described above are often composed of multiple branches or jets which merge and diverge over time and respond to bathymetry (Sokolov and Rintoul, 2007, 2009). These studies also find that the frontal locations derived from SSH are consistent with more traditional, hydrographic criteria and that contours of absolute SSH can be used to identify the location of ACC fronts over large spatial scales.

The frontal structure of the ACC is closely connected to the formation and properties of the Southern Ocean water masses. Subantarctic Mode Water (SAMW) is formed north of the SAF as surface water is mixed downwards by deep convection (McCartney, 1977; McNeil et al., 2001) and then detrained as the mixed layer depth (MLD) shoals in summer (Carter et al., 2014). Antarctic Intermediate Water (AAIW) can be identified as a salinity minimum beneath SAMW and is mostly formed south of the SAF by the northward subduction of Antarctic Surface Water (AASW) along isopycnals (Carter et al., 2014). These mode and intermediate waters are important for ventilating the sub-tropical thermocline, providing nutrients for biological production at lower latitudes and sequestering atmospheric CO₂ (Sarmiento et al., 2004; Sallée et al., 2012; Jones et al., 2016a).

Circumpolar Deep Water (CDW) is the most voluminous water mass in the Southern Ocean (Pardo et al., 2012) and is usually divided into Upper Circumpolar Deep Water (UCDW) and Lower Circumpolar Deep Water (LCDW). UCDW is

characterised by an oxygen minimum (Callahan, 1972) due to the age of this water mass. LCDW originates as North Atlantic Deep Water (NADW) and is identified by its high salinity. As LCDW travels around the ACC, it is, on average, transported northwards into the subtropical basins of the Indian and Pacific Oceans where its oxygen concentration and density are reduced, before returning southwards in the UCDW density class (Sloyan and Rintoul, 2001b).

The densest water in the global oceans is Antarctic Bottom Water (AABW) which is created around the Antarctic continent. The formation of AABW involves complex interactions between the ocean, the atmosphere, sea ice and ice shelves which are poorly captured in current global models (Meijers, 2014). Upwelled CDW becomes denser through mixing with High Salinity Shelf Water (HSSW) and heat loss to the atmosphere. Cooling and brine rejection from sea ice formation are especially strong in polynyas where open water is maintained (Rintoul, 1998; Ohshima et al., 2013). The coldest and densest AABW is Weddell Sea Deep Water (WSDW) which is formed in the Weddell Sea (Gill, 1973; Orsi et al., 1999) and is thought to be the largest source of AABW (Pardo et al., 2012; Meredith, 2013). The warmest and saltiest type of AABW is Ross Sea Bottom Water (RSBW) which ventilates the Pacific and Indian basins (Orsi et al., 1999; Jacobs et al., 1970). The third major AABW formation region is the Adelie and George V coasts (Rintoul, 1998; Williams et al., 2010) where Adelie Land Bottom Water (ALBW) is created. Other ice production regions in East Antarctica could also contribute to AABW (Williams et al., 2010) and Cape Darnley (65-69 ° East) has recently been identified as a source of bottom water (Ohshima et al., 2013).

The water masses described above comprise the Southern Ocean component of the meridional overturning circulation (Figure 1.4) which is broadly divided into an upper and a lower cell (Lumpkin and Speer, 2007). CDW outcrops south of the PF and some of it moves northwards, becoming fresher due to precipitation, before eventually being subducted as SAMW or AAIW. Some of the CDW which upwells south of the ACC undergoes processes in the high latitude and coastal Southern Ocean which transform it into AABW, thereby forming the lower cell of the cir-

ulation. The strength and location of these circulation cells is thought to have implications for carbon uptake and climate over various timescales (see Section 1.4).

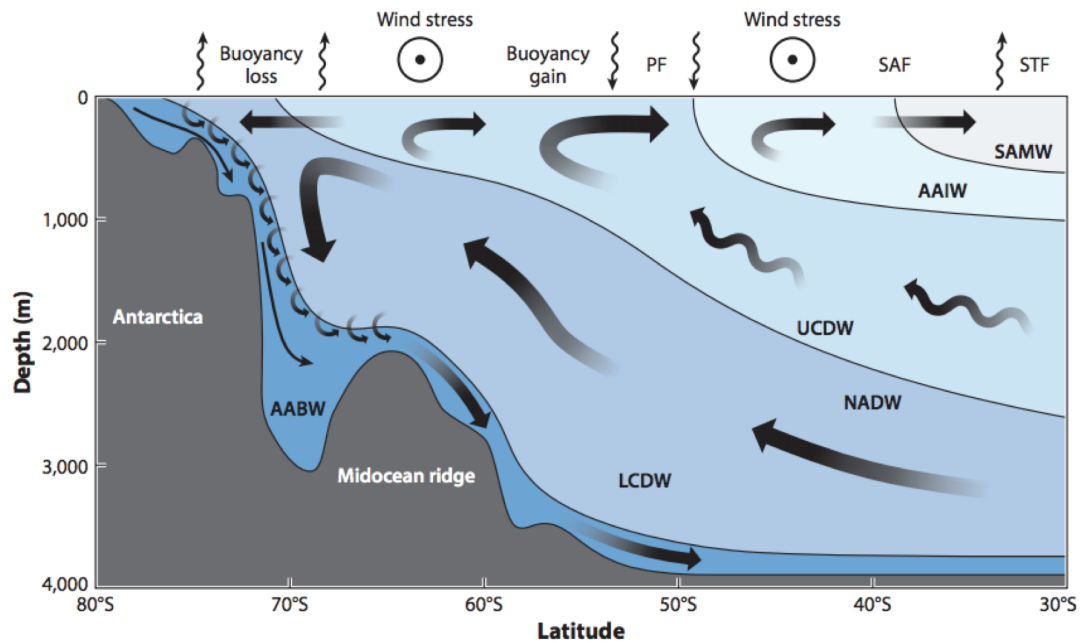


Figure 1.4: Schematic of the Southern Ocean meridional overturning circulation with water masses and atmospheric forcing. Taken from Gent (2016), adapted from Speer et al. (2000).

1.3.2 Drake Passage and the Scotia Sea

Drake Passage is the narrowest constriction of the ACC (Figure 1.3) and is the most studied part of the Southern Ocean, providing an ideal location to observe the fronts and water masses of the ACC (Meredith et al., 2011). The three main fronts of the ACC are clearly defined in Drake Passage and show multiple branches merging into single jets (Lenn et al., 2008). Displacement of the fronts and the abundance of eddies can cause water mass properties to vary over time at a given location (Provost et al., 2011).

The two main hydrographic sections occupied across Drake Passage are SR1 in the west and SR1b in the east (Figure 1.5). Between the two sections lies a region of complex bathymetry, including the Shackleton Fracture Zone (SFZ), which influences the mixing and movement of deep water masses across the passage (Sudre

et al., 2011). WSDW is found in the eastern Drake Passage, having exited the Weddell Sea through Orkney Passage and travelled westwards (Naveira Garabato et al., 2002b). In the LCDW density class, South Pacific Deep Water is observed in the west of Drake Passage (Sievers and Nowlin, 1984; Naveira Garabato et al., 2002b). Above CDW lies AAIW formed in the Bellingshausen Sea (Naveira Garabato et al., 2009) and SAMW formed in the southeast Pacific.

Immediately to the east, and downstream, of Drake Passage lies the Scotia Sea which is bounded by island arcs on its northern, eastern and southern edges (Figure 1.5). The SAF and PF are topographically constrained through deep channels in the North Scotia Ridge (Smith et al., 2010a) whereas the SACCF continues eastwards and leaves the Scotia Sea to the south west of South Georgia. To the south, the Scotia Sea is separated from the Weddell Sea basin by the South Scotia Ridge. The deep passages of the South Scotia Ridge are important conduits for WSDW into the Scotia Sea, where it then spreads westwards towards Drake Passage and eastwards towards the Georgia Passage (Naveira Garabato et al., 2002b). The transition from the waters of the ACC to the waters of the Weddell Gyre is known as the Weddell-Scotia confluence. In this region, the water masses of the Scotia Sea are modified through interactions with Weddell Sea waters and recently ventilated shelf waters from the Antarctic Peninsula (Whitworth et al., 1994; Thompson and Youngs, 2013).

There is intense modification of the deep water masses of the ACC in the Scotia Sea (Naveira Garabato et al., 2002b), including the cooling and freshening of CDW as it crosses the basin (Locarnini et al., 1993). These modifications are caused by the inflow of WSDW and strong diapycnal mixing related to the complex topography (Heywood et al., 2002), although there may be significant spatial and temporal variability in this deep mixing (Meredith et al., 2014). The A23 section (Figure 1.5) runs from the northern Weddell Sea, crosses the South Scotia Ridge and the SACCF and finishes just south of South Georgia. The section has been occupied ten times since 1995 with the primary aim of investigating AABW variability. Repetition of the A23 section has highlighted a warming of AABW in the Scotia Sea (Mered-

ith et al., 2008b) as well as some very strong gradients in bottom water properties, thought to be caused by episodic flushing of deep trenches (Meredith et al., 2013).

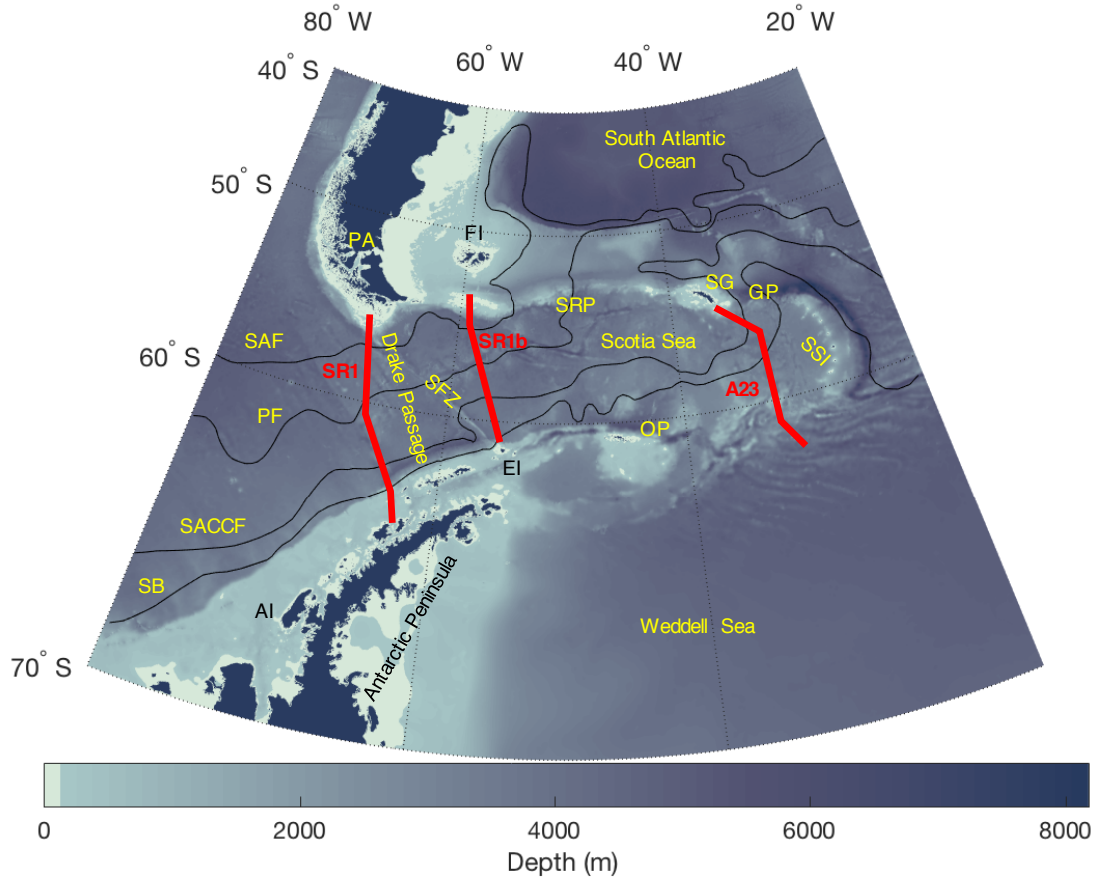


Figure 1.5: Map of the Scotia Sea region. Mean ACC frontal positions from Orsi et al. (1995) shown as black lines with data from the catalogue of Australian Antarctic and sub-Antarctic metadata. Bathymetry data are from Smith and Sandwell (1997). Abbreviated features are: Sub-Antarctic Front (SAF), Polar Front (PF), Southern ACC Front (SACCF), Southern Boundary (SB), Falkland Islands (FI), Elephant Island (EI), Adelaide Island (AI), Orkney Passage (OP) on the South Scotia Ridge, the South Sandwich Islands (SSI), South Georgia (SG), Georgia Passage (GP), Shag Rocks Passage (SRP) on the North Scotia Ridge, Punta Arenas (PA) and the Shackleton Fracture Zone (SFZ). Red lines show the approximate cruise tracks of the SR1, SR1b and A23 hydrographic sections.

1.3.3 The West Antarctic Peninsula

The Antarctic Peninsula extends about 1500 km from the main Antarctic continent to Drake Passage, separating the waters of the Bellingshausen Sea and the south

east Pacific from the Weddell Sea (Figure 1.5). The eastern side of the peninsula forms the western boundary of the Weddell Gyre and has large ice shelves which play an important role in bottom water formation (Van Caspel, 2016). The West Antarctic Peninsula (WAP) is mountainous and highly glaciated with a complex and convoluted coastline. Its continental shelf is, on average, 200 km wide and 430 m deep (Ducklow et al., 2007) and the proximity of the ACC means that the marine environment of the WAP is strongly influenced by oceanic waters. UCDW intrudes onto the shelf, bringing heat, carbon and nutrients, reducing ice cover and stimulating phytoplankton growth (Martinson and McKee, 2012; Prézelin et al., 2004). A large part of the WAP is seasonally covered by sea ice which greatly influences the ecology (Ducklow et al., 2013) and carbon cycling processes (Section 1.4.3).

In the second half of the twentieth century the Antarctic Peninsula experienced a rapid increase in air temperature (Vaughan et al., 2003; Turner et al., 2005) and coincident changes in the temperature and stratification of the ocean west of the Antarctic Peninsula have been observed (Meredith and King, 2005). However, a recent study shows that since the late 1990s there has been an absence of warming on the peninsula, driven by changes in atmospheric circulation and consistent with natural variability (Turner et al., 2016). Most glaciers on the peninsula have been retreating (Cook et al., 2005) and, unlike other parts of the Southern Ocean, the WAP shelf and southern Bellingshausen Sea have experienced a decrease in sea-ice cover (Stammerjohn et al., 2008; Comiso and Nishio, 2008; Parkinson and Cavalieri, 2012). Interannual to decadal variability in the atmospheric circulation of the region has also been observed. The Southern Annular Mode (SAM) is a measure of the atmospheric pressure difference between mid and high latitudes of the southern hemisphere. There has been a trend towards the positive phase of the SAM over recent decades with a concordant intensification of westerly winds (Thompson and Solomon, 2002; Marshall, 2003). The changes in wind are thought to be responsible for part of the observed warming on the peninsula (Marshall et al., 2006) and changes in ice dynamics in the region (Holland and Kwok, 2012). The strong sea-

sonal and interannual variability makes the region an ideal location to study carbon system processes and their interactions on various timescales.

Summer data from the Palmer Long-Term Ecological Research (Pal-LTER) grid show that carbonate chemistry on the WAP shelf is primarily influenced by primary production (Hauri et al., 2015) which is known to be strongly influenced by wind and sea ice conditions (Vernet et al., 2008; Montes-Hugo et al., 2009; Venables et al., 2013). During the summer, surface water DIC decreases due to a reduction in vertical mixing and an increase in primary production (Montes-Hugo et al., 2010), causing CO₂ undersaturation, especially in near shore waters (Carrillo et al., 2004). In winter, mixing with carbon-rich UCDW increases surface DIC, increasing $f\text{CO}_2$ and decreasing the saturation state of calcium carbonate minerals (Hauri et al., 2015). Due to the large spatial and temporal variability it is difficult to determine the net impact of these processes on ocean-atmosphere CO₂ fluxes on the WAP. In near-shore areas of the West Antarctic, freshwater inputs also affect carbonate chemistry through the dilution of carbonate ions. However, the influence of primary production dominates; biological CO₂ uptake in spring and summer increases the pH and the carbonate ion concentration, increasing Ω (Mattsdotter Björk et al., 2014; Hauri et al., 2015). A better mechanistic understanding of these seasonal processes is needed in order to understand how the carbonate system in the region will respond to environmental changes.

The Rothera Oceanographic and Biological Time Series (RaTS) is located in Ryder Bay, 4 km offshore of Rothera base on Adelaide Island (Figure 1.5) on the WAP. Full depth (500m) CTD profiles have been taken roughly weekly since 1998, providing a unique record of water column structure and chlorophyll distribution. There is a clear seasonal cycle in primary production in the bay with a summer diatom bloom occurring in January (Clarke et al., 2008). Sediment traps suggest that only about 1% of this organic matter is exported to 200m (Weston et al., 2013), although the inaccuracies of sediment traps may mean that this figure is an underestimate (Buesseler et al., 2007). Ryder Bay is seasonally covered by sea ice and this strongly affects water column structure and therefore primary production. Winters

with less sea ice allow deeper mixing and this reduced stratification causes more heat uptake and less primary production during the following summer (Venables et al., 2013; Venables and Meredith, 2014). The Bay is also strongly influenced by glacial runoff and this is found to be an even larger source of freshwater than sea ice melt (Meredith et al., 2008a). Glacial melt affects the vertical stability of the water column and delivers iron to the surface water, alleviating iron limitation and increasing primary production (Dierssen et al., 2002; Annett et al., 2015).

1.4 The role of the Southern Ocean in carbon uptake

1.4.1 Glacial timescales

Ice core data show that there is a strong correlation between atmospheric CO₂ and temperature over the glacial-interglacial cycles of the last 800 thousand years, with lower CO₂ during glacials (Lüthi et al., 2008). Although these cycles were most likely triggered by orbital forcing, their amplitude and timing, and the relationship between temperature and atmospheric CO₂ are not fully understood (Sigman et al., 2010). The strong correspondence between atmospheric CO₂ and Antarctic temperatures (which are distinct from temperature variations at other latitudes) suggests that the Southern Ocean plays an important role in controlling atmospheric CO₂ (Watson et al., 2015). Several mechanisms have been suggested for the connection between the Southern Ocean and atmospheric CO₂, most of which relate to reduced ventilation of deep water during glacials.

At lower temperatures, salinity has a greater effect on density than temperature. This means that the low salinity of AASW became more important during glacials and strengthened stratification (Sigman et al., 2010). Salinity and temperature reconstructions from pore waters suggest that the deep Southern Ocean was more stratified during glacials than today (Adkins et al., 2002). As density differences are inversely proportional to mixing rates this suggests less mixing in the deep Southern Ocean which would have resulted in a net lengthening of the pathway by which AABW mixes up, into overlying waters (Watson and Naveira Garabato,

2006). Isotopic data from deep-sea corals in Drake Passage and foraminifera in the Pacific further support this reduced ventilation during glacials (Burke and Robinson, 2012; Siani et al., 2013).

It is thought that during glacials NADW was replaced with Glacial North Atlantic Intermediate Water (GNAIW), a less dense water mass which upwelled further north than CDW does today (Sigman et al., 2010). This isolated the deep ocean resulting in less outgassing of CO₂. Also, due to a larger region of buoyancy loss, upwelled water spent longer at the surface, allowing more preformed nutrients to be utilised, increasing CO₂ drawdown (Watson et al., 2015). The more northerly latitude of the upwelling region during glacials was likely related to an equator-ward shift in the westerly winds. With the main wind stress not aligned with Drake Passage the meridional flow would have been weaker, leading to weaker upwelling and less CO₂ outgassing during glacials (Toggweiler et al., 2006).

Increased sea ice cover during glacials may also have provided a positive feedback to climate through Southern Ocean ventilation. An increased ice extent would have limited gas exchange in regions of deep water ventilation, thereby reducing CO₂ outgassing (Stephens and Keeling, 2000). Furthermore, sea ice cover across the upwelling region of the ACC during glacials would have reduced the buoyancy gain by warming and reduced the strength of upwelling in the upper cell (Watson and Naveira Garabato, 2006). Finally, an increase in deep water DIC concentration, caused by reduced Southern Ocean ventilation would have decreased the saturation state of calcium carbonate causing carbonate sediments to dissolve, increasing TA and allowing more CO₂ to be taken up by the ocean (Watson and Naveira Garabato, 2006).

The mechanisms described above are not mutually exclusive (Watson and Naveira Garabato, 2006) so it is likely that all or some of them have played a roll in modulating atmospheric CO₂ and temperature over glacial-interglacial cycles. Indeed, the stepped chronology of the CO₂ decrease into glacials may reflect the progressive action of more than one of these mechanisms (Sigman et al., 2010).

1.4.2 Contemporary Southern Ocean CO₂ uptake

The Southern Ocean plays an important role in the exchange of CO₂ between the atmosphere and the interior of the ocean and therefore modulates atmospheric CO₂ and global climate. There are, however, marked regional differences in the CO₂ sink within the Southern Ocean. The Sub-Antarctic Zone (SAZ), between the Sub-Tropical Front (STF) and the SAF, is a large sink region due to biological production and winter cooling and is estimated to take up about 1 PgC.yr⁻¹ which is roughly half of the annual global ocean uptake (Metzl et al., 1999; Takahashi et al., 2012). In the high latitude Southern Ocean, south of 58°S, processes are complex and data are sparse. Ocean inversions suggest a weak sink of atmospheric CO₂, whereas observations of ΔpCO₂ suggests the ocean is a weak source (Lenton et al., 2013). The seasonal ice zone appears to make a small contribution to CO₂ flux on an annual basis despite large seasonal changes (Takahashi et al., 2009, 2012; Lenton et al., 2013). However, as Arrigo et al. (2008) points out, most estimates are based on open ocean data and neglect the uptake of CO₂ in the productive shelf regions of the Antarctic.

Overall, surface observations suggest that the region south of 44 °S is a small sink of about 0.3 PgC.yr⁻¹, resulting from the balance between a substantial out-gassing of natural CO₂ at high latitudes and a strong uptake of atmospheric CO₂ further north (Gruber et al., 2009; Lenton et al., 2013). This uptake of atmospheric CO₂ includes anthropogenic CO₂ (C_{ant}) which is carbon released by human activities such as fossil fuel burning, cement production and land use changes. The ocean takes up about 26% of the anthropogenic carbon released to the atmosphere on an annual basis (Le Quéré et al., 2016) and it is estimated that more than 40% of anthropogenic carbon in the ocean has entered south of 40 °S (Khatiwala et al., 2009).

SAMW and AAIW make the largest contribution to C_{ant} uptake by the Southern Ocean and the greatest inventories are found in, and downstream of, regions with strongest subduction (Sallée et al., 2012; Tanhua et al., 2017). C_{ant} concentrations are approximately 37 μmol kg⁻¹ in SAMW and 19 μmol kg⁻¹ in AAIW

(Pardo et al., 2014). These mode and intermediate waters transport anthropogenic carbon northwards into the interior of the subtropical oceans. As a result, although it makes up a large proportion of the global ocean C_{ant} uptake, the Southern Ocean south of 50°S only stores about 9% of the oceanic inventory (Sabine et al., 2004). Due to its age, CDW has low C_{ant} concentrations of around $5 \mu\text{mol kg}^{-1}$ (Ríos et al., 2010) but because it is so voluminous CDW makes up the largest fraction of the Southern Ocean C_{ant} inventory (Pardo et al., 2014). The concentration of C_{ant} in AABW varies between study regions and methods from 0 to $\sim 20 \mu\text{mol kg}^{-1}$ (Lo Monaco et al., 2005). Considering that the overall uncertainty on C_{ant} calculations is usually $\sim 6 \mu\text{mol kg}^{-1}$, confident quantification of C_{ant} in deep and bottom water masses of the Southern Ocean is challenging.

Anthropogenic carbon cannot be measured directly, but can be calculated using three groups of methods. All three groups have inherent assumptions and limitations, some of which are especially problematic in the Southern Ocean. Back calculation methods (Gruber et al., 1996; Sabine et al., 2004) use oxygen and TA data to calculate the amount of organic matter remineralisation and calcium carbonate dissolution since the water was last at the surface. Subtracting the DIC due to remineralisation, dissolution and pre-industrial CO_2 uptake from the measured DIC leaves anthropogenic carbon. Back calculation methods can be sensitive to inaccuracies in oxygen data (Ito et al., 2004; Van Heuven et al., 2011b) and difficulties estimating preformed TA (Pérez et al., 2002). Transit time distribution (TTD) methods (Hall et al., 2002; Waugh et al., 2004) estimate a ventilation age from tracer data and combine this with the known time history of atmospheric CO_2 . Both back calculation and TTD methods suffer from the fact that the extent of the equilibration of gases when the water was last ventilated is largely unknown and can be variable. This is especially true for AABW which may have spent very little time at the surface in a region where ice cover influences gas exchange. Multiple linear regression (MLR) methods (Wallace and Johnson, 1994; McNeil et al., 2001; Tanhua et al., 2017) can be used to investigate the change in anthropogenic carbon between repeat sections. They correlate DIC with other variables from one cruise and then

apply this predictive relationship to another cruise. Deviations from the predicted DIC indicate anthropogenic carbon. These methods are vulnerable to biases in the data and also assume a steady state ocean, which is generally not the reality (Tanhua et al., 2017).

Changes in temperature, biology and circulation all affect surface ocean CO₂ on a variety of temporal and spatial scales and are interdependent. This complexity makes it very challenging to achieve the mechanistic understanding required to predict future changes of the Southern Ocean CO₂ sink. Quantification and understanding of the Southern Ocean CO₂ sink is also hampered by lack of data, especially at high latitudes and during winter. Nevertheless, several studies have made progress in advancing our understanding of the changing Southern Ocean CO₂ sink. A decrease in the Southern Ocean CO₂ sink between 1981 and 2004 was found using an atmospheric inversion (Le Quéré et al., 2007) and was attributed to increased upwelling of deep water, caused by stronger westerlies which are related to a more positive phase of the SAM. Since the 1960s there has been a trend to a more positive phase of the SAM (Thompson and Solomon, 2002; Jones et al., 2016b), which leads to stronger westerlies in the Antarctic and Polar Frontal Zone of the Southern Ocean, causing more northward Ekman transport and leading to more upwelling (Hall and Visbeck, 2002). This increase in carbon delivery to the surface may be partly offset by increased export production and increased CO₂ solubility due to cold sea surface temperature anomalies (Lovenduski, 2005) but overall, a positive SAM is expected to decrease the Southern Ocean sink strength (Lenton and Matear, 2007). The summertime increase in the SAM since the mid 1960s is thought to be unprecedented over the last 600 years and is likely caused by anthropogenic forcing (Jones et al., 2016b).

More recently, a reinvigoration of the Southern Ocean CO₂ sink has been observed (Landschützer et al., 2015). The increase in sink strength cannot be caused by a reversal of the SAM trend as this has not been observed. Instead it is attributed to a combination of thermally driven and circulation driven changes, with regional variability. In the Pacific sector there has been a persistent cooling trend whereas

in the Atlantic and Indian sectors there has been a reduction in surface ocean CO₂ caused by reduced upwelling (Landschützer et al., 2015). This is supported by modelling results which found that weaker upper ocean circulation led to increased carbon uptake during the 2000s, especially in the Atlantic and Indian sectors (DeVries et al., 2017).

Models predict that the Southern Ocean CO₂ sink will continue to increase due to weakening upper ocean circulation and increasing atmospheric CO₂ (Ito et al., 2015; Wang et al., 2016). However, as atmospheric CO₂ continues to rise, there may come a point where the decrease in C_{ant} uptake caused by decreased ventilation may outweigh the reduced outgassing of natural CO₂, decreasing the ocean CO₂ sink (DeVries et al., 2017). Currently, the models used to predict the future CO₂ sink lack realistic representation of several important features and processes such as eddies, sea ice, bottom water formation and ecological feedbacks, all of which are likely to affect the ocean uptake of CO₂. Furthermore, many ocean biogeochemical models fail to capture the magnitude of the seasonal cycle of CO₂ at high latitudes (Lenton et al., 2013), due to biases in the timing and amplitude of primary production and sea surface temperature (Kessler and Tjiputra, 2016). This inability to reconcile modelled and observed CO₂ fluxes highlights our poor understanding of the high-latitude carbon cycle and limits confidence in our ability to predict future changes to Southern Ocean CO₂ uptake.

1.4.3 Sea ice and the carbonate system

Sea ice is a major contributor to our poor understanding of the oceanic carbonate system at high latitudes. Not only does ice cover hinder data collection and therefore limit the scope of observational flux estimates, it also adds complexity to the carbon cycle through its effect on gas exchange, vertical stability and biological production. Roughly 15 million km² of the Southern Ocean is seasonally covered by sea ice, yet its net effect on ocean carbon uptake on an annual basis remains uncertain.

Figure 1.6 shows a conceptual model of the effect of sea ice on the carbonate system over one seasonal cycle. As ice forms, solutes are rejected, increasing DIC

and TA in the under-ice water. The sinking of this dense water to depth could therefore provide a pathway for the export of carbon (Rysgaard et al., 2011), although recent modelling results suggest that less than 2% of this rejected DIC is exported to depth (Moreau et al., 2016). During winter, the high CO_2 surface water is prevented from outgassing to the atmosphere by the ice. However, sea ice does not act simply as an impermeable barrier to gas exchange and ice-atmosphere CO_2 fluxes have been measured in the Antarctic (Nomura et al., 2013; Delille et al., 2014). Estimation of ocean-atmosphere CO_2 fluxes in partly ice covered waters is challenging and the conventional approach of linearly scaling the gas transfer velocity by the fraction of open water may be inadequate because of the effect of ice on surface ocean turbulence (Loose and Schlosser, 2011; Loose et al., 2014). However, recent eddy covariance measurements suggest that the effect of turbulence may be less than expected (Butterworth and Miller, 2016).

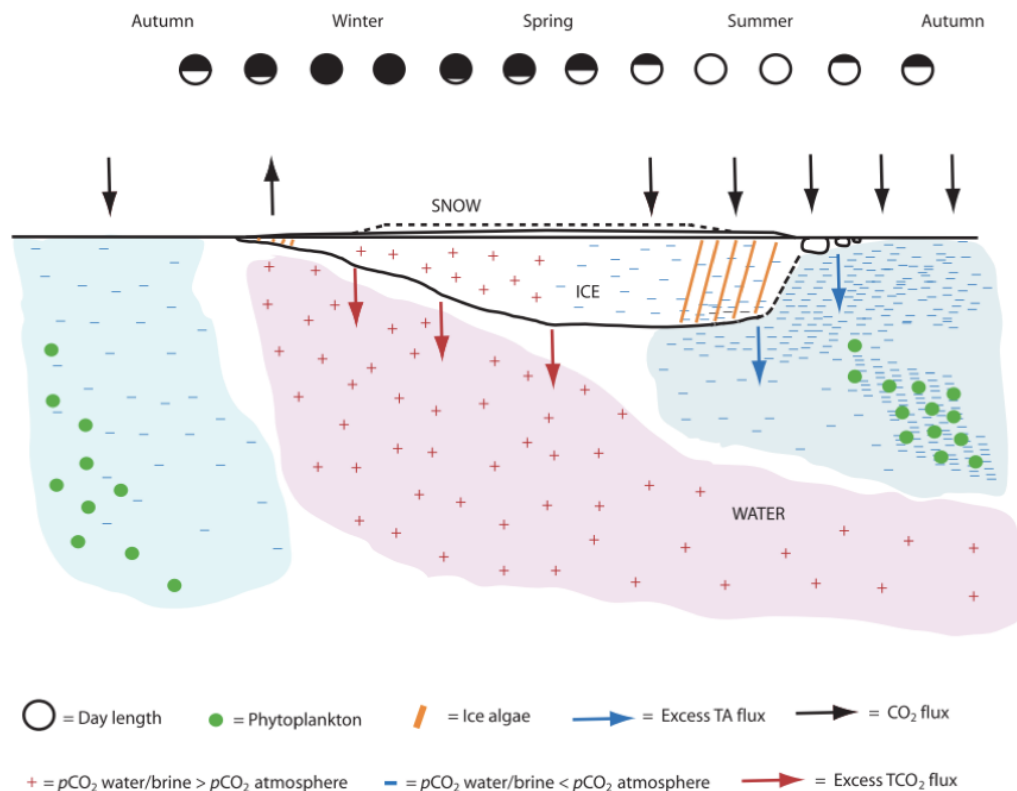


Figure 1.6: A conceptual model of the effects of seasonal sea ice on the carbonate system, taken from Rysgaard et al. (2011).

The hydrated calcium carbonate mineral ikaite ($\text{CaCO}_3 \cdot 6\text{H}_2\text{O}$) has been observed in Arctic and Antarctic sea ice (Dieckmann et al., 2008; Geilfus et al., 2013) and it is thought that the precipitation and dissolution of ikaite may act as a sink of atmospheric CO_2 (Rysgaard et al., 2007). As ice forms, the precipitation of ikaite retains TA in the ice and increases pCO_2 in the remaining brine, some of which drains into the underlying water (Rysgaard et al., 2011). Furthermore, when the ice melts in spring, ikaite crystals become a source of TA to the seawater, increasing the TA:DIC ratio in meltwater (excess TA flux in Figure 1.6), lowering CO_2 and contributing to an ocean sink of atmospheric CO_2 (Jones et al., 2010; Rysgaard et al., 2012; Fransson et al., 2013; Geilfus et al., 2016). The importance of ikaite precipitation and dissolution for atmospheric CO_2 uptake depends on the magnitude and exact timing of ikaite precipitation in sea ice which are currently not well understood (Delille et al., 2014).

An increase in day length and a reduction in snow cover on the ice increase the light available to ice algae in spring (Thomas and Dieckmann, 2002). Sea ice melt in spring also promotes phytoplankton production through stratification, increased light availability and iron release (Lizotte, 2001; Lannuzel et al., 2007). The relative timing of sea ice melt and the onset of primary production is important in determining the direction and magnitude of ocean-atmosphere CO_2 flux. If primary production reduces the pCO_2 of the surface ocean to below atmospheric pCO_2 prior to ice melt then, once the ocean surface is exposed to the atmosphere, the ocean will be a sink of atmospheric CO_2 (Yager et al., 1995). Observations during spring in the Antarctic confirm that primary production associated with ice melt is important in reducing surface ocean CO_2 (Bakker et al., 2008; Jones et al., 2010; Shadwick et al., 2014; Roden et al., 2016).

Very few studies have observed a full seasonal cycle of inorganic carbon in the seasonally ice-covered Southern Ocean. Two full annual cycles of inorganic carbon have been characterised in Prydz Bay, East Antarctica (Gibson and Trull, 1999; Roden et al., 2013). These studies were separated by 15 years and showed the same general pattern of a build up of DIC under ice in winter followed by rapid

biological drawdown of inorganic carbon in summer. However, significant differences between the two study periods were apparent, with higher DIC and lower pH in the more recent dataset which the authors attribute to a combination of ocean acidification and variations in primary production (Roden et al., 2013). This comparison highlights the challenges inherent in determining reliable decadal trends in a dynamic, sparsely-sampled environment. Multi-year datasets from different locations are required to understand the drivers of the carbonate system and their changes in both time and space.

1.5 Aim and objectives of this thesis

The aim of this thesis is to use observations to build a better understanding of how carbonate system dynamics in the Southern Ocean affect the uptake of CO₂ from the atmosphere.

Chapters 3 and 4 focus on seasonal processes in coastal Southern Ocean. The net effect of the high-latitude, seasonally sea ice covered Southern Ocean on atmospheric CO₂ remains uncertain and our ability to predict future changes in this region remains limited by a poor mechanistic understanding of the carbonate system processes underlying the ocean-atmosphere flux of CO₂. The objectives of these chapters are to calculate the ocean-atmosphere flux of CO₂ in a seasonally sea ice covered bay on the West Antarctic Peninsula and to quantify the carbonate system processes driving the seasonal cycle of DIC.

Chapters 5 and 6 use measurements from research cruises to investigate variability in Southern Ocean water masses. The overturning circulation of the Southern Ocean plays an important role in modulating atmospheric CO₂. Processes which modify the carbonate system in upwelling deep water, recently formed bottom water or subducting mode water may therefore have significant effects on the uptake of atmospheric CO₂. The objectives of Chapter 5 are to characterise the carbonate system on the Drake Passage and A23 repeat sections and to investigate differences in the carbonate system in deep water masses between these sections. The objectives

of Chapter 6 are to characterise and quantify the zonal variability of components of DIC in the deep water masses of the ACC and to investigate temporal changes in DIC in SAMW since 1990.

Chapter 2

Methods

2.1 Methods outline

This chapter describes the procedures used for the sampling and analysis of the two novel datasets presented in this thesis: the RaTS carbonate time series (discussed in Chapters 3 and 4) and the JR299 biogeochemical cruise dataset (discussed in Chapter 5). The sections below explain which methods are common between these two datasets and which methods are unique to one or other dataset. Methods and calculations which are specific to individual chapters are described in the relevant chapters.

This chapter also includes an investigation into the effect of defrosting on nutrient samples (Section 2.3.3.2) and an investigation into the sensitivity of calculated carbonate system variables to nutrient concentrations (Section 2.3.3.3).

Finally, this chapter describes the secondary quality control procedure applied to the JR299 dataset and documents the publicly accessible databases which the JR299 and RaTS datasets have been submitted to (Section 2.4).

A list of abbreviations used in this thesis is given in Appendix H.

2.2 Sampling

2.2.1 RaTS sampling

Samples for Dissolved Inorganic Carbon (DIC) and Total Alkalinity (TA) were collected between December 2010 and February 2014 at the Rothera Time Series (RaTS), about 4 km offshore, in Ryder Bay, on the West Antarctic Peninsula (Figure 2.1). Sampling was undertaken by the Rothera marine assistants from a rigid inflatable boat or through a hole in the ice approximately weekly in summer and every two weeks in winter, weather and ice permitting. If partial ice cover prevented access to the main RaTS site (site 1, Figure 2.1) then a secondary site was used (site 2, Figure 2.1). Most samples were taken at 15 m depth and some were taken at 40 m. Samples were collected in 250 mL or 500 mL borosilicate glass bottles, poisoned with 50 μ L of mercuric chloride per 250 mL of sample and sealed with greased stoppers (Dickson et al., 2007). They were transported back to the University of East Anglia at the end of each field season for analysis.

Sea ice type and fraction of ice cover were visually estimated by the marine assistants. Fast ice is sea ice which is attached to land or to the front of a glacier. Brash ice consists of floating fragments, broken from other forms of sea ice. Pack ice is an accumulation of smaller pieces of ice, connected to each other but not attached to land or a glacier. Whilst these sea ice estimates are inherently somewhat subjective, the Rothera data have been found to agree well with wider scale satellite estimates (Wallace, 2007). Temperature, salinity, fluorescence and pressure were measured during full depth (500 m at site 1) CTD casts. Discrete water samples were taken at 15 m depth for chlorophyll-a, macronutrients and salinity. For further details on sampling at RaTS see Venables et al. (2013) and Clarke et al. (2008).

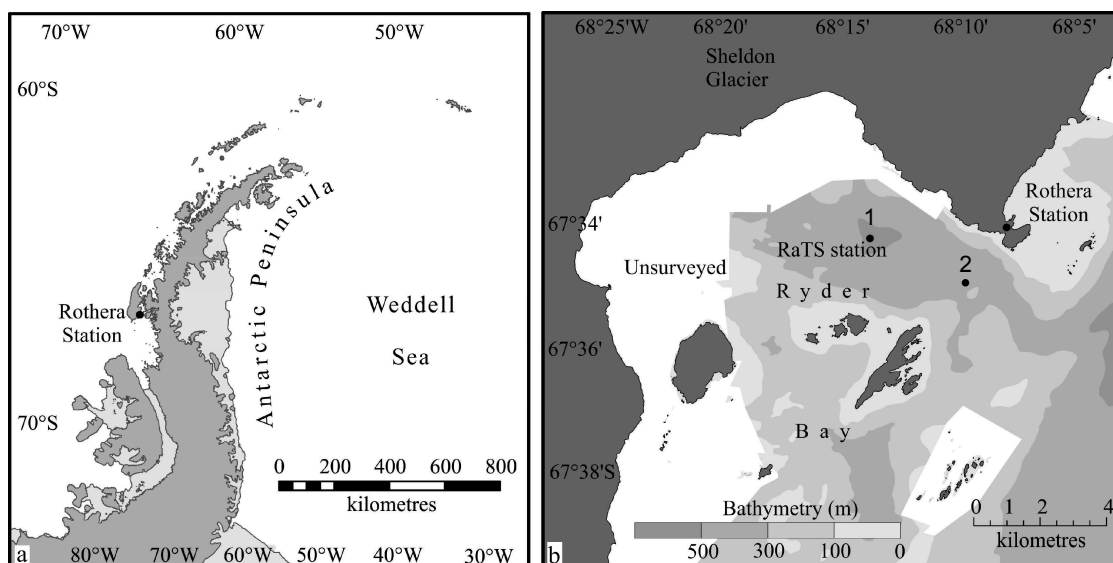


Figure 2.1: a: Location of Rothera on Adelaide Island at the West Antarctic Peninsula. b: Location of RaTS sites 1 and 2 in Ryder Bay. Modified from Venables et al. (2013)

2.2.2 Cruise sampling

Inorganic carbon samples were drawn into 250 mL borosilicate glass bottles from the 10 L Niskin bottles of the CTD rosette using tygon tubing. Bottles were rinsed twice before filling and were overflowed for 20 seconds, allowing the bottle volume to be flushed twice. Samples were stored in coolboxes prior to fixing and were fixed as soon as possible, usually within two hours of sampling. On fixing, a 2.5 mL headspace was created to allow for expansion due to warming and 50 μ L of saturated mercuric chloride was added to each 250 mL bottle (Dickson et al., 2007). Bottles were then sealed using stoppers greased with Apiezon grease, secured with elastic bands and stored in the dark. Twelve to sixteen depths were sampled from deep stations with fewer samples being taken on shallower casts. Approximately every fourth depth sampled for carbon was sampled in duplicate in order to quantify uncertainty associated with sampling, storage and analysis and to provide a running check on instrument performance when analysing samples (Section 2.3.1). The locations of CTD stations sampled for DIC and TA are shown in Figure 2.2. In total, 804 combined samples for DIC and TA were taken from 48 stations.

Nutrient samples were primarily taken in order to improve the accuracy of carbonate system calculations (Section 2.3.3.3) but are also useful for water mass identification and are of biogeochemical interest in their own right. Nutrient samples were taken from the same Niskin bottles as inorganic carbon samples and occasional duplicates were taken in order to quantify uncertainty associated with sampling and storage. Samples were drawn into 60 mL polyethylene pots, which were rinsed twice before filling. Care was taken not to touch spigots and the inside of lids and pots to avoid contamination. Samples for nitrate and phosphate were taken separately from those for silicate. Nitrate/phosphate sample pots were stored in the dark at approximately -20°C and silicate sample pots were stored in the dark at approximately 4°C due to concerns about incomplete silicate recovery from frozen samples (Section 2.3.3.2).

Discrete oxygen samples were taken in order to calibrate the SBE43 oxygen sensor on the CTD. Oxygen samples were drawn from Niskin bottles into 125 mL borosilicate glass flasks of calibrated volume using tygon tubing. Oxygen was the first parameter to be sampled from Niskins to avoid diffusion of oxygen into/out of the Niskin headspace altering results. The flask was inverted and rinsed with the tubing pushed to the base of the flask as the flask was rotated. To fill, the tubing was pinched to minimise flow and the flask was returned swiftly to upright and filled slowly. Once full and bubble free, the flask was overflowed for 30 seconds to allow the flask volume to be flushed roughly three times. During overflowing the temperature of water in the flask was taken using a digital temperature probe. Flow was minimised when removing tubing in order to avoid turbulence. Immediately after filling, 1 mL of a mixture of 8 M sodium hydroxide and 4 M sodium iodide (NaOH/NaI) followed by 1 mL of 3 M manganese chloride (MnCl_2) were dispensed to the bottom of the filled flask using 1 mL dispensers. The flask was then sealed with the corresponding ground glass stopper and shaken vigorously for 1 minute. The flared neck of the flask was filled with MilliQ. After sampling, all flasks were shaken again for 1 minute and the neck was refilled with MilliQ. Samples were stored in the dark before analysis and the MilliQ around the neck was kept topped

up. Six stations were sampled for oxygen (Figure 2.3). Bottle depths were chosen to give a range of oxygen values from a range of pressures. Most Niskins were sampled either in duplicate or triplicate in order to check analytical precision. In total, 154 samples for dissolved oxygen were taken from 6 stations.

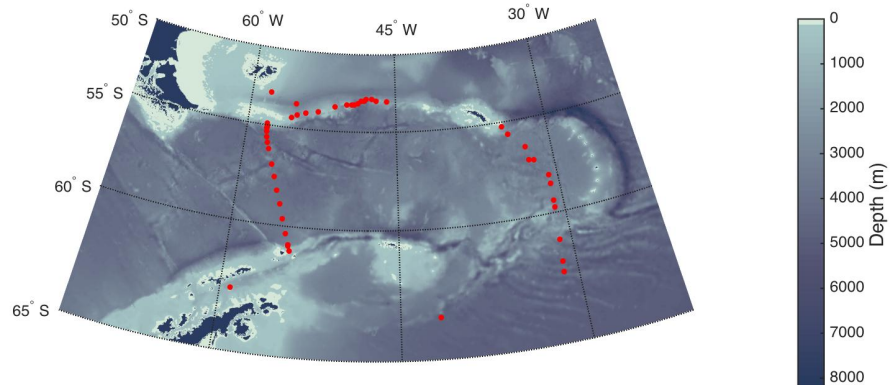


Figure 2.2: The location of casts sampled for DIC, TA and nutrients during JR299.

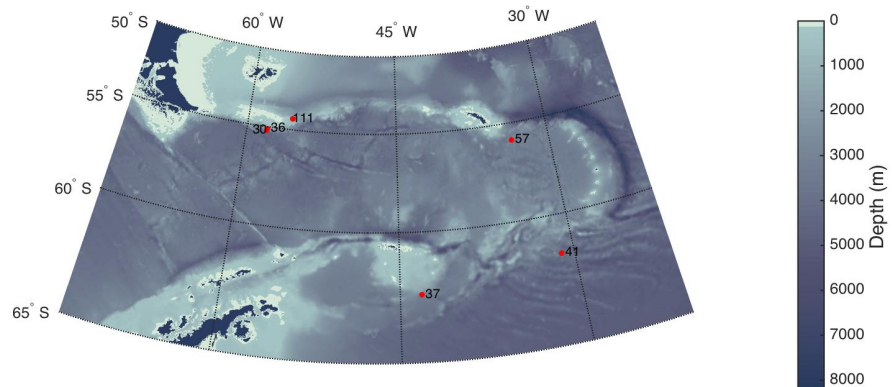


Figure 2.3: The location of casts sampled for discrete dissolved oxygen measurements during JR299. CTD numbers are given.

2.3 Chemical analyses

The DIC and TA analysis methods described below are the same for both the RaTS dataset and the JR299 cruise dataset. The oxygen and inorganic nutrient methods

described below are specific to the cruise dataset; oxygen is not routinely measured at RaTS and the nutrient analyses for RaTS are currently carried out by Ocean Scientific International Ltd. (OSIL) for the British Antarctic Survey.

2.3.1 DIC and TA

DIC was measured by coulometry (Johnson et al., 1985) following Standard Operating Procedure (SOP) 2 of Dickson et al. (2007) and TA was measured by potentiometric titration (Mintrop et al., 2000) following SOP 3b of Dickson et al. (2007). DIC and TA were measured using two VINDTAs (versatile instrument for the determination of titration alkalinity, version 3C, Marianda, Germany). The instruments were calibrated using Certified Reference Materials (CRMs) from the Scripps Institution of Oceanography. At least two 500 mL CRMs were measured per coulometer cell. The precision of DIC and TA measurements for both the RaTS and JR299 datasets are detailed below. Different measures of precision provide different information about the uncertainty of these measurements. Repeat (same bottle) precision (not given here but used during analysis as a check on instrument performance) gives an estimate of short term instrument precision. The precision of all CRM analyses during an analysis period gives an estimate of long-term instrument performance. Finally, replicate (different bottle) precision incorporates errors from both sampling and analysis and so is probably the most useful estimate of the overall precision of the data. As these VINDTA data are all corrected using certified values there is no true measure of accuracy. The precision is therefore the best available measure of the uncertainty of these data.

RaTS DIC and TA samples were analysed on VINDTAs V4 and V7 in three batches, corresponding to the three field seasons. The 2010-12 samples were analysed and processed by Gareth Lee and Dorothee Bakker. The 2012-13 and the 2013-14 samples were analysed and processed by Ollie Legge. CRM batch 107 was used for all three years. Although instrument precision remained fairly stable between the different batches of samples (long term standard deviation of CRMs of $2.2 \mu\text{mol kg}^{-1}$ or less for both DIC and TA), there is considerable variation in

replicate precision between different field seasons. This could reflect differences in sampling, poisoning, storage and transport. The DIC and TA standard deviations in 2010-12 were $4.3 \mu\text{mol kg}^{-1}$ and $4.9 \mu\text{mol kg}^{-1}$ respectively. In 2012-13 they were $6.2 \mu\text{mol kg}^{-1}$ and $7.0 \mu\text{mol kg}^{-1}$ and in 2013-14 they were $3.4 \mu\text{mol kg}^{-1}$ and $1.5 \mu\text{mol kg}^{-1}$. These standard deviations were calculated as the square root of the mean of the variance between duplicates.

JR299 DIC and TA samples were analysed on VINDTAs V4 and V7 during January and February 2015, using CRM batch 133. For VINDTA 7, the standard deviation of DIC replicates was $2.1 \mu\text{mol kg}^{-1}$ and the standard deviation of DIC for all CRMs over the analysis period was $1.9 \mu\text{mol kg}^{-1}$ (75 individual CRM analyses). For VINDTA 4, the standard deviation of DIC replicates was $2.4 \mu\text{mol kg}^{-1}$ and the standard deviation of DIC for all CRMs over the analysis period was $3.3 \mu\text{mol kg}^{-1}$ (60 individual CRM analyses). For VINDTA 7, the standard deviation of TA replicates was $2.2 \mu\text{mol kg}^{-1}$ and the standard deviation of TA for all CRMs over the analysis period was $2.3 \mu\text{mol kg}^{-1}$ (79 individual CRM analyses). For VINDTA 4, the standard deviation of TA replicates was $3.4 \mu\text{mol kg}^{-1}$ and the standard deviation of TA for all CRMs over the analysis period was $3.6 \mu\text{mol kg}^{-1}$ (62 individual CRM analyses).

2.3.2 Dissolved oxygen

Samples were stored for at least 12 hours prior to analysis. The stopper was removed and 1 mL of 5M sulphuric acid (H_2SO_4) and a magnetic stirrer bar were added to the sample. The sample was then mixed briefly to allow the precipitate to dissolve. Titration with 0.2 M sodium thiosulphate ($\text{Na}_2\text{S}_2\text{O}_3$) was performed using a custom built photometric detector to determine the endpoint. Room temperature at the time of each titration was recorded using a digital temperature probe. Before analysing each batch of samples, blanks and sodium thiosulphate standards were run.

For standards, a flask was filled with MilliQ and a magnetic stirrer bar was added. 1 mL of 23.36 mM potassium iodate (KIO_3) solution was added using a Metrohm Dosimat. 1 mL of sulphuric acid, 1 mL of NaOH/NaI and 1 mL of

MnCl₂ were added (in that order) using 1 mL dispensers and the flask was topped up to the neck with MilliQ. This solution was then titrated with Na₂S₂O₃ using a Metrohm Dosimat and the volume of titrant corresponding to the equivalence point was recorded. Room temperature at KIO₃ addition and at Na₂S₂O₃ titration was recorded using a digital temperature probe. In sample oxygen concentration calculations a mean of the standardisations is used for Na₂S₂O₃ concentration.

For blanks, a flask was filled with MilliQ and 0.1 mL of KIO₃ was added using a pipette. A magnetic stirrer bar was inserted and 1 mL of sulphuric acid, 1 mL of NaOH/NaI and 1 mL of MnCl₂ were added (in that order) using 1 mL dispensers. This solution was then titrated with Na₂S₂O₃ and the volume of titrant corresponding to the equivalence point was recorded. After this initial titration a further 0.1 mL of KIO₃ was added using a pipette and the Na₂S₂O₃ titration was repeated. Room temperature was recorded at each titration using a digital temperature probe. The difference between the two titrant volumes was taken as the blank volume. In sample oxygen concentration calculations a mean of all blank values is used.

Oxygen profiles from the six stations sampled for oxygen are shown in Figure 2.4. Duplicate and triplicate Winkler analyses usually agreed to within 1 $\mu\text{mol kg}^{-1}$ and the dataset as a whole has a RMSE of 0.39 $\mu\text{mol kg}^{-1}$. The calibration for CTD 37 was alarmingly different for that of CTDs 30 and 36 (Figure 2.5). The period between CTDs 36 and 37 was the transit south, across the Scotia Sea to the northern Weddell Sea and it is suspected that the SBE43 sensor was allowed to freeze while on deck. Similar oxygen sensor failure has been observed previously which was also attributed to freezing (Hugh Venables, pers. comm.). Following CTD 37 the original SBE43 was replaced with a new sensor. The oxygen calibration is therefore split into two periods: one for the first sensor and one for the second (Figure 2.5).

The results from the first calibration period agree well with the calibration from the previous cruise (JR294) which used the same Winkler titration instrument, the same batches of reagents and the same SBE43 oxygen sensor. This close agreement between JR299 and JR294 calibrations suggests that the sensor was stable throughout the first leg of JR299, across the Drake Passage. The second calibration period

covers the stations along the A23 section, stations in the Argentine Basin and stations along the North Scotia Ridge. As Figure 2.5 shows, the data from the second calibration period are slightly noisier around the linear fit than those from the first calibration period. However, this may not be indicative of sensor stability or precision but may instead reflect the fact that CTDs 30 and 36 were geographically and oceanographically very similar whereas CTDs 41, 57 and 111 were more diverse. Factors such as a pressure effect may therefore have affected results differently at different stations. The two calibrations are given in Figure 2.5. The uncertainties of the first and second calibrations are $0.98 \mu\text{mol kg}^{-1}$ and $3.05 \mu\text{mol kg}^{-1}$, respectively and were calculated as the standard deviation of the residuals of the linear fits in Figure 2.5.

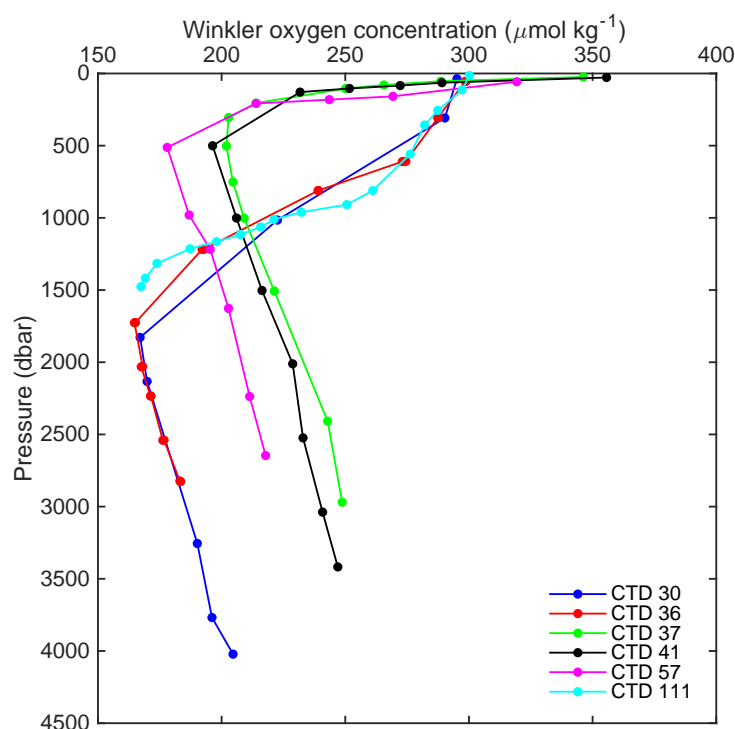


Figure 2.4: Profiles of dissolved oxygen for the 6 stations sampled for Winkler oxygen analysis. Most points are means of duplicates.

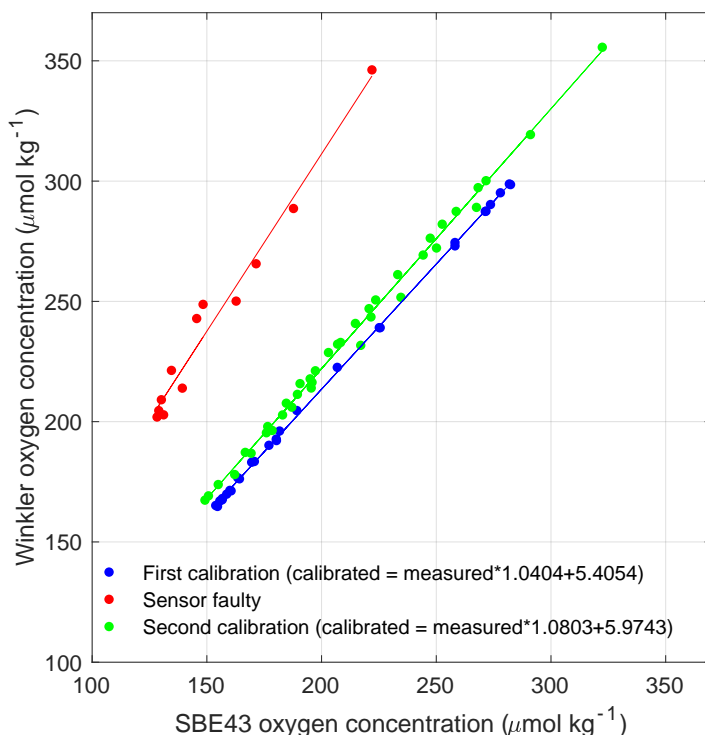


Figure 2.5: Calibration of SBE43 oxygen sensor using Winkler data. Blue represents the first calibration period (start of cruise until CTD 36), red represents attempted calibration following sensor damage, green represents the second calibration period (CTD 41 to end of cruise).

2.3.3 Inorganic nutrients

2.3.3.1 Nutrient analysis methods

Nitrate, phosphate and silicate samples were analysed by Andy Hind at the Centre for Ocean and Atmospheric Sciences at the University of East Anglia using a San++ Gas Segmented Continuous Flow Analyser (Skalar, Breda, The Netherlands). A six point calibration was made for each analyte using a mixed standard containing sodium nitrate, potassium dihydrogen phosphate and hexafluorosilicate. The standards and the wash solution were made using saline solution made from ultrapure water and NaCl, with an NaCl concentration of 35 g.L^{-1} . The NaCl for the saline solution was baked at 400°C for two hours to remove nitrate contamination.

Nitrate concentration was measured in accordance with the instrument manufacturers method (Skalar, 2009a). Nitrate is used here to refer to total oxidised ni-

trogen, NO_x ($\text{NO}_2 + \text{NO}_3$). The sample was buffered at pH 8.2 and passed through a copperised cadmium column which reduces all nitrate to nitrite. Nitrite was measured colorimetrically (Bendschneider and Robinson, 1952) using N-(1-naphthyl) ethylenediamine dihydrochloride and sulfanilamide. The intensity of the red dye was measured by a photometer with a 540 nm filter.

Phosphate concentration was measured in accordance with the instrument manufacturers method (Skalar, 2009b), using principles first developed by Murphy and Riley (1962). The sample was introduced to an acidified medium containing ammonium heptamolybdate and potassium antimony (III) oxide tartrate to form an antimony-phosphomolybdate complex. Ascorbic acid was then used to reduce this to a blue coloured complex which was measured colorimetrically at 880 nm.

Silicate concentration was measured in accordance with the instrument manufacturers method (Skalar, 2009c) based on the work of Brewer and Riley (1966). The sample was acidified with sulfuric acid and mixed with an ammonium heptamolybdate solution. Ascorbic acid was added to reduce the mixture, resulting in a blue colour which was measured colorimetrically using a 810 nm filter. Oxalic acid was used to reduce interference from phosphate.

Detection limits were taken as three times the standard deviation of repeated blank measurements (Taylor, 1987) and were calculated as $\sim 0.07 \mu\text{M}$, $\sim 0.13 \mu\text{M}$ and $\sim 0.09 \mu\text{M}$ for nitrate, phosphate and silicate respectively. The precision of nutrient analyses was calculated using duplicate measurements, sampled in separate pots. The standard deviations stated here were calculated as the square root of the mean of the variance between duplicates. Nitrate standard deviation was $1.70 \mu\text{M}$ (from 18 pairs of duplicates), phosphate standard deviation was $0.18 \mu\text{M}$ (from 18 pairs of duplicates) and silicate standard deviation was $1.64 \mu\text{M}$ (from 16 pairs of duplicates).

2.3.3.2 Defrosting tests

Freezing and thawing of nutrient samples can lead to significantly underestimated silicate concentrations due to polymerisation caused by freezing (Macdonald et al., 1986; Aminot et al., 2009). Up to a 30% reduction in silicate concentration has

been observed in thawed samples relative to chilled duplicates (Karel Bakker, pers. comm.). For marine samples it is recommended that samples are kept at room temperature for at least 24 hours prior to analysis (Aminot et al., 2009; Hydes et al., 2010), however for high silicate samples ($>40 \mu\text{M}$) it is recommended that the freezing and thawing procedures are checked to ensure they are appropriate (Hydes et al., 2010). As silicate concentrations $>40 \mu\text{M}$ are common in the Southern Ocean it was decided to test the effect of freezing and thawing on silicate recovery in JR299 samples.

All nutrient samples on JR299 were taken in duplicate with one replicate frozen at -20°C and one replicate stored at 4°C (Section 2.2.2). This duplicate sampling allowed for investigation of freezing and thawing on silicate recovery. Four stations of nutrient samples were used for defrosting tests so that the results of this test could inform how the rest of the samples were analysed. The four stations (CTDs 19, 38, 60 and 109) were selected to give a wide depth range and to represent the range of oceanographic regimes sampled during the cruise. In total, 56 pairs of duplicates (112 sample pots) were analysed.

Chilled samples were analysed for nitrate, phosphate and silicate as described in Section 2.3.3.1. Frozen samples were left at room temperature in the dark and were analysed for nitrate, phosphate and silicate immediately after thawing (approximately 16 hours, day 0). The thawed samples were then stored at 4°C and analysed again for silicate 2 days after thawing and again 7 days after thawing.

Figure 2.6 shows that when the samples were analysed immediately after thawing the silicate concentration was significantly lower than measured in their unfrozen counterparts, especially for samples with a higher silicate concentration. Overall, silicate recovery after 2 and 7 days of thawing look very similar and both sets of analyses have close to a 1:1 slope with unfrozen samples. However, at silicate concentrations of around $120 \mu\text{M}$ and above, there still appears to be incomplete silicate recovery after 2 days whereas the data from day 7 are much closer to the unfrozen values, suggesting that de-polymerisation continues even after 2 days of thawing.

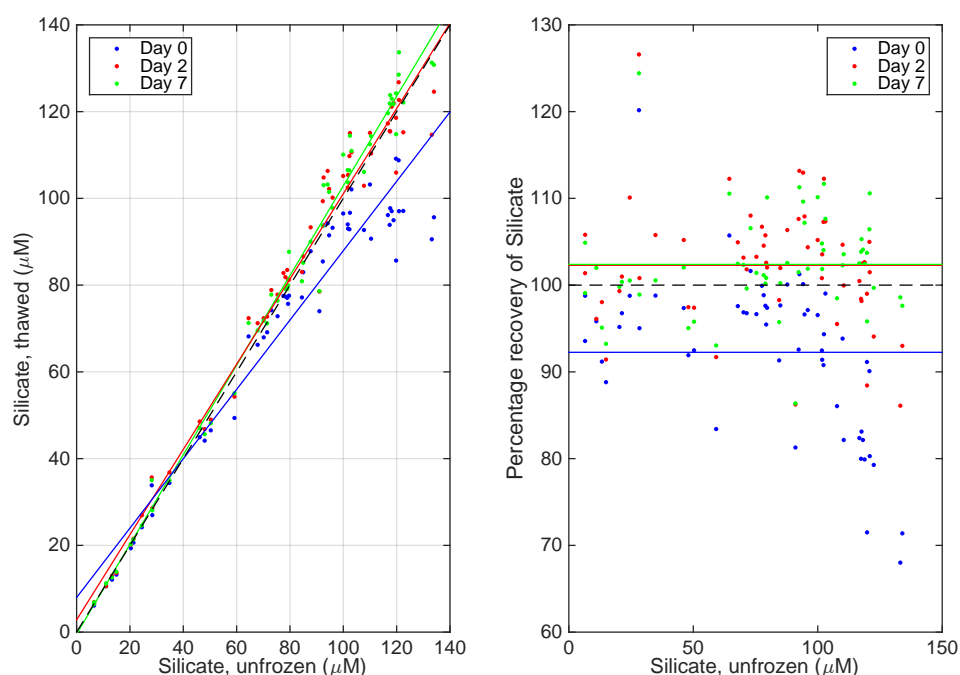


Figure 2.6: Silicate defrosting tests. Left panel: The concentration of silicate measured in unfrozen vs. thawed samples. Coloured lines represent linear fit of unfrozen samples vs. different thawing times: blue = day 0, red = day 2, green = day 7. Dashed black line represents 1:1 slope. Right panel: The percentage recovery of silicate, relative to unfrozen samples, after different thawing times: blue = day 0, red = day 2, green = day 7. Coloured lines show the mean percentage recovery for each analysis time.

The increase in measured silicate concentrations at each time step of the defrosting experiment is presented in Figure 2.7. The majority of silicate recovery occurs within the first two days after thawing (middle panel) but at concentrations of $\sim 120 \mu\text{M}$ and above, the measured concentrations also increased from day 2 to day 7 (bottom panel). An earlier study also found $120 \mu\text{M}$ to be a noticeable threshold for silicate recovery; Dore et al. (1996) only observed a significant difference between thawed and unfrozen treatments in samples with a silicate concentration higher than $120 \mu\text{M}$ and suggest that polymerised silicate in high concentration samples can be recovered by warming or prolonged thawing. For most samples with intermediate silicate concentrations of $60 - 100 \mu\text{M}$, a slight decrease in the measured silicate concentration from day 2 to day 7 is observed (bottom panel).

These results suggest that, to achieve accurate silicate measurements for samples with silicate concentrations above $\sim 120 \mu\text{M}$, the samples would have to be thawed for more than 2 days. However, it is possible that leaving samples to defrost for several days may allow biological processes to affect nitrate and phosphate concentrations. The possibility of using the unfrozen samples for nitrate and phosphate analyses as well as silicate analyses was considered. However, the concentration of nitrate and phosphate in unfrozen samples was found to be lower than in their frozen duplicates (Figure 2.8). This loss of nitrate and phosphate but not silicate in chilled samples is consistent with previous findings and is likely due to biological activity in chilled samples (Kremling and Wenck, 1986). Therefore, the unfrozen replicate from each pair of samples was analysed for silicate while its frozen counterpart was analysed for nitrate and phosphate immediately after thawing.

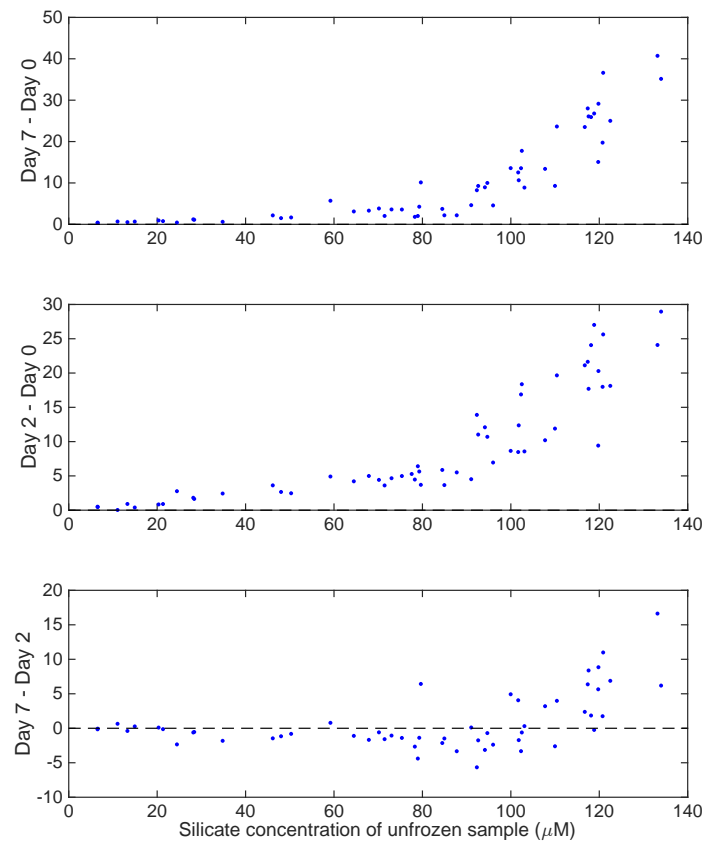


Figure 2.7: The difference in measured silicate concentrations (in μM) between different thawing times. Top panel: day 7 - day 0, middle panel: day 2 - day 0, bottom panel: day 7 - day 2. Note different y axis scales.

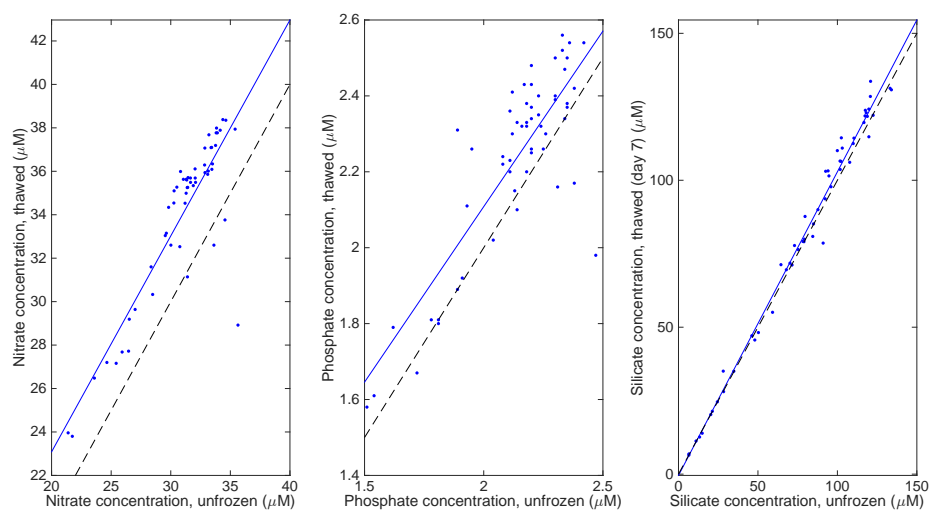


Figure 2.8: The concentration of nitrate (left panel), phosphate (middle panel) and silicate (right panel) measured in unfrozen vs. thawed samples. The thawed silicate data are from the longest thawing period (day 7). Dashed black lines represent 1:1 slopes.

2.3.3.3 Sensitivity of carbonate system calculations to silicate and phosphate concentrations

Silicate and phosphate ions contribute to the total alkalinity of a water sample (Dickson et al., 2007) and the concentration of these nutrients is used when computing TA from titration data. In order to quantitatively investigate the influence of silicate and phosphate data on the TA results presented here, the TA of JR299 carbon samples was recalculated from the raw titration data run on VINDTA number 7, using various nutrient concentrations. TA was recalculated for the whole dataset with the following modifications to the nutrient concentration data: doubled phosphate and silicate; halved phosphate and silicate; zero phosphate and silicate. The differences between the TA calculated using these modified nutrient concentrations and the TA calculated using measured nutrient concentrations are presented in Figure 2.9. These results show that changes to phosphate and silicate concentrations have a relatively small effect on the calculated TA and even the largest perturbations are an order of magnitude smaller than the precision of TA measurements.

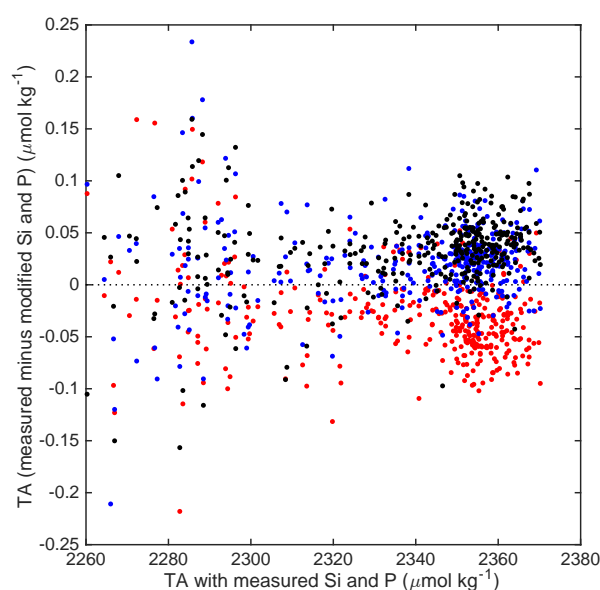


Figure 2.9: The sensitivity of TA results to different phosphate and silicate concentrations. Measured Si and P values have been halved (blue), doubled (red) and set to zero (black) for each TA measurement.

Although nutrient concentrations have a relatively small affect on TA data, it is known that they can have a significant affect on carbonate system parameters calculated from measured TA and DIC. Takahashi et al. (1982) compared carbonate system parameters calculated using various definitions of TA and found that for deep Antarctic waters at 1.5°C, the inclusion of silicate and phosphate in the definition of TA increased $p\text{CO}_2$ by 6.4% and decreased the carbonate ion concentration by 5.7% which is comparable to the uncertainty caused by TA and DIC measurement error.

The influence of silicate and phosphate measurements on carbonate system parameters calculated from JR299 TA and DIC measurements using the CO2SYS program (Van Heuven et al., 2011a) was investigated. CO2SYS was run using the dissociation constants of Lueker et al. (2000). Increasing (decreasing) the silicate and phosphate inputs to CO2SYS increases (decreases) the pH, the saturation state of calcite and the concentration of carbonate ions and decreases (increases) the fugacity of CO_2 (Figure 2.10). The effect on $f\text{CO}_2$ is especially striking, with up to a 14 μatm difference caused by doubling or zeroing silicate and phosphate concen-

trations which is equivalent to a 2.5% change in $f\text{CO}_2$. This demonstrates that the effect of nutrient concentrations on calculated $f\text{CO}_2$ could represent a non-trivial error when computing, for example, ocean-atmosphere CO_2 flux and the uncertainty on nutrient data should therefore be considered. This may be of particular importance when calculating CO_2 from pH sensor data from autonomous platforms, such as SOCCOM floats, without access to accompanying phosphate and silicate measurements (Wanninkhof et al., 2016; Williams et al., 2017). The influence of nutrient measurements on calculated pH should also be considered, especially when investigating long-term trends. The decrease in pH in the surface ocean over the last 3 decades of $0.0017 - 0.0018 \text{ yr}^{-1}$ (Bates et al., 2012; Lauvset et al., 2015) is an order of magnitude smaller than the error caused by the nutrient perturbations shown here.

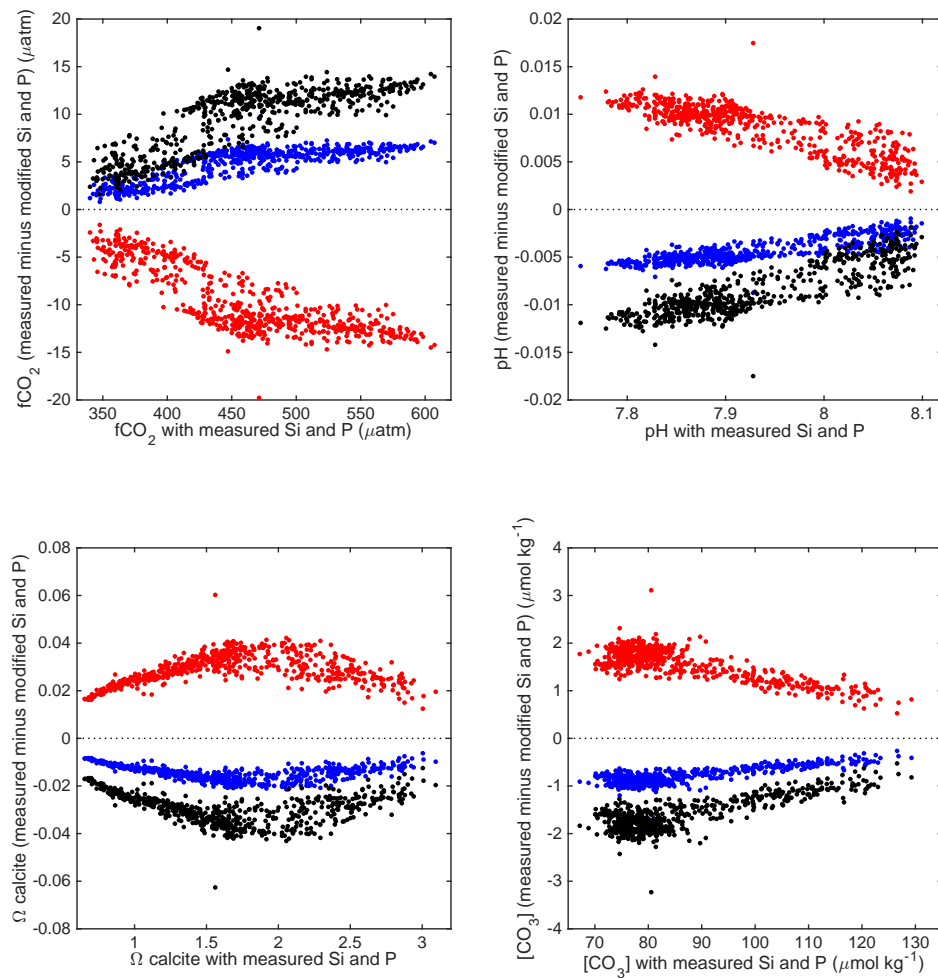


Figure 2.10: The sensitivity of calculated carbonate system parameters to different silicate and phosphate concentrations. Measured Si and P values have been halved (blue) doubled (red) and set to zero (black) for each value calculated by CO2SYS. pH is given on the total scale.

2.4 Datasets

2.4.1 Secondary quality control

In order to assess whether the biogeochemical variables measured on JR299 are affected by any systematic biases, secondary quality control has been performed using the crossover toolbox originally developed by Toste Tanhua for quality control of the CARINA dataset (Tanhua et al., 2010). This toolbox finds data from

a reference dataset which are within a certain horizontal and vertical range of the cruise data being investigated and calculates an offset. This information is a useful check of data accuracy and can be used to bias correct the data if required. Only deep measurements are compared because the properties of deep water masses are assumed to be sufficiently stable over time to assess biases, whereas shallower water masses are more variable with time. This assumption is less robust in regions such as the Southern Ocean, where deep water may have been recently ventilated, making identification of biases more challenging.

Here, the JR299 data are compared to cruise data from the GLODAPv2 dataset which have been rigorously quality controlled and corrected for bias and are therefore assumed to be internally consistent (Olsen et al., 2016). The offset of each variable is expressed either as an additive or as a multiplicative offset and is considered relative to a commonly used threshold, based on the usual measurement uncertainty of that variable. Any offset lower than this threshold is not considered sufficient justification for a bias correction. DIC and TA are given additive offsets and have thresholds of $4 \mu\text{mol kg}^{-1}$ and $6 \mu\text{mol kg}^{-1}$, respectively (Wanninkhof et al., 2003; Velo et al., 2009; Tanhua et al., 2010; Pierrot et al., 2010). Oxygen is given a multiplicative offset and has a threshold of 1% (Stendardo et al., 2009; Tanhua et al., 2010). Nutrients are given multiplicative offsets and have thresholds of 2% (Tanhua et al., 2009). Crossovers were run based on density rather than theta or pressure as this generally yields offsets with the lowest standard deviation (Tanhua et al., 2010). The maximum distance used here to define a station crossover is 2 degrees of latitude and the shallowest crossover depth is 1500m, following Tanhua et al. (2010). The results of the crossover analysis are presented in Table 2.1.

All DIC and TA offsets are smaller than the thresholds for these variables, suggesting that there is no significant, systematic bias in these variables. Nitrate and phosphate have both positive and negative offsets with mean offsets within their respective thresholds. No correction has therefore been made to these variables. The mean offset for silicate suggests that the JR299 data are biased low compared to GLODAPv2 data but crossovers with individual cruises show a large range (0.85

to 1.08). Visual comparison of JR299 silicate data with other Drake Passage and A23 sections confirmed that the JR299 data are biased low and a multiplicative correction of 1.1 has been applied. The oxygen offsets are all 0.97-0.98 which strongly suggests that the JR299 oxygen data are biased low compared to previous cruises in the region. A multiplicative correction of 1.03 has therefore been applied to the oxygen data. The oxygen and silicate data submitted to databases (Section 2.4.2) have been left uncorrected.

2.4.2 Data availability

The RaTS data presented here (DIC and TA) have been submitted, along with ancillary variables and metadata, to the British Oceanographic Data Centre (BODC) and the National Centers for Environmental Information (NCEI). These data are publicly available and, if used, should be cited as Legge et al. (2017). The JR299 data presented here (DIC, TA, nitrate, phosphate, silicate and oxygen) have been submitted, along with ancillary variables and metadata, to the BODC and will be submitted to the NCEI.

| Expocode | no. stations JR299 | no. stations crossover | DIC offset (+) | DIC SD of offset | TA offset (+) | TA SD of offset | Nit. offset (x) | Nit. SD of offset | Pho. offset (x) | Pho. SD of offset | Sil. offset (x) | Sil. SD of offset | Oxy offset (x) | Oxy SD of offset | Notes |
|----------------|-----------------------|---------------------------|-------------------|---------------------|------------------|--------------------|--------------------|----------------------|--------------------|----------------------|--------------------|----------------------|-------------------|---------------------|-------|
| 06AQ20050122 | 11 | 28 | 1.37 | 1.26 | 3.99 | 2.02 | 1.06 | 0.00 | 1.00 | 0.01 | 1.02 | 0.00 | 0.97 | 0.00 | DP |
| 06AQ20080210 | 11 | 25 | 1.37 | 1.26 | 3.99 | 2.02 | 1.06 | 0.01 | 1.01 | 0.00 | 1.08 | 0.01 | 0.97 | 0.01 | DP |
| 316N19720718.1 | 19 | 8 | | | | | 0.96 | 0.02 | 0.94 | 0.03 | 0.85 | 0.03 | 0.98 | 0.01 | |
| 316N19831007 | 14 | 11 | -0.94 | 4.75 | -3.24 | 2.86 | 0.97 | 0.02 | | | | | 0.97 | 0.01 | A23 |
| 33RO20050111 | 9 | 10 | 2.37 | 3.32 | -3.43 | 4.07 | 0.98 | 0.01 | | | 0.91 | 0.05 | 0.97 | 0.00 | A23 |
| 740H20090203 | 15 | 23 | -0.71 | 2.63 | -0.99 | 5.50 | 0.99 | 0.03 | 0.98 | 0.02 | 0.86 | 0.03 | 0.97 | 0.01 | DP x2 |
| 74JC19950320 | 20 | 31 | | | | | | | 1.03 | 0.03 | | | 0.98 | 0.00 | A23 |
| 74JC20100319 | 7 | 9 | 3.02 | 2.78 | -0.51 | 1.16 | 0.94 | 0.07 | 0.96 | 0.09 | 0.97 | 0.06 | 0.98 | 0.01 | |
| Mean | | | 1.02 | | -0.84 | | 0.99 | | 0.99 | | 0.95 | | 0.97 | | |

Table 2.1: Results of crossover analysis for JR299 DIC, TA, oxygen and nutrient data compared to cruises in the GLODAPv2 dataset (Olsen et al., 2016). Crossovers are based on sigma-4. The minimum crossover depth is 1500m and the maximum distance for crossovers is 2 degrees of latitude. Offsets are either additive (+) or multiplicative (x), depending of the variable. The offsets are coloured based on whether they are smaller (green) or greater (red) than the thresholds detailed in Section 2.4. The offset means are unweighted. The notes column shows if a crossover cruise occupied either the Drake Passage (DP) or A23 section.

Chapter 3

The seasonal cycle of ocean-atmosphere CO₂ flux in Ryder Bay

The majority of the work in this chapter has been published as: Legge, O.J., Bakker, D.C.E., Johnson, M.T., Meredith, M.P., Venables, H.J., Brown, P.J. and Lee, G.A. (2015), The seasonal cycle of ocean-atmosphere CO₂ flux in Ryder Bay, west Antarctic Peninsula, *Geophysical Research Letters*, 42, 2934-2942.

3.1 Rationale

Ocean-atmosphere CO₂ flux in the high-latitude, seasonally sea ice covered Southern Ocean remains poorly constrained due to a lack of observations, and our mechanistic understanding of CO₂ flux in this region remains weak. A better understanding of the processes driving seasonal and interannual variability in CO₂ flux is required to strengthen our predictions of future carbon uptake by the Southern Ocean. This is true especially for the productive coastal waters around Antarctica. The aims of this chapter are to:

- Quantify the ocean-atmosphere CO₂ flux in Ryder Bay to determine whether the ocean is a net source or sink of atmospheric CO₂.
- Investigate the seasonal and interannual variability in CO₂ flux and the causes of this variability.

3.2 Methods

The ocean-atmosphere flux of CO₂ was calculated for each day during the study period from the solubility of CO₂ at in-situ temperature and salinity, the difference in the fugacity of CO₂ between seawater and the air, and the gas transfer velocity. These calculations are described in full in Sections 3.2.1 to 3.2.3. A negative ocean-atmosphere flux signifies an uptake from the atmosphere by the ocean.

Windspeed and sea level atmospheric pressure are measured daily at Rothera but other data (seawater temperature and salinity, seawater $f\text{CO}_2$ and open water fraction) have been linearly interpolated into daily vectors. Atmospheric $x\text{CO}_2$ data are from weekly flask samples from Palmer Station, approximately 400 km northeast of Rothera (Dlugokencky et al., 2014). These discrete flask data were smoothed using a weighted linear least squares method and resampled into a daily vector (Figure 3.1). Atmospheric data from Rothera are available at www.antarctica.ac.uk/met/metlog. Atmospheric CO₂ from Palmer Station data are available from NOAA at <ftp://aftp.cmdl.noaa.gov>.

Figure 3.1 shows both the long term increase and the seasonal cycle of atmospheric CO₂ at both Palmer Station and the South Pole. The seasonal cycle at the South Pole (Keeling et al., 1976) has a smaller amplitude than that at the West Antarctic Peninsula because it is further away from the terrestrial and oceanic processes which create seasonal variability in CO₂. The Palmer time series is currently the best source of atmospheric CO₂ data to use for ocean-atmosphere CO₂ flux calculations in Ryder Bay due to the accuracy and frequency of the data as well as the proximity of Palmer Station to Rothera. Palmer and Rothera are both on the West Antarctic Peninsula and the air at both sites is therefore dominated by the same maritime westerlies and polar low pressure systems. The South Pole CO₂ data are available at <http://scrippsco2.ucsd.edu>.

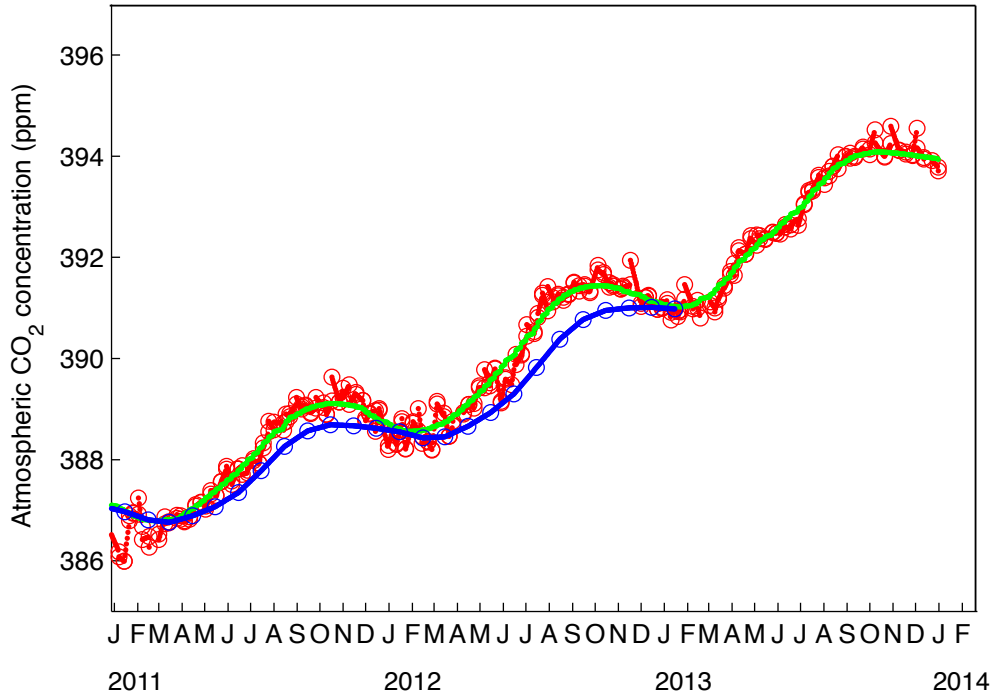


Figure 3.1: Atmospheric CO₂ concentration at Palmer station (Dlugokencky et al., 2014) and the South Pole (Keeling et al., 1976). Red circles are measured flask data from Palmer, red dots are a daily linear interpolation of these Palmer measurements and the green line represents the smoothed Palmer data, resampled daily. The blue circles are smoothed monthly means at the South Pole and the blue line represents these smoothed, monthly South Pole data, resampled daily.

3.2.1 Ocean and atmosphere CO₂ concentrations

The fugacity of CO₂ in water ($f\text{CO}_{2w}$) was calculated from dissolved inorganic carbon ($\mu\text{mol kg}^{-1}$), total alkalinity ($\mu\text{mol kg}^{-1}$), silicate ($\mu\text{mol kg}^{-1}$), phosphate ($\mu\text{mol kg}^{-1}$), seawater temperature ($^{\circ}\text{C}$), salinity and in situ pressure (dbar) using the CO2SYS program (Van Heuven et al., 2011a) and the dissociation constants of Goyet and Poisson (1989). Details of DIC and TA sampling and analyses are given in Chapter 2. Only data from 15m were used to calculate $f\text{CO}_{2w}$.

Atmospheric $f\text{CO}_2$ in moist air ($f\text{CO}_{2a}$, μatm) was calculated from seawater temperature (T , $^{\circ}\text{K}$), the atmospheric mole fraction of CO₂ ($x\text{CO}_{2a}$, $\mu\text{mol/mol}$), atmospheric pressure (P , atm) and water vapour pressure ($p\text{H}_2\text{O}$, atm) using the gas constant, R ($82.057 \text{ cm}^3 \text{ K}^{-1} \text{ mol}^{-1}$) and coefficients (B and D , $\text{cm}^3 \text{ mol}^{-1}$) from

Weiss (1974):

$$B = -1636.75 + 12.0408 \cdot T - 0.0327957 \cdot T^2 + 0.0000316528 \cdot T^3 \quad (3.1)$$

$$D = 57.7 - 0.118 \cdot T \quad (3.2)$$

$$f\text{CO}_{2a} = x\text{CO}_{2a} \cdot (P - p\text{H}_2\text{O}) \cdot \exp\left(\frac{P \cdot (B + 2 \cdot D)}{R \cdot T}\right) \quad (3.3)$$

Water vapour pressure ($p\text{H}_2\text{O}$, atm) was calculated from seawater temperature (T , °K) and salinity (S) following Weiss and Price (1980):

$$p\text{H}_2\text{O} = \exp\left(24.4543 - 67.4509 \cdot \frac{100}{T} - 4.8489 \cdot \log\frac{T}{100} - 0.000544 \cdot S\right) \quad (3.4)$$

The solubility of CO₂ in seawater (s , mol kg⁻¹ atm⁻¹) was calculated from seawater temperature (T , °K) and salinity (S) following Weiss (1974), taken from Dickson et al. (2007):

$$s = \exp\left(93.4517 \cdot \frac{100}{T} - 60.2409 + 23.3585 \cdot \log\frac{T}{100} + S \cdot (0.023517 - 0.023656 \cdot \frac{T}{100} + 0.0047036 \cdot (\frac{T}{100})^2)\right) \quad (3.5)$$

The CO₂ concentration difference between water and air (ΔC , μmol kg⁻¹) was calculated from the fugacity of CO₂ in water ($f\text{CO}_{2w}$, μatm), the fugacity of CO₂ in air ($f\text{CO}_{2a}$, μatm) and the solubility of CO₂ in seawater (s , mol kg⁻¹ atm⁻¹):

$$\Delta C = s \cdot (f\text{CO}_{2w} - f\text{CO}_{2a}) \quad (3.6)$$

This concentration difference was converted from $\mu\text{mol kg}^{-1}$ to volumetric units ($\mu\text{mol L}^{-1}$) by multiplying by seawater density (ρ , kg L^{-1}). Density was calculated from seawater temperature (T , $^{\circ}\text{C}$), salinity (S) and atmospheric pressure (P , atm) using the TEOS-10 thermodynamic equation of seawater (available at <http://www.teos-10.org/>)

$$\rho = \frac{\text{gsw_rho_t_exact}(S, T, P \cdot 10.1325)}{1000} \quad (3.7)$$

Pressure was multiplied by 10.1325 to convert from atm to db. Density was divided by 1000 to convert from kg m^{-3} to kg L^{-1} .

3.2.2 Ice cover and gas transfer velocity

Daily averaged windspeed and sea level pressure were measured at Rothera. Windspeed has been corrected from the measurement height of 42m to 10m above sea level following Fairall et al. (2011).

Gas transfer velocity (k) and its relationship with ice cover were calculated using two separate methods. Firstly, k_{W13} (cm hr^{-1}) was calculated from wind speed (u , m s^{-1}) and the Schmidt number (Sc) using the parameterisation of Wanninkhof et al. (2013) (Equation 3.8). The Schmidt number was calculated following Wanninkhof (1992) (Equation 3.9). As in previous studies, the gas transfer velocity was scaled linearly with sea ice cover by multiplying k by the fraction of open water. Even at 100% ice cover there is likely to be some gas exchange with the atmosphere due to leads, fractures and brine channels (Semiletov et al., 2004; Loose and Schlosser, 2011) so, consistent with other studies (Bates et al., 2006; Mucci et al., 2010; Roden et al., 2013), the minimum open water fraction has been set to 0.01. A scenario with no ice is also considered in which k is not modified by ice cover and also a scenario in which brash and grease ice do not affect k .

$$k_{W13} = 0.251 \cdot \left(\frac{Sc}{660}\right)^{-0.5} \cdot u^2 \quad (3.8)$$

$$Sc = 2073.1 - 125.62 \cdot T + 3.6276 \cdot T^2 - 0.043219 \cdot T^3 \quad (3.9)$$

Secondly, k_{L14} was calculated from ice speed (m s^{-1}), wind speed (m s^{-1}), sea ice concentration (%), surface water temperature (T , °C), air temperature (T , °C) and (optionally) relative humidity (%), mixed layer depth (m) and salinity using a parameter model for effective gas transfer velocity in sea ice covered waters (Loose et al., 2014). This model relates k to windspeed through mean squared wave slope and also includes shear-driven and convection-driven turbulence. Ice speed was not known so a fixed value of 0.01 m s^{-1} was used throughout. Mixed layer depth was defined as the depth at which the density difference relative to the surface is 0.05 kg m^{-3} (Venables et al., 2013). The model gives separate effective gas transfer velocities from ice and wave effects. These were summed to give the total effective gas transfer velocity and multiplied by 4.1667 to convert from m d^{-1} to cm hr^{-1} . The Schmidt number correction was then applied.

$$k_{L14} = (k_{\text{eff_ice}} + k_{\text{eff_wave}}) \cdot 4.1667 \cdot \left(\frac{Sc}{660}\right)^{-0.5} \quad (3.10)$$

The sensitivity of the parameter model of Loose et al. (2014) to ice speed was investigated by using a range of speeds from 0.0001 to 0.03 m s^{-1} . Ice speed made a small difference to the resulting ocean-atmosphere CO₂ flux and over the three year time series the cumulative flux calculated using an ice speed of 0.03 m s^{-1} was 0.1 mol m^{-2} greater than that calculated using an ice speed of 0.0001 m s^{-1} .

3.2.3 Ocean-atmosphere CO₂ flux

Ocean-atmosphere CO₂ flux (F , mol m⁻² yr⁻¹) was calculated from the gas transfer velocity (k_{W13} or k_{L14} , cm hr⁻¹) and the CO₂ concentration difference between water and air (ΔC , μmol L⁻¹)

$$F = \left(\frac{k}{100} \cdot \Delta C \cdot 1000\right) \cdot 0.0088 \quad (3.11)$$

k was divided by 100 to convert from cm hr⁻¹ to m hr⁻¹.

ΔC was multiplied by 1000 to convert from μmol L⁻¹ to μmol m⁻³.

Flux was multiplied by 0.0088 to convert from μmol m⁻² hr⁻¹ to mol m⁻² yr⁻¹.

3.2.4 Uncertainties

Uncertainties were calculated using a Monte Carlo approach to ensure that all nonlinearities in the carbon system calculations were accounted for in error propagation. This is hard to achieve using formal error propagation. The propagation of uncertainties was divided into two steps. Firstly, the uncertainty on water $f\text{CO}_2$ for each measurement of DIC and TA was calculated as follows: 10⁵ variable-value sets were created including the variables DIC, TA, silicate, phosphate, pK1 and pK2. For each variable, values were determined by random sampling from a distribution based on the measured value (or calculated value in the case of carbonate system constants) as the population mean with a standard deviation based on the measurement or variable uncertainty (Table 3.1). The CO2SYS program was run on each set of values to determine a probability density function (pdf) for $f\text{CO}_2$, twice the standard deviation of which was taken as a measure of that data point's uncertainty. The errors on measured values and carbonate system constants used in the uncertainty analysis (Table 3.1) were assumed to be normally distributed. One standard deviation was used to define the characteristics of the distribution of each of the input variables in the uncertainty analysis. Two standard deviations (approximately 95% confidence) is quoted when referring to calculated uncertainties.

The second step was the calculation of uncertainty on the daily-calculated

ocean-atmosphere flux. Following interpolation of all input variables on a daily basis the uncertainty on each daily-calculated flux was calculated as follows: 10⁵ variable-value sets were created for water $f\text{CO}_2$, air $f\text{CO}_2$ and k as described above. The uncertainty on water $f\text{CO}_2$ was taken from the previous step, the uncertainty on air $f\text{CO}_2$ is described in Table 3.1 and the uncertainty on k was taken as 20% (Wanninkhof, 2014) and given a uniform distribution. The ocean-atmosphere flux was calculated for each set of values as above and twice the standard deviation of the resulting pdf was taken as a measure of the uncertainty of that day's flux. The uncertainty on the cumulative flux was calculated as the square root of the sum of the squares of the uncertainties up to and including each point which assumes randomly distributed rather than systematic uncertainty. Uncertainties were only quantified for the fluxes calculated following Wanninkhof et al. (2013) with a linear scaling of ice cover and k . The uncertainty on the fluxes calculated following Loose et al. (2014) were not quantified as the uncertainties in this new model are not well understood.

| Parameter | Uncertainty (1 SD) | Unit | Source |
|-----------------------------|--------------------|-------------------------|--|
| DIC | 2.2 | $\mu\text{mol kg}^{-1}$ | long term precision of CRM analyses |
| TA | 1.3 | $\mu\text{mol kg}^{-1}$ | long term precision of CRM analyses |
| Silicate | 2.6 | % | precision quoted by analyst |
| Phosphate | 2.7 | % | precision quoted by analyst |
| pK1 | 0.0055 | - | Constant from Goyet and Poisson (1989). Uncertainty from Millero (2007) |
| pK2 | 0.01 | - | Constant from Goyet and Poisson (1989). Uncertainty from Millero (2007) |
| Atmospheric CO ₂ | 0.23 | ppm | RMSE of the smoothed, interpolated data vs. the measured values at Palmer station. |
| Gas transfer velocity | 20 | % | Wanninkhof (2014) |

Table 3.1: Uncertainties associated with measured parameters, carbonate system constants and the gas transfer velocity

3.3 Results and discussion

3.3.1 Seasonal and interannual variability

The three years of DIC data presented here (Figure 3.2) display a clear, highly asymmetric, seasonal cycle with an amplitude of $\sim 200 \mu\text{mol kg}^{-1}$. DIC decreases sharply during December/January due to the rapid increase of biological production and summer months are characterised by low and variable DIC values. There is a gradual increase from around April to maximum DIC concentrations of $\sim 2200 \mu\text{mol kg}^{-1}$ in September. This increase during autumn and winter is caused by net heterotrophy and mixing with relatively old, carbon-rich CDW as the mixed layer deepens. The rapid spring DIC drawdown is preceded by a more gradual decrease corresponding to reduced sea ice cover (Figure 3.2), an increase in photosynthetically active radiation and a shoaling and warming mixed layer. The gradual decrease prior to the main spring bloom is therefore likely to be caused by the onset of algal production in the water column and ice but may also be influenced by ikaite dissolution during ice melt (Section 3.3.2).

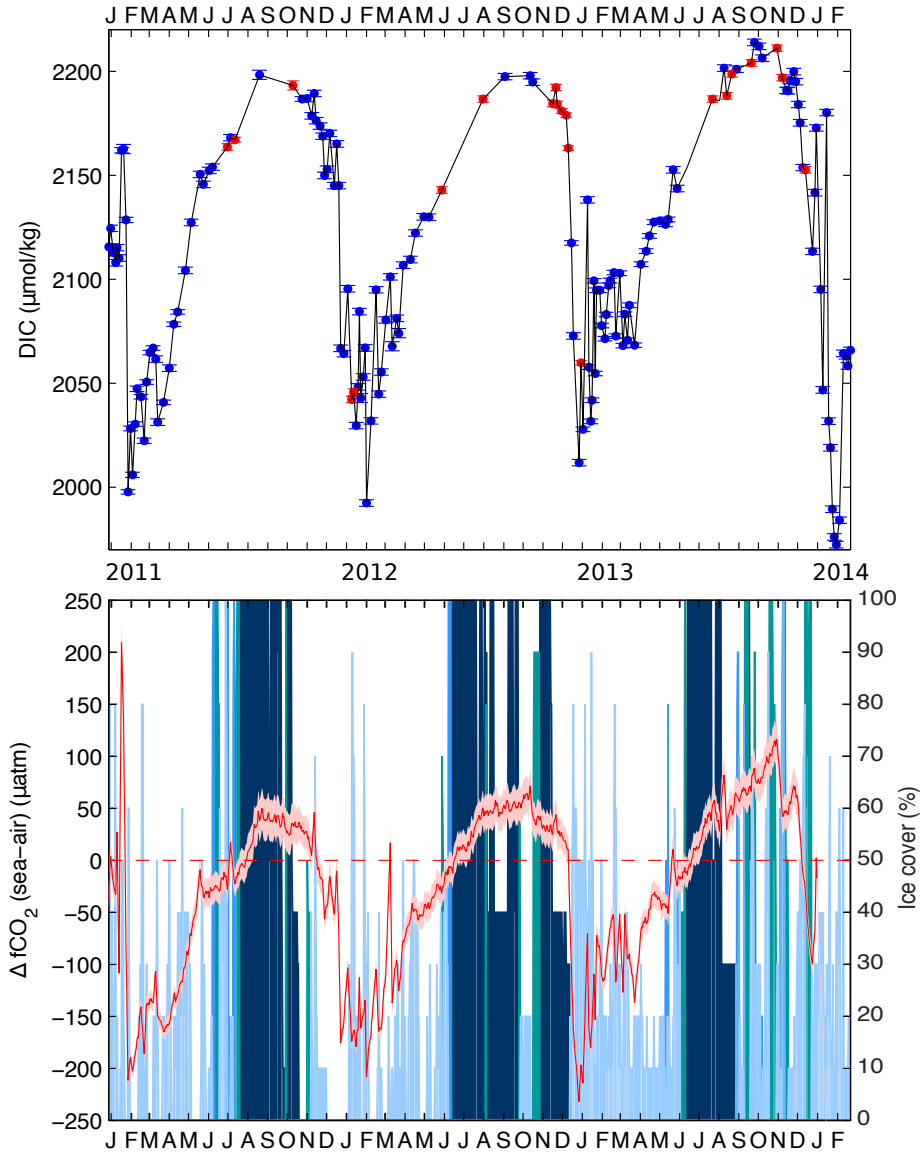


Figure 3.2: Top panel: The seasonal cycle of Dissolved Inorganic Carbon from December 2010 until February 2014 at 15m depth at RaTS. Blue points indicate data from site 1, red from site 2. Error bars are uncertainty (2SD) based on measurement precision. Bottom panel: the red line represents the seasonal cycle of $\Delta f\text{CO}_2$ with the shaded region representing approximate 95% confidence from uncertainty analysis. The red dashed line shows $\Delta f\text{CO}_2 = 0$ ie. ocean CO₂ concentration is at equilibrium with the atmosphere. Blue bars show percentage ice cover. Bar colour denotes ice type with dark blue representing fast ice, turquoise representing pack ice and light blue representing brash ice.

Due to the pronounced seasonal cycle in DIC, the $\Delta f\text{CO}_2$ changes sign between winter and summer (Figure 3.2), making the water column a potential source of CO₂

to the atmosphere during winter and a potential sink during summer. This gradient determines the direction of the CO₂ flux but its magnitude is strongly influenced by wind speed and ice cover. The daily ocean-atmosphere CO₂ flux, as calculated with a linear scaling between k and ice cover (Figure 3.3), ranges from approximately -15 mol C m⁻² yr⁻¹ in summer (into the ocean) to approximately 10 mol C m⁻² yr⁻¹ in winter (out of the ocean). In all three years sampled, the summer uptake of CO₂ by the ocean is greater than the winter out-gassing, making the water column in Ryder Bay a net sink of atmospheric CO₂ over an annual cycle. Summing the daily fluxes gives the cumulative ocean-atmosphere CO₂ flux (Figure 3.3), clearly showing a net ocean sink from all estimates. The mean net annual CO₂ uptake by the ocean from 1st January 2011 to 31st December 2013 was 0.59 mol C m⁻² yr⁻¹ as calculated using the linear scaling of k with ice cover (solid blue line, Figure 3.3) with net annual uptake ranging from 0.22 mol C m⁻² yr⁻¹ in 2013 to 1.03 mol C m⁻² yr⁻¹ in 2011. When calculated using the sea ice gas exchange model (solid red line, Figure 3.3), the mean net annual ocean uptake was 0.94 mol C m⁻² yr⁻¹ ranging from 0.47 mol C m⁻² yr⁻¹ in 2013 to 1.50 mol C m⁻² yr⁻¹ in 2011. The estimates of net annual ocean carbon uptake using a linear k scaling presented here are similar to the estimate of Roden et al. (2013) who calculated a net ocean uptake in Prydz Bay, East Antarctica of 0.54 ± 0.11 mol C m⁻² yr⁻¹, also using a linear scaling of k with ice cover. The estimates presented here are somewhat lower than the net annual CO₂ uptake of the Ross Sea, estimated using a biogeochemical model as 1.7 - 4.2 mol C m⁻² yr⁻¹ (Arrigo et al., 2008).

There is significant interannual variability in the ocean-atmosphere flux of CO₂, especially in the amount of winter out-gassing (Figure 3.3). Atmospheric CO₂ increases by roughly 2.3 ppm/yr from ~387 ppm in January 2011 to ~394 ppm in January 2014, with a seasonal amplitude of ~3 ppm (Figure 3.1). Despite this increase in atmospheric CO₂ during the study period, the ocean to atmosphere CO₂ flux increases through each successive winter in the three observed years. This interannual variability is likely caused by two main drivers. Firstly, higher water f CO₂ in winter increases the concentration gradient of CO₂ between the ocean and

the atmosphere (Figure 3.2), making the ocean a stronger potential source of CO₂ to the atmosphere. The increase in $f\text{CO}_2$ and DIC in surface water in winter is likely caused by increased mixing of CDW into the surface layer and this theory is supported by a slight increase in winter salinity from 2011 to 2013. Reduced ice cover in Ryder Bay during winter allows enhanced mixing due to the exposed water surface and this can result in reduced stratification in the following spring (Venables and Meredith, 2014). A decrease in ice cover could therefore affect ocean-atmosphere CO₂ fluxes by increasing the mixing of CDW into the surface and increasing surface water $f\text{CO}_2$ and DIC.

Secondly, a reduction in ice cover during winter, when $\Delta f\text{CO}_2$ is positive, allows more gas exchange across the air-water interface. The three consecutive winters shown here exhibit increasing $\Delta f\text{CO}_2$ and a longer period during which $\Delta f\text{CO}_2$ is positive while ice cover is below 50%. These factors combined result in increased out-gassing of CO₂ to the atmosphere and a reduced net CO₂ sink over the seasonal cycle. When the effect of ice cover on k is ignored, the water column is still found to be a net sink of atmospheric CO₂ (dashed lines, Figure 3.3) although the strength of this sink is reduced compared with the equivalent calculations including ice cover (solid blue and red lines, Figure 3.3). The role of winter sea ice cover in reducing CO₂ flux from the ocean to the atmosphere is consistent with previous observations (Gibson and Trull, 1999; Sweeney, 2003; Bakker et al., 2008) and supports the hypothesis that increased Antarctic sea ice cover during glacial periods could have lowered atmospheric CO₂ by reducing deep water ventilation (Stephens and Keeling, 2000).

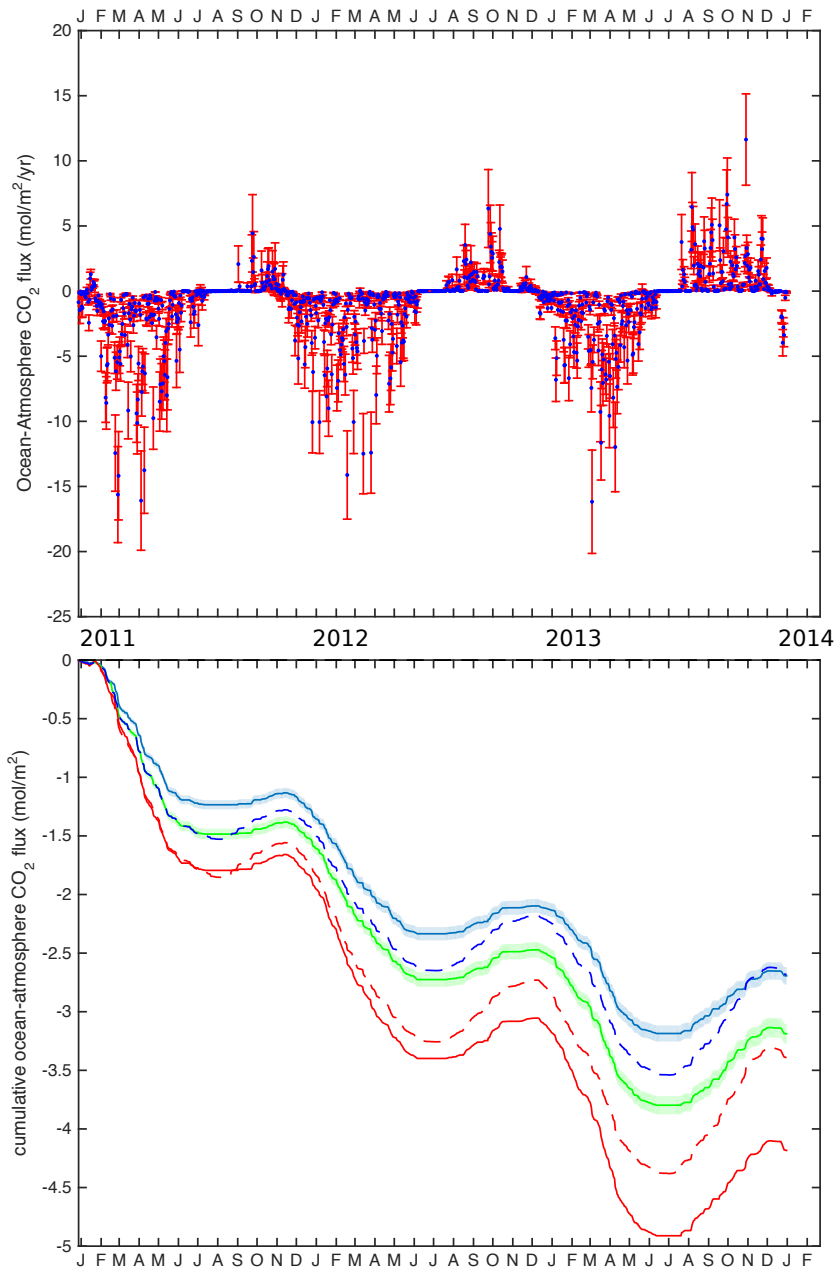


Figure 3.3: Top panel: Ocean-atmosphere CO₂ flux at RaTS, calculated using a linear scaling between k and all ice types (corresponds to solid blue line in the lower panel). Error bars represent approximate 95% confidence. Bottom panel: Cumulative ocean-atmosphere flux of CO₂ at RaTS. Blue line represents flux calculated following Wanninkhof (2013) with a linear scaling of k to sea ice cover. Green line also represents flux calculated following Wanninkhof (2013) but excluding brash ice. Shaded regions represent approximate 95% confidence, calculated as the square root of the cumulative sum of the squares. Blue dashed line represents flux calculated following Wanninkhof (2013) assuming no ice cover. Red line represents flux calculated using the model of Loose et al. (2014), including all ice types. Red dashed line represents flux calculated with the model of Loose et al. (2014) but assuming no ice cover.

3.3.2 Unresolved complexity

Quantification of the gas transfer velocity in ice covered or partially ice covered waters is challenging, particularly as different ice types are likely to affect gas fluxes in different ways and this heterogeneity is not well understood. To investigate the sensitivity of the flux estimates to different ice types, ocean-atmosphere CO₂ flux was also calculated with brash ice ignored (green line, Figure 3.3). This scenario results in a stronger annual ocean uptake of CO₂ than when k is affected by all ice types (solid blue line) because brash ice predominates in summer, when the $\Delta f\text{CO}_2$ is negative, so its removal allows more CO₂ flux into the water. The parameter model of Loose et al. (2014) (red line, Figure 3.3) gives higher k values and therefore a larger net annual sink than the scenario using a linear scaling of k with ice cover. This is partly caused by the way in which these two methods calculate k from wind speed. The contribution of this factor can be seen as the difference between the red and blue dashed lines which do not include ice effects. Another reason for the discrepancy between the linear scaling and the parameter model is the inclusion in the model of shear-driven and convection-driven turbulence which can increase the gas transfer velocity by 40% (Loose et al., 2014). However, a recent study found that the effect of turbulence on k may be less than suggested and that a linear scaling of k with ice cover is more accurate (Butterworth and Miller, 2016). It is important to note that the uncertainty caused by the handling of ice cover and ice type in gas flux estimates dwarfs that caused by uncertainty in the carbonate parameters and the gas transfer velocity (shading on blue and green lines, Figure 3.3). More observational data, from both laboratory ice tank experiments and field studies, are needed to increase our confidence in calculating ocean-atmosphere gas flux in seasonally ice covered waters.

As carbon samples were collected from 15m depth, the seawater $f\text{CO}_2$ used for flux calculations may not accurately represent surface concentrations when the mixed layer shoals to above this depth in summer. Due to biological activity in the surface mixed layer it is likely that the water $f\text{CO}_2$ is over-estimated between approximately December and March, giving an underestimate of the difference be-

tween the concentration of CO₂ in the atmosphere and the sea water. The net annual ocean CO₂ uptake presented here is therefore likely to be an underestimate. Mixed layer depth data are presented in Figure 4.2.

Sea ice does not simply act as a cap to ocean-atmosphere gas exchange; sea ice-atmosphere CO₂ exchange has been observed in both the Arctic and Antarctic (Gosink et al., 1976; Semiletov et al., 2004; Delille, 2006; Zemmeling et al., 2006; Miller et al., 2011b; Nomura et al., 2013). The estimates of CO₂ flux presented here do not account for these ice-atmosphere interactions and so may over or underestimate the net annual sink of the water column. Although sea ice has been demonstrated to act as both a source and sink of CO₂ over the seasonal cycle (Delille et al., 2014), the maximum flux of CO₂ from Antarctic sea ice to the atmosphere of 1.9 mmol m⁻² d⁻¹ observed by Delille et al. (2014) has been applied in order to obtain a first order estimate of the maximum possible reduction in CO₂ sink strength caused by ice cover. Multiplying the percentage cover of fast or pack ice in Ryder Bay during the study period by this value results in a weakening of the net annual sink of atmospheric CO₂ of approximately 0.2 mol m⁻² yr⁻¹.

As well as modulating gas exchange via physical processes, sea ice also affects CO₂ flux through its affect on carbonate chemistry. The precipitation of the hydrated calcium carbonate mineral ikaite (CaCO₃·6H₂O) in sea ice increases CO₂ in brine and its dissolution on ice melt reduces CO₂ of the seawater (Rysgaard et al., 2011). Although no carbon measurements in sea ice were made here, ikaite has been observed in Antarctic sea ice (Dieckmann et al., 2008) and has been found to significantly increase brine pCO₂ during precipitation and decrease brine pCO₂ on dissolution (Papadimitriou et al., 2004; Delille et al., 2007; Geilfus et al., 2012). Rysgaard et al. (2012) found the dissolution of ikaite during sea ice melt to correspond to an air-sea CO₂ uptake of ~3.9 mol C m⁻² yr⁻¹, given a reduction in ice thickness of 0.2 m per week. This process is of a significant magnitude compared to the ocean-atmosphere CO₂ fluxes presented here (Figure 3.3). It is likely that some of the increase in water *f*CO₂ observed during winter in Ryder Bay is caused by the release of high CO₂ brine from sea ice and similarly, that some of the *f*CO₂

decrease observed in spring is caused by ikaite dissolution. However, the quantification of the impact of ice formation/melt on carbonate chemistry in Ryder Bay is complicated by the fact that an observed change in ice cover is not directly related to ice formation/melt as much of the brash and pack ice may be blown in/out of the bay rather than forming/melting in situ (Meredith et al., 2010). Biological production by ice algae was also not quantified here and almost certainly contributes to reducing DIC and $f\text{CO}_2$ in the surface layer, increasing the ocean uptake of CO₂ in spring.

3.3.3 Conclusions

- Ryder Bay is a net sink of atmospheric CO₂ of 0.90 - 1.39 molC m⁻² yr⁻¹ (average of 3 years).
- During spring and summer, primary production in the surface ocean reduces $f\text{CO}_2$ and promotes atmospheric CO₂ uptake. In winter, higher DIC, caused by net heterotrophy and vertical mixing with CDW, results in outgassing of CO₂ from the ocean. Interannual variability in ice cover and mixing with deep water influences the strength of the ocean CO₂ sink.
- Seasonal sea ice cover modifies the ocean CO₂ sink but large uncertainty remains regarding the effect of sea ice on gas exchange.

Chapter 4

The seasonal cycle of carbonate system processes in Ryder Bay

The majority of the work in this chapter has been published as: Legge, O.J., Bakker, D.C.E, Meredith, M.P., Venables, H.J., Brown, P.J., Jones, E.M., Johnson, M.T. (2017), The seasonal cycle of carbonate system processes in Ryder Bay, West Antarctic Peninsula. *Deep-Sea Research II*, 139, 167-180.

4.1 Rationale

The carbon cycle in seasonally sea-ice covered waters remains poorly understood due to both a lack of observational data and the complexity of the system. Primary production, calcium carbonate precipitation, vertical mixing, and air-sea flux all affect the marine carbonate system. Glacial ice and seasonal sea ice also influence water column structure, ocean-atmosphere gas fluxes and biogeochemical cycling. While the the effect of these processes on the carbonate system may be understood in isolation, their interactions and combined effects over a full seasonal cycle are much harder to estimate. Time series observations allow this integrated view but very few studies have measured the carbonate system over a full seasonal cycle in seasonally ice covered, polar waters. The aims of this chapter are to:

- Characterise the seasonal cycle of the carbonate system in the surface water of Ryder Bay

- Quantify the effect of four processes on DIC: ocean-atmosphere CO₂ flux; the mixing of different source waters; photosynthesis and respiration; the precipitation and dissolution of calcium carbonate.
- Describe the mechanisms behind the observed seasonal cycle and interannual variability.

4.2 Methods

4.2.1 Sampling and analysis

Sampling and ice observations at the RaTS site are described in Section 2.2.1 and the analysis of DIC and TA samples are described in Section 2.3.1. Mixed layer depth was defined as the depth at which density is 0.05 kg m⁻³ greater than at a reference depth (Venables et al., 2013). From November to April the sea surface was used as the reference depth but from May to October a reference depth of 10 m was used in order to prevent shallow, small-scale melt water events affecting the results. A measure of stratification is also presented, defined as the potential energy (in J/m²) that would be required to homogenise the top 100 m of the water column (Venables and Meredith, 2014).

The fugacity of CO₂ in water ($f\text{CO}_2$), the saturation state of the calcium carbonate minerals calcite and aragonite, and the pH were calculated from measurements of DIC, TA, temperature, salinity, silicate and phosphate using the CO2SYS program (Van Heuven et al., 2011a). The dissociation constants of Goyet and Poisson (1989) were used due to their suitability at low temperatures (Brown et al., 2014). Here, pH is presented on the seawater scale (Goyet and Poisson, 1989).

Ice samples for DIC, TA and phosphate endmember values were collected between November and March 2014. Sea ice samples were taken from cores of fast ice in Hangar Cove, north of Ryder Bay. Glacial samples were taken from the Sheldon Glacier (Figure 2.1). Ice samples were sealed in Tedlar bags and air was removed using a hand pump. The samples were melted in the dark at lab temperature (18-20°C) for 20-24 hours and were then transferred to 250 mL borosilicate bottles, poisoned with mercuric chloride, sealed and stored in the dark until analysis. DIC

and TA were measured at Rothera using a VINDTA 3C, as described in Section 2.3.1. Ice phosphate samples were drawn from the Tedlar bags, filtered ($0.2 \mu\text{M}$) and stored in the dark at -20°C until analysis at the Royal Netherlands Institute for Sea Research. Seawater samples for oxygen isotope analysis were collected in 150 mL glass medical bottles, which were sealed with caps with rubber inserts, and parafilm to prevent slippage. They were transported to the UK via dark cool stow, for analysis by stable isotope mass spectrometry on an Isoprime spectrometer. Full details are provided in Meredith et al. (2017).

4.2.2 Quantifying carbonate system processes

The processes affecting surface water DIC and TA at the study site were divided into four groups: the air-sea flux of CO_2 ; mixing of water masses; photosynthesis and respiration; the precipitation and dissolution of calcium carbonate. The rate of each of these process groups was quantified throughout the three year time series of carbon measurements using the approaches detailed in Sections 4.2.2.1 to 4.2.2.3. When calculating process rates, data were not binned or averaged; instead process rates were calculated using the change in measured variables from each discrete sampling time to the next in order to preserve as much of the observed variability as possible. The time between discrete sampling times will be referred to as time steps.

A Monte Carlo approach was used to propagate uncertainty through the calculations, ensuring that all non-linearities in the carbonate system calculations were accounted for. Each calculation described below was carried out with 10^5 variable-value sets, randomly sampled from the statistical distributions of the variables, as described in Section 4.2.3.

4.2.2.1 Air-sea CO_2 flux

The calculation of air-sea CO_2 flux is described fully in Chapter 3. For the purpose of this chapter, the gas transfer velocity was calculated following Wanninkhof et al. (2013) with a linear scaling to the fraction of open water, including all ice types. The daily calculated flux was divided by density and mixed layer depth to give the

change to the mixed layer DIC concentration caused by air-sea flux. These daily values were summed over each time step and then divided by the length of the time step to give a process rate in units of $\mu\text{mol of DIC kg}^{-1} \text{d}^{-1}$. This estimate does not account for ice-atmosphere fluxes which are expected to be small compared to air-sea fluxes but may be significant over larger temporal and spatial scales (Delille et al., 2014).

4.2.2.2 Contribution of mixing

Water in Ryder Bay can be characterised as a mixture of three main sources: Circumpolar Deep Water (CDW), sea-ice melt and meteoric water (glacial melt and precipitation) (Meredith et al., 2008a). This complexity means that a simple two end-member salinity normalisation of TA or DIC will fail to remove some of the variability caused in these variables by mixing. In order to capture the influence of the three water sources on DIC and TA, measurements of salinity and oxygen isotopes ($\delta^{18}\text{O}$) are used to solve the following three endmember mass balance equations (Meredith et al., 2008a, 2017).

$$\begin{aligned} f_{si} + f_{met} + f_{cdw} &= 1 \\ S_{si} \cdot f_{si} + S_{met} \cdot f_{met} + S_{cdw} \cdot f_{cdw} &= S \\ \delta_{si} \cdot f_{si} + \delta_{met} \cdot f_{met} + \delta_{cdw} \cdot f_{cdw} &= \delta \end{aligned} \quad (4.1)$$

where f_{si} , f_{met} and f_{cdw} represent the fractions of sea-ice melt, meteoric water and CDW, respectively, which comprise the water sample in question. The salinity and $\delta^{18}\text{O}$ of the water sample are represented by S and δ respectively. S_{si} , S_{met} and S_{cdw} represent the salinity of the three endmembers and δ_{si} , δ_{met} and δ_{cdw} represent the $\delta^{18}\text{O}$ values of the three endmembers. Oxygen isotope and salinity samples were taken at the same time and location as the carbonate chemistry samples so the percentage contributions calculated here directly correspond to the DIC and TA data points in time and space.

To quantify the change in DIC and TA due to mixing during each time step, the change in the percentage contribution of each endmember over that time step

was multiplied by its concentration of DIC and TA (Equation 4.2). The endmember concentrations used for salinity, $\delta^{18}O$, DIC and TA in CDW, sea-ice melt and meteoric water are detailed in the Section 4.2.3.

$$\Delta DIC_{mix} = \Delta CDW \cdot [DIC]_{cdw} + \Delta MET \cdot [DIC]_{met} + \Delta SI \cdot [DIC]_{si} \quad (4.2)$$

where ΔDIC_{mix} is the change in DIC due to mixing over a given time step, ΔCDW , ΔMET and ΔSI are the changes in fractional contributions of the three water sources over the time step and $[DIC]_{cdw}$, $[DIC]_{met}$ and $[DIC]_{si}$ are the DIC concentrations of the three endmembers. The same method was used for TA. The change in DIC due to mixing over each time step was divided by the length of the time step to give a process rate in units of $\mu\text{mol kg}^{-1} \text{d}^{-1}$.

4.2.2.3 Quantifying net dissolution and net respiration

Once the effects of mixing and air-sea flux have been removed, any remaining change observed in DIC and TA over a time step must come from the balance of precipitation and dissolution of calcium carbonate and from the balance of photosynthesis and respiration. These processes were quantified simultaneously using their known effects on the relative concentrations of DIC and TA. The method detailed below is believed to be novel and is a useful tool when quantifying carbonate system processes as it explicitly quantifies the precipitation and dissolution of calcium carbonate rather than leaving these processes as a residual.

The formation and dissolution of calcium carbonate changes TA and DIC in a 2:1 ratio (Zeebe and Wolf-Gladrow, 2001) as one mole of DIC and two negative charge equivalents are consumed to produce one mole of calcium carbonate (Equation 1.7). Photosynthesis reduces the concentration of DIC in the water as it is incorporated into organic matter and the reverse is true for respiration. As described in Section 1.2.2, photosynthesis and respiration do not have a direct effect on carbonate alkalinity although they do cause a slight TA increase and decrease,

respectively, due to the assimilation and remineralisation of nutrients. The ratio of the influence of photosynthesis and respiration on DIC and TA therefore depends on the carbon to nitrogen ratio of the organic matter and this has been accounted for in the uncertainty analysis (Section 4.2.3). For brevity, the balance of calcium carbonate precipitation and dissolution will be referred to as net dissolution because a positive rate indicates increasing DIC through net dissolution. Similarly, the balance of photosynthesis and respiration will be referred to as net respiration.

For each time step, the change in DIC and TA due to net respiration and net dissolution was calculated by using the known slopes of these processes in DIC/TA space (green and cyan coloured lines, Figure 4.1). The DIC and TA values at the intersection of these process slopes were calculated using Equations 4.3 and 4.4. This intersection allows the calculation of the change in both DIC and TA caused by each process. The change in DIC due to net respiration and the change in DIC due to net dissolution were then divided by the length of the time step to give rates for these processes in units of $\mu\text{mol kg}^{-1} \text{d}^{-1}$. The graphical example in Figure 4.1 highlights the Monte Carlo approach whereby the process rates for each time step were calculated 10^5 times to incorporate various uncertainties (Section 4.2.3).

$$\text{DIC}_i = \frac{(\text{TA}_2 - M_{diss} \cdot \text{DIC}_2) - (\text{TA}_1 - M_{resp} \cdot \text{DIC}_1)}{M_{resp} - M_{diss}} \quad (4.3)$$

$$\text{TA}_i = M_{resp} \cdot (\text{DIC}_i - \text{DIC}_1) + \text{TA}_1 \quad (4.4)$$

where i denotes the DIC or TA at the intersection between the two process slopes (the point where green and cyan lines meet in Figure 4.1), M_{resp} is the slope of photosynthesis and respiration in DIC/TA space and M_{diss} is the slope of precipitation and dissolution of calcium carbonate in DIC/TA space. The subscript $_1$ denotes the DIC or TA concentration at the start of the time step, after the effects of mixing and air-sea CO_2 flux have been accounted for. The subscript $_2$ denotes the DIC or TA

concentration at the end of the time step.

4.2.2.4 Quantifying net respiration from phosphate

Phosphate data were used to obtain an estimate of net respiration, independent of the carbon measurements. Firstly, the effect of mixing on phosphate concentration over each time step was calculated using the endmember approach described above for DIC and TA. The endmember values of phosphate in CDW, sea ice and meteoric water are detailed in Section 4.2.3. It should be noted that inaccuracies in the percentage contribution of the three end member water masses affects both carbon and phosphate-derived net respiration estimates. Once the effect of mixing was removed from the measured changes, the remaining change in phosphate concentrations over each time step was multiplied by the ratio of phosphorus to carbon in organic matter. Variability in the elemental ratios of organic matter has been accounted for in the Monte Carlo approach and is discussed in Section 4.2.3.

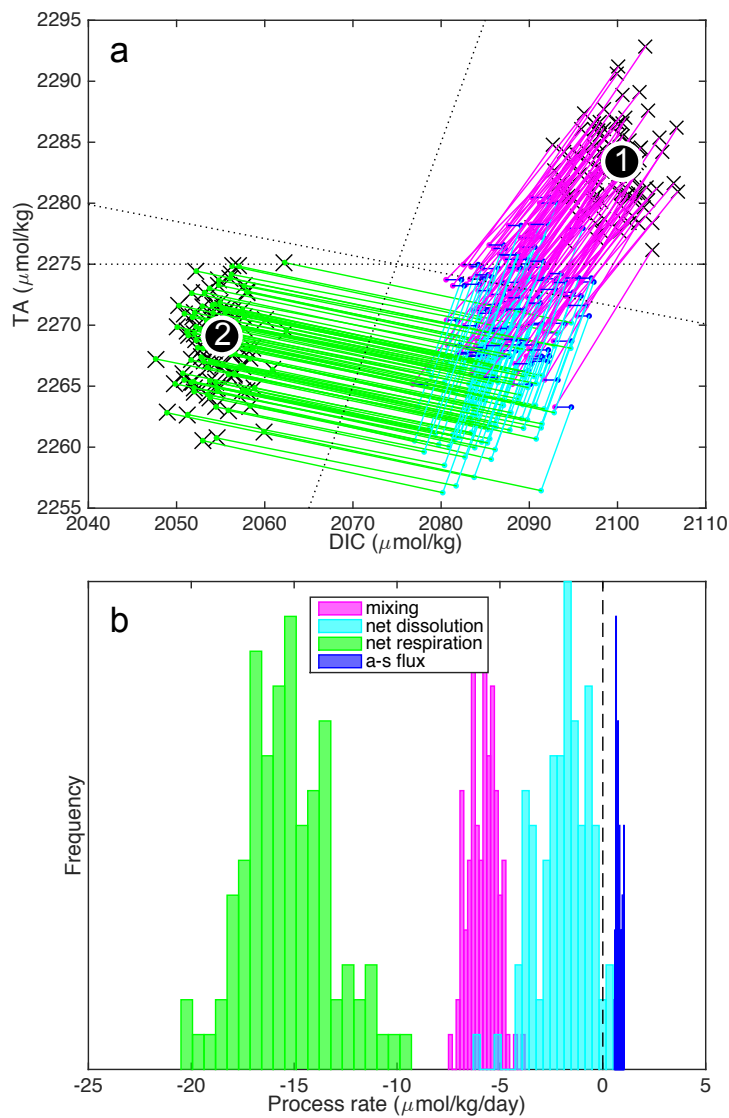


Figure 4.1: A graphical example of process rate calculations in DIC/TA space for one time step. a) The paths taken through DIC/TA space by a random subset of the Monte Carlo runs for this time step. A subset is used for visual clarity. The points marked '1' and '2' show the measured DIC and TA at the start (19th January 2013) and end (21st January 2013) of the time step respectively. Crosses represent the DIC and TA values used in the Monte Carlo analysis for the start and end of the time step and their spread represents the uncertainty on DIC and TA measurements. Pink lines represent the change in DIC and TA due to mixing, dark blue lines represent the change in DIC and TA due to air-sea CO_2 flux, cyan lines represent the change in DIC and TA due to the precipitation and dissolution of calcium carbonate and green lines represent the change in DIC and TA due to photosynthesis and respiration. See Section 4.2.3 for a description of the uncertainties used in the Monte Carlo analysis. b) Probability distributions for the processes affecting DIC during this time step. The same subset of Monte Carlo runs is shown as in panel a.

4.2.3 Distribution of variables

In order to perform the Monte Carlo analysis, each value of each variable was given a distribution to represent its uncertainty and this distribution was randomly sampled 10^5 times. DIC and TA were given normal distributions with the population mean being the measured value and the uncertainty defined using replicate precision specific to each of the three field seasons. The reason for using different uncertainty estimates for different field seasons is that, although instrument precision remains fairly stable between different years (long term standard deviation of certified reference material of $2.2 \mu\text{mol kg}^{-1}$ or less for both DIC and TA), there is considerable variation in replicate precision between different field seasons. This could reflect differences in sampling, poisoning, storage and transport. The DIC and TA standard deviations in 2010-12 were $4.3 \mu\text{mol kg}^{-1}$ and $4.9 \mu\text{mol kg}^{-1}$ respectively. In 2012-13 they were $6.2 \mu\text{mol kg}^{-1}$ and $7.0 \mu\text{mol kg}^{-1}$ and in 2013-14 they were $3.4 \mu\text{mol kg}^{-1}$ and $1.5 \mu\text{mol kg}^{-1}$. The uncertainty used here for a given DIC or TA value is the replicate precision of the relevant field season divided by the square root of the number of replicates from that time and location.

Phosphate was given normal distributions with the population mean being the measured value and the uncertainty defined as precision determined by the analyst (2.7 %). The dissociation constants of Goyet and Poisson (1989) were used in CO2SYS and were given normal distributions with uncertainties of 0.0055 for pK1 and 0.01 for pK2 (Millero, 2007). The sum of the air-sea CO_2 flux during each time step was given a uniform distribution of 30% either side of the calculated value to account for the high degree of uncertainty associated with this process. In order to account for uncertainties in the endmember approach used to quantify mixing processes, each endmember was given distributions for salinity, $\delta^{18}\text{O}$, DIC, TA and phosphate (Table 4.1). Most of the uncertainty in the $\delta^{18}\text{O}$ /salinity method to quantify water mass contributions comes from the value of the $\delta^{18}\text{O}$ and salinity endmembers (Meredith et al., 2017). This is largely a systematic uncertainty and therefore cancels out when the change over a time step is calculated.

The relative influence on DIC and TA by photosynthesis and respiration is

determined by the carbon to nitrogen ratio of primary producers (Section 4.2.2.3). Studies in the region find the C:N ratio to be close to Redfieldian (Rubin et al., 1998; Martiny et al., 2013; Hauri et al., 2015) so the C:N ratio has been assigned a normal distribution with a mean of 6.6 and a standard deviation of 0.25. Clarke et al. (2008) found an average nitrate to phosphate ratio of 15.3 in Ryder Bay. When using phosphate data to calculate net respiration in Section 4.2.2.4 the C:N distribution described above is used, multiplied by 15.3.

| | CDW | Meteoric | Sea Ice |
|---------------------------------------|------------------|-------------|---------------|
| Salinity | 34.62 ± 0.01 | 0 | 7 ± 1 |
| $\delta^{18}\text{O}$ (‰) | 0.08 ± 0.01 | -22 to -13 | 1.8 to 2.7 |
| DIC ($\mu\text{mol kg}^{-1}$) | 2253 ± 20 | 16 ± 5 | 277 ± 150 |
| TA ($\mu\text{mol kg}^{-1}$) | 2350 ± 20 | 100 ± 5 | 328 ± 150 |
| Phosphate ($\mu\text{mol kg}^{-1}$) | 2.2 to 2.6 | 0 to 0.03 | 0.5 ± 0.7 |

Table 4.1: Distributions of endmember variables. Distributions with \pm are normal and have been truncated at zero. Distributions with a range are uniform. Salinity and $\delta^{18}\text{O}$ endmembers are based on Meredith et al. (2008a). CDW DIC and TA endmembers are based on Hauri et al. (2015). The CDW phosphate endmember is based on Henley et al. (2017). Sea ice and glacial ice DIC, TA and phosphate endmembers are from ice samples collected close to the study site (Section 4.2.1).

4.2.4 Method limitations

The method used here to quantify water mass contributions gives a good first order estimate of the effect of mixing on the carbonate system. However, it does not resolve some physical processes influencing DIC and TA in Ryder Bay and these inaccuracies may affect the calculated rates of net respiration and net dissolution. Firstly, using water mass contributions based on the conservative tracers salinity and $\delta^{18}\text{O}$ will not capture changes caused by advection and may cause the rate of biogeochemical processes to be over- or underestimated. This limitation is probably responsible for much of the short-term variability in the calculated net respiration and net dissolution rates because, although the surface water in the whole bay is expected to follow broadly the same seasonal pattern, there is likely to be significant horizontal variability in primary production and mixing over shorter spatial and temporal scales. Monthly and seasonal averages of process rates should therefore

provide more representative rate estimates for the bay as a whole. Secondly, the end member method used here calculates the net change in the percentage contribution of each water mass over each time step, but it is likely that during a time step there are gross changes which are not captured by this method and which deliver carbon or nutrients to the sampling depth. If some of these chemicals are taken up and retained in the surface water, then the change will be attributed to biogeochemical processes and the mixing term will be underestimated. Finally, characterising CDW as one homogeneous endmember is an over-simplification. In reality there are vertical gradients of DIC, TA and nutrients in the water column and, due to biogeochemical processes, these gradients are unlikely to be conservative with the calculated percentage of CDW. More data on the vertical and horizontal variability of DIC, TA and nutrients would allow a more sophisticated calculation of mixing.

It is important to note that, when calculating net dissolution and net respiration from surface DIC and TA concentrations (Section 4.2.2.3), the signal of these processes within sea ice will also be captured. However, there may be some time delay in the process rate estimates as any ice-derived signal is not measured until the ice melts or brine is released into the underlying water.

A caveat to the air-sea flux calculations is that during summer the water column can be highly stratified with a mixed layer shallower than the 15 m sampling depth (Figure 4.2). The water $f\text{CO}_2$ used in the flux calculations may therefore not be representative of the $f\text{CO}_2$ in contact with the atmosphere. It is expected that this results in an underestimation of the ocean uptake of atmospheric CO_2 because surface water is likely to have lower $f\text{CO}_2$ than the sampling depth due to ice melt and photosynthesis.

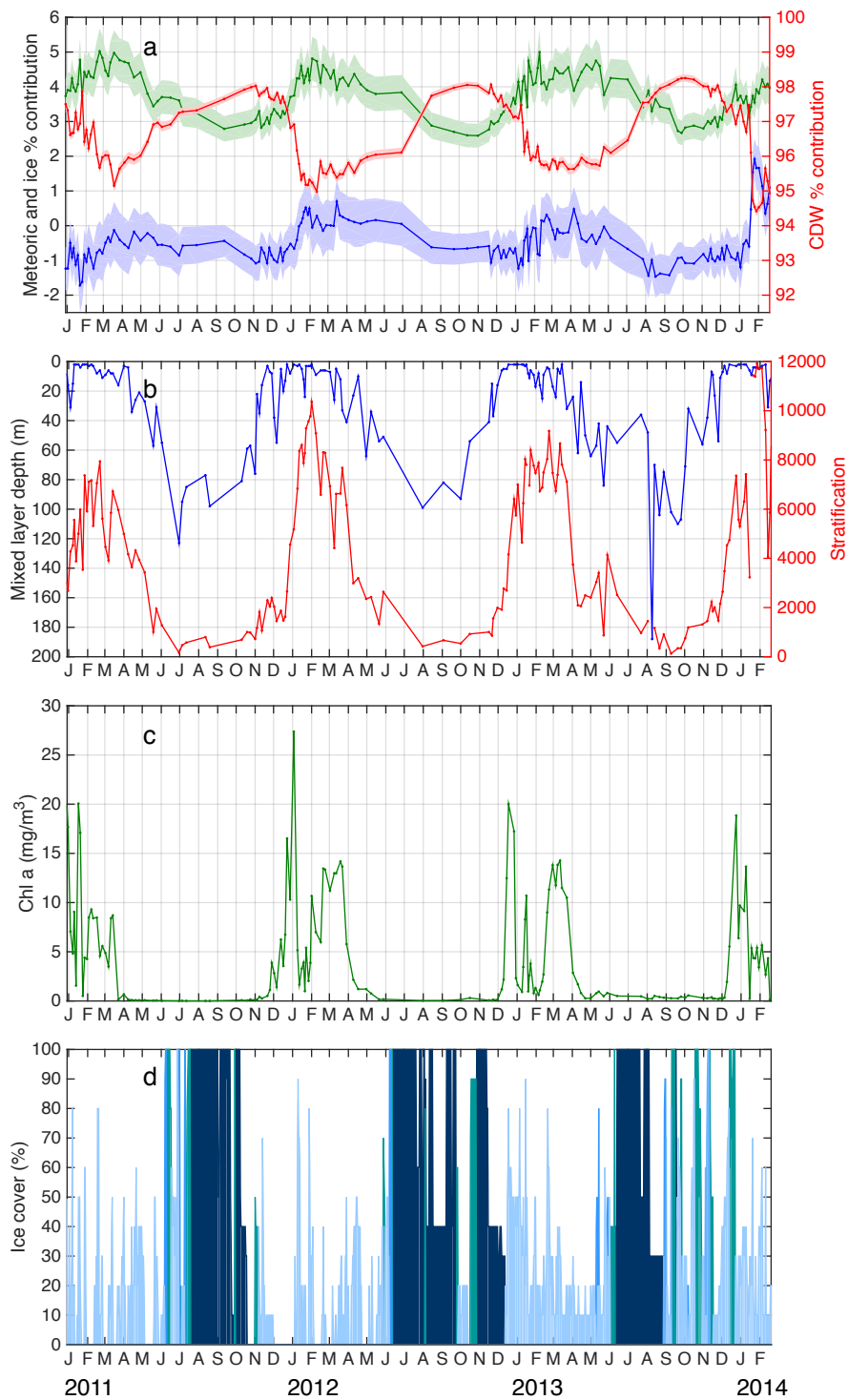


Figure 4.2: Factors influencing the carbonate system in Ryder Bay. a) Percentage contribution of meteoric water (green), sea ice (blue) and CDW (red) to the water at 15 m; b) Mixed layer depth (blue) and stratification (red). Stratification is expressed as the energy in Joules/m² required to homogenise the top 100 m; c) Chlorophyll-a concentration at 15 m depth; d) Percentage ice cover. Bar colour denotes ice type. Dark blue represents fast ice, turquoise represents pack ice and light blue represents brash ice.

4.3 Results

4.3.1 The observed carbonate system

Both DIC and TA data exhibit a strong, asymmetric seasonal cycle (Figure 4.3). Their concentrations increase gradually during the autumn and winter to maximum values of $\sim 2200 \mu\text{mol kg}^{-1}$ of DIC and $\sim 2295 \mu\text{mol kg}^{-1}$ of TA in September. The rapid decrease in DIC and TA in December and January is preceded by a more gradual decrease during October and November. An interesting feature which recurs in each of the three years sampled is a rapid, short-lived decrease in TA in March of about $30 \mu\text{mol kg}^{-1}$ relative to surrounding values.

The fugacity of CO_2 in water largely follows the seasonal pattern of DIC and has an amplitude of $\sim 300 \mu\text{atm}$ (Figure 4.4). The $f\text{CO}_2$ of the water is greater than in the overlying atmosphere in winter and lower in the summer, leading to a change in the direction of the air-sea flux of CO_2 , with the ocean being a net sink of atmospheric CO_2 in summer and a net source in winter (Chapter 3). The pH and the saturation states of the calcium carbonate minerals calcite and aragonite show a rapid increase in December - January followed by a more gradual and variable decrease to a winter minimum (Figure 4.4). The pH ranges from ~ 7.95 to ~ 8.4 . The saturation state of calcite ranges from ~ 1.5 to ~ 4.5 whereas the more soluble calcium carbonate polymorph, aragonite, has saturation states ranging from ~ 1.0 to ~ 2.8 .

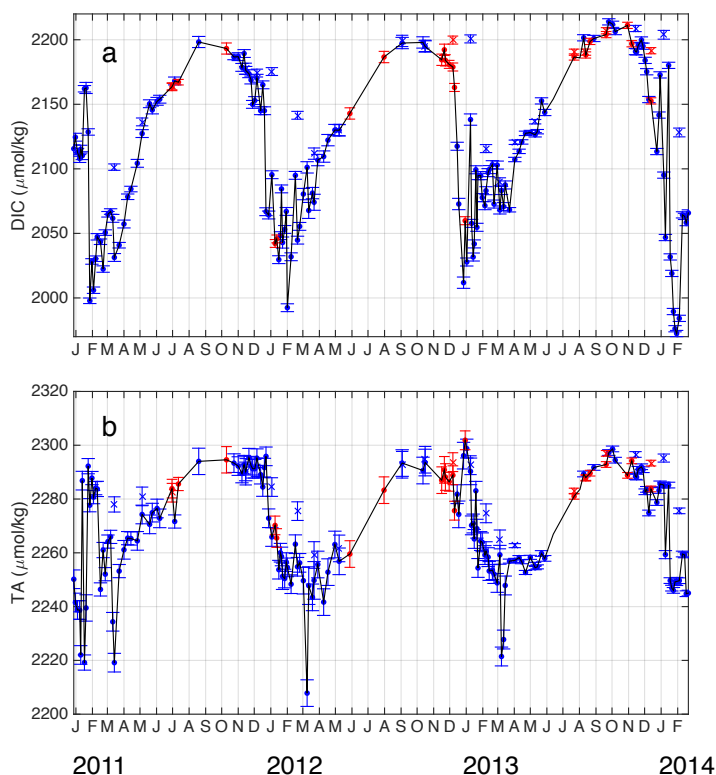


Figure 4.3: Measured carbonate system variables. a) Dissolved inorganic carbon, b) total alkalinity. Dots represent data from 15 m, crosses represent data from 40 m. Blue points are from RaTS site 1 and red points are from site 2. Error bars represent approximate 95% confidence based on measurement precision.

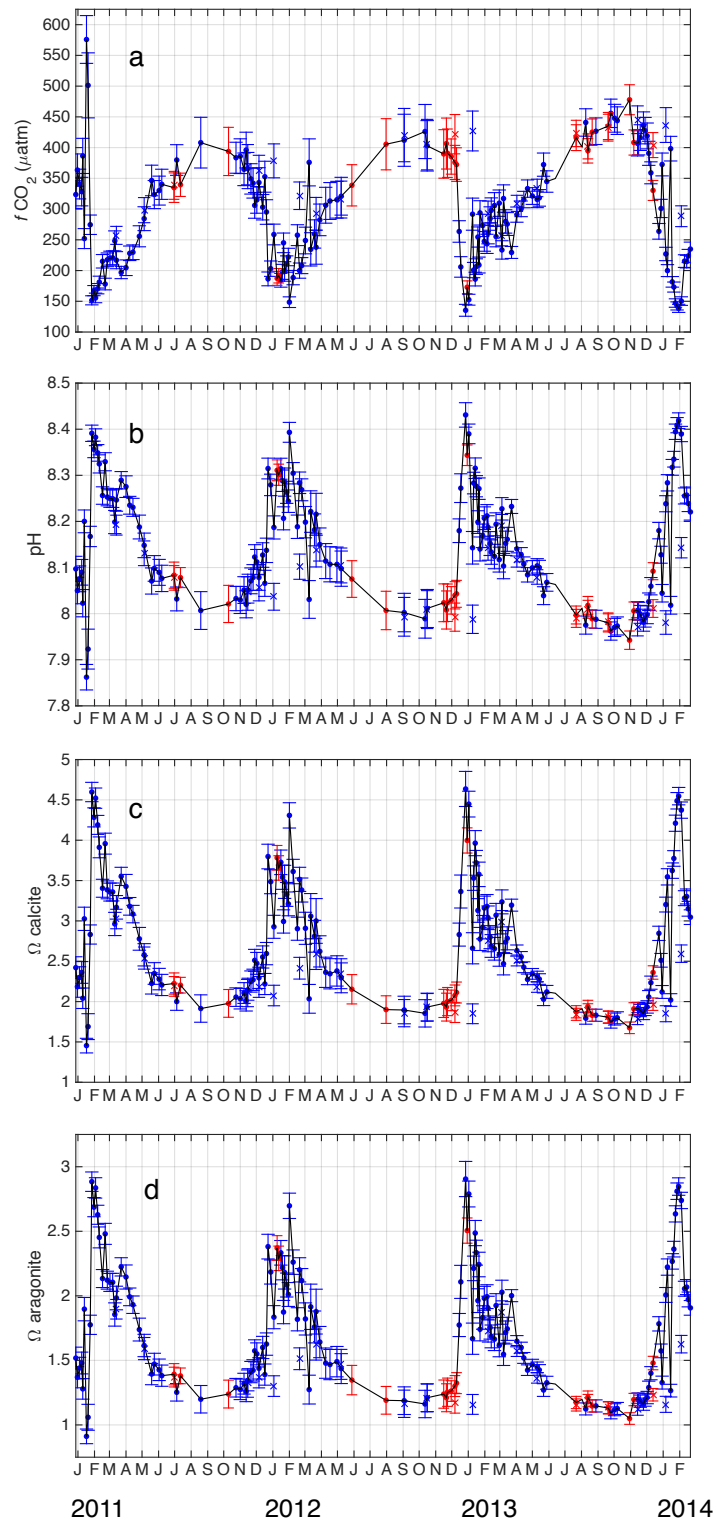


Figure 4.4: Calculated carbonate system variables. a) $f\text{CO}_2$, b) pH, c) calcite saturation state and d) aragonite saturation state. Dots represent data from 15 m, crosses represent data from 40 m. Blue points are from RaTS site 1 and red points are from site 2. Error bars represent approximate 95% confidence based on measurement precision and dissociation constants.

Carbonate system data from the two RaTS sampling sites generally agree well. During the winter months, when the water column is well mixed, DIC and TA data from the two sampling depths agree closely but as the water column stratifies in spring and summer the 15 m values decrease more rapidly than those from 40 m, due to primary production in the surface layer and the persistent influence of CDW at depth. Although the seasonal cycle of the carbonate system variables is broadly consistent between the three observed years, there is intriguing interannual variability. The DIC and water $f\text{CO}_2$ is greater in winter 2013 than in the two preceding years (Chapter 3) and there is a corresponding decrease in winter pH and calcium carbonate saturation states. The exact timing and magnitude of the main, summer DIC drawdown is not identical between the four years and the TA appears to behave slightly differently in each of these productive periods. At the very start of the time series in December 2010 - January 2011 there are unseasonably low TA values compared to the other years, leading to low pH and calcium carbonate saturation states (Figure 4.4).

4.3.2 Processes

The method presented here allows the seasonal cycle of the four processes affecting the carbonate system to be quantified and their relative importance during the year to be determined. Figure 4.5 shows the process rates calculated for each measured time step. All process rates are greatest between November and March and are very low in winter. There is very large variability in process rates, especially net respiration which ranges from -35 to $25 \mu\text{mol kg}^{-1} \text{d}^{-1}$ during the productive summer season.

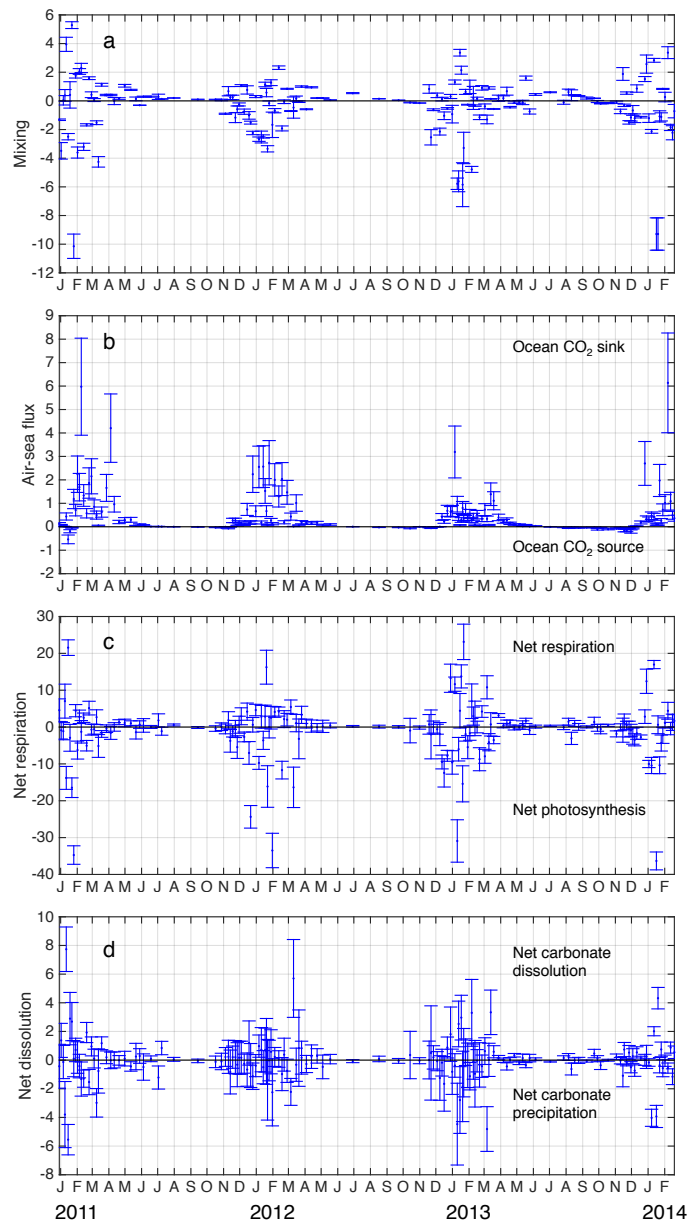


Figure 4.5: Calculated rates of processes affecting DIC in the surface water of Ryder Bay, expressed in $\mu\text{mol DIC kg}^{-1} \text{d}^{-1}$. a) Mixing, b) air-sea CO₂ flux, c) net respiration and d) net dissolution. Error bars represent approximate 95% confidence from Monte Carlo analysis.

Monthly and seasonal averages of process rates (Figures 4.6 and 4.7) present the seasonal cycle more clearly and average out some of the shorter time scale variability, which is likely caused by advection (Section 4.2.4). Mixing reduces the DIC concentration between October and March and increases the DIC concen-

tration from April to September. The largest change due to mixing is in January, although there is significant interannual variability between the four observed years (Figure 4.6). The results of the salinity and $\delta^{18}O$ method to determine water mass contributions are shown in Figure 4.2 and are investigated thoroughly by Meredith et al. (2017). The water in Ryder Bay is dominated by CDW (95-98%). Meteoric and sea ice components decrease in the austral winter and increase in the austral summer with meteoric contributions being consistently greater than sea ice contributions. Negative sea ice contributions indicate that there has been a net sea ice production from that water prior to it being sampled. Percentage contributions of sea ice do not coincide directly with ice cover due to different advection of ice and water into and out of Ryder Bay (Meredith et al., 2008a).

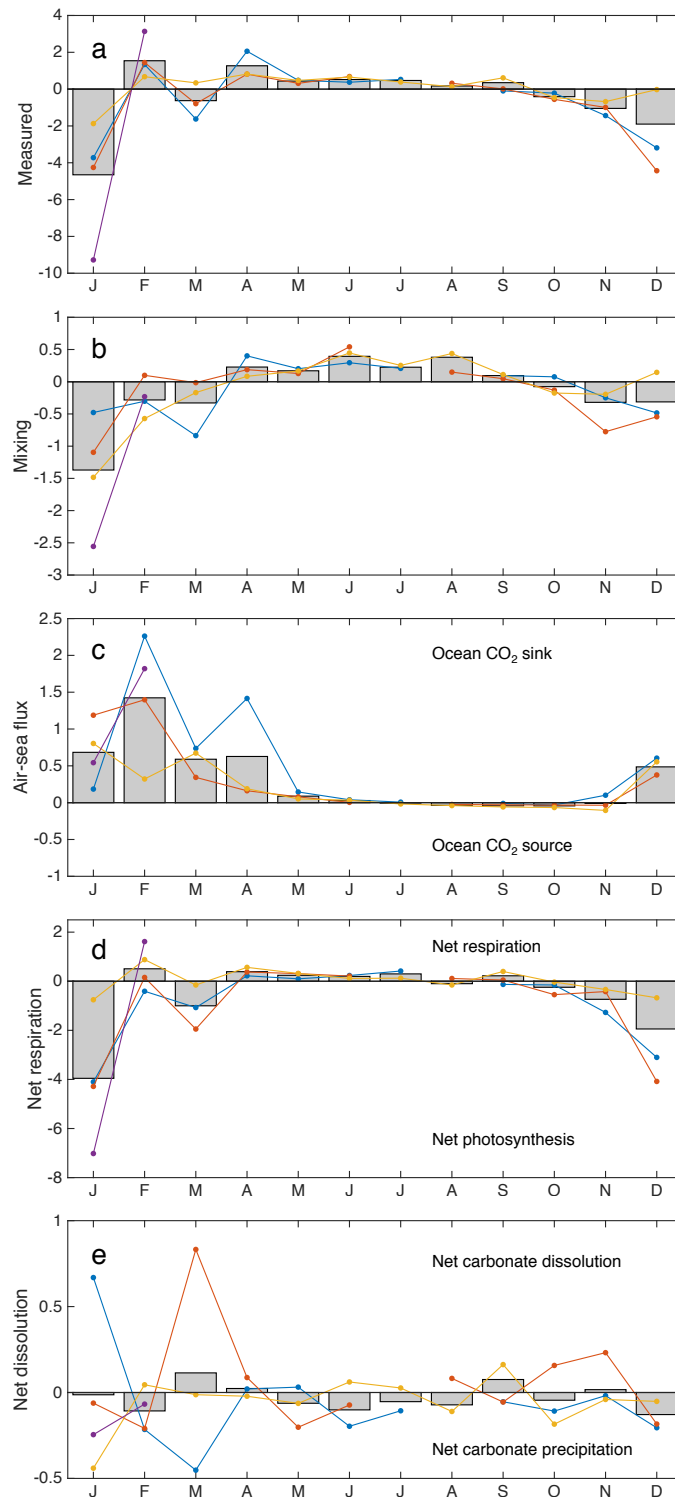


Figure 4.6: Monthly mean rates of processes affecting DIC in the surface water of Ryder Bay. a) Measured rate of change of DIC, b) mixing, c) air-sea CO_2 flux, d) net respiration, e) net dissolution. All rates are expressed in units of $\mu\text{mol DIC kg}^{-1} \text{d}^{-1}$. Grey bars are the monthly averages including data from all years of carbon sampling. Coloured points represent monthly means of individual years (blue: 2011, red: 2012, yellow: 2013, purple: 2014). Note the different scale for different processes.

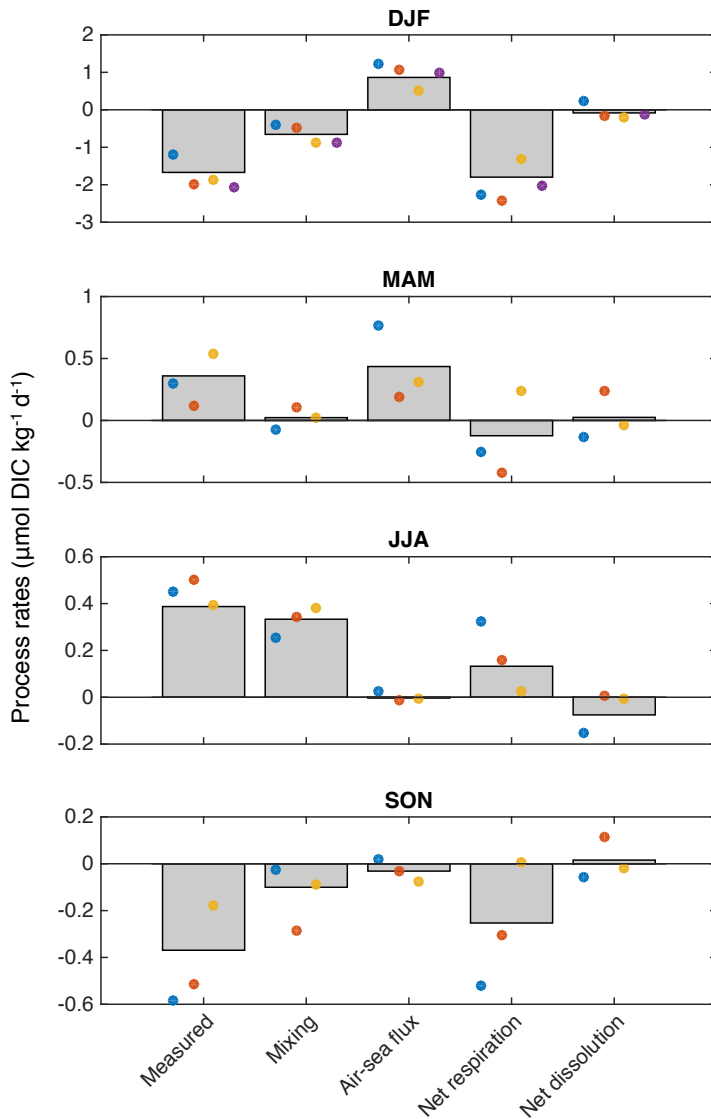


Figure 4.7: Seasonal mean rates of processes affecting DIC in the surface water of Ryder Bay. Grey bars represent the seasonal mean process rates from all years of carbon sampling. Dots represent seasonal means from individual years of the time series (blue: 2011, red: 2012, yellow: 2013, purple: 2014). All rates are expressed in units of $\mu\text{mol DIC kg}^{-1} \text{d}^{-1}$. The seasonal means have been calculated as the mean of the three monthly means in each season (DJF, MAM, JJA and SON) to avoid sampling bias. Note different scale for different seasons.

The strong seasonal cycle of air-sea CO_2 flux increases the surface ocean DIC concentration in summer and reduces it in winter, and in all three years the summer uptake exceeds the winter outgassing (Figure 4.6). This seasonal asymmetry is accentuated when the air-sea flux is expressed in $\mu\text{mol kg}^{-1} \text{d}^{-1}$ for the mixed

layer because the mixed layer depth is greatest in winter, making the change to the DIC concentration smaller for a given flux of CO₂ across the water-air interface. There is considerable interannual variability in the monthly mean flux rates. In 2013, air-sea fluxes were lower than average in both summer and winter (Figures 4.6 and 4.7), resulting in a weaker net ocean sink of atmospheric CO₂ in 2013 than in the previous two years.

Primary production also shows a clear seasonal cycle with net respiration increasing DIC concentrations during the winter months and net photosynthesis reducing DIC in summer (Figure 4.6). Net photosynthesis is consistently highest in December and January although there is large interannual variability in the magnitude of the monthly means in these months. The monthly averaged rates of net calcium carbonate dissolution (Figure 4.6) are low (less than 0.15 $\mu\text{mol kg}^{-1} \text{d}^{-1}$) and in only one month (December) do all year's monthly means agree on the sign of the process, making identification of a seasonal pattern impossible.

4.4 Discussion

4.4.1 Saturation states

The seasonal cycle of Ω aragonite presented here is very similar in timing and amplitude to that observed in the coastal Ross Sea (Sweeney, 2003; McNeil et al., 2011), although the Ross Sea study lacked winter data. Comparison with Prydz Bay in East Antarctica is more challenging as the two seasonal cycles of pH and Ω observed there in 1993-95 (Gibson and Trull, 1999; McNeil et al., 2011) and 2010-11 (Roden et al., 2013) are quite different in timing and amplitude. The Ω data show a similar pattern to the more recent Prydz Bay data (2010-11) although Ω in Ryder Bay reaches much higher values; Ω aragonite in Prydz Bay did not exceed 2 during summer 2010-11 (Roden et al., 2013). The results presented here broadly corroborate the estimates of Hauri et al. (2015) who used pCO₂, salinity and temperature data from the Pal-LTER grid to calculate aragonite saturation state for the waters of the WAP shelf between 1999 and 2013. They found large interannual variability

and more than 20% of their calculated winter and spring values fell below 1.2.

Some Arctic studies have found that melting ice can lower Ω through dilution of carbonate ions in the water (Chierici and Fransson, 2009; Yamamoto-Kawai et al., 2009). However, consistent with other Southern Ocean studies (Mattsdotter Björk et al., 2014; Shadwick et al., 2013), increasing percentage contributions of glacial and sea-ice melt in summer coincide with increasing Ω , suggesting that DIC uptake by primary production outweighs any dilution effect in Ryder Bay. It is worth noting, however, that the sampling depth is at the typical chlorophyll maximum in Ryder Bay (Clarke et al., 2008) and the dilution effect of melt water on pH and Ω in the highly stratified water above may be more significant relative to primary production.

4.4.2 The seasonal cycle of carbonate processes

4.4.2.1 Summer (December, January, February)

The dominant carbonate system process in summer (December, January and February) is primary production; the reduction in DIC caused by photosynthesis is roughly twice as large as the reduction in DIC due to mixing (Figure 4.7). In all years the highest rates of photosynthesis are in December and January, coincident with the main phytoplankton bloom and rapidly increasing stratification (Figure 4.2) and the main periods of net photosynthesis broadly correspond to increasing chlorophyll concentrations (Figure 4.8). The interannual variability in the magnitude of net photosynthesis in December and January (Figure 4.6) is largely caused by slight differences in the timing of the main bloom between years and is consistent with earlier observations of significant interannual variability in the intensity, timing and depth of blooms in Ryder Bay (Clarke et al., 2008). The summer seasonal averages for the four years are more similar, showing that, when process rates are averaged over the whole growing season, there is less variability between years.

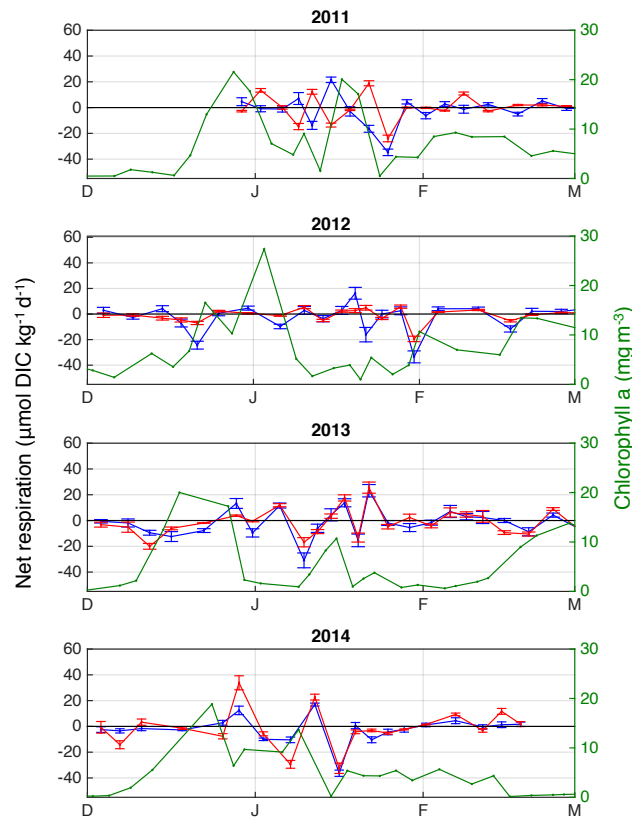


Figure 4.8: Carbon (blue) and phosphate (red) derived net respiration rates during the four summer seasons. Rates >0 indicate net respiration and rates <0 indicate net photosynthesis. Error bars represent uncertainty from Monte Carlo analysis. Chlorophyll-a concentration at 15 m is shown in green.

Ice melt, warming and a reduction in wind speed cause stratification of the water column in summer (Meredith et al., 2004, 2010) which restricts mixing of deeper, carbon-rich water into the mixed layer. The increase in ice melt and decrease in CDW is greatest in January (Figure 4.2) resulting in a strong reduction in DIC (Figure 4.6). Particularly high percentage contributions of sea-ice melt and low contributions CDW are observed in January 2014 which results in a larger reduction in DIC than in previous years. Here, the influence of sea-ice melt on the carbonate system is accentuated because several weeks of ice melt signal are integrated into one mixing event; stratification and mixed layer depth during December 2013 and early January 2014 indicate a shallow, stable surface layer (Figure 4.2) and it is the

effect of this fresher, low DIC water that is observed in mid-January as it is mixed to the sampling depth. This period therefore serves as a useful example of how ice melt reduces surface ocean DIC concentration in Ryder Bay during summer.

Alkalinity data show a sudden and short-lived increase at the end of December 2012, at the end of the main DIC drawdown, and a similar pattern occurs at the end of January/ start of February 2011 (Figure 4.3). During both of these periods the mixed layer is very shallow and sea ice cover is decreasing. In both cases, concurrent with the increase in TA, water temperature at 15 m increases by at least 1°C (Figure 4.9) and it is possible that the observed alkalinity increase may be caused by dissolution of the calcium carbonate mineral ikaite ($\text{CaCO}_3 \cdot 6\text{H}_2\text{O}$) as it is released from overlying, melting ice (Rysgaard et al., 2007, 2011; Dieckmann et al., 2008; Fransson et al., 2013).

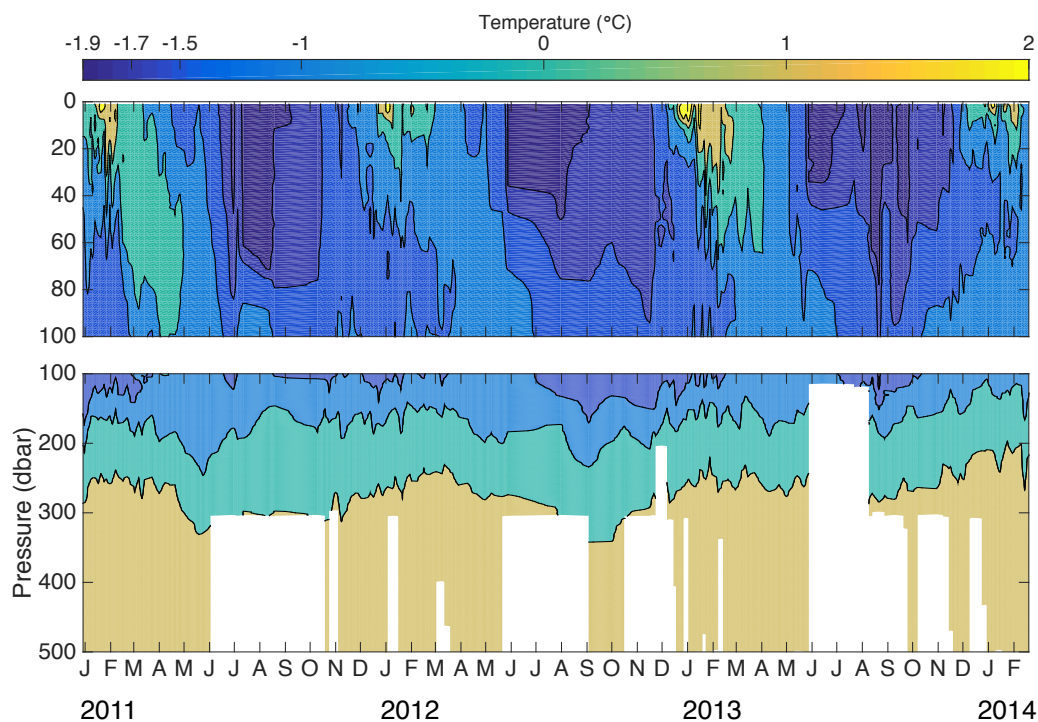


Figure 4.9: A full depth plot of temperature at RaTS site 1 during the carbon time series.

At the start of the time series, in January 2011, the measured TA is highly variable, reaching values roughly $30 \mu\text{mol kg}^{-1}$ lower than the same period in the following three years (Figure 4.3). This causes unusually low pH and Ω (Figure

4.4). A large decrease in TA relative to DIC suggests the precipitation of calcium carbonate, either by biological calcification or the formation of ikaite in ice, but the observed changes are probably too sudden to be purely biogeochemical and this variability is also likely to be caused by advection. Both advection and biogeochemical processes are influenced by larger scale physical forcings and the unusual behaviour of the carbonate system in January 2011 may be related to wind forcing. The percentage ice cover in the winter preceding these low TA values was lower than in the three subsequent winters and the percentage contribution to the water from sea ice was more negative, suggesting that a greater area of exposed water led to more heat loss and more ice formation and subsequent ice export (Meredith et al., 2010). The winds during the ice season of 2010 were stronger and more northerly than during the three subsequent years (Figure 4.10), allowing more ice to be produced and exported from the southward facing Ryder Bay in late 2010. This observed interannual variability in wind strength and direction is likely related to the large scale atmospheric changes driven by the SAM and the El Niño Southern Oscillation (ENSO) which had strong positive and negative anomalies, respectively, in 2010.

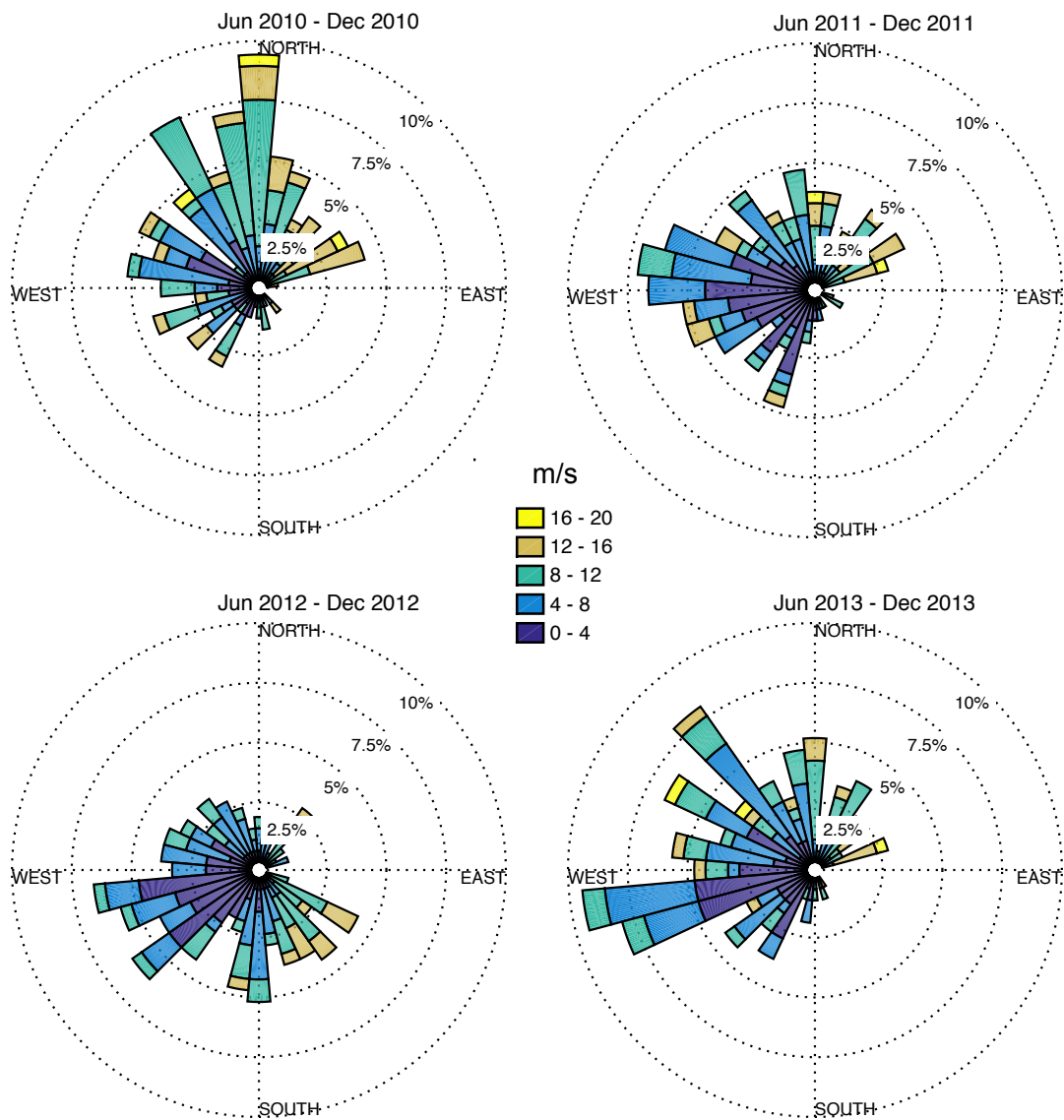


Figure 4.10: Wind direction and speed (in m/s) for June-December in 2010, 2011, 2012 and 2013. Daily wind data from Rothera were taken from www.antarctica.ac.uk/met/metlog.

Some of the observed carbonate system variability at the start of the time series may also be related to vertical mixing. The percentage contribution of CDW at the sampling depth is higher and more variable during January 2011 than during the following three Januaries and salinity profiles indicate higher salinity water reaching shallower in the water column. This is likely caused by increased mixing due to stronger northerlies and the related low ice cover. The data presented here do not

provide sufficient spatial or temporal resolution to resolve a mechanistic connection between interannual variability in wind and ice cover, and alkalinity.

4.4.2.2 Autumn (March, April, May)

On average, the dominant carbonate system process in autumn (March, April and May) is air-sea flux which increases the DIC concentration (Figure 4.7). Although the rate of DIC change due to air-sea flux is often smaller than that due to mixing or net respiration over short timescales (Figure 4.5), its influence on a monthly or seasonal scale is large because it consistently acts in one direction during this period. The ocean uptake of CO₂ in autumn is greater in 2011 than the two following years due to the lower water $f\text{CO}_2$ in April 2011 (Figure 4.4). In all years sampled there is an increase in net respiration from January to February and a decrease from February to March (Figure 4.6). This pattern reflects the chlorophyll-a climatology which suggests a late season chlorophyll peak in March, separate from the initial summer bloom (Clarke et al., 2008).

The rapid decrease in TA in March in all three years sampled (Figure 4.3) appears to be caused by significant precipitation of calcium carbonate, quickly followed by dissolution although the mechanism behind this recurring signal remains unclear. This may be caused by calcifying organisms although there is no information of significant numbers of calcifiers in Ryder Bay. Alternatively, this signal could originate from sea ice processes although in all three years the bay had been free of pack and fast ice for at least two months by early March.

4.4.2.3 Winter (June, July and August)

In winter (June, July and August), the deepening mixed layer increases the percentage contribution of CDW, resulting in an increase in DIC. Ice formation, as evidenced by negative percentage contribution of sea ice (Figure 4.2), also increases the DIC and CO₂ concentrations of the underlying water due to brine rejection, causing a decrease in the saturation state of calcium carbonate minerals (Rysgaard et al., 2007; Chierici et al., 2011; Miller et al., 2011a; Shadwick et al., 2011; Fransson et al., 2013). Mixing is the dominant influence on the carbonate system in winter. Day length, temperature and ice cover limit primary production during the

winter and the surface water in Ryder Bay is slightly net heterotrophic from April to September (Figure 4.6), although there is considerable interannual variability in the magnitude of this net respiration.

4.4.2.4 Spring (September, October and November)

The rapid drawdown of DIC in December and January is preceded by a more gradual DIC decrease in November and there is net photosynthesis in November in all three years (Figure 4.6). The chlorophyll concentration at 15 m during October and November is very low (Figure 4.2) and it is possible that some of this early season photosynthesis signal comes from ice algae which make a significant contribution to primary production in the Antarctic (Arrigo et al., 2010), especially in early spring and late summer (Meiners et al., 2012). The relative timing of primary production and ice melt have the potential to greatly affect the air-sea CO₂ flux and thereby the strength of the ocean carbon sink. Studies in the Ross Sea (Sweeney, 2003), Prydz Bay (Gibson and Trull, 1999; Roden et al., 2013), the Weddell gyre (Bakker et al., 2008) and the Weddell-Scotia confluence (Jones et al., 2010) found a significant decrease in water $f\text{CO}_2$ due to primary production prior to complete ice melt, creating a sink for atmospheric CO₂. In Ryder Bay, during the three years presented here, the ice season is shorter than that observed by the above studies and the majority of $f\text{CO}_2$ drawdown occurs in the main bloom period in December and January, after most fast and pack ice have melted. There is a significant fraction of open water in Ryder Bay for a period of weeks or months prior to the rapid increase in chlorophyll (Figure 4.2). In all three spring periods the reduction of $f\text{CO}_2$ in October and November, prior to the main chlorophyll increase, is insufficient to make the water $f\text{CO}_2$ lower than that of the atmosphere so the ocean remains a source of CO₂ to the atmosphere until the main bloom.

Meltwater from sea ice and glacial ice reduces surface water DIC and $f\text{CO}_2$ in spring, prior to the main phytoplankton bloom. Meltwater therefore influences the air-sea flux of CO₂ (Rysgaard et al., 2011) and contributes to the net annual ocean sink for atmospheric CO₂ in Ryder Bay (Chapter 3). The percentage contribution of meteoric water to the bay is greater than that of sea ice (Figure 4.2) and its seasonal

amplitude is also slightly greater, making glacial meltwater more influential than sea-ice melt in terms of its direct impact on carbonate chemistry in Ryder Bay.

The DIC reached higher values during September and October 2013 than in the two previous years (Figure 4.3) causing higher surface water $f\text{CO}_2$ which, combined with a reduction in ice cover, leads to an increase in the calculated flux of CO_2 from the ocean to the atmosphere (Chapter 3). The higher DIC values in 2013 are likely caused by increased mixing of carbon-rich CDW to the surface; this is supported by the higher percentage contribution of CDW (Figure 4.2) and by the observation that higher salinity water reaches shallower in the water column (Figure 4.11). A reduction in ice melt could also lead to higher surface water DIC due to a reduction in dilution and stratification. The higher DIC concentration during September and October 2013 also leads to lower pH and calcium carbonate saturation states than in the two previous years (Figure 4.4) and brings Ω aragonite very close to 1. These observations suggest that future changes to the delivery of CDW to the surface ocean may significantly affect carbonate chemistry in the surface ocean with implications for the ocean sink of atmospheric CO_2 and the life cycle of calcifying organisms.

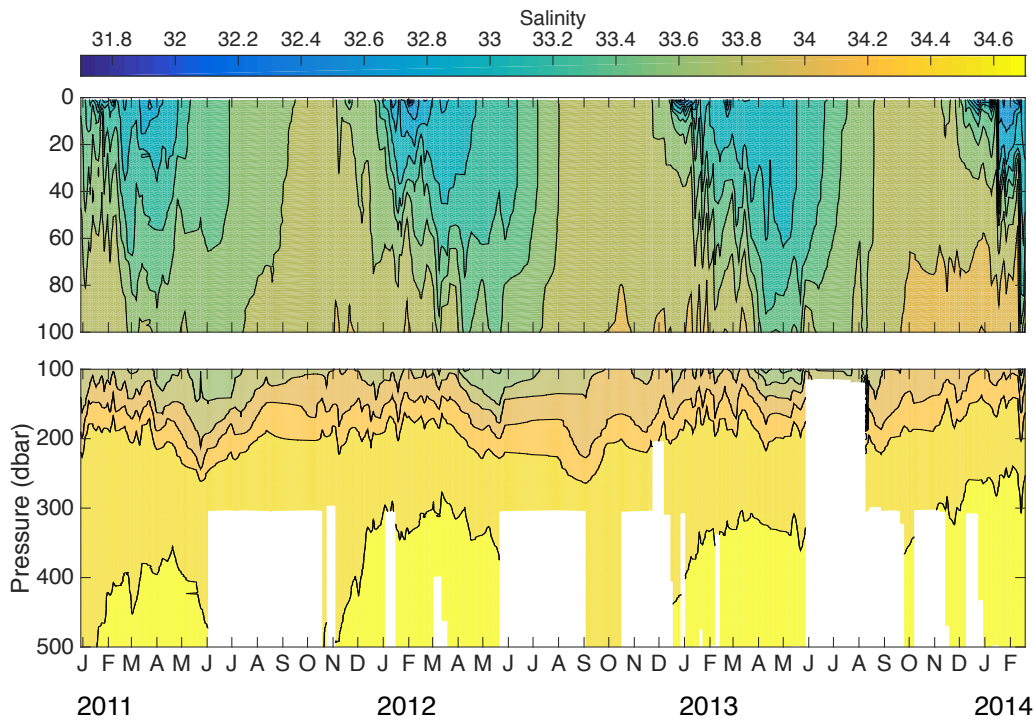


Figure 4.11: A full depth plot of salinity at RaTS site 1 during the carbon time series.

4.4.3 Comparison of carbon and phosphate derived net respiration

A comparison of the net respiration rates in summer derived from carbonate system calculations and those calculated from phosphate gives mixed results (Figure 4.8). Carbon and phosphate estimates agree well both in direction and magnitude during the summer of 2013 and show broad agreement during the summers of 2012 and 2014. In 2011 however, the two methods agree less well, disagreeing on the sign of the process for much of January. Much of the disagreement between the carbon and phosphate methods may be related to mixing and it is worth noting that inaccuracies in the mixing term (Section 4.2.4) may affect phosphate more than DIC because surface phosphate values show a greater range relative to their deep concentrations than DIC. On average, the carbon based estimate of photosynthesis exceeds the nutrient based estimate. This pattern is not uncommon (Laws, 1991; Sambrotto et al., 1993; Brzezinski et al., 2003; Green and Sambrotto, 2006) and has been

attributed to preferential recycling of limiting nutrients (Thomas et al., 1999; Bozec et al., 2006). However, overall, nutrient utilisation at RaTS is expected to be close to Redfieldian (Clarke et al., 2008) and much of the difference is likely caused by inaccuracies in the mixing term. With carbonate and phosphate data predominantly from one sampling depth it is not possible to resolve net community production over the full depth of the water column during the study period. Vertical profile data, especially during the summer season would allow a vertically integrated measure of primary production using a carbon and nutrient deficit approach (Hoppema et al., 2002a; Shadwick et al., 2011; Weston et al., 2013; Jones et al., 2017).

4.5 Conclusions

- There is a strong, asymmetric seasonal cycle in the carbonate system in Ryder Bay, driven by physical processes and primary production.
- In summer, melting glacial ice and sea ice and a reduction in mixing with deeper water reduce the concentration of DIC in surface waters. The dominant process affecting the carbonate system is net photosynthesis which reduces DIC and $f\text{CO}_2$, making the ocean a net sink of atmospheric CO_2 .
- In winter, mixing with deeper, carbon-rich water and net heterotrophy increase surface DIC concentrations, resulting in pH as low as 7.95 and aragonite saturation states close to 1.
- There is no clear seasonal cycle of calcium carbonate precipitation/dissolution but some short-lived features of the carbonate time series suggest that significant precipitation of calcium carbonate does occur in the Bay.
- The method developed here for the simultaneous quantification of photosynthesis/respiration and calcification/dissolution from DIC and TA measurements may be useful in future time series studies.

Chapter 5

Carbonate system modifications in deep waters of the Scotia Sea

5.1 Rationale

The Scotia Sea is an important pathway for WSDW from its source in the Weddell Sea to the main ocean basins and, due to its complex bathymetry, it is known to be an area of intense mixing between deep water masses (Figure 5.1). The thermohaline properties of bottom water and the overlying CDW are modified during their passage through the Scotia Sea but changes to the carbonate system in the deep waters of the basin are largely unexplored. The aims of this chapter are to:

- Characterise the carbonate system along the Drake Passage, A23 and North Scotia Ridge hydrographic sections.
- Investigate differences in the carbonate system between deep water masses of the Drake Passage and the A23 sections in order to better understand the role of the Scotia Sea in the Southern Ocean carbon cycle.

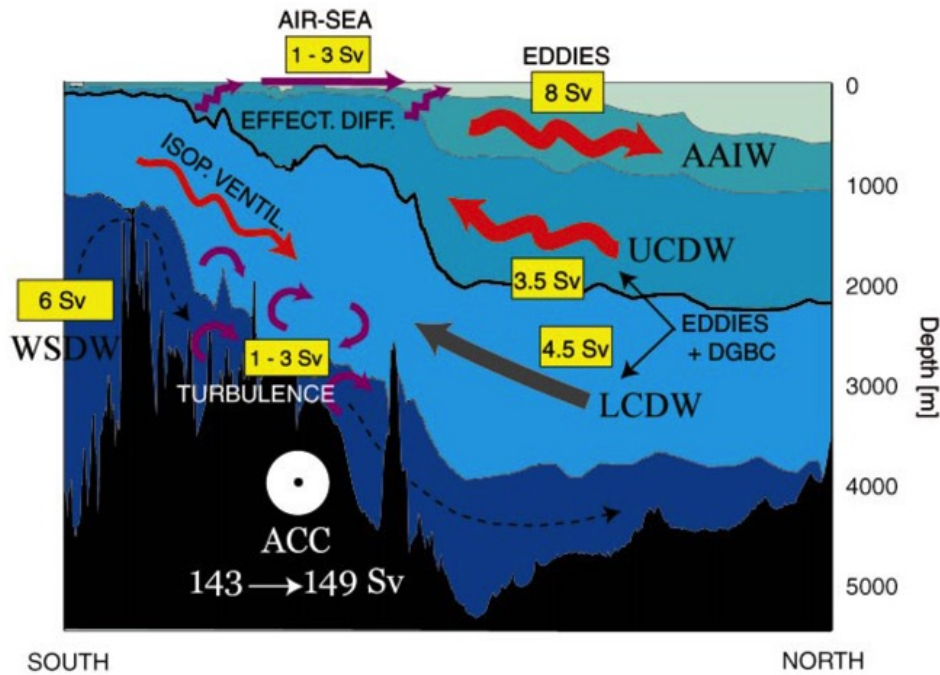


Figure 5.1: A schematic of the overturning circulation across the ACC in the Scotia Sea, taken from Naveira Garabato et al. (2003). Transports (in Sverdrups) were calculated using an inverse model. Strong diapycnal mixing between LCDW and WSDW are related to the rough bathymetry of the region. Isopycnal exchange with the northern Weddell Gyre cools and freshens CDW as it crosses the Scotia Sea.

5.2 Data and methods

5.2.1 Cruise information

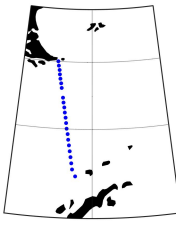
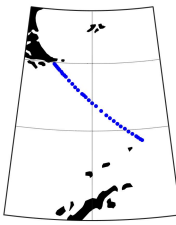
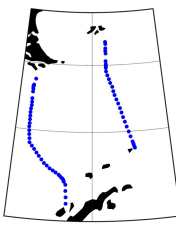
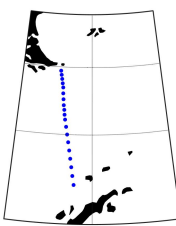
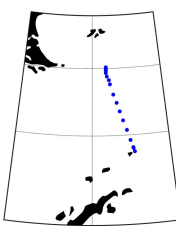
In order to characterise the carbonate system along the Drake Passage (DP) and A23 sections, and investigate changes in water masses between these sections in detail, carbonate system measurements were compiled from cruises along these sections. The cruise JR299 occupied the DP, A23 and North Scotia Ridge sections and the sampling and analysis methods for this cruise are described in Chapter 2. As well as the samples collected on JR299 there are also *RV Ronald H. Brown* data from Rik Wanninkhof and *RRS James Clark Ross* data from Dorothee Bakker as well as several cruise datasets from the Global Ocean Data Analysis Project version 2 (GLODAPv2) merged data product (Tables 5.1 and 5.2). The GLODAPv2 merged data product contains data from 724 scientific cruises throughout the global oceans,

including the Southern Ocean (Olsen et al., 2016). Data for the twelve core variables (including DIC and TA) have been subjected to extensive quality control, including crossover analysis (Tanhua et al., 2010) and corrected for any significant systematic bias between cruises. Any bias corrections applied to the DP and A23 cruises used in this analysis are given in Tables 5.1 and 5.2.

Other carbonate system variables (pH, $f\text{CO}_2$, the Revelle factor and the saturation states of calcite and aragonite) were calculated from measured DIC and TA using the CO2SYS program (Van Heuven et al., 2011a) using the dissociation constants of Lueker et al. (2000). These calculated variables are only used in the plots and analysis shown here when they correspond to Niskin bottles which have a data quality flag of 2 (good) for DIC, TA, phosphate and silicate. This is because the error on these calculated carbonate system variables caused by missing or erroneous nutrient data (Section 2.3.3.3) is material compared to the changes being investigated here, especially in deeper waters which exhibit a smaller range of measured values (Figure 5.10).

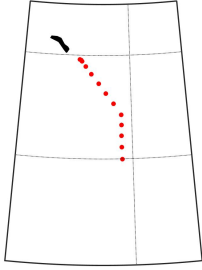
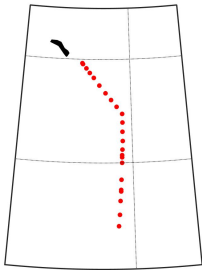
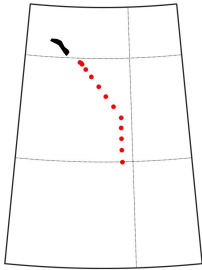
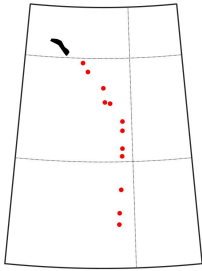
The fugacity of carbon dioxide ($f\text{CO}_2$) was measured during the two *Laurence M. Gould* cruises across the DP. However, these measured $f\text{CO}_2$ data appear to be systematically higher than other DP $f\text{CO}_2$ data, calculated from DIC and TA. $f\text{CO}_2$ is not one of the core GLODAP variables and has not been rigorously quality controlled and bias adjusted. It was therefore decided to exclude the measured $f\text{CO}_2$ from the *Laurence M. Gould* from this analysis and all $f\text{CO}_2$ presented here have been calculated from DIC and TA.

Table 5.1: Drake Passage cruise information

| Year, ship, carbon P.I., section codes, expocode and reference | Measured carbonate system variables (GLODAP adjustment, if made) | Station locations* |
|---|---|--|
| March 2006 Laurence M. Gould Sweeney CLIVAR A21 (SR1) 33LG20060321 Munro et al. (2015) | DIC (+4 $\mu\text{mol.kg}^{-1}$) $f\text{CO}_2$ Source: GLODAPv2 |  |
| April 2008 Polarstern de Baar and van Heuven CLIVAR A12, ANT-XXIV/3 06AQ20080210 Van Heuven et al. (2011b) | DIC TA (-4 $\mu\text{mol.kg}^{-1}$) Source: GLODAPv2 |  |
| February 2009 James Cook Bakker JC031, SR1 and SR1b 740H20090203 Schuster et al. (2014) | DIC TA (-6 $\mu\text{mol.kg}^{-1}$) Source: GLODAPv2 |  |
| September-October 2009 Laurence M. Gould Sweeney CLIVAR A21 (SR1) 33LG20090916 Munro et al. (2015) | DIC (+4 $\mu\text{mol.kg}^{-1}$) $f\text{CO}_2$ Source: GLODAPv2 |  |
| March 2014 James Clark Ross Legge JR299, SR1b | DIC TA Source: author's data |  |

*All maps on the same axes from 50° to 65° South and from 50° to 70° West.

Table 5.2: A23 cruise information

| Year, ship, carbon P.I., section codes, exocode and reference | Measured carbonate system variables (GLODAP adjustment, if made) | Station locations* |
|--|---|---|
| January-February 2005 R.H. Brown Wanninkhof, Feely, Millero CLIVAR A16 33RO20050111 Wanninkhof and Doney (2006) | DIC TA (+5 $\mu\text{mol.kg}^{-1}$) $p\text{CO}_2$ Source: GLODAPv2 |  |
| April 2010 James Clark Ross Bakker JR239/JR235, A23 | DIC TA Source: D.C.E. Bakker |  |
| January-February 2013 R.H. Brown Wanninkhof CLIVAR A16 | DIC TA $p\text{CO}_2$ pH Source: R. Wanninkhof |  |
| April 2014 James Clark Ross Legge JR299, A23 | DIC TA Source: author's data |  |

*All maps on the same axes from 52° to 64° South and from 25° to 40° West. South Georgia is shown in the northwest corner.

Following crossover analysis, some bias correction adjustments were made to the JR235 dataset (Peter Brown, pers. comm.). Oxygen data were multiplied by

1.03, silicate data were multiplied by 1.02, nitrate data were multiplied by 1.01 and phosphate data were multiplied by 1.03. For JR299, multiplicative corrections of 1.03 and 1.1 were applied to oxygen and silicate, respectively (Section 2.4.1).

5.2.2 Defining vertical and horizontal boundaries

The oceanography of the Scotia Sea is strongly influenced by the fronts of the ACC (Section 1.3.1). In order to define and understand the movement of water masses in the region it is therefore useful to define the location of these fronts and to do so in a way which is consistent between the many cruise datasets used here. Absolute dynamic topography (hereinafter dynamic height) from Aviso (Rio and Hernandez, 2004) was used to define frontal locations in the Scotia Sea. Venables et al. (2012) found that uniform dynamic height frontal definitions are generally applicable in the Scotia Sea region and they can therefore be used when comparing the DP and A23 sections. The dynamic height frontal definitions of Venables et al. (2012) were validated against mean potential temperature sections from DP and A23 (Appendix B) and the chosen dynamic height values for the fronts are given in Table 5.3. As fronts are likely to be in different locations during different cruises, comparing measured variables from different hydrographic sections based on their dynamic height is more oceanographically relevant than using fixed spatial coordinates such as latitude or longitude.

Table 5.3: Dynamic height frontal definitions used for DP and A23 sections.

| Front | Dynamic height definition (dyn. m) |
|----------------------------|------------------------------------|
| Sub-Antarctic Front (SAF) | 0.09 |
| Polar Front (PF) | -0.61 |
| Southern ACC Front (SACCF) | -1.05 |
| Southern Boundary (SB) | -1.21 |

In the vertical, water masses were defined using neutral density (γ^{θ}), a continuous version of discretely referenced potential density surfaces, which allow density surfaces to be computed and compared globally (Jackett and McDougall, 1997). Water mass neutral density boundaries were based on those of Naveira Garabato et al. (2002a) and are shown in Table 5.4. In reality, fronts are not sharp lines but

are regions of increased gradients and are therefore not perfectly represented by single value definitions (Venables et al., 2012). Similarly, the boundaries between water masses are not a sudden transition from water of one type to another, due to mixing. However, in order to investigate change in various water masses using data which are relatively sparsely distributed, boundaries were chosen to facilitate comparisons.

Table 5.4: Water mass definitions based on Naveira Garabato et al. (2002a). The LCDW/WSDW boundary is the lowest neutral density value which excludes SPDW from the WSDW density class, as described in Section 5.3.2.

| Water mass | Neutral density boundaries (kg.m^{-3}) |
|-------------------------------------|---|
| Upper Circumpolar Deep Water (UCDW) | $27.55 < \gamma^n < 28$ |
| Lower Circumpolar Deep Water (LCDW) | $28 < \gamma^n < 28.273$ |
| Weddell Sea Deep Water (WSDW) | $28.273 < \gamma^n$ |

5.2.2.1 Tools for comparisons

When investigating water mass modifications between DP and A23, only data from between the SB and the PF are used. This is so that roughly the same cross section of the ACC is compared between the different sections and also to prevent waters of the northern Weddell Sea complicating the analysis. The effect of the different dynamic height range between these two sections on the results is minimal and is explained in Appendix B.

Box plots are used to compare measured variables in each water mass from the two sections. Figure 5.2 provides an explanation of this representation of the data. Water mass properties are not only influenced by whether the water is measured at DP or at A23 but also have a relationship with dynamic height and neutral density within each water mass. In order to quantify the relationship between the variables of interest and several predictor variables, multiple linear regressions (MLRs) were used. For each variable, for each water mass, an MLR was constructed with neutral density, dynamic height and 'section' as predictor variables, where section is a categorical variable representing whether the data point is from DP or A23. These

regressions provide an estimate of the slope and the significance of the relationship between the variable of interest and each predictor. Some of the MLR results are discussed below and MLR statistics are shown in Appendix C. When deciding on predictor variables for the MLRs, visual inspection of the data showed that there are relationships between the variables studied here and dynamic height, neutral density and section (DP or A23). These were therefore clear choices for predictor variables in the MLRs. A second set of MLRs were created which included the year as a fourth predictor variable in order to test for time trends. The inclusion of the year as a predictor variable did not generally improve the R^2 of the models and gave trends which were very small and/or insignificant at the 95% level. This is unsurprising given the relatively short time span of the dataset (<10 years).

Box plots provide a visually clear way of assessing differences between the two sections and MLRs provide a quantitative measure of the strength and significance of the relationship between the variables and various predictors. However, in order to use these techniques, the data have been binned into discrete water masses which inherently hides some of the more subtle variability in the data. Scatter plots of variables against neutral density present this variability more thoroughly.

When considering the difference between measurements across different sections it is important to consider the accuracy of the data as well as the statistical significance of the difference. The GLODAPv2 dataset is believed to be consistent to better than 0.005 in salinity, 1% in oxygen, $4 \mu\text{mol.kg}^{-1}$ in DIC, $6 \mu\text{mol.kg}^{-1}$ in TA and 5% for chlorofluorocarbons (CFCs) (Olsen et al., 2016). Temporal variability was considered during GLODAP secondary quality control and makes identification of biases difficult in regions with possible time trends in deep waters such as the polar oceans (Olsen et al., 2016). By combining multiple, independent cruise datasets over both the DP and A23 sections, the likelihood of measurement bias significantly affecting the results is reduced.

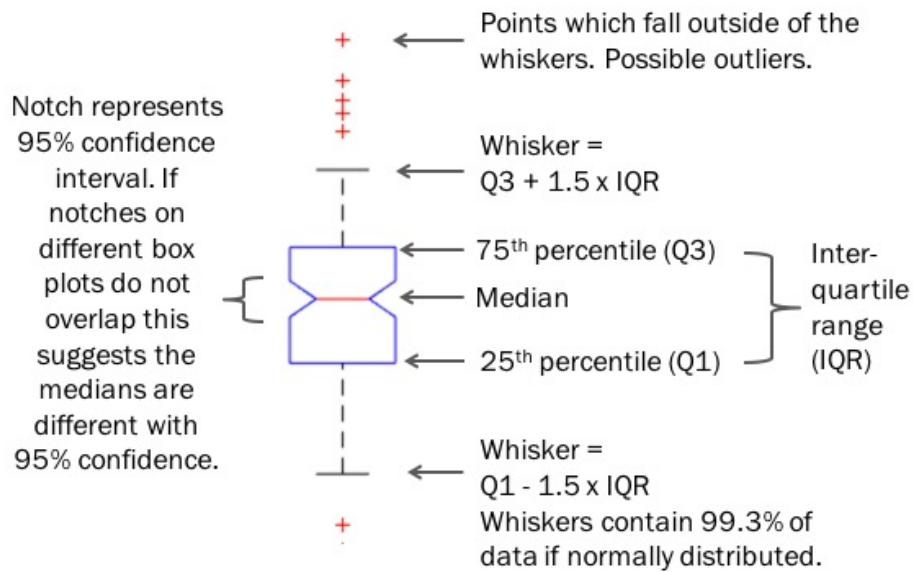


Figure 5.2: An explanation of the anatomy of a box plot.

5.3 Results and discussion

5.3.1 Characterising the carbonate system on the Drake Passage and A23 sections

Figures 5.3 to 5.6 show interpolated section plots of measured and calculated carbonate system variables as well as measured potential temperature, salinity, oxygen and silicate. Data from all cruises have been interpolated and plotted against depth and dynamic height rather than latitude or longitude in order to avoid artifacts caused by the movement of fronts between cruises and to allow mean frontal positions to be shown. The interpolation in each plot is truncated at the convex hull of the data (the outside edge of the data points when plotted in dynamic height/depth space). Plots of the DP and A23 data from JR299 are presented in Appendix D.

The water mass structure in DP is shown in Figure 5.3. The salinity maximum in LCDW and a strong oxygen minimum in UCDW are evident, as is the warmer surface water north of the SAF. The temperature panel also shows that, south of the PF, UCDW is warmer than the overlying surface water. There is a silicate maximum in the deepest LCDW, just south of the PF. This high silicate water is South Pacific

Deep Water (SPDW) which has previously been observed below the 28.20 neutral density isopycnal in DP (Sievers and Nowlin, 1984; Naveira Garabato et al., 2002a). There is an $f\text{CO}_2$ maximum in UCDW, reaching values of over $550 \mu\text{atm}$ (Figure 5.4) caused by respiration of organic matter in this relatively old water mass. The concentration of DIC is high throughout UCDW and LCDW whereas the concentration of TA is greatest in LCDW. The high DIC relative to TA in UCDW results in a lower pH than in the intermediate and surface waters above or in the LCDW below. The high DIC/TA ratio in UCDW also means that this water mass has the highest Revelle factor in the section. This indicates that UCDW is especially sensitive to increases in CO_2 so that small increases in DIC will strongly decrease pH and the saturation states of calcium carbonate minerals. Below about 2000m, pH and Ω aragonite decrease steadily with depth due to the effect of pressure on these variables.

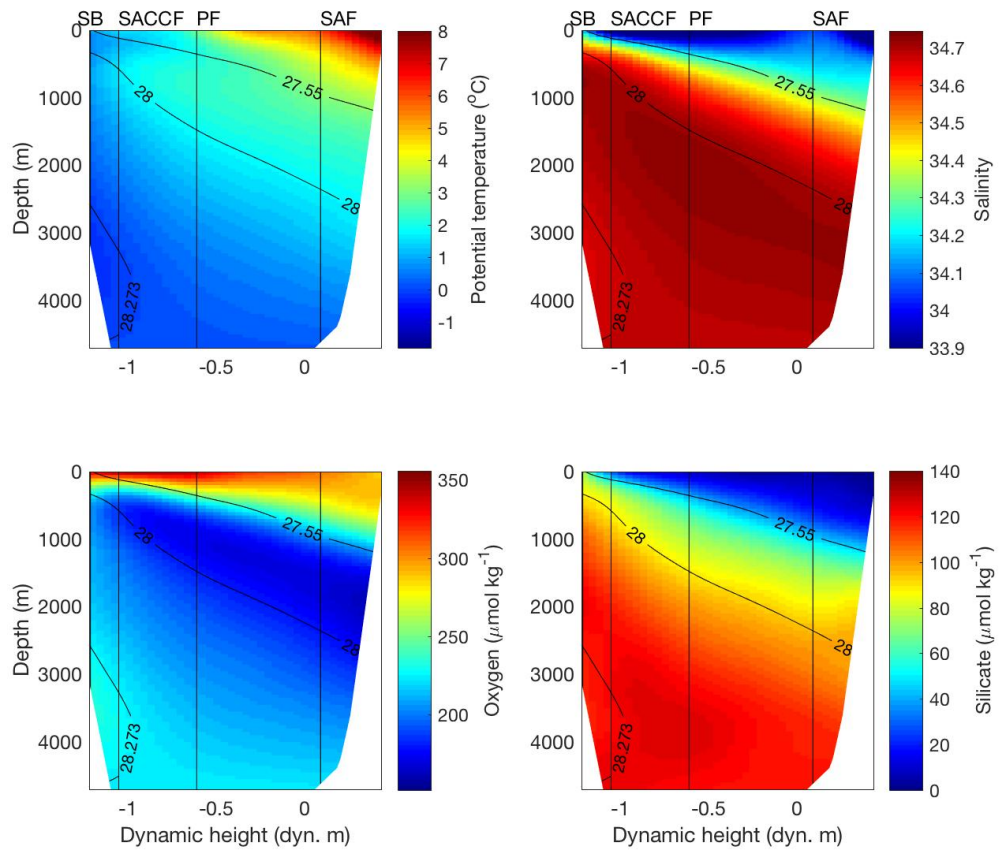


Figure 5.3: Average section plots of temperature, salinity, oxygen and silicate across Drake Passage. Neutral density boundaries used to define deep water masses and mean frontal positions (vertical lines) are shown in black.

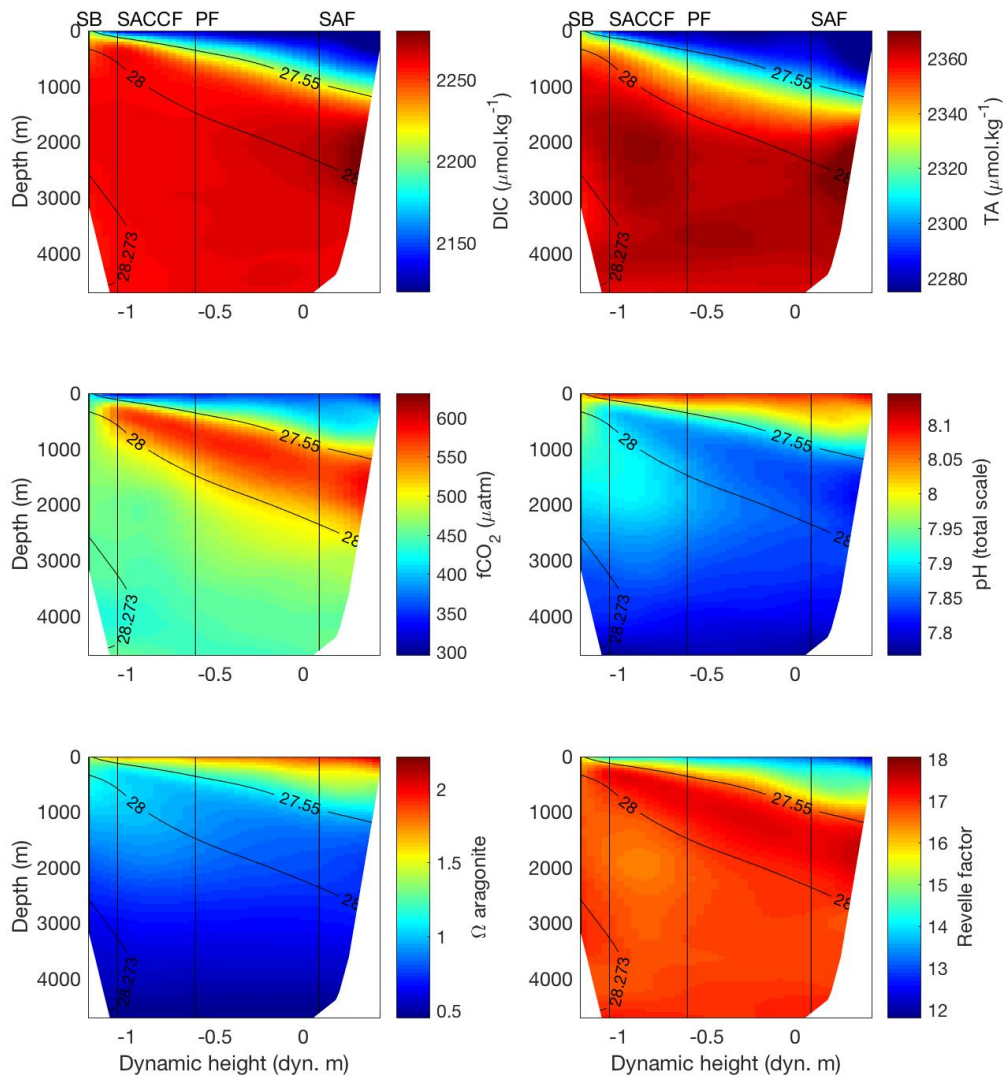


Figure 5.4: Average section plots of measured (DIC and TA) and calculated ($f\text{CO}_2$, pH, Ω , and Revelle factor) carbonate system variables across Drake Passage. Neutral density boundaries used to define deep water masses and mean frontal positions (vertical lines) are shown in black.

Due to the location of the ACC fronts, the A23 section excludes the northern end of the dynamic height range shown on the DP section. Antarctic Intermediate Water and Sub-Antarctic Mode Water are therefore not observed. However, the features described above for denser water masses along DP are also apparent at A23 such as the LCDW salinity maximum and the clear wedge of UCDW with low oxy-

gen and high $f\text{CO}_2$. The A23 section also extends southwards, crossing the SB into the Weddell-Scotia Confluence and the northern Weddell Sea. Figures 5.5 and 5.6 show the corresponding change in the water column structure. South of the SB the surface water is much colder than the surface water of the ACC, with temperatures at, or close to, the freezing point of seawater and sea ice being common, especially at the southern end of A23. Below the surface lies Winter Water, the remnant of the previous winter's surface water, characterised by a temperature minimum and neutral density between 27.55 and 28 (Brown et al., 2015). Beneath these cold, fresh, well ventilated surface layers there is evidence of Warm Deep Water (WDW). This relatively warm, salty water mass originates as CDW and becomes further enriched in DIC and depleted in oxygen by the remineralisation of organic matter during its stay in the Weddell Sea (Hoppema et al., 2002b). The presence of WDW is also shown in carbonate system variables as a tongue of high $f\text{CO}_2$ water at the southern end of the A23 section. Also evident at the southern end of the A23 section is WSDW. This deep, recently ventilated water is fresher and colder than the overlying WDW and CDW and has lower DIC and $f\text{CO}_2$ (Figure 5.6).

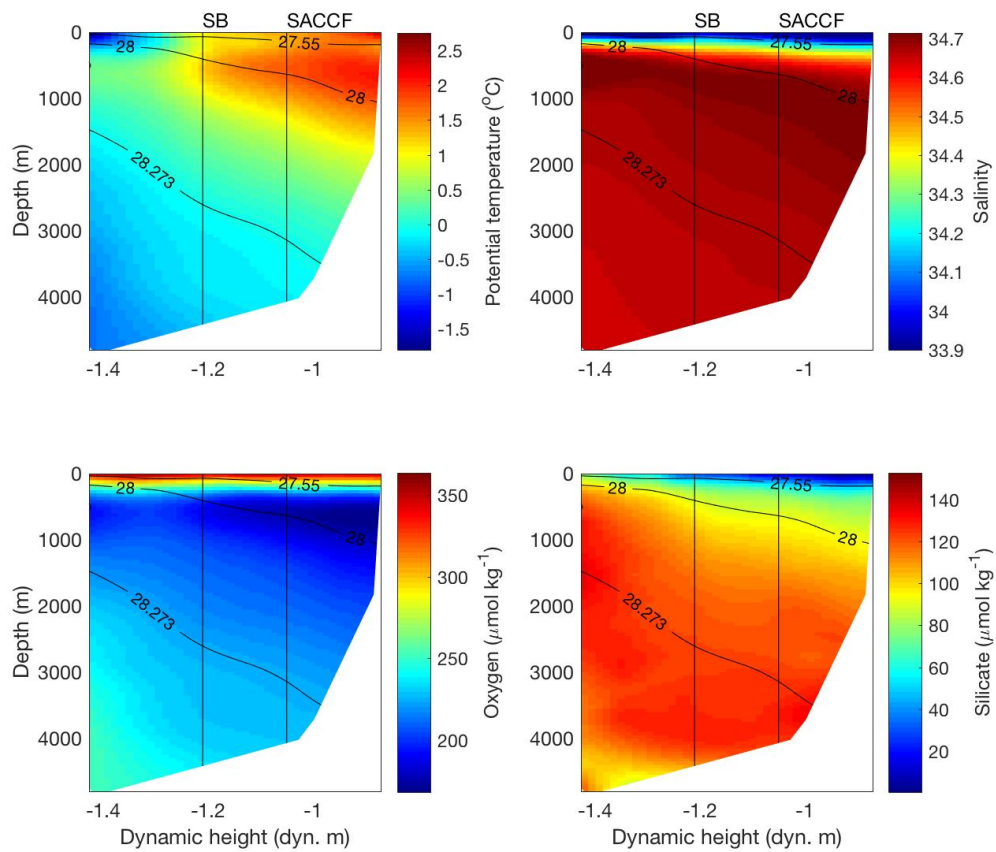


Figure 5.5: Average section plots of temperature, salinity, oxygen and silicate along the A23 section. Neutral density boundaries used to define deep water masses and mean frontal positions (vertical lines) are shown in black.

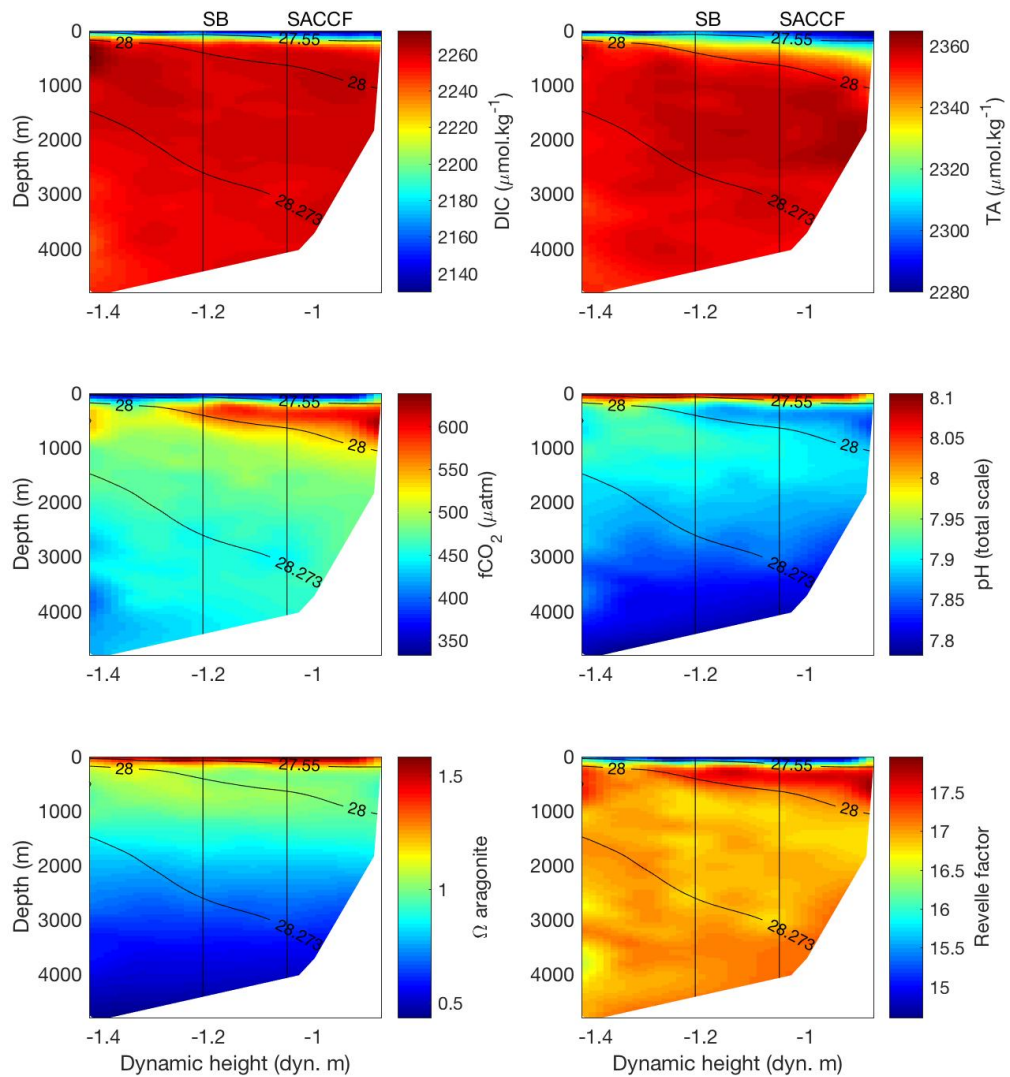


Figure 5.6: Average section plots of measured (DIC and TA) and calculated ($f\text{CO}_2$, pH, Ω , and Revelle factor) carbonate system variables along the A23 section. Neutral density boundaries used to define deep water masses and mean frontal positions (vertical lines) are shown in black.

5.3.2 Longitudinal variation in Drake Passage

The cruise tracks in Tables 5.1 and 5.2 show that, whereas the four A23 repeat cruises followed the same path, the five DP cruises shown here took several different routes. Therefore, before comparing the water masses of DP with those of A23, the data from DP will be examined to investigate variability caused by differences in

cruise tracks. The cruise JC031 provides a good starting point to assess longitudinal changes in water masses in DP because it included both the SR1 and SR1b sections, the former running from the north western edge of the Antarctic Peninsula towards the southernmost tip of South America and the latter running from near Elephant Island towards the Falkland Islands. The potential temperature-salinity (Θ S) plots of the densest waters sampled on this cruise (Figure 5.7) show some clear differences between these western and eastern sections.

LCDW is saltier in the west than in the east and this is especially apparent in the coldest, deepest portion of this water mass which has a strong bifurcation in Θ S space. The saltier LCDW further west also has a higher silicate concentration of around $130 \mu\text{mol.kg}^{-1}$. This high salinity, high silicate water is South Pacific Deep Water (SPDW) which is found below the 28.2 neutral density isopycnal, between the PF and the SB (Sievers and Nowlin, 1984; Naveira Garabato et al., 2002a). When data from all DP cruises are plotted in Θ S space the same pattern is evident (Figure 5.8); sections in the west of DP, to the west of the Shackleton Fracture Zone (SFZ), contain SPDW whereas LCDW in sections to the east of the SFZ appears to follow a straighter mixing line between the high salinity core of LCDW and the colder, fresher WSDW. This is consistent with the findings of Sudre et al. (2011) who found SPDW from 2500 m down to the seafloor on the SR1 section but noted that the SFZ prevents SPDW moving eastwards. Close examination of other variables reveals that SPDW has slightly lower oxygen concentrations than the LCDW further east but there is no discernable influence on carbonate system variables, largely due to the precision of the data. Naveira Garabato et al. (2002a) use the 28.26 isopycnal to distinguish between LCDW and WSDW. However, the high salinity of SPDW means that some of the samples clearly influenced by SPDW, shown in Figures 5.7 and 5.8, are denser than 28.26. In order to clarify the subsequent comparison between DP and A23, 28.273 is used as the the neutral density boundary between LCDW and WSDW (Table 5.4), as this is the lowest density value which excludes all SPDW points from WSDW.

The second major difference between eastern and western DP sections is the

absence of WSDW on the western transects (Figure 5.8) as the SFZ prevents this dense water from travelling through the DP to the Pacific Ocean (Orsi et al., 1999; Naveira Garabato et al., 2002a), although a small amount may find its way westwards through the Shackleton Gap at the very southern edge of the ridge (Sudre et al., 2011).

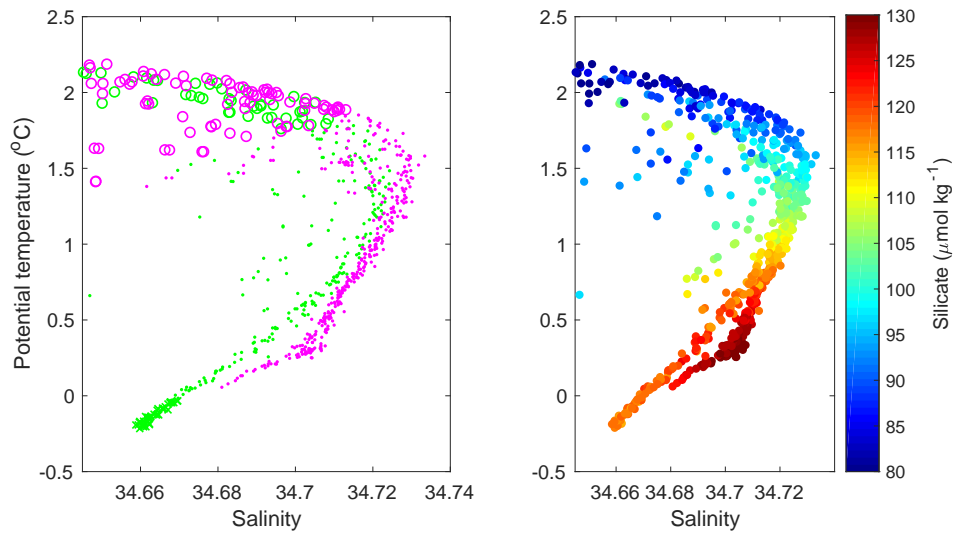


Figure 5.7: Θ/S plots of the dense waters of the eastern and western Drake Passage sections of JC031. Left panel: pink = west, green = east. crosses = WSDW, dots = LCDW, circles = UCDW. Right panel: silicate concentrations. Only the densest part of the Θ/S plot is shown and therefore some less dense UCDW is off the scale.

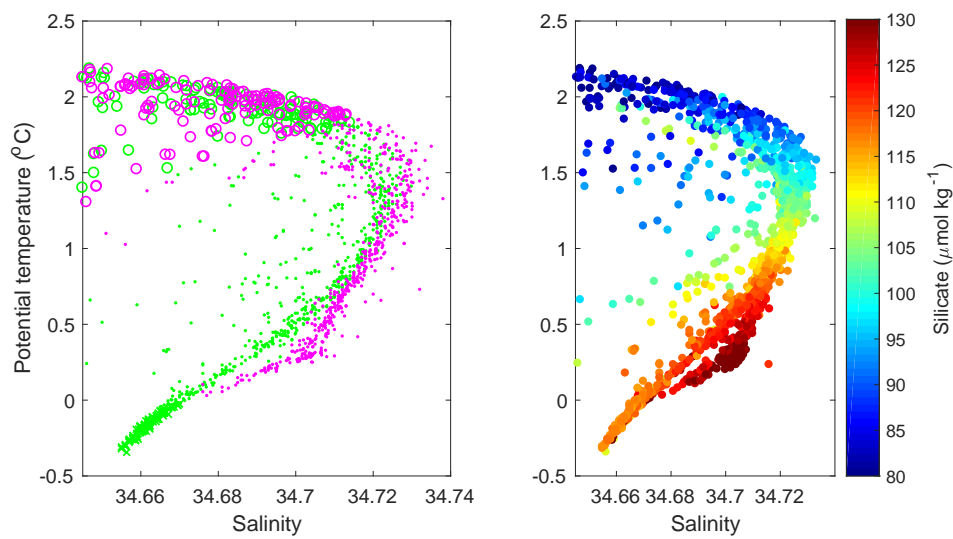


Figure 5.8: Θ/S plots of the dense waters of the eastern and western Drake Passage sections using 6 cruise datasets (Table 5.1). Left panel: pink = west (Gould 2006, Gould 2009, Cook 2009 west), green = east (Polarstern 2008, Cook 2009 east, JCR 2014). crosses = WSDW, dots = LCDW, circles = UCDW. Right panel: Silicate concentrations (silicate data from for all cruises except Gould 2006). Only the densest part of the Θ/S plot is shown and therefore some less dense UCDW is off the scale.

5.3.3 Water mass modifications

Comparing the Θ/S plots of DP and A23 data from between the PF and the SB it is apparent that the densest waters of the ACC show different properties across these sections. For example, LCDW is fresher and WSDW appears to be slightly saltier at A23 than at DP (Figure 5.9). Sections 5.3.3.1 to 5.3.3.3 investigate the differences in WSDW, LCDW and UCDW between DP and A23 in more detail.

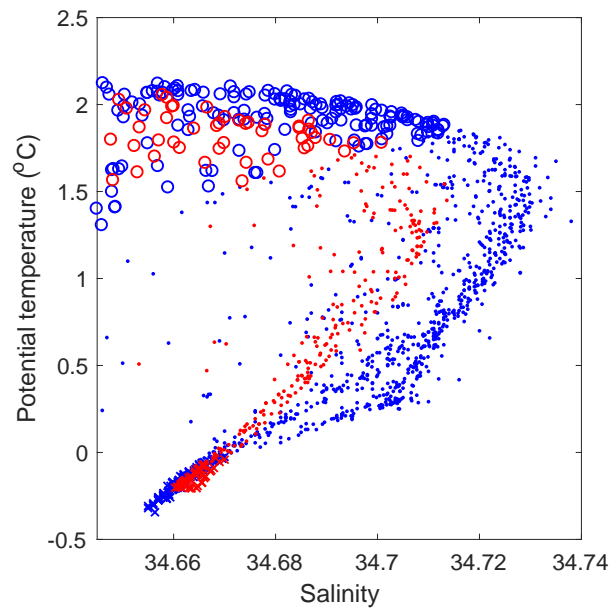


Figure 5.9: Θ/S plot of the densest waters of the Drake Passage (blue) and A23 sections (red) between the Southern Boundary and the Polar Front. Crosses = WSDW, dots = LCDW, circles = UCDW. Only the densest part of the Θ/S plot is shown and therefore some less dense UCDW is off the scale.

5.3.3.1 Weddell Sea Deep Water

The WSDW measured at the A23 section has higher salinity and lower oxygen than the WSDW measured in DP (Figure 5.10). Although these differences are small, the box plots and MLRs (Appendix C) suggest that they are significant. One explanation for these observed changes is that the WSDW at the A23 section, in the east of the Scotia Sea, has mixed more with the overlying LCDW than the WSDW in DP and therefore its measured properties are modified towards the values found in the higher salinity, lower oxygen LCDW. A second explanation concerns the origins of the WSDW. Naveira Garabato et al. (2002a) found the WSDW flowing westwards along the north side of the South Scotia Ridge towards DP to be colder and fresher than that flowing eastwards. This colder, fresher WSDW has been more recently ventilated along the northeastern Antarctic Peninsula (Gordon et al., 2001) and therefore also has a higher oxygen concentration than the eastward flowing WSDW. It is also possible that more saline WSDW may reach the eastern Scotia Sea from the South Sandwich Trench through the Georgia Passage (Naveira Garabato

et al., 2002a). Although only containing data from one cruise from DP (2008) and one from A23 (2005), Figure 5.12 shows that the concentration of CFC12 in WSDW is greater at DP than A23 confirming that the WSDW at DP has either been more recently ventilated or has mixed less with older, overlying water.

Differences in the carbonate system in WSDW between DP and A23 are small (Figure 5.10) and the DIC difference of $\sim 1 \mu\text{mol.kg}^{-1}$ is found to be insignificant by the MLR. Both box plot and MLR suggest a significantly lower concentration of TA at A23 than at DP, resulting in higher $f\text{CO}_2$ and lower pH. However, the number of data points is relatively small (Figure 5.10) and the TA difference ($\sim 1.5 \mu\text{mol.kg}^{-1}$) is well within the threshold for GLODAP bias adjustment ($6 \mu\text{mol.kg}^{-1}$). Furthermore, the 6 samples with the highest TA in WSDW at DP are all from one cruise (JC031). It is therefore very possible for this apparent signal to be caused by small offsets in the TA calibration between cruises.

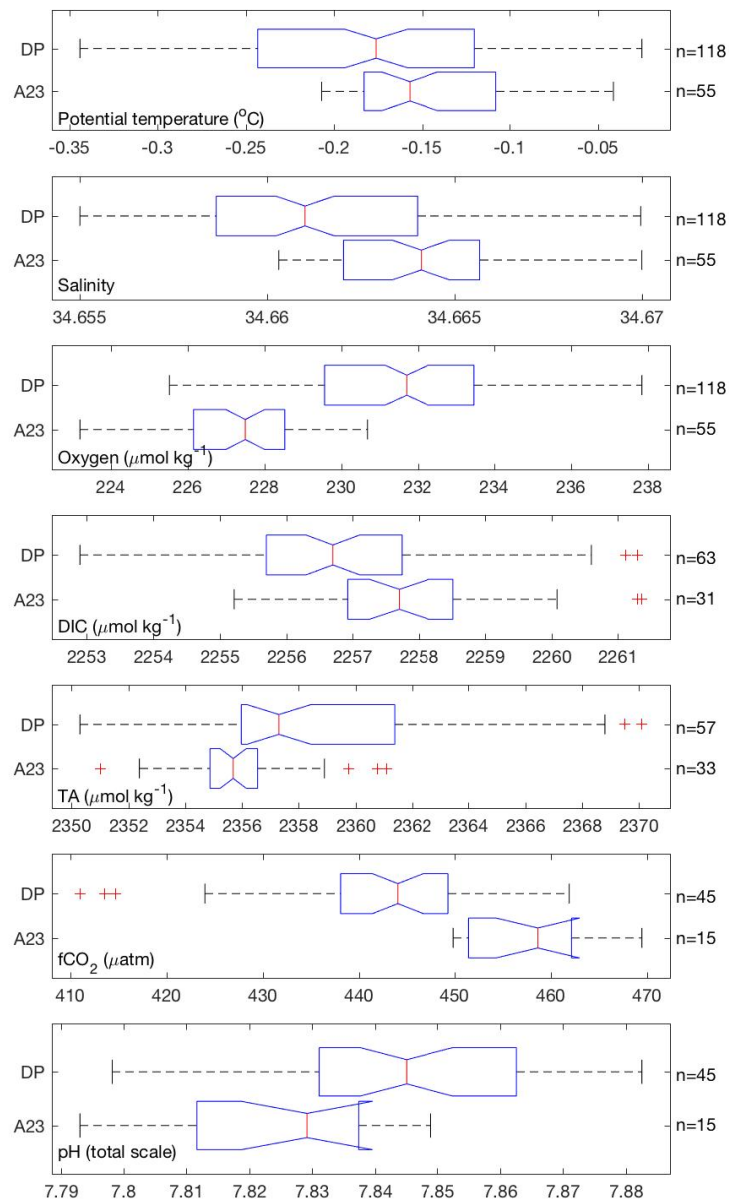


Figure 5.10: Box plots of measured (Potential temperature, salinity, oxygen, DIC and TA) and calculated ($f\text{CO}_2$ and pH) variables in Weddell Sea Deep Water. In each panel the top box plot represents data from Drake Passage and the bottom box plot represents data from A23. The number of data points in each box plot is given on the right of each panel. Figure 5.2 provides a guide to interpreting box plots.

5.3.3.2 Lower Circumpolar Deep Water

The LCDW measured at the A23 section is fresher than that measured in DP (Figures 5.11 and 5.12). The box plots suggest that there is no difference between the potential temperature of LCDW in DP and A23 (Figure 5.11) but the profile in Figure 5.13 shows that, for a given density, LCDW is colder at A23 than DP and the MLR finds this difference to be significant. The freshening and cooling of LCDW from DP to A23 is due to intense mixing with the fresher, colder, underlying WSDW (Naveira Garabato et al., 2002a) which is related to the strong, bottom-reaching flow of the ACC and the rough topography of the Scotia Sea (Heywood et al., 2002). As well as diapycnal mixing with water below it, LCDW also freshens as it moves eastwards in the Scotia Sea due to isopycnal exchange with waters of the Weddell-Scotia Confluence to the south (Naveira Garabato et al., 2003). Figure 5.1 shows the main mixing pathways for the deep water masses of the ACC in the Scotia Sea.

The profiles of potential temperature (Figure 5.13), salinity, oxygen and CFC12 (Figure 5.12) show a scattered group of data points in the LCDW density class at DP which are colder and fresher than the bulk of the data and have higher oxygen and CFC12 concentrations. These data points have lower dynamic heights than the bulk of the data, as demonstrated for potential temperature in Figure 5.13 and therefore lie further south. This suggests that, although the bulk of LCDW at DP is saltier and warmer than that at A23, the LCDW at the very southern end of DP is influenced by cold, fresh, ventilated waters of the Antarctic Peninsula. This influence is more apparent in UCDW (Section 5.3.3.3).

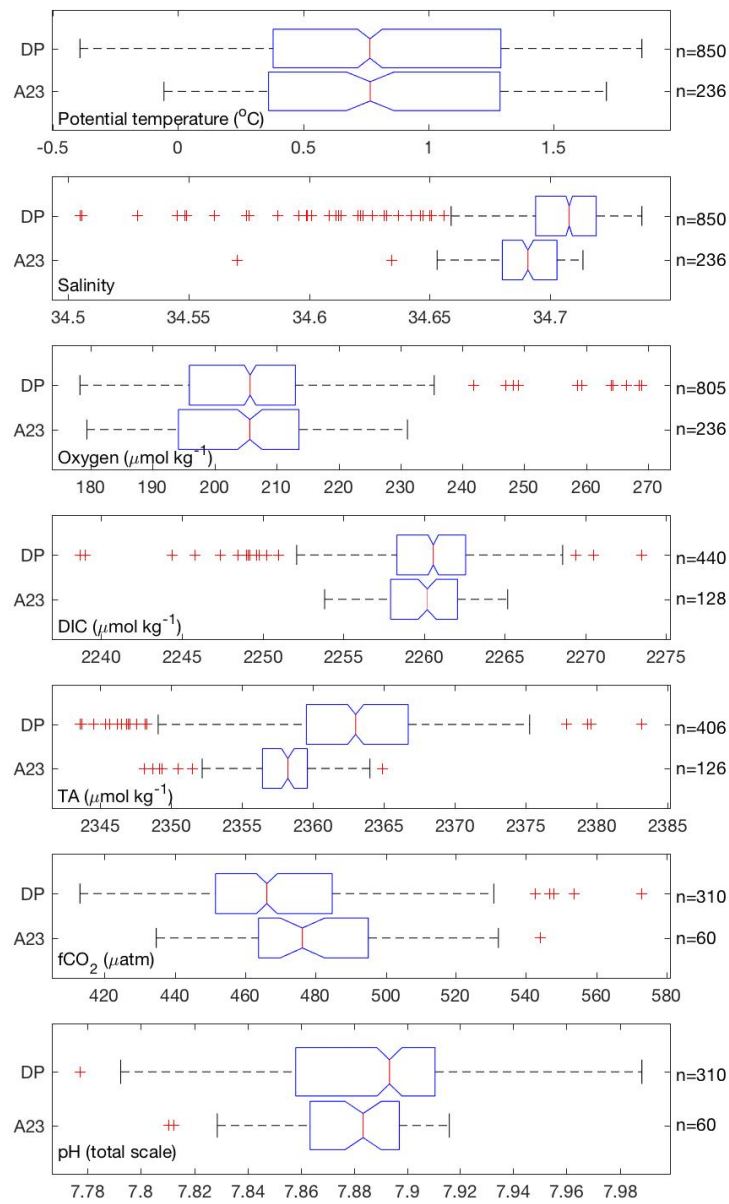


Figure 5.11: Box plots of measured (Potential temperature, salinity, oxygen, DIC and TA) and calculated ($f\text{CO}_2$ and pH) variables in Lower Circumpolar Deep Water. In each panel the top box plot represents data from Drake Passage and the bottom box plot represents data from A23. The number of data points in each box plot is given on the right of each panel. Figure 5.2 provides a guide to interpreting box plots.

There is no significant difference in DIC concentration in LCDW between

DP and A23 but there is significantly more TA at DP than at A23 (Figures 5.11 and 5.14). We can be more confident in this signal than the possible TA difference in WSDW because the difference in LCDW is greater (medians differ by $\sim 5 \mu\text{mol.kg}^{-1}$) and there are many more data. The decrease in TA from DP to A23 is also consistent with decreasing salinity. The influence of colder, fresher, more ventilated water from the Antarctic Peninsula, discussed above, is evident for DP in the DIC and TA box plots as the red dots which lie below the value of the whiskers. The salinity maximum in LCDW (Figure 5.12) occurs at γ of about 28.05 whereas the TA maximum (Figure 5.14) occurs at slightly higher densities. This is due to the non-conservative accumulation of carbonate dissolution products deeper in the water column due to the decrease in the saturation state of carbonate minerals with pressure.

The decrease in TA relative to DIC causes an increase in $f\text{CO}_2$ in LCDW from DP to A23 (Figures 5.11 and 5.14). As LCDW shoals and moves southwards it influences the chemistry of the mixed layer south of the SACCF. In the deep passages of the South Scotia Ridge the net flow in the LCDW density class is southwards, into the Weddell Sea (Brown et al., 2015). In the Weddell Gyre, LCDW replenishes Warm Deep Water (Klatt et al., 2002) which mixes with the surface layer in winter (Gordon and Huber, 1990), reducing the ocean sink of atmospheric CO_2 in the region (Brown et al., 2015). The increase in LCDW $f\text{CO}_2$, caused by a reduction in TA, is therefore likely to reduce the uptake of CO_2 by the surface waters of the Weddell Gyre.

The increasing DIC:TA ratio from DP to A23 also results in significant decreases in pH and Ω aragonite and an increase in the Revelle factor in LCDW (see MLR results in Appendix C). The increase in Revelle factor is visible in Figure 5.15 but the decreases in pH and Ω aragonite are not clearly visible because of their strong relationship with dynamic height, discussed below. The upwelling LCDW communicates these carbonate system changes to the surface water south of the ACC. TA exchange in the deep Scotia Sea therefore makes the surface ocean more sensitive to increases in CO_2 and potentially affects calcifiers such as pteropods by

reducing the saturation state of calcium carbonate minerals.

There is a strong relationship between pH and dynamic height in LCDW in DP, with lower pH at greater dynamic heights (further north). There is also a decrease in calcium carbonate saturation states with increasing dynamic height in LCDW in DP. The reason pH and Ω show relationships with dynamic height, whereas DIC, TA and $f\text{CO}_2$ do not, is that LCDW shoals from north to south and so LCDW at greater dynamic heights (further north) is, on average, at a greater pressure. Increasing pressure decreases pH and the concentrations of CO_3^{2-} ions (Culberson and Pytkowicz, 1968), reducing Ω . A graphical demonstration of the influence of pressure on pH and Ω in LCDW in DP is shown in Appendix E. This pressure effect is also evident in the A23 data but the dynamic height and pressure ranges are smaller, so the pattern is not as striking.

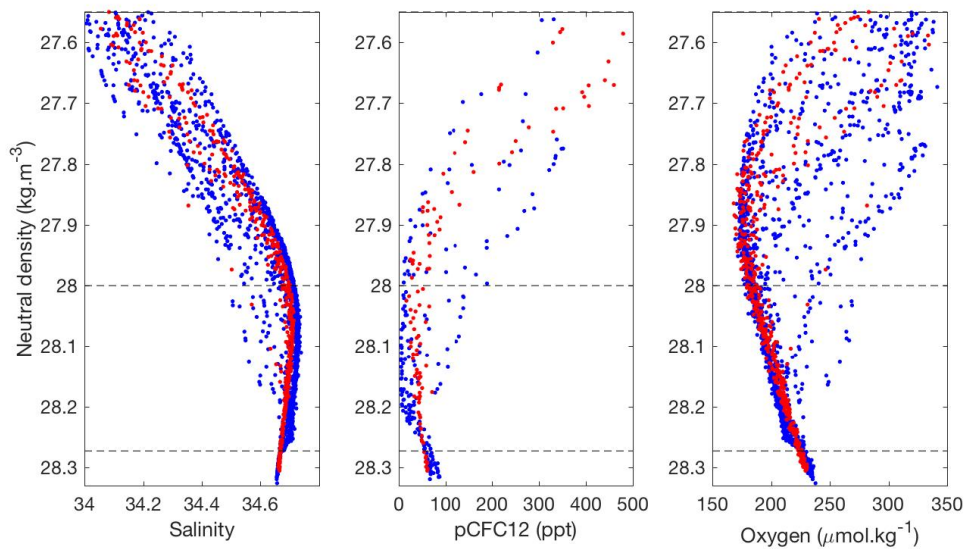


Figure 5.12: A comparison of DP (blue) and A23 (red) salinity (left panel), pCFC12 (centre panel) and oxygen (right panel). Horizontal dashed lines represent the boundaries between UCDW and LCDW ($\gamma^{\theta} = 28$) and LCDW and WSDW ($\gamma^{\theta} = 28.273$).

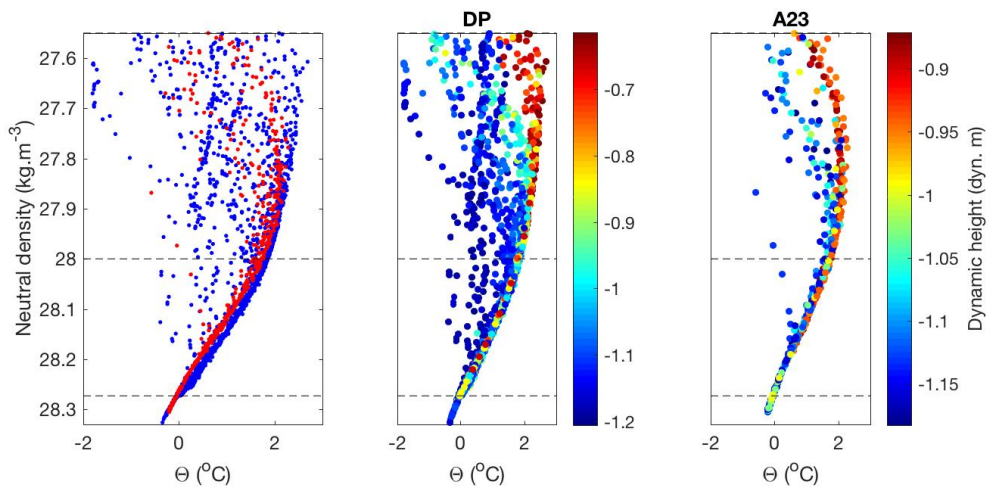


Figure 5.13: A comparison of DP (blue) and A23 (red) potential temperature (left panel). Centre and right panels show the DP and A23 data, respectively, coloured by dynamic height (note different dynamic height ranges). Horizontal dashed lines represent the boundaries between UCDW and LCDW ($\gamma^l = 28$) and LCDW and WSDW ($\gamma^l = 28.273$).

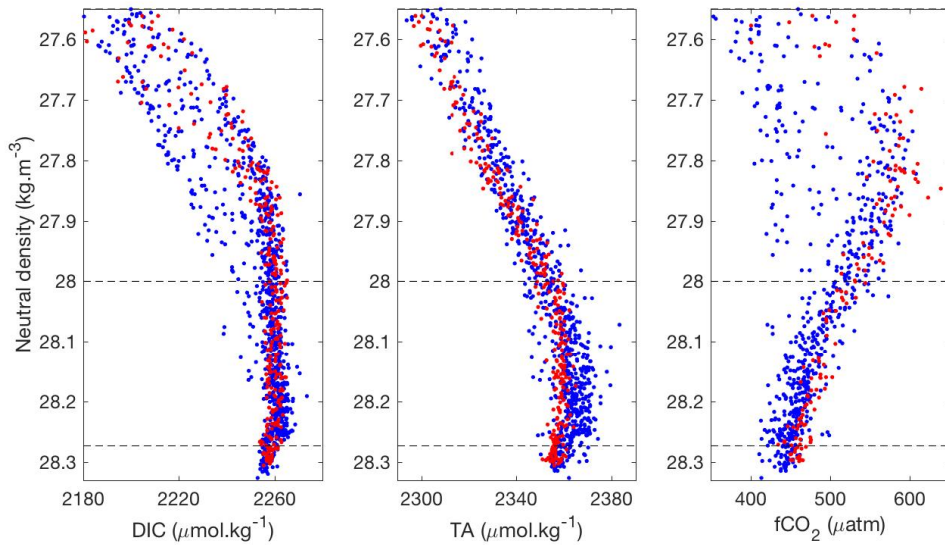


Figure 5.14: A comparison of DP (blue) and A23 (red) DIC (left panel), TA (centre panel) and $f\text{CO}_2$ (right panel). Horizontal dashed lines represent the boundaries between UCDW and LCDW ($\gamma^l = 28$) and LCDW and WSDW ($\gamma^l = 28.273$).

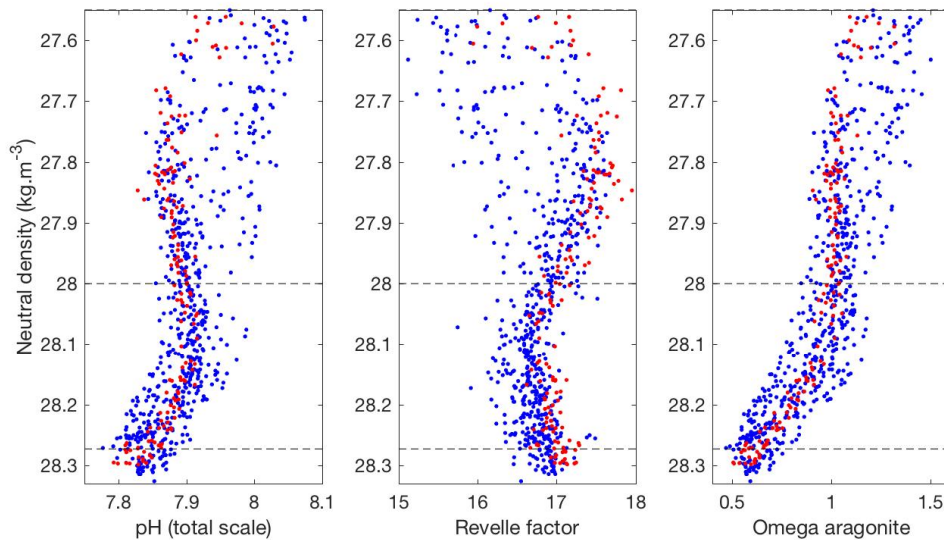


Figure 5.15: A comparison of DP (blue) and A23 (red) pH (left panel), Revelle factor (centre panel) and Ω aragonite (right panel). Horizontal dashed lines represent the boundaries between UCDW and LCDW ($\gamma^t = 28$) and LCDW and WSDW ($\gamma^t = 28.273$).

5.3.3.3 Upper Circumpolar Deep Water

As isopycnals shoal southwards across in the ACC, water in the the UCDW density class becomes shallower and mixes with more recently ventilated surface waters, south of the PF (Figure 5.1). As a result of this mixing with surface waters, the core of this water mass becomes colder and fresher from DP to A23 (Figures 5.12 and 5.13). The further south in the ACC (at lower dynamic heights), the shallower UCDW is and the more it is influenced by mixing with surface waters. On both the DP and A23 sections, the 27.55 kg.m^{-3} isopycnal (the upper boundary of UCDW) shoals to a depth of less than 150 m at the SACCF. This southerly surface influence is evidenced by the scattered data points in the UCDW density class which have low dynamic height values and are colder, fresher and more oxygen-rich than the majority of data points which form the main mixing line, contiguous with LCDW data (Figures 5.12 and 5.13).

These colder, fresher and more ventilated measurements are especially prevalent in the DP dataset, suggesting that UCDW in the south of DP is strongly influenced by mixing with surface waters of the Antarctic Peninsula. As well as out-

cropping and direct contact of UCDW with the atmosphere, other mechanisms may introduce this more recently ventilated shelf water to depth in DP. Eddies, associated with topography and meanders in the ACC fronts, mix water from the Antarctic Peninsula shelf northwards, into the DP, ventilating CDW (Provost et al., 2011). Another mechanism for introducing colder, fresher shelf water to depth in DP was demonstrated by Meredith et al. (2003) who, using an 8 year time series of bottom temperature from 1040 m on the continental slope north of Elephant Island, found large cold spikes during the winter, indicating convection events dense enough to mix into the resident CDW. It is also possible that some of the colder, fresher water observed here at DP may be transported into the CDW density class in DP at depth, via the passages of the South Scotia Ridge. A westward flowing slope current has been observed north of Elephant Island which is significantly colder and fresher than CDW in the same neutral density range (28.2 to 28.26 kg.m^{-3}) and which may be an extension of the Antarctic Slope Current which has crossed the South Scotia Ridge from the Weddell Sea (Meijers et al., 2016). However, most of the colder, fresher waters discussed here have a lower density than those of the slope current discussed by Meijers et al. (2016), suggesting that this is not the dominant cause of the cold, fresh, oxygen rich water in the UCDW and LCDW density classes shown here.

Mixing with recently ventilated surface waters also affects the carbonate system in UCDW in the south of DP. Figures 5.14 and 5.15 show that this colder, fresher UCDW in the south of DP has lower DIC, $f\text{CO}_2$ and Revelle factor, and higher pH and $\Omega_{\text{aragonite}}$. As UCDW is affected by the atmosphere in this region, through mixing with surface waters, it follows that the atmosphere is affected by UCDW. The implication for ocean-atmosphere CO_2 flux is that upwelling UCDW in this region, combined with isopycnal mixing by eddies off the Antarctic Peninsula, increases the DIC in the surface water, causing the ocean to be source of CO_2 to the atmosphere. This is consistent with the CO_2 flux maps of (Brown et al., 2015), based on the SOCATv2 $f\text{CO}_2$ dataset (Bakker et al., 2014), interpolated using a neural network technique (Landschützer et al., 2013), which show that the

ocean downstream of the tip of the Antarctic Peninsula is a strong net source of CO₂ to the atmosphere in winter and spring, suggesting that this region is an important site of deep water ventilation. This region of strong winter CO₂ outgassing in the far south of DP and downstream of the Peninsula contrasts with the area slightly further north in DP, between the PF and the SACCF, which is found to be a small sink of atmospheric CO₂ in winter (Munro et al., 2015).

As a result of the strong surface influence in the south of DP, the box plots comparing DP and A23 suggest that UCDW gets warmer and saltier from DP to A23 (Figure 5.16). However, as discussed above, the density profiles show that for a given density, the core of UCDW is colder and fresher at A23 than DP (Figures 5.12 and 5.13). The results of the box plots are also affected by sampling bias because, on most of the cruises used here, sampling frequency was higher across the shelf break at the southern edge of DP, magnifying the influence of the colder, fresher water in the south of the section.

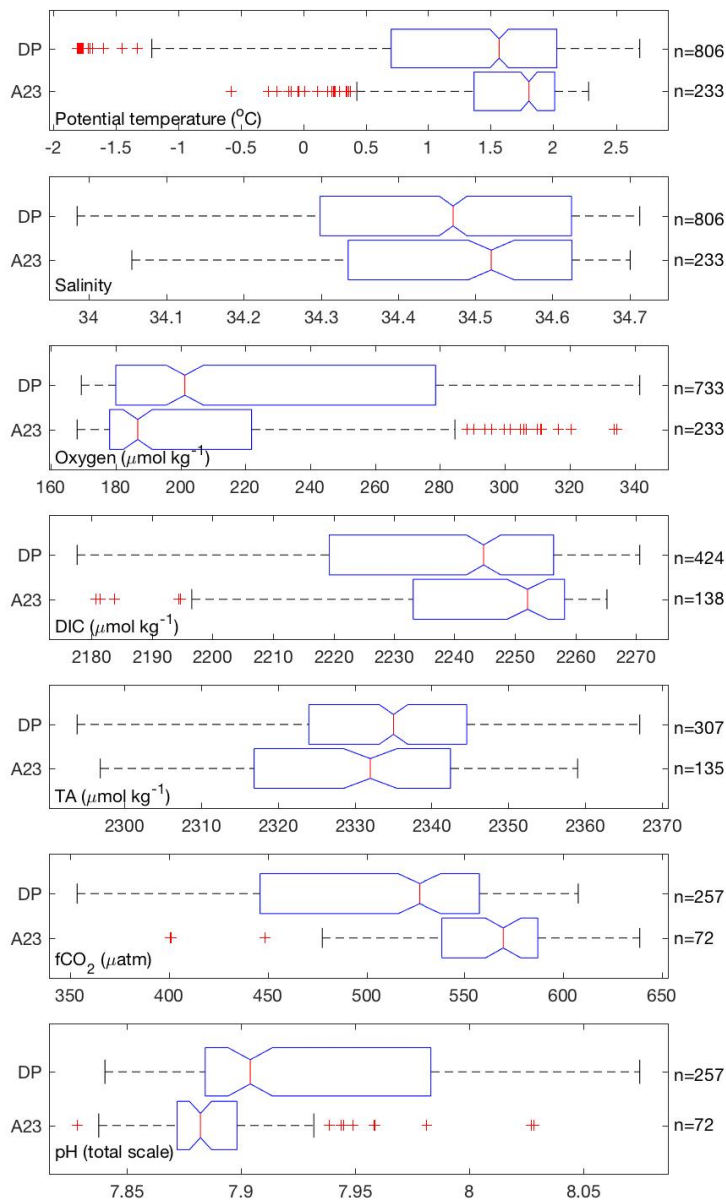


Figure 5.16: Box plots of measured (Potential temperature, salinity, oxygen, DIC and TA) and calculated ($f\text{CO}_2$ and pH) variables in Upper Circumpolar Deep Water. In each panel the top box plot represents data from Drake Passage and the bottom box plot represents data from A23. The number of data points in each box plot is given on the right of each panel. Figure 5.2 provides a guide to interpreting box plots.

5.3.4 North Scotia Ridge

Figure 5.17 shows the DIC, TA, oxygen and silicate concentrations for a section of the North Scotia Ridge, including Shag Rocks Passage. Due to sampling constraints, the horizontal resolution of the data is fairly sparse for much of the section but it is sufficient to resolve the main frontal features. The SAF and the PF are visible at $\sim 55^{\circ}\text{W}$ and $\sim 48^{\circ}\text{W}$ respectively, evidenced by steeply sloping isopycnals and a corresponding change in the concentrations of DIC, TA, oxygen and silicate. This is thought to be the first time the carbonate system has been measured at depth along the North Scotia Ridge. This dataset therefore provides a unique snapshot of the carbonate system in this region and will be a useful reference point if these measurements are repeated in the future.

There are not sufficient data here to present a detailed analysis of water mass differences between DP and the North Scotia Ridge but some patterns are evident (Figure 5.18). Consistent with Smith et al. (2010a) we detected no WSDW crossing the North Scotia Ridge though Shag Rocks Passage and LCDW at the North Scotia Ridge is fresher than at DP due to mixing with WSDW in the Scotia Sea (Naveira Garabato et al., 2002a). It is also notable that UCDW data are more tightly constrained at the North Scotia Ridge than at DP. This is because the majority of the North Scotia Ridge data are from north of the PF and are therefore deeper and less influenced by mixing with surface water than some UCDW in DP (Section 5.3.3.3). Due to the scarcity of data and the precision of the measurements, differences in carbonate system variables between DP and the North Scotia Ridge cannot be discerned.

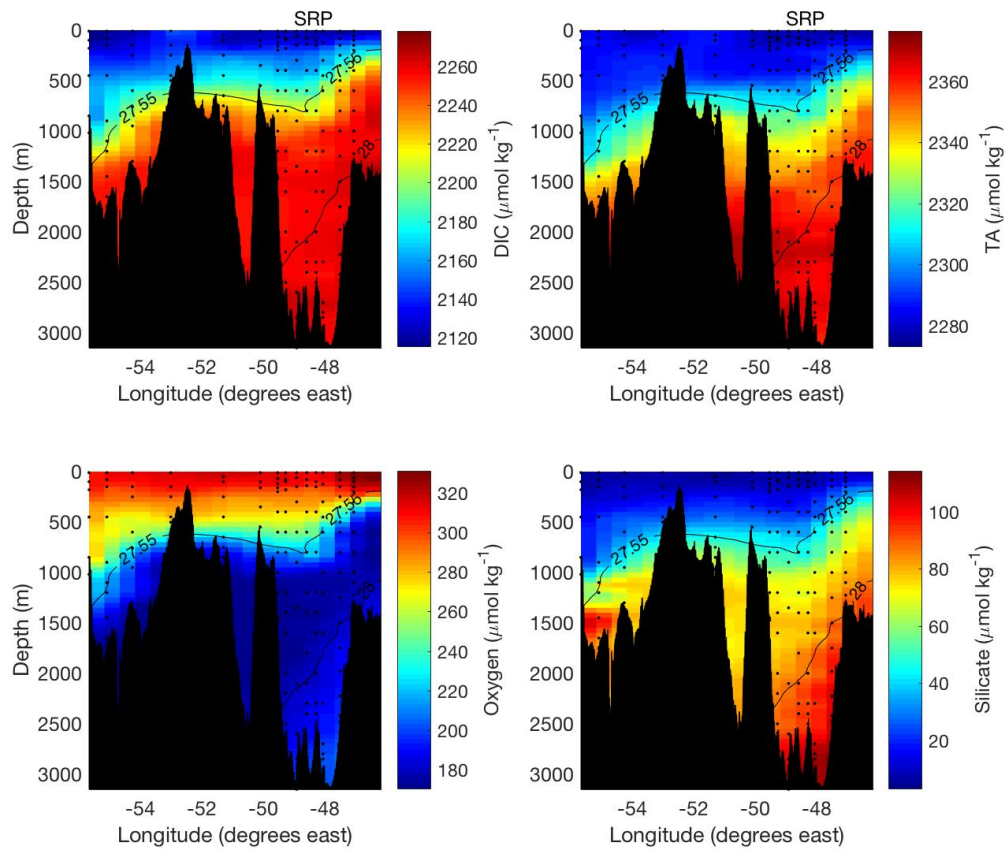


Figure 5.17: DIC, TA, oxygen and silicate concentrations along the North Scotia Ridge section of JR299. Neutral density contours pertinent to water mass definition are overlaid (Section 5.2.2). Black dots indicate sample locations. Bathymetry data from Smith and Sandwell (1997). SRP indicates location of Shag Rocks Passage.

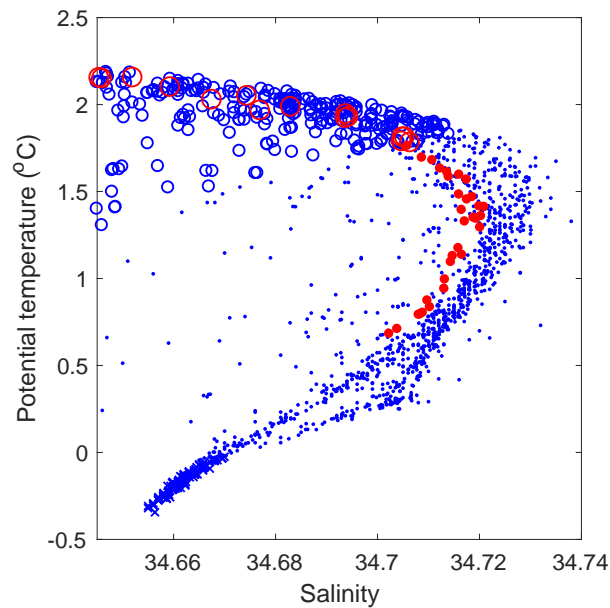


Figure 5.18: Θ/S plot of the densest waters of the Drake Passage (blue) and North Scotia Ridge section (red). Crosses = WSDW, dots = LCDW, circles = UCDW. Only the densest part of the Θ/S plot is shown and therefore some less dense UCDW is off the scale.

5.4 Conclusions

- There are differences in water column structure either side of the Shackleton Fracture Zone in DP. The influence of SPDW in the LCDW density class is observed to the west of the SFZ but not to the east. WSDW is observed to the east of the SFZ but not to the west.
- WSDW at A23 is saltier and has a lower oxygen concentration than WSDW at DP. This is likely due to the pathways of WSDW exiting the Weddell Sea over the South Scotia Ridge and also due to mixing with overlying LCDW in the Scotia Sea. No clear differences are found in the carbonate system between A23 and DP in WSDW.
- LCDW is colder and fresher at A23 than at DP due to diapycnal mixing with WSDW and isopycnal mixing with waters of the Weddell Scotia Confluence. This freshening from DP to A23 coincides with a decrease in TA in which causes an increase in $f\text{CO}_2$ and the Revelle factor and a decrease in pH and

Ω . This mechanism of TA exchange in the deep Scotia Sea may reduce the uptake of CO_2 by the high latitude Southern Ocean through the influence of LCDW on surface waters of the Weddell Sea.

- The core of UCDW is colder and fresher at A23 than at DP due to mixing with surface waters in the Scotia Sea. However, UCDW and, to a lesser extent, LCDW, in the south of DP are influenced by mixing with colder, fresher water from the Antarctic Peninsula shelf. This increases the oxygen concentrations in UCDW in the south of DP and lowers its $f\text{CO}_2$ and DIC. The ventilation of UCDW in the south of DP suggests that this is an important region for the release of CO_2 from UCDW to the atmosphere.
- Hydrographic data from Shag Rocks Passage on the North Scotia Ridge are consistent with earlier studies. More, high quality carbonate data would be necessary in order to discern any carbonate system modifications between DP and North Scotia Ridge.

Chapter 6

Circumpolar patterns in the Southern Ocean carbonate system

6.1 Rationale

The water masses of the Southern Ocean are an important part of the global thermohaline circulation, transporting heat, salt and carbon both zonally and meridionally. Consequently, changes to these water masses could have significant impacts on global ocean circulation and climate. The DIC contained in these water masses is made up of different components, resulting from different processes. Understanding how these different components of DIC vary spatially and temporally helps to explain the biogeochemistry of the Southern Ocean and provides a basis for predicting future changes. The aims of this chapter are to:

- Characterise the zonal variability of components of DIC in the deep water masses of the ACC.
- Investigate temporal changes in DIC in Sub-Antarctic Mode Water since 1990.

6.2 Methods

This study uses data from south of 40°S from the Global Ocean Data Analysis Project version 2 (GLODAPv2) merged data product (Olsen et al., 2016). The core variables have been quality controlled and examined for biases, and are believed to

be consistent to better than 0.005 in salinity, 1% in oxygen, $4 \mu\text{mol.kg}^{-1}$ in DIC, $6 \mu\text{mol.kg}^{-1}$ in TA and 5% for CFCs (Olsen et al., 2016). As in Chapter 5, dynamic height is used to define the fronts of the ACC and neutral density is used to define water masses. The circumpolar application of these boundaries is described below.

6.2.1 Defining vertical and horizontal boundaries

The ACC fronts have been found to be associated with particular dynamic height contours which remain nearly constant in time and around the circumpolar path of the ACC (Sokolov and Rintoul, 2009). Potential temperature section plots from various meridional sections around the ACC were examined in order to validate the dynamic height definitions for the Sub-Antarctic Front (SAF), Polar Front (PF) and Southern ACC Front (SACCF) against traditional hydrographic frontal definitions (Section 1.3.1). Figure 6.1 shows a circumpolar average potential temperature section. Potential temperature plots for individual meridional sections, used for validating dynamic height frontal definitions, are shown in Appendix F. The circumpolar dynamic height frontal definitions used here are given in Table 6.1.

Table 6.1: Circumpolar dynamic height frontal definitions.

| Front | Dynamic height definition (dyn. m) |
|----------------------------|------------------------------------|
| Sub-Antarctic Front (SAF) | 0.09 |
| Polar Front (PF) | -0.7 |
| Southern ACC Front (SACCF) | -0.95 |

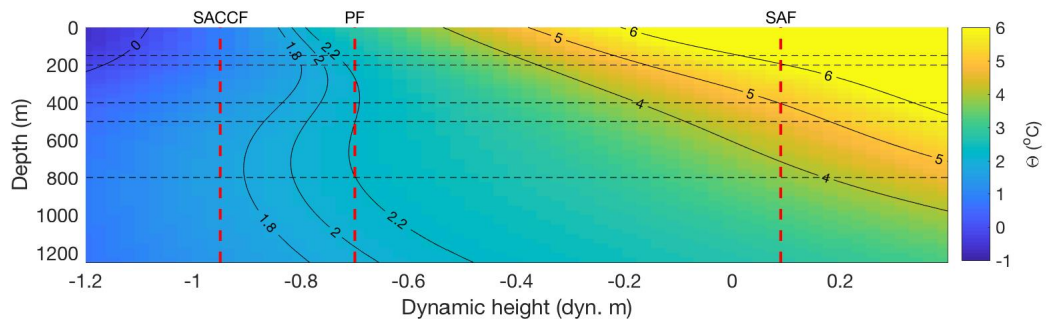


Figure 6.1: Validation of dynamic height frontal definitions for an average circumpolar meridional section, using data from GLODAPv2. Potential temperature contours (solid black lines) and depth contours (horizontal dashed lines) used in the literature for defining frontal positions are shown (Section 1.3.1). See Appendix F for similar plots of specific hydrographic sections.

The satellite altimetry data used for calculating dynamic height is only available from 1993 onwards (Rio and Hernandez, 2004). In order to include GLODAPv2 data from before 1993, earlier data points were given the average dynamic height value from their latitude, longitude and month. Averaged dynamic heights were also created for the period with altimetry data so that measured and averaged dynamic heights could be compared. Figure 6.2 shows that the measured and average values agree well. However, the use of averaged dynamic heights will introduce some error into the frontal definitions, especially in regions where the position of the fronts is more variable.

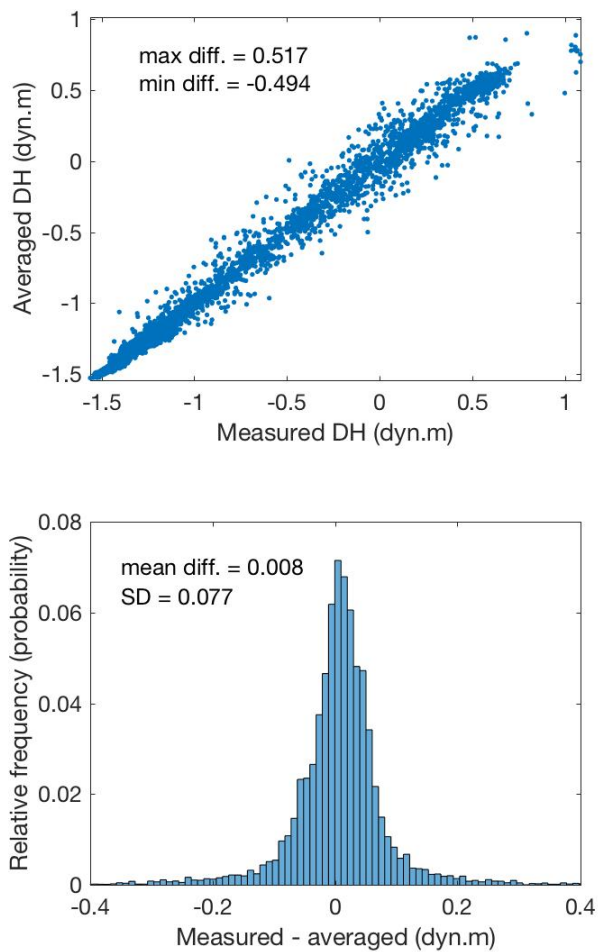


Figure 6.2: A comparison of measured and averaged dynamic heights. Top panel: measured vs. averaged dynamic height values for GLODAPv2 datapoints after 1993. Bottom panel: a histogram of the residuals. The mean difference and standard deviation are given.

Water masses were defined using the neutral density definitions of Sloyan and Rintoul (2001a,b) and are presented in Table 6.2. Figure 6.3 shows that these boundaries are consistent with the salinity maximum in LCDW and the $f\text{CO}_2$ maximum and oxygen minimum in UCDW.

Table 6.2: Circumpolar water mass definitions based on Sloyan and Rintoul (2001a,b).

| Water mass | Neutral density boundaries ($\text{kg}\cdot\text{m}^{-3}$) |
|-------------------------------------|--|
| Sub-Antarctic Mode Water (SAMW) | $26 < \gamma^n < 27$ |
| Antarctic Intermediate Water (AAIW) | $27 < \gamma^n < 27.4$ |
| Upper Circumpolar Deep Water (UCDW) | $27.4 < \gamma^n < 28$ |
| Lower Circumpolar Deep Water (LCDW) | $28 < \gamma^n < 28.2$ |
| Antarctic Bottom Water (AABW) | $28.2 < \gamma^n$ |

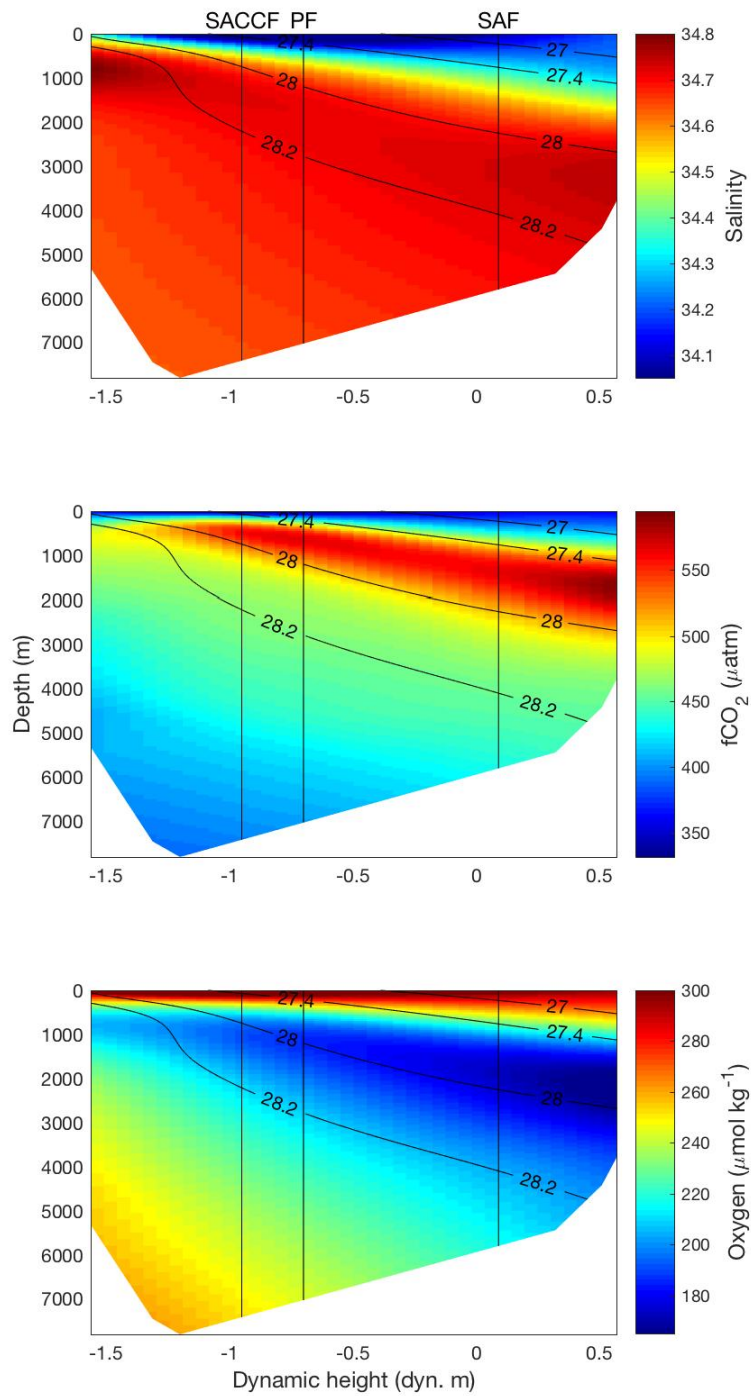


Figure 6.3: Mean meridional circumpolar sections of salinity, $f\text{CO}_2$ and oxygen. Neutral density contours used for water mass boundaries are shown. The position of the SACCF, PF and SAF are indicated.

6.2.2 Carbon partitioning

Measured DIC (DIC^{meas}) was partitioned into several components based on the framework of Sarmiento and Gruber (2006) and Williams and Follows (2011) which follows the approach of Brewer (1978) and Chen and Millero (1979).

$$DIC^{meas} = DIC^{soft} + DIC^{carb} + DIC_{pre}^{sat} + DIC^{res} \quad (6.1)$$

DIC^{soft} is the DIC produced by the remineralisation of organic matter and is calculated from the ratio of carbon and oxygen in organic matter and the apparent oxygen utilisation (AOU). The nutrient ratios used here are C:N:P:O = 106:16:1:170, following Williams and Follows (2011). Natural deviations from this stoichiometry will cause errors in the DIC partitioning results.

$$DIC^{soft} = -R_{C:O} \cdot AOU \quad (6.2)$$

AOU is used to infer the amount of respiration which has taken place since the water was last at the surface and is calculated as the difference between the saturated oxygen concentration at in-situ temperature and salinity, and the measured oxygen concentration. Oxygen solubility was calculated from potential temperature and salinity using the equations of (García and Gordon, 1992). Any disequilibrium of oxygen when the water left the air-sea interface will cause an error in the AOU term and therefore also in DIC^{soft} . Rapid heat loss, ice cover and convective mixing can cause significant oxygen disequilibrium in polar waters (Anderson et al., 1991) meaning that respiration, and therefore DIC^{soft} is often overestimated (Ito et al., 2004).

$$AOU = O_2^{sat}(\theta, S) - O_2 \quad (6.3)$$

DIC^{carb} is the DIC produced by the remineralisation of carbonate minerals and is calculated from the difference between measured TA and preformed TA, with a correction for the remineralisation of charged nutrients.

$$\text{DIC}^{carb} = 0.5 \cdot (\text{TA} - \text{TA}^{pre} - R_{N:O} \cdot \text{AOU}) \quad (6.4)$$

Preformed TA is the TA which the water had when it was last at the surface and is calculated using the empirically determined relationship of Gruber et al. (1996).

$$\text{TA}^{pre} = 367.5 + 54.9 \cdot S + 0.074 \cdot \text{PO} \quad (6.5)$$

Alkalinity changes in the surface ocean are dominated by salinity but are also influenced by nutrient concentrations, especially in the Southern Ocean where high nutrient deep water is upwelled. The inclusion of the tracer PO (similar to the conservative tracer introduced by Broecker (1974)) is therefore important when calculating TA^{pre} in this region (Gruber et al., 1996).

$$\text{PO} = \text{O}_2 - R_{P:O} \cdot \text{PO}_4^{3-} \quad (6.6)$$

The DIC_{pre}^{sat} term describes the saturated DIC concentration of the water at equilibrium with a preindustrial atmospheric CO_2 concentration and was calculated with the CO2SYS program (Van Heuven et al., 2011a) using in-situ salinity, in-situ potential temperature, preformed TA (Equation 6.5) and a preindustrial CO_2 of 278 ppm.

The residual term, DIC^{res} , is therefore comprised of anthropogenic CO_2 and any CO_2 disequilibrium when the water was last at the surface. This disequilibrium may be significant given the long equilibration timescale of CO_2 , the potentially short surface residence time of Southern Ocean waters and the influence of sea ice on gas exchange. The value of DIC^{res} will also be affected by any errors in the other DIC components.

$$\text{DIC}^{res} = \text{DIC}^{meas} - (\text{DIC}^{soft} + \text{DIC}^{carb} + \text{DIC}_{pre}^{sat}) \quad (6.7)$$

When calculating the DIC components above, only data points with a WOCE flag 2 (good) for DIC, TA, phosphate and oxygen were used. Although this ensures the most accurate results, it reduces the number of data points for these derived

variables. Of approximately 68,000 data points flagged 2 for DIC, about 35,000 of them are also flagged 2 for TA, phosphate and oxygen.

The remineralisation of organic matter can also be expressed using regenerated phosphate (PO_4^{reg}), which is analogous to DIC^{soft} and is calculated as

$$\text{PO}_4^{reg} = -R_{P:O} \cdot \text{AOU} \quad (6.8)$$

P^{reg} can then be used to quantify the proportion of phosphate which is biologically regenerated, which can be thought of as the efficiency of nutrient utilisation. This proportion is termed P^* (Ito and Follows, 2005). P^* ranges from 0, indicating that all the phosphate was present when the water subducted, to 1, indicating that all the phosphate is the result of the remineralisation of organic matter. Because of its dependency on AOU, P^* , like DIC^{soft} , is susceptible to errors caused by oxygen disequilibrium which may cause P^* to be overestimated by up to 0.2 (Ito et al., 2004).

$$P^* = \frac{\text{PO}_4^{reg}}{\text{PO}_4^{3-}} \quad (6.9)$$

6.2.3 Pentadal trends in SAMW

SAMW was defined using the neutral density boundaries in Table 6.2 and data from shallower than 200m were excluded to reduce the influence of seasonally varying surface waters. The dataset was truncated at 40°S and this ensures that the observed SAMW has been ventilated within a few years of being measured. To reduce spatial sampling bias, all data were gridded to produce a temporal mean field (in dynamic height, neutral density space) of each variable, with a grid size of 0.022 dyn.m by 0.005 kg.m⁻³. The closest grid point of this temporal mean field was then subtracted from individual data points to give an anomaly for each data point. This is similar to the method of Böning et al. (2008) although here, due to the scarcity of biogeochemical data in the Southern Ocean, the dataset used to create the mean field is the same as the one being analysed. If there is a temporal bias in the sampling distribution then this will affect the mean field and the resulting

anomalies. Although this method should reduce sampling bias in the density and dynamic height dimensions, it does not remove any zonal sampling bias. Temporal trends will therefore be affected by sampling location and this is discussed further in Section 6.3.2.2. Anomalies for each variable were binned into 5 year bins (pentades) and represented with box plots in order to provide a simple estimate of pentadal variability. Only data between 1990 and 2010 (inclusive) were included as there are too few data before and after this period.

6.3 Results and discussion

6.3.1 Zonal observations

In Chapter 5 we saw that the DIC in the Scotia Sea is relatively constant in waters with a neutral density greater than about 27.8 kg.m^{-3} (Figure 5.14). However, this is not the case throughout the circumpolar path of the ACC. Figures 6.4 and 6.5 show properties of the densest waters of the ACC, coloured by degrees east from Drake Passage (taken as 65°W). Only data between the SACCF and SAF are shown. The Scotia Sea data are evident as the darkest blue points, with WSDW (within the AABW density class) and LCDW DIC concentrations of about $2260 \mu\text{mol.kg}^{-1}$.

Between neutral densities of about 27.9 and 28.2 kg.m^{-3} , representing LCDW and the bottom of UCDW, there is a strong zonal gradient in DIC, oxygen and salinity around the ACC which contrasts with the relative zonal homogeneity of the water above and below this density class (Figures 6.4 and 6.5). Within this density class, DIC increases and oxygen and salinity decrease around the circumpolar path of the ACC from the Atlantic sector to the Drake Passage and Scotia Sea. The cause of this pattern is the input of North Atlantic Deep Water (NADW) into the top of the LCDW density class in the Atlantic sector of the ACC. NADW is saltier than UCDW and AABW and is responsible for the circumpolar salinity maximum in LCDW. NADW has also been more recently ventilated than the bulk of LCDW in the ACC and therefore less remineralisation of organic matter has take place in this water mass, leading to lower DIC and higher oxygen concentrations. As this newly

introduced NADW moves eastwards around the ACC, it mixes with CDW, reducing the salinity and oxygen and increasing the DIC in this density class. Although most of this zonal trend in oxygen and DIC is caused by mixing, some respiration also takes place locally, within the ACC, further reducing the oxygen and increasing the DIC.

For most of their density profiles, changes in DIC and oxygen are mirrored; the DIC maximum in UCDW corresponds to an oxygen minimum and the zonal increase in DIC in LCDW corresponds to a zonal decrease in oxygen. This is to be expected, given that their concentrations are largely controlled by the remineralisation of organic matter. However, this mirrored pattern is less apparent in the densest waters of the ACC, where both DIC and oxygen increase from LCDW to AABW (Figure 6.4). Shadwick et al. (2014) explained this increase in DIC and oxygen in the densest waters in the Mertz Polynya as a result of the differing equilibration timescales of CO₂ and O₂, suggesting that the remineralization of organic matter increases DIC beyond what can be lost by ocean-atmosphere CO₂ flux while the water is at the surface. While the DIC increase with depth is partly explained by CO₂ disequilibrium, there is also a contribution from the dissolution of carbonate minerals, as evidenced by the relative behaviour of salinity and alkalinity. Figure 6.5 shows that the salinity maximum occurs at $\gamma = 28.05 \text{ kg.m}^{-3}$, corresponding to the top of LCDW, whereas the TA maximum occurs deeper in the water column, roughly at the boundary of LCDW and AABW at $\gamma = 28.2 \text{ kg.m}^{-3}$. The reason for this non-conservative behaviour of TA is the dissolution of calcium carbonate minerals caused by the decrease in their saturation states with increasing pressure. The majority of UCDW and LCDW, and all of AABW are undersaturated with respect to aragonite whereas the calcite saturation horizon occurs at roughly the boundary between LCDW and AABW (Figure 6.6).

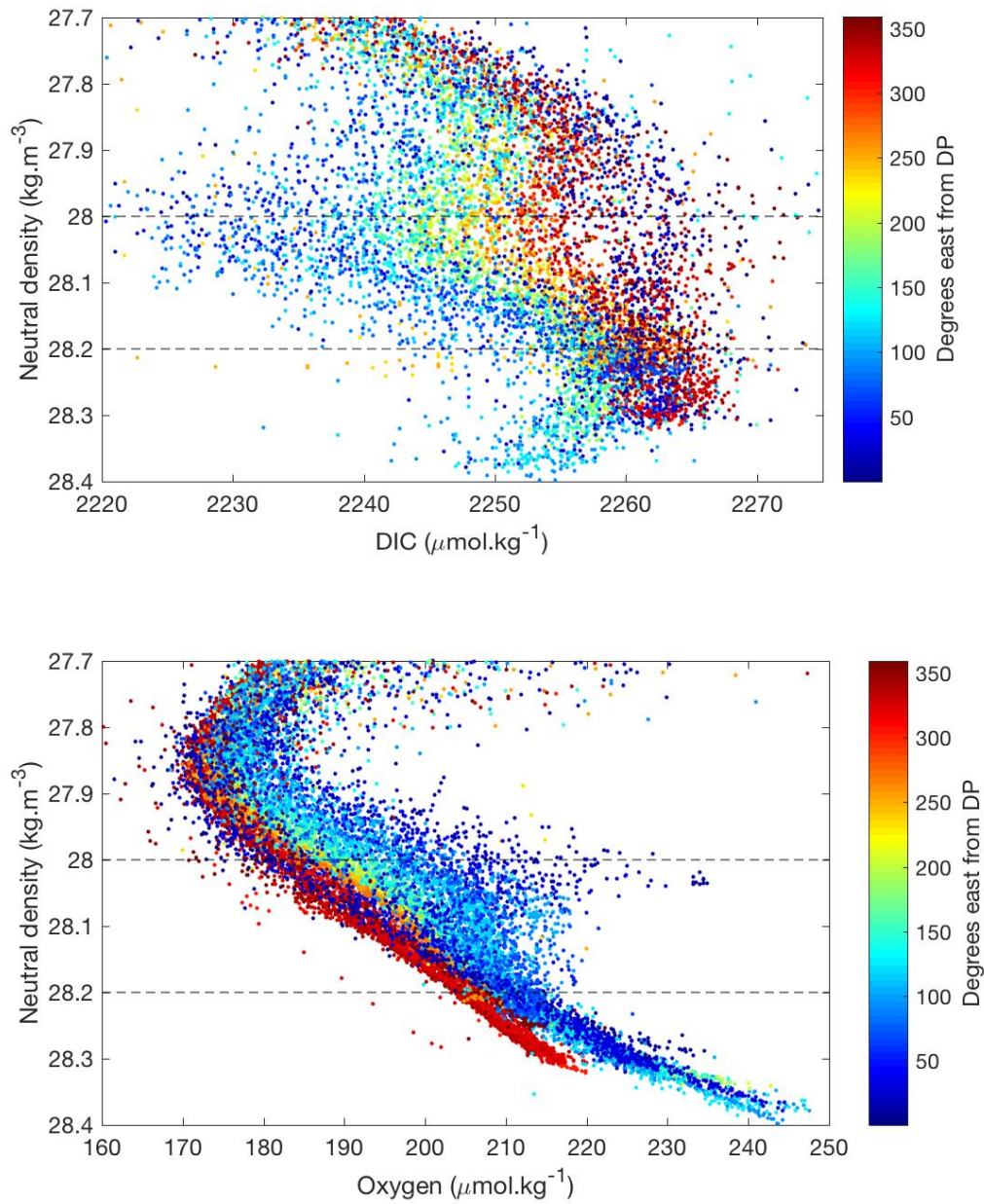


Figure 6.4: DIC (top panel) and oxygen (bottom panel) profiles for the densest waters of the ACC, between the SACCF and the SAF. The UCDW density class is truncated at 27.7 kg.m⁻³ in order to focus on the variability in the densest waters. Points are coloured by longitude from Drake Passage which is taken as 65°W.

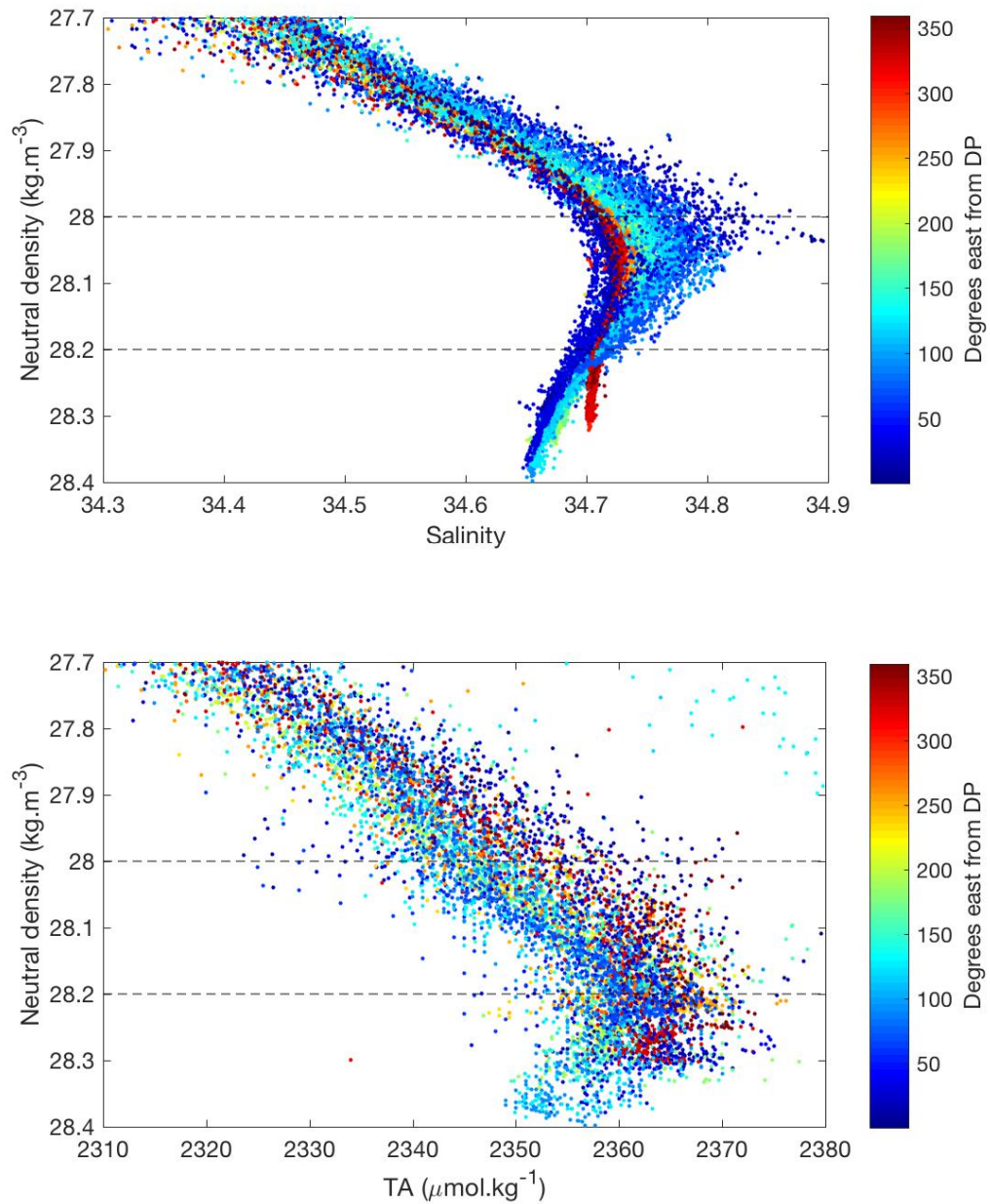


Figure 6.5: Salinity (top panel) and TA (bottom panel) profiles for the densest waters of the ACC, between the SACCF and the SAF. The UCDW density class is truncated at 27.7 kg.m^{-3} in order to focus on the variability in the densest waters. Points are coloured by longitude from Drake Passage which is taken as 65°W .

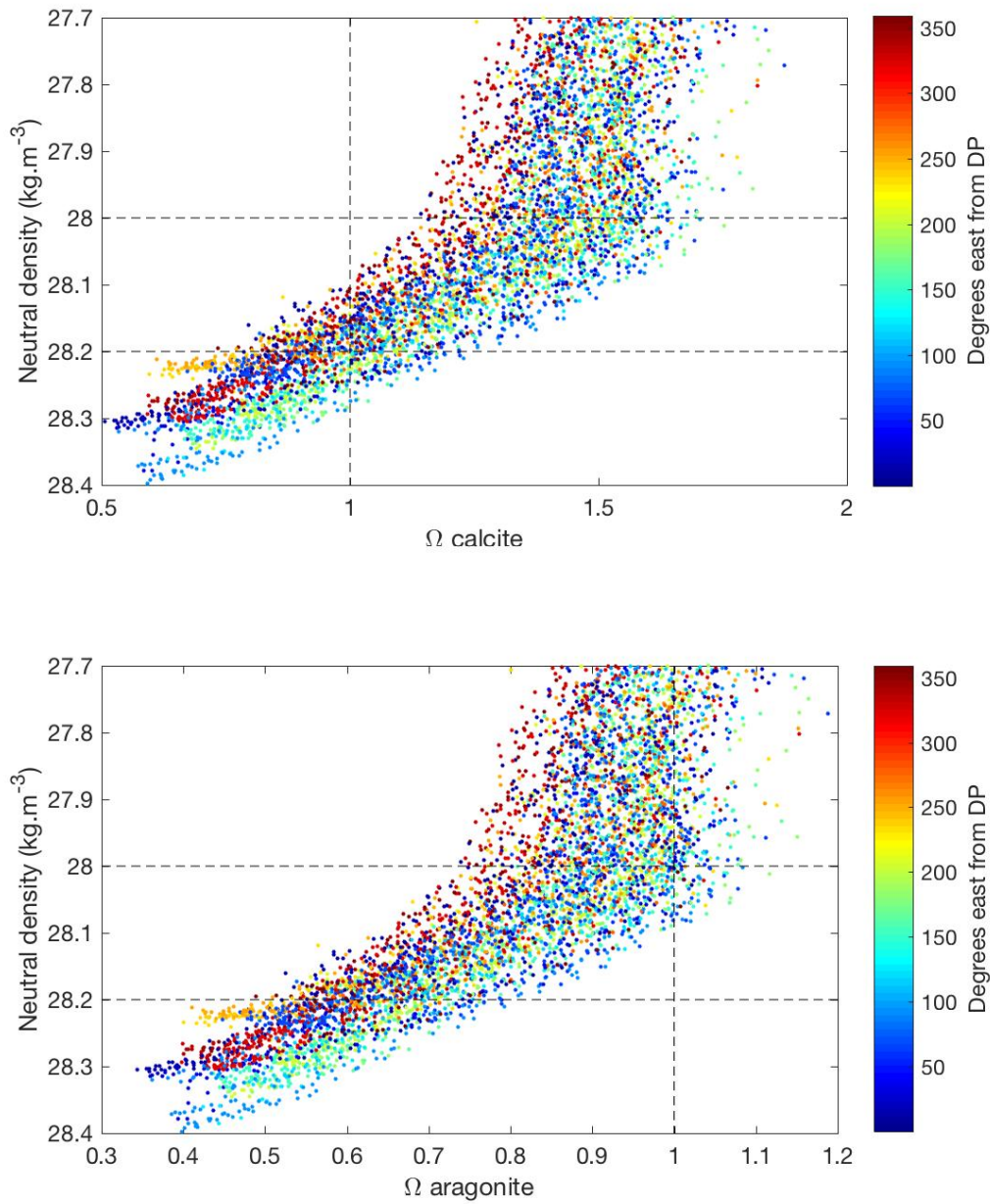


Figure 6.6: Calcite (top panel) and aragonite (bottom panel) saturation state profiles for the densest waters of the ACC, between the SACCF and the SAF. The UCDW density class is truncated at 27.7 kg.m⁻³ in order to focus on the variability in the densest waters. Points are coloured by longitude from Drake Passage which is taken as 65°W.

The zonal section plots in Figure 6.7 show which processes are responsible for

the observed changes in DIC and where in the circumpolar path of the ACC the variability occurs. The largest component is DIC_{pre}^{sat} , which increases with density fairly uniformly around the ACC. This is because the solubility of CO_2 is largely determined by temperature (Weiss, 1974) which decreases towards the bottom in these deep water masses. In a pre-industrial ocean, with no biological activity, the solubility pump alone would control the ocean DIC concentration. However, in reality, the remineralisation of organic matter, dissolution of calcium carbonate and increasing atmospheric CO_2 contribute to the total DIC and it is these components which are responsible for the zonal variation in measured DIC in the deep water masses of the ACC.

UCDW has high concentrations of DIC^{soft} of up to $100 \mu\text{mol.kg}^{-1}$, resulting from the age of this water mass but this concentration is not zonally uniform. There is a minimum in the Atlantic sector where inflowing NADW reduces DIC^{soft} in LCDW and UCDW. Much of this NADW injection into the ACC occurs in the southwestern Argentine basin (Whitworth and Nowlin, 1987). The DIC data from the Scotia Sea (Chapter 5) show no evidence of being influenced by this low DIC NADW, meaning that the modification of LCDW and UCDW by NADW occurs outside, and downstream, of the Scotia Sea, consistent with Naveira Garabato et al. (2002a) and Smith et al. (2010a). The low-DIC signal is eroded in the South Atlantic as the newly injected NADW is mixed into lighter water above and denser water below, as indicated by a divergence in the salinity flux at the UCDW/LCDW boundary (Evans et al., 2017). The concentration of DIC^{soft} in LCDW and UCDW continues to increase eastwards through the Indian and Pacific sectors as older waters from these basins join the ACC (Sloyan and Rintoul, 2001b). The strong zonal structure in DIC^{soft} shown here is in contrast to the description of Williams and Follows (2011) who found the waters around Antarctica to be relatively homogenous with respect to DIC^{soft} .

DIC^{carb} increases with depth due to dissolution of calcium carbonate minerals (Figure 6.6) and is responsible for up to about $30 \mu\text{mol.kg}^{-1}$ of the DIC in AABW. The zonal variability of DIC^{carb} is largely caused by variability in respiration prod-

ucts, DIC^{soft} . This is because water which has accumulated a greater concentration of soft-tissue remineralized carbon has a lower pH and a lower concentration of CO_3^{2-} ions, reducing the saturation state of calcium carbonate minerals (Williams and Follows, 2011). DIC^{carb} in LCDW and UCDW is therefore lowest in the Atlantic sector and increases eastwards, reaching a maximum in the Pacific sector. There is also likely to be a small component of the zonal DIC^{carb} pattern which is caused by pressure because, on average, isopycnals deepen slightly in the south east Pacific and shoal in the Atlantic and Indian sectors and this will influence the saturation states of calcium carbonate minerals.

DIC^{res} generally decreases with depth with very low values ($<5 \mu\text{mol.kg}^{-1}$) in LCDW and AABW. The negative values in the densest waters probably have two main causes. Firstly, the likely overestimation of DIC^{soft} , caused by oxygen disequilibrium, will cause the residual term to be underestimated. Secondly, DIC^{res} includes any CO_2 disequilibrium when the water was last at the surface. As these deep waters were cooling at the time of subduction they would not have been able to fully equilibrate with the atmosphere, giving a slightly negative DIC^{res} (Williams and Follows, 2011). It is likely that these disequilibrium signals are masking a small concentration of anthropogenic carbon in AABW which has been observed by previous studies (McNeil et al., 2001; Sabine et al., 2002; Lo Monaco et al., 2005; Williams et al., 2015). Also, as these observations are all within the ACC, AABW will have mixed to some degree with overlying LCDW since subducting in its formation regions, making the small anthropogenic carbon signal hard to discern (Williams et al., 2015). DIC^{res} increases towards the top of UCDW representing mixing with AAIW above, which has been more recently ventilated and contains anthropogenic carbon concentrations in excess of $20 \mu\text{mol.kg}^{-1}$ (Lo Monaco et al., 2005; Pardo et al., 2014).

There appears to be a region of particularly low DIC^{res} in AABW at about $50 - 60^\circ\text{E}$. This is probably caused by spatial sampling bias because the observations in this longitude range are mostly from the northern edge of ACC (see top panel in Figure 6.7) and will therefore be less directly influenced by bottom waters

from the high latitude Southern Ocean which contain anthropogenic carbon. This is supported by CFC12 measurements (not shown) which exhibit a minimum at this longitude with higher concentrations to the east and west, suggesting that the more northerly AABW has mixed more with the overlying deep water (Gladyshev et al., 2008; Gonzalez-Davila et al., 2011).

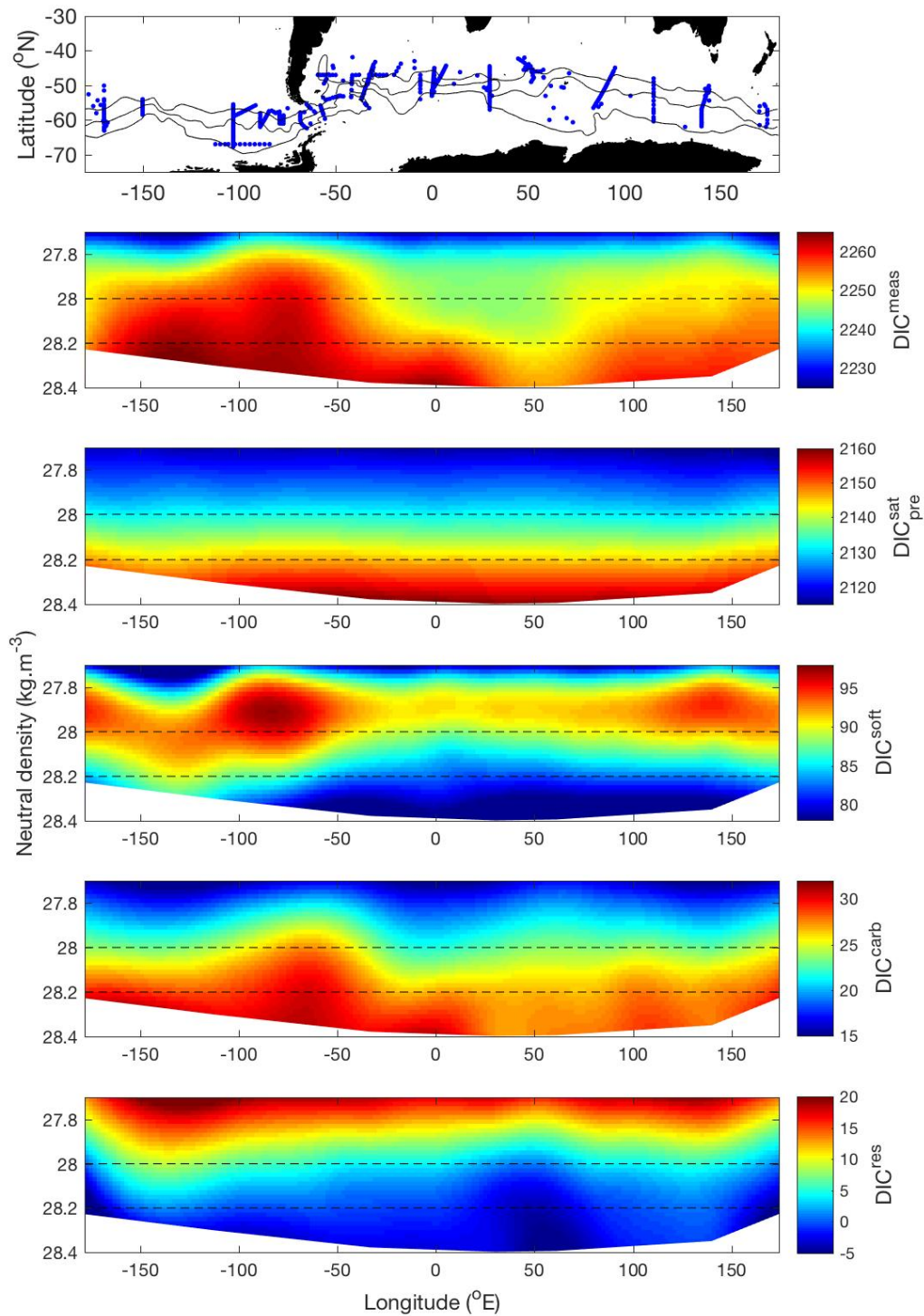


Figure 6.7: Zonal plots of DIC components in the densest waters of the ACC in units of $\mu\text{mol.kg}^{-1}$ (note different scales). Horizontal dashed lines represent the nominal boundaries between UCDW, LCDW and AABW. Station locations and frontal positions (Orsi et al., 1995) are shown in the top panel.

The zonal variability in deep water masses of the ACC is also evident in other carbonate system variables. Figure 6.8 shows the circumpolar variability of $f\text{CO}_2$, pH and the Revelle factor which are strongly influenced by the processes described above. UCDW has $f\text{CO}_2$ and Revelle factor maxima, and pH minima in the south Pacific and Australian sectors of the ACC as a result of the high DIC^{soft} component. Between -50°E and 150°E there is a deep pH maximum at roughly the boundary between UCDW and LCDW, with lower pH water above and below. This is the result of the combined effects of DIC and pressure; pH is reduced in the UCDW above by the high concentrations of DIC^{soft} and in the water below by increasing pressure.

In the Atlantic and Indian sectors the Revelle factor is lowest in LCDW. In the UCDW above the DIC:TA ratio is elevated by soft tissue remineralisation (DIC^{soft}) whereas in AABW below, DIC:TA is increased by high CO_2 solubility in the low temperature bottom water ($\text{DIC}_{\text{pre}}^{\text{sat}}$). Any anthropogenic carbon invasion into AABW would also increase the DIC:TA ratio and this probably contributes to the higher Revelle factor in AABW, relative to LCDW.

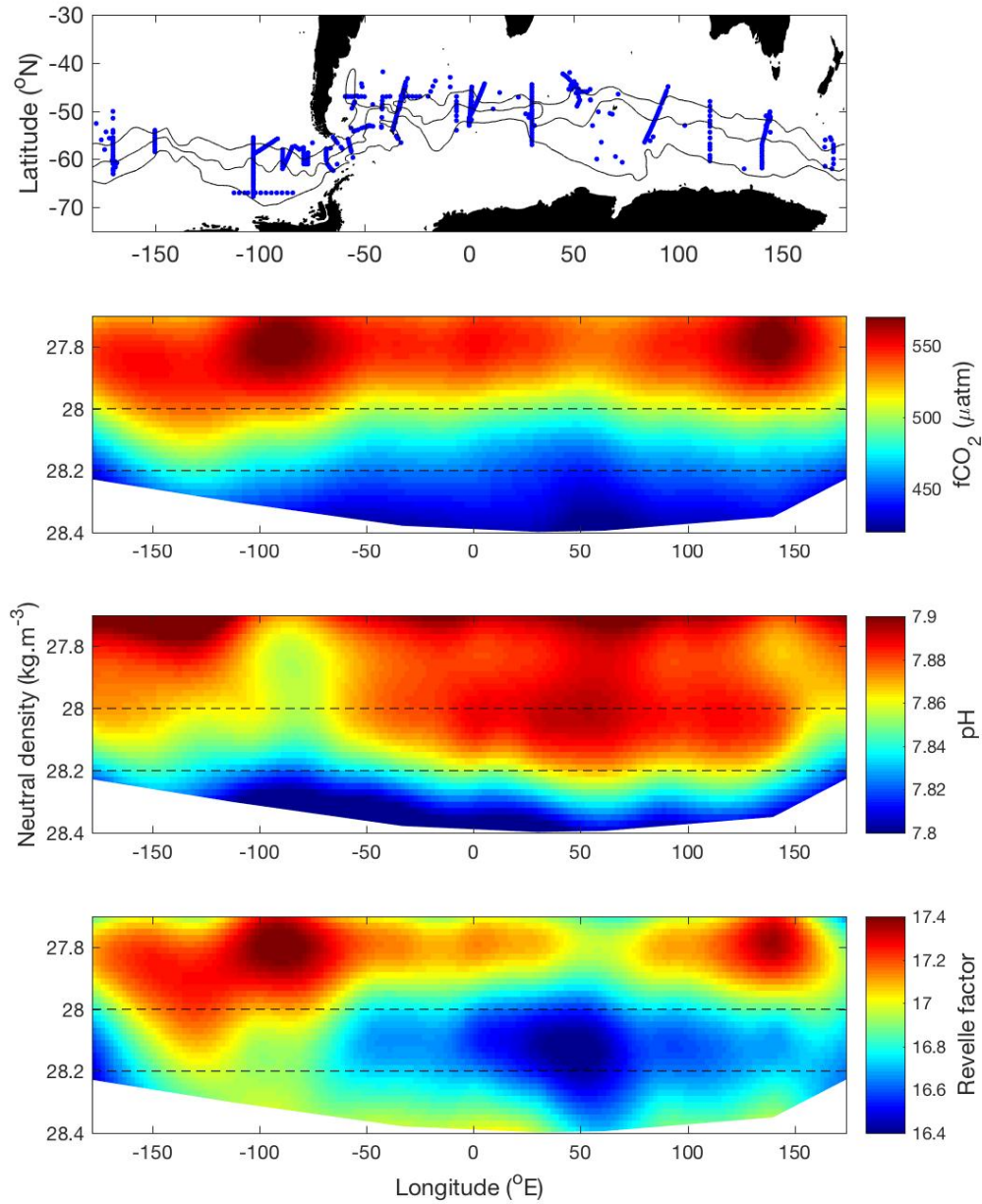


Figure 6.8: Zonal plots of $f\text{CO}_2$, pH and the Revelle factor in the densest waters of the ACC. Horizontal dashed lines represent the nominal boundaries between UCDW, LCDW and AABW. Station locations and frontal positions (Orsi et al., 1995) are shown in the top panel.

Recent studies have highlighted the regional variability in the physical drivers of the overturning circulation of the Southern Ocean. There is strong zonal asym-

metry in heat flux in the ACC (Tamsitt et al., 2016) and zonal asymmetry in the SAM, leading to zonal differences in wind strength and mixed layer depth (Sallée et al., 2010b). Regional variability in wind strength affects sea ice drift (Holland and Kwok, 2012) which redistributes freshwater northwards (Abernathey et al., 2016). In the ACC, both heat flux and freshwater flux contribute to the buoyancy flux which is important in driving the overturning circulation (Speer et al., 2000; Cerovecki et al., 2011). There is also strong regional variability in thermocline ventilation caused by bathymetry (Sallée et al., 2010a).

Regional variation in the physical drivers of the overturning circulation are likely to cause regional differences in the strength of the ocean CO₂ sink through differences in the upwelling of CDW and the subduction of mode and intermediate waters as well as differences in temperature and stratification affecting gas solubility and primary production (Bernardello et al., 2014). Assessing regional variability in the Southern Ocean CO₂ sink is made very challenging by the scarcity of observations but Landschützer et al. (2015) find that the recent reinvigoration of the sink, apparent throughout the Southern Ocean, south of 35°S, is driven by different mechanisms in different sectors. They suggest that the increased CO₂ uptake is dominated by anomalous downwelling in the Atlantic sector, reducing surface ocean CO₂, whereas in the Pacific sector surface cooling dominates, increasing the uptake of CO₂. A recent modelling study also finds zonal variability in the physical drivers of the Southern Ocean CO₂ sink and suggests that weaker upper ocean circulation in the Atlantic and Indian sectors of the Southern ocean accounts for most of the increase in CO₂ uptake during the 2000s (DeVries et al., 2017).

These studies highlight a growing awareness and understanding of the importance of regional variability on the Southern Ocean carbon sink. However, the focus remains on zonal differences in physical mechanisms such as variation in the amount of CDW upwelling. The data presented here demonstrate significant zonal variability in the carbonate system in the upwelling waters of the ACC. The implication of this zonal structure in the carbonate system is that, when it comes to air-sea CO₂ flux, all upwelling CDW is not equal. The zonal heterogeneity of

the chemistry of the upwelling water should therefore be considered as well as the zonal heterogeneity of the upwelling itself.

6.3.2 Temporal observations in SAMW

6.3.2.1 DIC components

Figure 6.9 shows that SAMW became cooler and fresher from the late 1990s to the early 2000s which is consistent with the changes on isopycnal surfaces observed by Bindoff and McDougall (2000), Aoki et al. (2005) and Böning et al. (2008). Cooling and freshening on isopycnal surfaces may result from an increase in precipitation, relative to evaporation (Wong et al., 1999), but may also result from the warming of subducting surface waters (Bindoff and McDougall, 1994, 2000). A recent study suggests that a significant part of the observed freshening may be caused by an increase in the northward wind-driven transport of sea ice (Haumann et al., 2016). TA decreased in the SAMW density class due to the decrease in salinity but DIC increased from the late 1990s to the early 2000s (Figure 6.9). The increase in DIC and decrease in TA cause an increase in the Revelle factor of about 0.75 over the period shown here. This indicates a reduction in the water's ability to buffer CO₂ uptake and therefore a decrease in the the CO₂ uptake capacity (Sabine et al., 2004; Egleston et al., 2010; Hauck and Völker, 2015).

The results of the carbon partitioning show that DIC^{res} is responsible for the majority of the increase in DIC (Figure 6.10), with an increase of about 12 $\mu\text{mol.kg}^{-1}$ over the two decades which is comparable to the rate of anthropogenic CO₂ increase previously reported in SAMW (Murata et al., 2007; Waters et al., 2011). Because we would not expect the disequilibrium of CO₂ to change significantly over this time period (Gruber et al., 1996; Lo Monaco et al., 2005), we can assume that the majority of the change observed in DIC^{res} represents an increase in anthropogenic CO₂. The same principle applies for the disequilibrium of oxygen, so, while the absolute values of AOU and DIC^{soft} may be overestimated, the change over time is likely to be more reliable as the uncertainty regarding disequilibrium cancels out. There is a small ($<0.5 \mu\text{mol.kg}^{-1}$) increase in DIC_{pre}^{sat} between 1995

and 2010 which corresponds to the decreasing temperature over this period. This increase is smaller than expected, given the known sensitivity of DIC to temperature of roughly $9 \mu\text{mol.kg}^{-1}$ for every 1°C (Sarmiento and Gruber, 2006). The contribution of the dissolution of carbonate minerals to DIC (DIC^{carb}) does not show any clear trend over the study period.

The circumpolar results shown here suggest an increase in the DIC^{soft} component of SAMW from the 1990s to the 2000s (Figure 6.10). While the change is small (roughly $5 \mu\text{mol.kg}^{-1}$), it is worth considering the possible causes of this increase. A change in the strength or position of the upper cell of the Southern Ocean circulation could affect the amount of DIC^{soft} in SAMW. DeVries et al. (2017) found a decrease in upper ocean circulation in the Southern Ocean from the 1990s to the 2000s which they suggested increased the Southern Ocean CO_2 sink over this period through decreased outgassing of carbon rich deep water. As well as decreased Antarctic upwelling, a weakened circulation leads to less mode water formation. A decrease in mode water subduction would allow phytoplankton to take up more CO_2 and decrease the export of preformed nutrients out of the surface layer, leading to an increase in the concentration of DIC^{soft} in SAMW (Lauderdale et al., 2013). The pentadal P^* results (Figure 6.11) show the same pattern as the DIC^{soft} component, with an increase in the proportion of regenerated nutrients from the 1990s to the 2000s. Due to the number of variables required to calculate the DIC components, the distribution of these results is quite sparse and unevenly distributed in time and space, with especially few data between 1990 and 1995 (Figure 6.12). Some or all of the observed increase in DIC^{soft} may therefore arise from a spatial sampling bias. However, the agreement of the P^* results - which require fewer variables than the DIC partitioning and therefore have more available data - supports the observed increase in DIC^{soft} . Data distributions for salinity, DIC and P^* are shown in Appendix G.

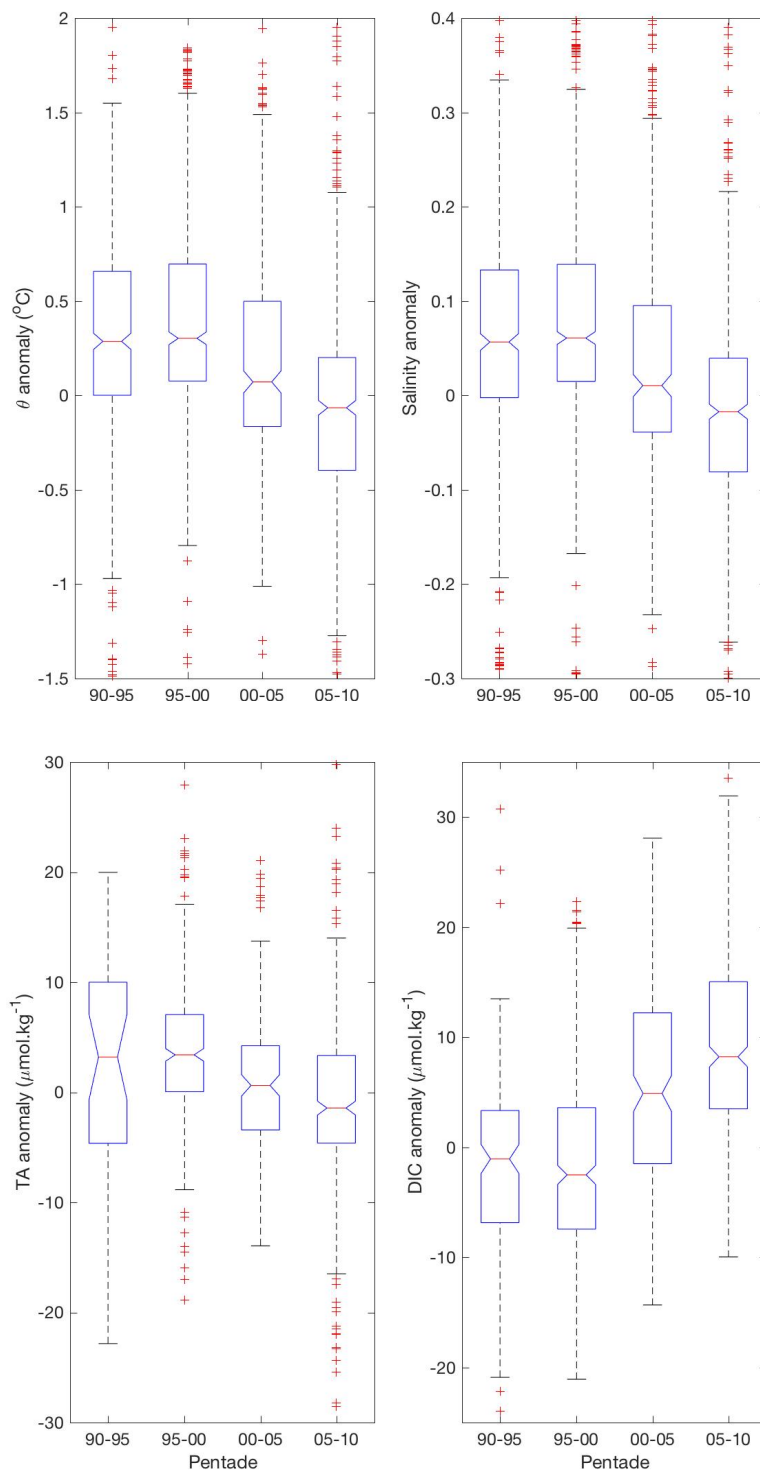


Figure 6.9: Pentadal box plots of potential temperature, salinity, TA and DIC anomalies in SAMW in the 1990s and 2000s.

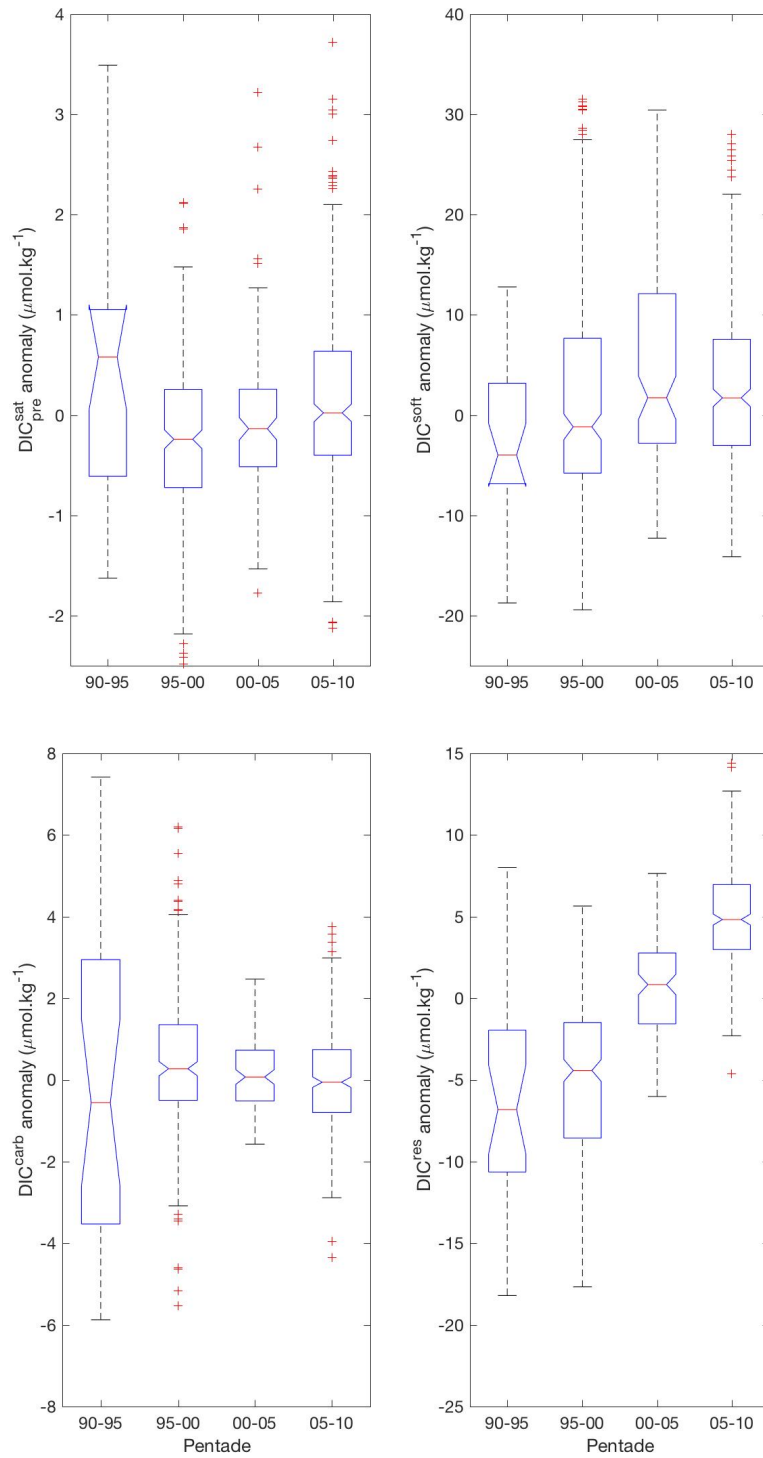


Figure 6.10: Pentadal box plots of DIC component anomalies in SAMW in the 1990s and 2000s.

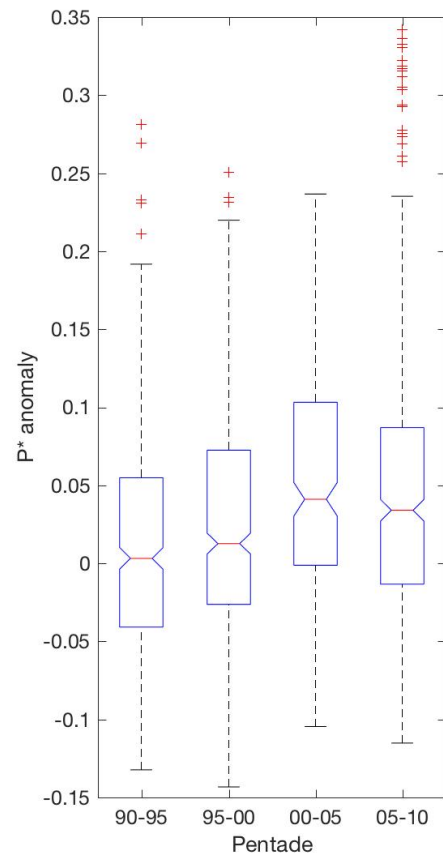


Figure 6.11: Pentadal box plot of P^* anomaly in SAMW in the 1990s and 2000s.

Contrary to DeVries et al. (2017), Waugh et al. (2013) and Ting and Holzer (2017) found a continued increase in overturning circulation strength from the 1990s to the 2000s with more recently ventilated SAMW in the later decade. They attribute this to increased northward Ekman transport, driven by stronger westerlies, connected to stratospheric ozone depletion (Thompson et al., 2011). A possible explanation for increased SAMW DIC^{soft} in a scenario with stronger circulation could be an increase in the amount of UCDW mixed into the SAMW density class. However, one would expect an increase in UCDW mixing to increase the salinity in SAMW which is not consistent with the observed freshening (Figure 6.9). It is possible that the freshwater forcing from above overrides the salinity increase from UCDW mixing while the UCDW mixing dominates changes in DIC^{soft} . It is also

possible that the observed freshening caused an increase in stratification which allowed more primary production but this is unlikely as phytoplankton in this region are largely iron limited and an increase in stratification would probably lead to less primary production (Deppeler and Davidson, 2017).

As well as calculating the age of subducted mode water, Ting and Holzer (2017) also investigated the location of this subduction. They found that the ventilation of mode water south of 40°S occurred less between the SB and the SAF, and more north of the SAF in the 2000s compared to the 1990s. This change was found to be coherent across the P16 (Pacific), A16 (Atlantic) and S3 (Australian) sections. This spatial change in SAMW subduction may affect the concentration of DIC^{soft} in the subducted water in two ways. Firstly, if this northward movement of the region of last ventilation represents an increase in the distance and time that this water spends at the surface, then it could allow more primary production, reducing preformed nutrients and increasing DIC^{soft} in the subducting water. Secondly, more northerly subduction may allow more primary production in the water because chlorophyll concentrations are generally higher north of the SAF than south of it, especially in the Indian and Pacific sectors between 90°E and 150°W (Figure 2 of Deppeler and Davidson (2017)), where many of these carbon partitioning data originate (Figure 6.12).

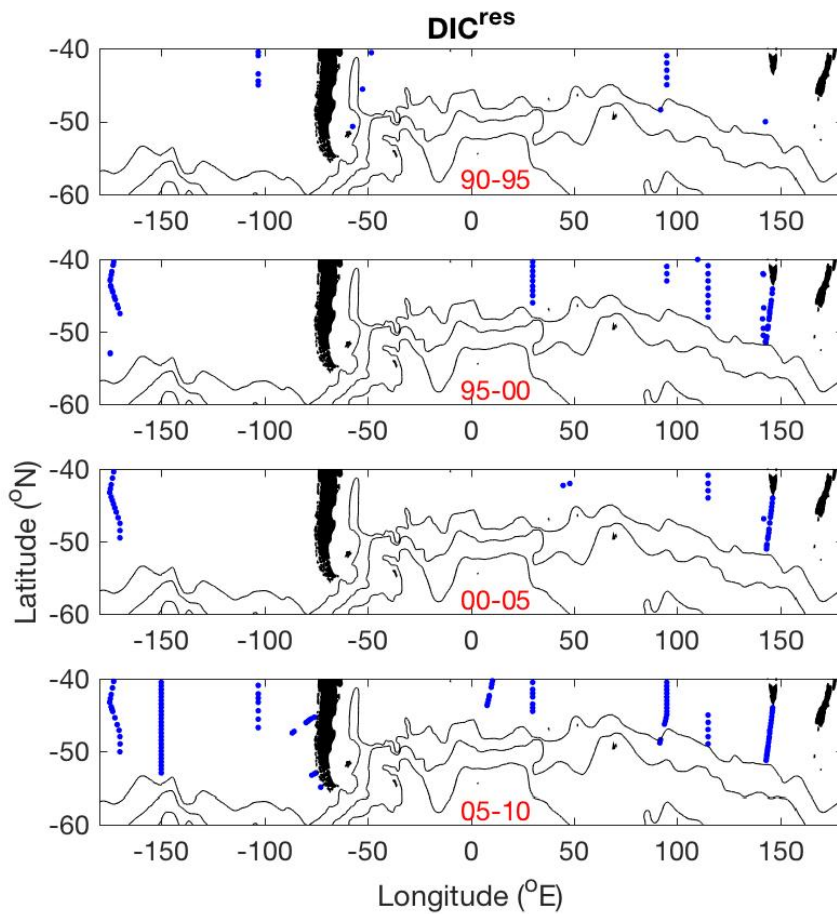


Figure 6.12: The circumpolar distribution of data points in SAMW used for DIC partitioning in each of the four pentades (time periods given in red). DIC partitioning required data flagged 'good' for DIC, TA, oxygen and phosphate.

6.3.2.2 Open questions

This study attempts to assess recent changes in the circumpolar components of DIC in SAMW and suggests that there may have been an increase in the DIC^{soft} component from the 1990s to the 2000s. However, due to the small magnitude of this change and limitations of the carbon partitioning calculations this trend remains very uncertain. The distribution of data in time and space is sparse, making it possible that temporal and spatial trends are being conflated. Data are particularly sparse in the first pentade (1990-1995), giving low confidence that data in this pentade are representative of the average value in circumpolar SAMW. Furthermore, there is likely to be significant regional variability in the processes affecting DIC in SAMW

(Murata et al., 2007; Álvarez et al., 2011) which are not captured by a crude amalgamation of circumpolar data.

To achieve a better understanding of both the temporal and spatial variability of DIC components in SAMW, similar analysis should be performed on specific repeat sections but, due to data availability, there are few sections for which this is possible (Figure 6.12). One of the few sections with sufficient repeat biogeochemical data is the SR3 section, south of Tasmania, where a recent study has investigated DIC components in the water masses of the Southern Ocean between 1995 and 2011 using a back calculation method (Pardo et al., 2017). They also found significant freshening in the SAMW layer and found the DIC increase in SAMW of about $1.1 \mu\text{mol.kg}^{-1}.\text{yr}^{-1}$ to be explained almost entirely by an increase in anthropogenic carbon ($0.92 \mu\text{mol.kg}^{-1}.\text{yr}^{-1}$). They found no significant trend in DIC^{bio} which represents a combination of the DIC^{soft} and DIC^{carb} terms used here. Similarly, when comparing data from cruises in the South Pacific in 1991 and 2005, Sabine et al. (2008) found very little change in DIC due to AOU.

The subduction of SAMW accounts for much of the Southern Ocean CO_2 uptake (Sabine et al., 2004; Gruber et al., 2009) but it remains difficult to predict how climatic changes have and will affect this important sink of atmospheric CO_2 because we do not fully understand the overall effect of several complex and interacting mechanisms such as the strength and location of upwelling and subduction, wind changes, stratification, buoyancy forcing, and primary production. A key part of this puzzle is how physical changes will affect the efficiency of the biological pump and therefore alter the DIC^{soft} component. This biological carbon uptake may become increasingly important as the buffer capacity of the surface ocean decreases (Hauck and Völker, 2015). It is therefore essential to continue to collect high quality, co-located biogeochemical data on repeat hydrographic sections so that changes in the DIC components can be quantified and regional variability can be investigated.

6.4 Conclusions

- There is strong zonal variability in the carbonate system in deep waters of the ACC caused by the inflow of NADW in the Atlantic sector and addition of UCDW with high DIC^{soft} in the Indian and Pacific sectors.
- This zonal variability means that upwelling CDW in different regions has different carbonate chemistry, affecting air-sea CO₂ flux. Given that the physical drivers of the overturning circulation are expected to vary regionally, zonal variations in the carbonate chemistry of upwelling waters should be considered when predicting future changes in the Southern Ocean CO₂ sink.
- SAMW TA decreased during the 1990s and 2000s, consistent with the observed freshening. Combined with the DIC increase, this caused an increase in the Revelle factor, reducing the CO₂ uptake capacity of SAMW.
- Most of the DIC increase in SAMW is attributed to rising atmospheric CO₂ concentration due to anthropogenic emissions. There is also weak evidence for a small increase in the amount of DIC from remineralised soft tissue which may be related to changes in the strength of overturning circulation and the location of ventilation.
- There is a continued need for high quality, co-located DIC, TA, oxygen and nutrient measurements on repeat hydrographic sections which cross the ACC, in order to better understand how the uptake of carbon by SAMW responds to climatic changes and increasing atmospheric CO₂.

Chapter 7

Discussion and future work

7.1 Overview

The aim of this thesis has been to build a better understanding of how carbonate system dynamics in the Southern Ocean affect the uptake of CO₂ from the atmosphere. Chapters 3 and 4 have focused on carbonate system processes in the surface waters of the seasonally sea ice covered, coastal Southern Ocean. The RaTS time series has been used to characterise the seasonal cycle of carbonate system variables in Ryder Bay, to quantify ocean-atmosphere CO₂ flux and to calculate the rates of processes affecting surface ocean DIC. Ryder Bay is found to be a net annual sink of atmospheric CO₂ (Section 3.3). This result supports the theory that the coastal Southern Ocean is a strong sink of atmospheric CO₂ (Arrigo et al., 2008) and may be disproportionately important for CO₂ uptake compared to the open ocean due to the high biological productivity of coastal regions. In summer, net photosynthesis is the dominant process affecting the carbonate system in the surface water in the bay, reducing DIC and $f\text{CO}_2$, making the ocean a sink of atmospheric CO₂ (Section 4.4.2). Melting glacial ice and sea ice, and less mixing with deeper water also reduce DIC. In winter, mixing with deeper, carbon-rich water and net heterotrophy increase surface DIC concentrations, resulting in pH as low as 7.95 and aragonite saturation states close to 1. No clear seasonal cycle of calcium carbonate precipitation/dissolution is observed but some short-lived features suggest that significant precipitation of calcium carbonate does occur in the Bay (Section

4.4.2). The observed variability demonstrates that changes in mixing and sea-ice cover significantly affect carbon cycling in this dynamic environment. Section 7.2, below, discusses possible future changes to the carbonate system in the seasonally sea ice covered Southern Ocean, in the context of the mechanistic understanding developed in Chapters 3 and 4. A simple model is proposed to investigate how ocean-atmosphere CO₂ flux will respond to future climatic forcings.

Chapters 5 and 6 have investigated the spatial variability in carbonate system in water masses of the Southern ocean using cruise datasets. In the Scotia Sea, LCDW becomes colder and fresher from Drake Passage in the west to the A23 section in the east, due to intense deep mixing. This freshening coincides with a decrease in TA in which causes an increase in $f\text{CO}_2$ and the Revelle factor and a decrease in pH and Ω (Section 5.3.3). This mechanism of TA exchange in the deep Scotia Sea may reduce the uptake of CO₂ by the high latitude Southern Ocean through the influence of LCDW on surface waters of the Weddell Sea. Measurements in the south of Drake Passage suggest that this region is important for the ventilation of upwelling UCDW. Around the circumpolar path of the ACC, strong zonal variability is observed in the carbonate system in CDW, caused mainly by zonal differences in the contribution of soft tissue remineralisation and calcium carbonate dissolution to DIC. In the Atlantic sector of the Southern Ocean, the addition of NADW lowers the DIC concentration. This low DIC signal is eroded around the course of the ACC by mixing with higher DIC waters above and below, including UCDW from the Pacific and Indian basins, containing high concentrations of remineralised organic carbon (Section 6.3.1). Section 7.3 discusses the possible implications of the observed variability for the Southern Ocean CO₂ sink and highlights research topics which may help to improve the representation of the Southern Ocean CO₂ sink in models.

Our ability to quantify and predict the Southern Ocean carbon sink, and to understand the mechanisms behind it remain hampered by a lack of data in the region. In particular, observations are very sparse during winter in the vast majority of the Southern Ocean (Bakker et al., 2016; Olsen et al., 2016) and the role of the high-latitude, seasonally sea ice covered Southern Ocean remains uncertain (Lenton

et al., 2013). Furthermore, the importance of productive coastal areas for the uptake of atmospheric CO₂ remains poorly constrained (Arrigo et al., 2008). Section 7.4 discusses the potential for future observations to address these knowledge gaps.

7.2 Surface ocean processes

7.2.1 The future of the carbonate system in Ryder Bay

Large-scale climatic changes are likely to affect carbonate system processes in the future, thereby altering the ocean CO₂ sink. Given the climatic forcings affecting the waters of the WAP shelf, what can we predict about how the carbonate system in Ryder Bay will change and are these mechanisms scaleable to a wider geographical area?

- *Decreasing winter sea ice cover.* A reduction in ice cover on the WAP would modify ocean heat content and circulation, increasing deep mixing and possibly further reducing ice cover (Venables and Meredith, 2014). Increased winter mixing would deliver more CDW to the surface, increasing surface ocean DIC and $f\text{CO}_2$, thereby reducing pH and Ω and increasing the flux of CO₂ from the ocean to the atmosphere. Winters with less ice cover permit more air-sea gas transfer (Section 3.3.1), further increasing winter out-gassing of CO₂ to the atmosphere. Several studies have found primary production to be strongly connected to sea ice dynamics on the peninsula (Vernet et al., 2008; Montes-Hugo et al., 2009; Ducklow et al., 2013; Venables et al., 2013), which suggests that decreasing winter ice cover would affect carbon cycling in the spring and summer. Less ice melt in spring will also result in higher $f\text{CO}_2$ at the surface (Section 4.4.2), delaying the transition from the ocean being a source to a sink of atmospheric CO₂ and resulting in a weaker net annual uptake of atmospheric CO₂ by the ocean.
- *Increased glacial melt.* Changes to the freshwater budget on the WAP such as increased glacial melt (Cook et al., 2005) and increased precipitation (Thomas

et al., 2008) are likely to impact the coastal carbonate system, both directly and indirectly through changes to stratification, turbidity, primary production and sea ice cover (Dierssen et al., 2002). An increase in the volume of glacial meltwater delivered to the coastal ocean of the WAP in spring would increase stratification, potentially increasing phytoplankton growth (Venables et al., 2013) and thereby reducing surface DIC and CO_2 . Increased delivery of freshwater from glacial melt and subsequent stratification would also lower surface $f\text{CO}_2$ in spring, increasing the uptake of atmospheric CO_2 (Section 4.4.2). Although increasing glacial melt would have most impact in near-shore regions with high glacial run-off, such as Ryder Bay, there may also be significant influences on primary production much further offshore (Dierssen et al., 2002).

- *Increased wind stress.* An increase in wind stress may lead to an increase in upwelling of CDW, supplying more inorganic carbon to the surface ocean and thereby potentially weakening the strength of the Southern Ocean CO_2 sink. Higher surface water DIC concentrations in Ryder Bay in the spring of 2013 do appear to be driven by an increase in mixing with deeper, carbon-rich water (Section 4.4.2). This results in more release of CO_2 to the atmosphere and lower pH and Ω . The relationship between wind direction and ice in Ryder Bay highlights that, as well as large scale effects on ocean circulation, changes in wind strength and direction may have very localised effects in coastal areas (Section 4.4.2). Finally, an increase in wind stress would increase gas transfer velocity and thereby enhance air-sea CO_2 flux although the direction of the flux is determined by the CO_2 concentration gradient between water and air.
- *Atmospheric temperature.* The observed atmospheric warming on the West Antarctic Peninsula during the second half of the 20th century (Turner et al., 2005) resulted in increased summertime surface ocean temperatures (Meredith and King, 2005). As well as affecting the carbonate system indirectly through sea ice and stratification, an increase in surface ocean temperature

influences the carbonate system directly, by reducing the solubility of CO₂ in surface waters, weakening the ocean sink of atmospheric CO₂. However, this warming trend has not been evident since the late 1990s, suggesting that decadal-scale variability on the peninsula is driven more by natural atmospheric variability than global temperature increase (Turner et al., 2016). The impact of changing temperature on the carbonate system on the WAP shelf therefore remains uncertain.

- *Increasing atmospheric CO₂*. The continued increase in the concentration of CO₂ in the atmosphere in contact with the surface water of the Southern Ocean (Dlugokencky et al., 2014) will act to increase the amount of CO₂ taken up by the ocean each year. However, with continued CO₂ uptake, the buffering capacity of the surface ocean may decrease, slowing the increase in uptake (Sabine et al., 2004).

Overall, the observations presented here suggest that reduced winter ice cover and increased upwelling of carbon-rich deep water in future would reduce the rate at which the region takes up atmospheric CO₂. Furthermore, a reduction in the spring phytoplankton bloom in Ryder Bay following winters with reduced sea ice cover has been found (Venables et al., 2013) and it has been suggested that a continued reduction in WAP sea ice cover is likely to lead to reduced phytoplankton blooms in the region. A reduction in winter sea ice would therefore not only increase winter outgassing but would also reduce summer uptake of CO₂ by the ocean, further reducing the net annual CO₂ sink. However, the combined effect on the carbonate system of the mechanisms outlined above is difficult to predict as they do not act in isolation and their relative importance is likely to vary with time and space. Modelling of the carbonate system in Antarctic coastal waters would help to predict how this complex region will respond to climatic forcings.

7.2.2 A RaTS-based carbonate system model

The RaTS time series presents an opportunity to constrain a simple model of the carbonate system in Ryder Bay and an outline of the possible structure of such a model is suggested here. Initially, the model would use existing data from the RaTS time series to attempt to reproduce the observed seasonal cycles of DIC and TA. Eventually the model could be used to quantitatively investigate how the ocean uptake of CO₂ would change given certain forcings such as increased upwelling of CDW, increased wind speed, decreased ice cover or a combination of these factors.

Figure 7.1 shows a schematic of a possible first version of this model. The starting conditions would be determined by measurements from a point in the time series. The starting variables would be: mixed layer depth, DIC concentration, TA concentration, nitrate concentration and the percentage contributions of the three end members to the mixed layer. For each time step the model would then calculate the DIC and TA in the mixed layer, per unit area, as follows. Numbers correspond to the numbers in Figure 7.1.

1. The mixed layer depth would be defined, giving the volume of the box.
2. Any change in the percentage contribution of CDW, sea ice and meteoric water would be used to calculate the change in DIC, TA and nitrate caused by the changing contributions of these endmembers. Initially, while attempting to reproduce observations, the change in percentage contributions and the mixed layer depth would be independent. However, when developing the model to run with test scenarios, the endmember contributions and mixed layer depth would be coupled because an increase in mixed layer depth necessarily increases the proportion of CDW in the box.
3. The net influence of photosynthesis and respiration on DIC and TA would be calculated from the difference between measured nitrate and endmember-normalised nitrate. This makes the model dependent on nitrate data and prevents the biology from varying if different physical forcings are applied. Once observed DIC and TA can be recreated using photosynthesis/respiration cal-

culated from nitrate then a more advanced biology component should be introduced which is independent of nutrient measurements and is allowed to vary based on day length, MLD and nutrient delivery by endmembers.

4. Air-sea CO_2 flux would be calculated from modelled DIC and TA, and measured ice cover, windspeed and atmospheric CO_2 concentration.

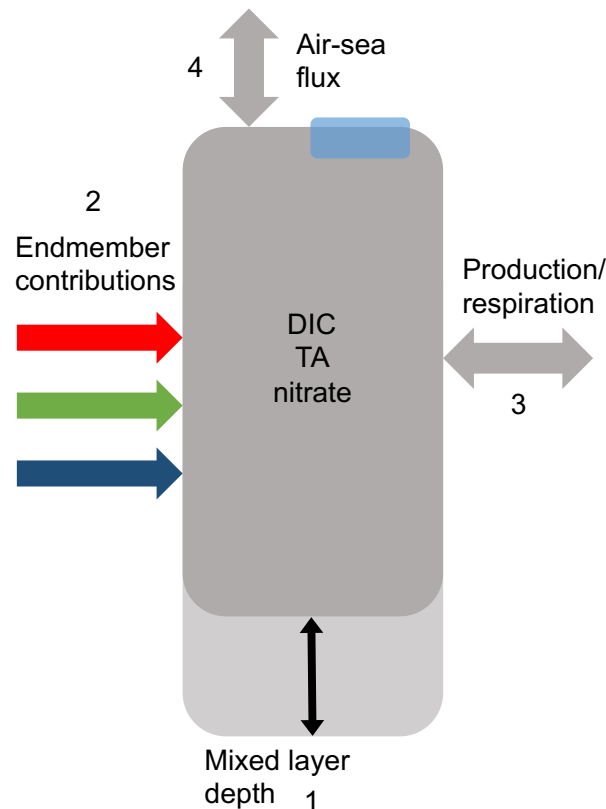


Figure 7.1: A schematic of a simple model to investigate the effect of physical forcings on the ocean CO_2 sink in Ryder Bay.

7.2.3 Wider applicability

It is expected that the consumption of DIC in summer by primary production in Ryder Bay is higher than would be found farther offshore due to near-shore glacial influence on stratification and nutrient delivery. Marguerite Bay, adjoining Ryder Bay, has persistently higher chlorophyll concentrations than other areas of the WAP (Marrari et al., 2008) and summer studies have found higher oxygen saturations, lower CO_2 saturations and higher net community production in Marguerite Bay

than on the rest of the WAP shelf (Carrillo et al., 2004; Tortell et al., 2015), suggesting that the net respiration and air-sea CO₂ flux rates calculated here are not scalable to the WAP shelf as a whole. Part of this spatial gradient in primary production is caused by differences in iron supply to the surface ocean. Sea ice melt, glacial meltwater and upwelling CDW have all been found to be important sources of iron to primary producers in the coastal Southern Ocean (Sedwick and Ditullio, 1997; Gerringa et al., 2012; Annett et al., 2015). Whereas future changes in iron supply are unlikely to have a significant effect on production in Ryder Bay, as it is not considered to be iron limited (Venables et al., 2013; Annett et al., 2015), they may affect production in areas of the open Southern Ocean which are iron limited (de Baar et al., 2005; Jickells et al., 2005). As well as investigating possible changes to the carbonate system through time, the simple model suggested above could also be used to address such spatial variability in the carbonate system, thereby extending the mechanistic understanding gained in Ryder Bay to a wider geographical area. For example, the model could be run for different spatial grid boxes on the WAP shelf, with glacial iron input and stratification decreasing with distance offshore.

7.2.4 Changes in SAMW carbon uptake

Temporal changes in SAMW were investigated in Chapter 6. TA decreased in this water mass during the 1990s and 2000s, consistent with the decrease in salinity. The concentration of DIC increased which, combined with the decrease in TA, caused an increase in the Revelle factor, reducing the CO₂ uptake capacity of this water mass. Most of the observed DIC increase in SAMW is attributed to rising atmospheric CO₂ concentration due to anthropogenic emissions. There is also weak evidence for a small increase in the amount of DIC from remineralised soft tissue which may be related to changes in the strength of overturning circulation and the location of ventilation (Section 6.3.2). It is still poorly understood how changes in the strength and location of ventilation, temperature, and ocean acidification will affect the DIC^{soft} component in SAMW and therefore the strength of the biological

pump. Considering the importance of SAMW for CO₂ uptake (Tanhua et al., 2017) and the potential for increased organic matter production in this water mass (Sigman et al., 2010), this remains an important open question. The observations used here do not permit an unequivocal identification of a temporal trend in DIC^{soft} on a circumpolar scale due to spatial sampling biases and possible regional variability. Continued biogeochemical measurements are needed in order to better understand how the uptake of carbon by SAMW responds to climatic changes and increasing atmospheric CO₂ (Section 7.4).

7.3 Deep water mass variability

7.3.1 Implications of zonal carbonate system variability

There is a growing awareness of zonal variations in the Southern Ocean overturning circulation and how this might affect the ocean sink of atmospheric CO₂ in different regions (Sallée et al., 2012; Landschützer et al., 2015; Tamsitt et al., 2016; DeVries et al., 2017). However, as well as variability in the physics of the overturning circulation, there is also significant zonal variation in the carbonate chemistry of deep waters of the ACC (Chapter 6). For example, CDW which upwells south of the Polar Front in the Atlantic sector of the Southern Ocean is likely to have lower DIC, *f*CO₂ and Revelle factor and higher pH than that which upwells in the southeast Pacific sector. The partial pressure of CO₂ observed at the surface (Takahashi et al., 2012; Landschützer et al., 2014) is therefore affected by both the amount of upwelling of old, carbon-rich CDW and also the carbonate chemistry of this upwelled water. This zonal variability may drive significant zonal variability in the ocean-atmosphere flux of CO₂, especially during winter when mixing with deep water strongly influences surface ocean pCO₂. The scarcity of wintertime surface ocean CO₂ observations at high latitudes (Bakker et al., 2016) makes this hard to verify.

The zonal variability in the carbonate system in upwelling deep water is also likely to have implications for calcifying organisms in the Southern Ocean such as pteropods. Calcifiers in regions where the upwelling CDW has a lower pH and Ω

aragonite, such as the WAP shelf, may be more vulnerable to future decreases in pH and saturation state. However, the seasonal cycle in Ω aragonite experienced by these organisms is large compared to changes due to anthropogenic ocean acidification, suggesting that pteropods may be able to endure large changes in Ω aragonite (McNeil et al., 2011). The zonal variability described here is consistent with a data-based estimate of pH in the Southern Ocean which shows lower pH south of the Polar Front in the Pacific sector than in the Atlantic sector of the Southern Ocean during winter (McNeil and Matear, 2008).

7.3.2 Regional modelling challenges

The current generation of global coupled ocean-atmosphere general circulation models predict stronger and poleward shifted westerly winds around the Southern Ocean and increased upwelling of CDW in the latter half of the twenty first century (Meijers, 2014). Given the influence of CDW upwelling on surface ocean CO_2 in the high latitude Southern Ocean, and the predicted increase in upwelling, accurate representation of the carbonate system in this water mass by models is necessary in order to predict changes in the Southern Ocean CO_2 sink. A comparison of air-sea CO_2 fluxes simulated by models of the Coupled Model Intercomparison Project phase 5 (CMIP5) with observation-based estimates (Frolicher et al., 2015), showed that the modelled air-sea CO_2 flux is too large in the southeast Pacific sector of the Southern Ocean and in the south of Drake Passage close to the Antarctic peninsula, and is too small in the Atlantic sector of the Southern Ocean (Figure 7.2). These regional biases in modelled air-sea CO_2 flux are consistent with the models not accurately representing the observed zonal variability of DIC in CDW (Chapter 6) and therefore overestimating the DIC in CDW upwelled in the Atlantic sector and underestimating the DIC in CDW upwelled in the southeast Pacific sector. It would be instructive to compare the observed zonal variability in the carbonate system with the model fields from CMIP5 models, given the hypothesis: regional biases in modelled air-sea CO_2 flux south of the Polar Front are caused by inadequate representation of zonal variability in the carbonate system in CDW.

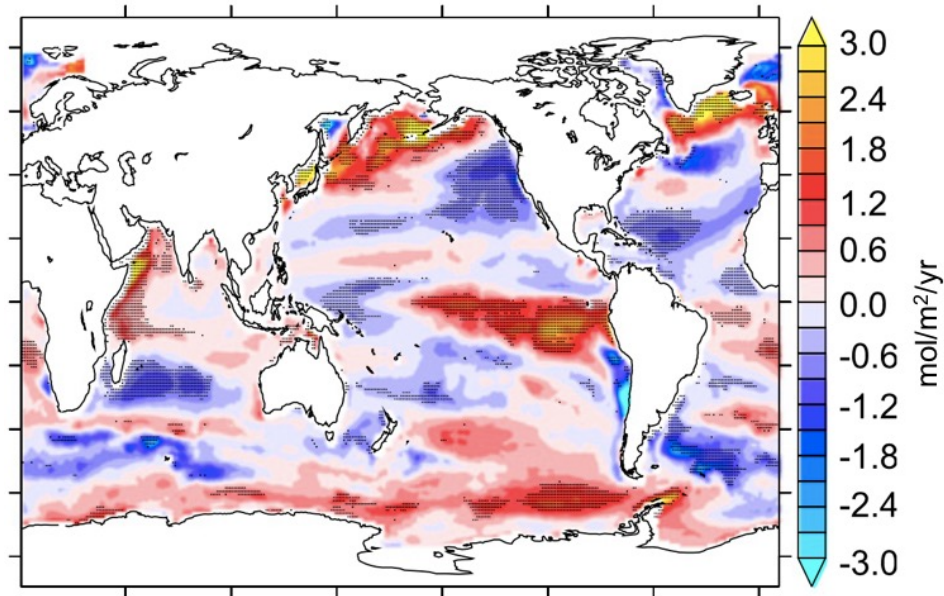


Figure 7.2: A comparison of modelled and observed air-sea CO_2 flux, taken from Frolicher et al. (2015). The modelled flux is the mean of several CMIP5 models and the observations are from Landschützer et al. (2014), based on a neural network approach. Red areas indicate regions where models calculate a greater ocean uptake of CO_2 than observed. Stippled areas represent regions where at least 82% of the models share a common positive or negative bias.

One of the main causes of the observed zonal variability in deep waters of the ACC is the inflow of NADW which affects carbonate chemistry in the South Atlantic sector of the Southern Ocean (Section 6.3.1). The Scotia Sea represents the last point in the ACC before this NADW influence is apparent. CDW in the Drake Passage and Scotia Sea therefore exhibit higher DIC and $f\text{CO}_2$ concentrations than regions downstream, outside of the Scotia Arc. The high DIC concentration in upwelling CDW in this region, combined with strong mixing processes (Meredith et al., 2003; Provost et al., 2011; Tamsitt et al., 2017), make Drake Passage and the Scotia Sea important locations for the ventilation of CDW and the release of CO_2 to the atmosphere (Section 5.3.3). The region downstream of the tip of the Antarctic Peninsula exhibits the highest overestimation of air-sea CO_2 flux by CMIP5 models anywhere in the Southern Ocean (Figure 7.2). This is possibly partly caused by the zonal variability in CDW DIC, discussed above. It is also likely that models overestimate air-sea flux here because they do not represent eddies which are abundant in

this area and are important for ventilating CDW. This highlights that the inclusion of eddies in future large scale models is necessary for the accurate representation of air-sea CO₂ fluxes in the Southern Ocean.

7.4 Future observations

In order to better understand the mechanistic connections between climatic changes and carbonate system processes it is crucial that high quality, co-located biogeochemical measurements continue to be made in the Southern Ocean. The repetition of existing hydrographic sections will allow temporal changes in the carbonate system in the water masses of the ACC to be assessed. The measurement of multiple biogeochemical variables (DIC, TA, oxygen, macronutrients), as well as physical properties, will allow the influence of changes in biological processes to be investigated, as well as the influence of changes in the overturning circulation. Spatial variability in physical and biological properties and processes requires that temporal changes are investigated on a regional or basin scale, necessitating the maintenance of multiple, meridional hydrographic sections.

The use of autonomous instrumentation is able to provide much denser temporal and spatial sampling than traditional cruise measurements and, crucially, can provide data during the austral winter, when ship-based observations are very limited. The development of floats with biogeochemical sensors (oxygen, nitrate, pH, transmission, and fluorescence) such as those deployed by the Southern Ocean Carbon and Climate Observation and Modeling (SOCCOM) program will hopefully vastly improve our understanding of processes affecting the carbonate system in the upper 2000 m of the open Southern Ocean. These floats still require calibration from ship-based measurements but, the accuracy of biogeochemical sensor data is improving and approaching that of datasets such as GLODAP (Johnson et al., 2017). However, as only one carbonate system variable (pH) is measured by these floats, full characterisation of the carbonate system relies on algorithms to estimate TA (Williams et al., 2017). Uncertainties in this TA estimation and that of phosphate

and silicate concentrations (Section 2.3.3) adds uncertainty to calculated carbonate system variable estimates.

The marginal ice zone remains very difficult to observe and its net impact on ocean-atmosphere CO₂ flux remains uncertain. Autonomous instruments designed to measure biogeochemical variables in the surface ocean during ice formation and melting may help to elucidate the relative timing and importance of processes affecting the carbonate system such as stratification, primary production and ikaite formation. Ice-tethered profilers (Toole et al., 2011), developed for use in the Arctic, could be a starting point for similar platforms in the Antarctic marginal ice zone. In particular, the relative timing of ice melt and primary production is likely to be critical for determining the direction of the CO₂ flux across the air-sea interface (Bakker et al., 2008). Deployment of autonomous systems in different areas may improve our understanding of this poorly sampled, transitional period in the seasonal cycle. Laboratory sea ice chambers can also help us to understand mechanisms in seasonally sea ice covered waters. Specifically, the controlled chamber environment may allow better quantification of air-ice CO₂ fluxes and the effect of sea ice on air-sea CO₂ fluxes.

Time series datasets are invaluable for characterising temporal changes in the marine environment and developing a process-based understanding of these changes. The carbonate system time series in Ryder Bay has already provided valuable insights into carbonate system processes in seasonally sea-ice covered coastal waters and will continue to do so. Observations of seasonal and interannual variability, and potentially, longer term trends will continue to improve our mechanistic understanding of processes governing ocean-atmosphere CO₂ flux in this region and may aid the development and evaluation of models. Sampling for DIC and TA in Ryder Bay has been ongoing since December 2010 and preparation for the next field season is underway.

Appendix A

Ocean circulation and acidification demonstration

I have developed a physical model to demonstrate ocean acidification and ocean circulation to students, school children and the general public. The following description will give suggestions on how to carry out the demonstration, including resources and the explanation of the key science concepts. The demonstration takes a minimum of 20 minutes to complete.

A.1 Resources

- Large, clear glass or clear plastic tank with an open top
- Clear beaker or bottle
- Drinking straws
- Pure water (MQ, distilled or reverse osmosis)
- Bottle with bung and tube
- Plastic container with flat bottom
- Clamp stand
- Pasteur pipettes
- Light box or white background
- Print out of images to aid explanation. Examples shown below
- approximately 0.2 M NaOH solution*
- Bromothymol blue pH indicator*

- Dry ice*

*The appropriate risk assessments should be carried out for these materials and they should be handled accordingly.

A.2 Part One - CO₂ and pH

Half fill a beaker with tap water and add a few drops of bromothymol blue. The water should turn blue-green (depending on the pH of the local tap water). Breathe through a straw into the water, bubbling air through the solution. After a short period of blowing, the water should start to turn green-yellow. Explain that the bromothymol blue indicates the pH and show a picture of its colour at different pH (Figure A.1). Explain that the CO₂ in our breath dissolves into the water and makes the water more acidic.



Figure A.1: Bromothymol blue indicator in waters of different pH.

A.3 Part Two - Ocean acidification

Before starting the demonstration, fill the tank with pure water and add several mL of bromothymol blue. The more indicator you add, the stronger the colour and the clearer the demonstration. The reason for using pure water rather than tap water is that the carbonates in the tap water buffer the pH changes and prevent part three of the demonstration working. With a more advanced group you could discuss this buffering. Pure water at equilibrium with the atmosphere is slightly acidic, making

the indicator green-yellow. For the demonstration we need a higher pH (closer to the ocean) so that the water starts off blue. Add a few mL of NaOH solution and stir until the water in the tank is a rich blue colour. Leave the water to settle while you carry out part one of the demonstration.

Explain that the concentration of CO₂ in the atmosphere is rising rapidly, largely due to man's activities. Show the Keeling curve (Figure A.2) and discuss (the causes of atmospheric CO₂ increase, seasonal cycles etc). You could also put this modern increase in context of the ice core record and point out that current atmospheric CO₂ is higher than that observed at any point in the last 800 thousand years. Explain that about a quarter of emissions are taken up by the oceans on an annual basis, reducing global warming. Draw people's attention to the very surface of the water - it should be blue, like the rest of the tank.

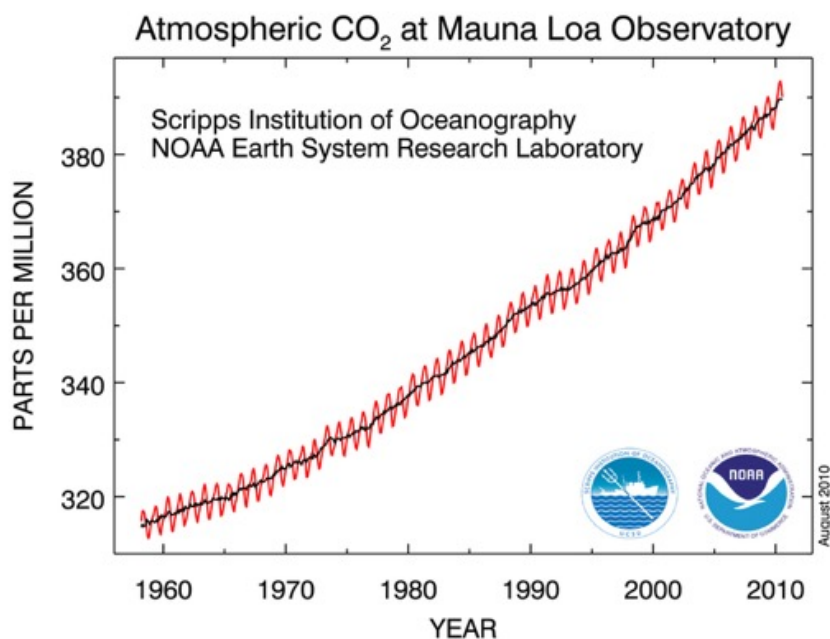


Figure A.2: Time series measurements of atmospheric CO₂ from Hawaii (Keeling et al., 2005).

Put a few granules of dry ice into a bottle and add a splash of water (this helps the dry ice to sublimate). Put the bung in the bottle and use the tube to direct the

gaseous CO_2 into the headspace of the tank - the model atmosphere above the model ocean (Figure A.3). This simulates a massive increase in atmospheric CO_2 . Fill the headspace of the tank with CO_2 , being careful not to disturb the water surface. As CO_2 is denser than air it will sink to the water surface and does not need to be directed there. Explain that dry ice is pure CO_2 .

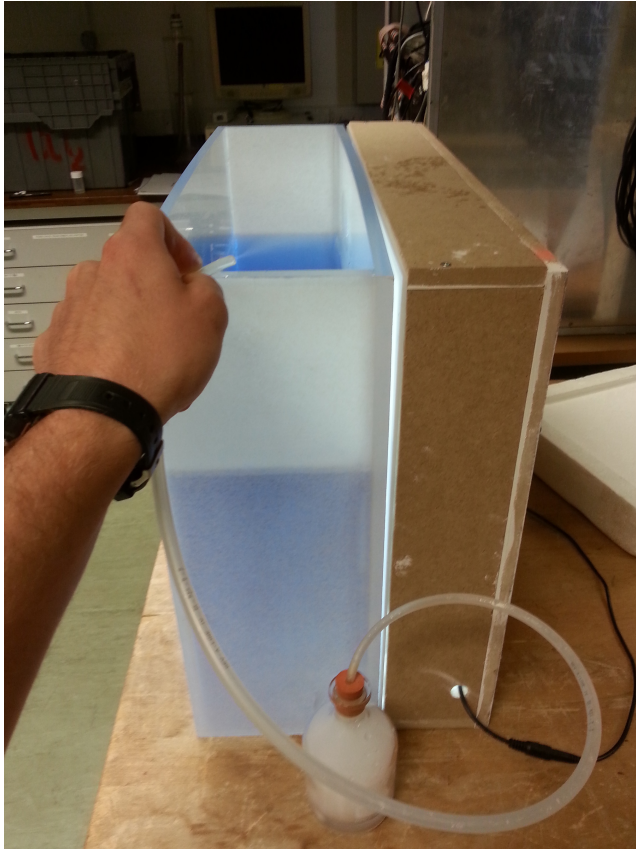


Figure A.3: Increasing the CO_2 concentration in the model atmosphere using dry ice.

Get everyone to look closely at the water surface. A very thin but distinct yellow surface layer will develop (Figure A.4). You need to have the water surface at eye level so people may have to bend down. Consider whether wheelchair users will be able to get their eyes level with the water surface.

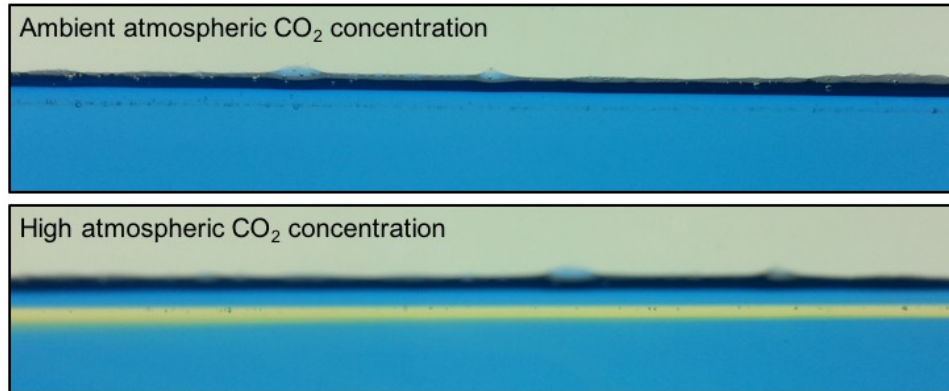


Figure A.4: The surface of the model ocean before (top panel) and after (bottom panel) increasing the CO₂ concentration in the overlying air.

Discuss the observed acidification of the model surface ocean. You could show time series data which demonstrates this process occurring in the real surface ocean (Figure A.5). Talk about the possible implications for marine calcifiers and food-webs (Figure A.6).

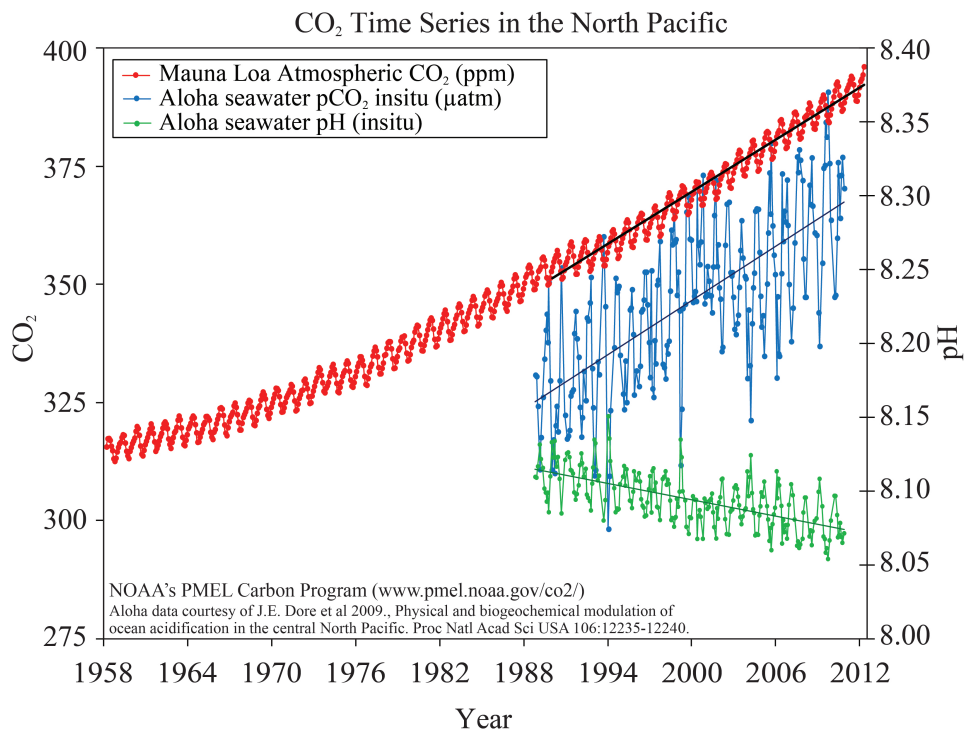


Figure A.5: Observations of atmospheric CO₂, seawater CO₂ and seawater pH from the North Pacific (Dore et al., 2009).



Figure A.6: Examples of marine calcifiers: warm and cold water corals, pteropod, coccolithophores, lobster and mussels.

A.4 Part Three - Deep water formation

Put a couple of handfuls of dry ice into the flat-bottomed container. Do not tighten the lid. Let people briefly feel how cold the container is and then suspend it about 5mm above the water surface at one end of the tank. Do not let it touch the water. Explain that this represents atmospheric cooling of the surface ocean at the polar end of the model ocean. Explain that the differences in temperature and salinity in the ocean cause density gradients which lead to movement of water. Show a schematic of the global overturning circulation, or ocean conveyor belt (Figure A.7).

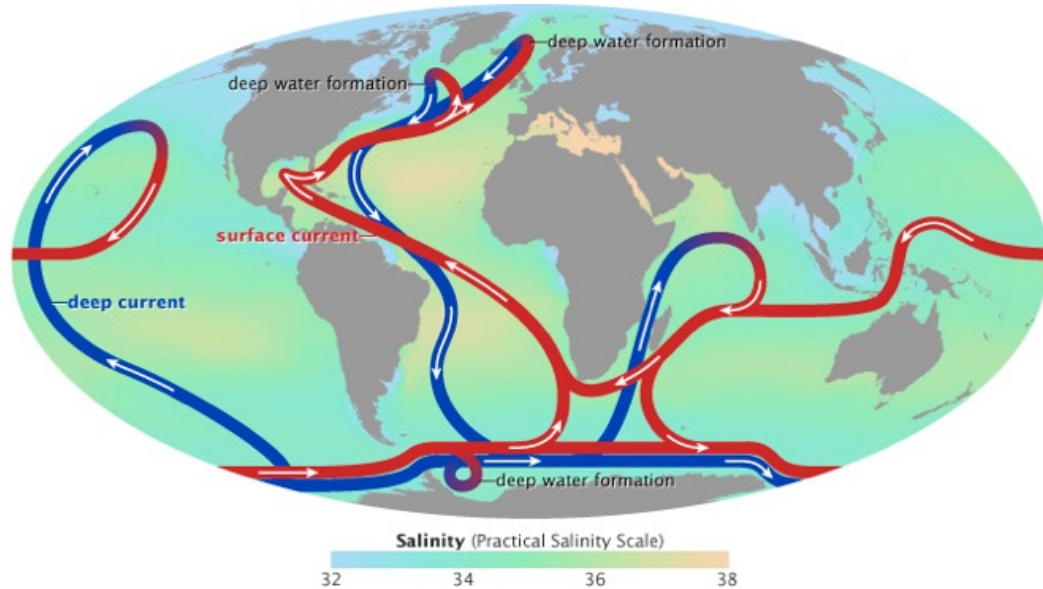


Figure A.7: Schematic of the global ocean conveyor belt (NASA).

The strong cooling forcing at the 'polar' end of the tank causes high CO_2 surface water to sink and the pH indicator acts as a tracer, allowing people to see deep water being formed in the model ocean (Figure A.8). Discuss that this sinking, cold, CO_2 rich bottom water transports CO_2 away from contact with the atmosphere for hundreds of years, slowing the increase in atmospheric CO_2 . After a few minutes you can remove the dry ice container and deep water formation will cease, leaving a stratified ocean with cold, yellow, deep water with blue water overlying it and a thin yellow layer at the surface. Leave time for discussion and questions.

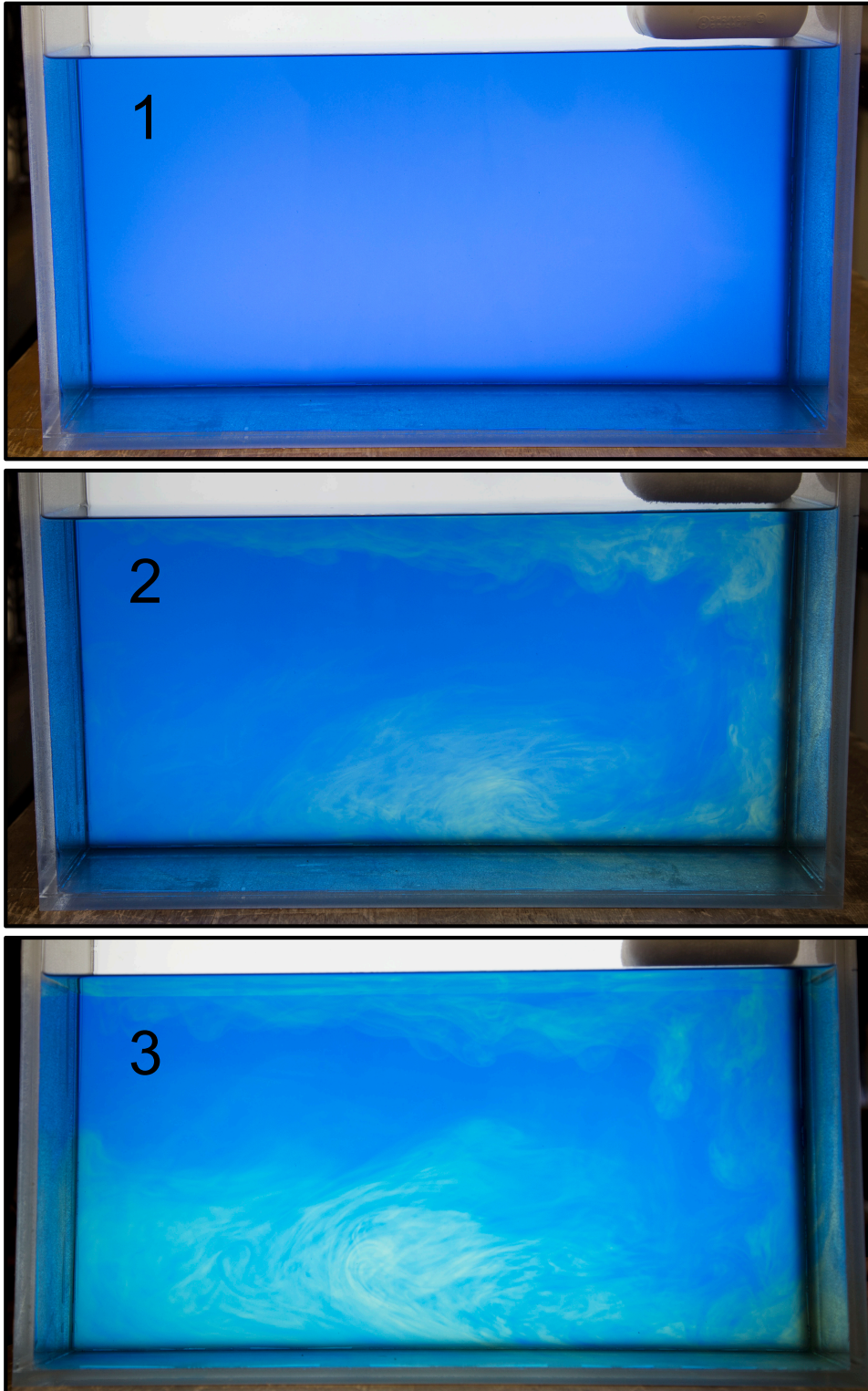


Figure A.8: The formation of deep water in a model ocean. Panel 1 shows the tank before cooling forcing is applied. Panel 2 shows cold, deep water being formed at the right hand side of the tank, transporting high CO_2 , low pH water to the bottom of the tank. Panel 3 shows the tank after several minutes of cooling forcing. Cold, low pH water fills the bottom of the tank. Photos: Rob Harber.

Appendix B

The dynamic height of ACC fronts on DP and A23 sections

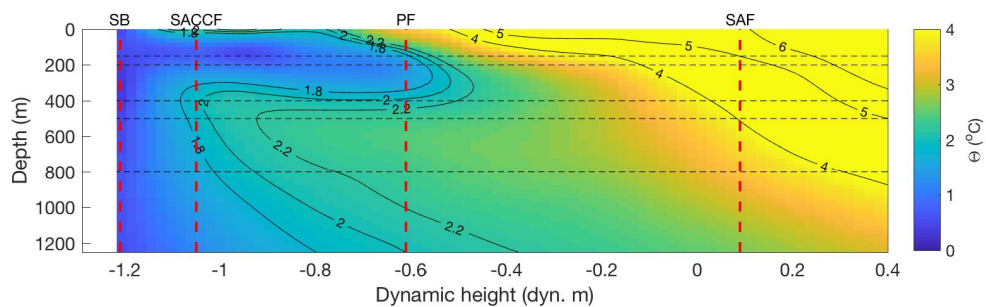


Figure B.1: Validation of dynamic height frontal definitions in Drake Passage. Potential temperature and depth contours used in the literature for defining frontal positions are shown (Section 1.3.1). The SB definition was chosen as the minimum dynamic height on DP to allow comparison with the A23 section.

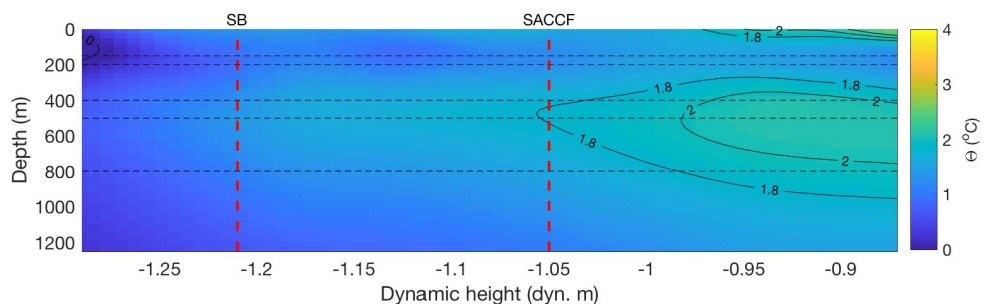


Figure B.2: Validation of dynamic height frontal definitions on the A23 section. Potential temperature and depth contours used in the literature for defining frontal positions are shown (Section 1.3.1). The SB definition was chosen as the minimum dynamic height on DP to allow comparison with the A23 section.

In Chapter 5, data from between the SB and the PF, from both DP and A23 sections are compared. However, the PF does not cross A23 which means that the DP data represent a wider DH range (Figure 1.5 and Figure B.1). In order to rule out this difference in dynamic height range as a cause of the observed water mass differences between the two sections, the analysis was repeated with the dynamic height range truncated at -0.87 dyn. m (the maximum dynamic height on the A23 section, just south of South Georgia), instead of -0.61 dyn. m (the PF). In this way, data from the same dynamic height range are compared across the two sections. Reducing the dynamic height range reduces the amount of data available from DP but the differences in water masses between the two sections remain broadly the same as those described in Section 5.3.3. WSDW and LCDW results are almost unchanged with the exception of pH in LCDW at DP which has a noticeably higher median when the DH range is reduced. This is consistent with the strong relationship between pH and DH observed in LCDW and results in a significant decrease in pH from DP to A23 when the narrower DH range is used. Given the narrower DH range, the differences in water mass properties in UCDW between DP and A23 shown in Figure 5.16 remain unchanged in direction but increase in magnitude. This is because, by removing data from the north of the section, the influence of the colder, fresher water from the peninsula is relatively more important. Reducing the DH range therefore makes the observed DP UCDW colder, fresher, more oxygen rich and lower in $f\text{CO}_2$.

Appendix C

Scotia Sea MLR results

Tables C.1 and C.2 show the multiple linear regression results for WSDW and LCDW, using data from between the SB and the PF on the DP and A23 sections. The UCDW data are not normally distributed and display some heteroscedasticity (unequal variability across their range). The MLR results for UCDW are therefore less robust and are not presented. I have experimented with using the SACCF as the southern limit of the data instead of the SB, in order to reduce the influence of water from the peninsula and thereby reduce the skewness of the UCDW data. However, this drastically reduces the data from A23 and prevents any meaningful comparison of the two sections.

| WSDW | | | | | | | |
|--------------|-------------|------------|------------|-----------|-----------|-----|-------|
| Variable | Predictor | Estimate | SE | T-stat | P-value | N | R2 |
| Theta | (Intercept) | 165.64 | 2.1536 | 76.915 | 1.91E-133 | 173 | 0.977 |
| | Section | -0.0018742 | 0.0018053 | -1.0381 | 3.01E-01 | | |
| | Gamma | -5.8589 | 0.076254 | -76.834 | 2.27E-133 | | |
| | Dynheight | 0.034926 | 0.0094741 | 3.6865 | 3.06E-04 | | |
| Salinity | (Intercept) | 41.458 | 0.29735 | 139.42 | 2.16E-176 | 173 | 0.818 |
| | Section | -0.001569 | 0.00024927 | -6.2945 | 2.56E-09 | | |
| | Gamma | -0.24 | 0.010529 | -22.795 | 1.97E-53 | | |
| | Dynheight | 0.0038117 | 0.0013081 | 2.9139 | 4.05E-03 | | |
| Oxygen | (Intercept) | -5200.4 | 241.16 | -21.564 | 2.15E-50 | 173 | 0.854 |
| | Section | 3.1736 | 0.20216 | 15.699 | 7.77E-35 | | |
| | Gamma | 191.92 | 8.5388 | 22.477 | 1.18E-52 | | |
| | Dynheight | 1.6139 | 1.0609 | 1.5213 | 1.30E-01 | | |
| pCFC12 | (Intercept) | -11296 | 2321.1 | -4.8667 | 1.43E-05 | 49 | 0.53 |
| | Section | 10.173 | 2.3487 | 4.3313 | 8.20E-05 | | |
| | Gamma | 402.61 | 82.153 | 4.9008 | 1.28E-05 | | |
| | Dynheight | 32.239 | 12.539 | 2.5711 | 1.35E-02 | | |
| DIC | (Intercept) | 3677.9 | 441.47 | 8.3311 | 8.44E-13 | 94 | 0.174 |
| | Section | -0.61533 | 0.37633 | -1.6351 | 0.10553 | | |
| | Gamma | -50.211 | 15.635 | -3.2115 | 1.83E-03 | | |
| | Dynheight | -0.25769 | 1.7792 | -0.14484 | 8.85E-01 | | |
| TA | (Intercept) | 3939.3 | 1032 | 3.817 | 2.54E-04 | 90 | 0.167 |
| | Section | 3.0005 | 0.80067 | 3.7475 | 3.23E-04 | | |
| | Gamma | -55.926 | 36.537 | -1.5307 | 1.30E-01 | | |
| | Dynheight | 1.134 | 3.9139 | 0.28975 | 7.73E-01 | | |
| fCO2 | (Intercept) | 8591 | 3206.6 | 2.6791 | 9.67E-03 | 60 | 0.387 |
| | Section | -13.121 | 2.996 | -4.3795 | 5.26E-05 | | |
| | Gamma | -288.34 | 113.51 | -2.5403 | 1.39E-02 | | |
| | Dynheight | -20.78 | 12.61 | -1.6478 | 1.05E-01 | | |
| pH | (Intercept) | 27.418 | 3.5692 | 7.6819 | 2.59E-10 | 60 | 0.756 |
| | Section | 0.02831 | 0.0033347 | 8.4895 | 1.22E-11 | | |
| | Gamma | -0.69888 | 0.12634 | -5.5317 | 8.67E-07 | | |
| | Dynheight | -0.15758 | 0.014036 | -11.226 | 5.86E-16 | | |
| Revelle fac. | (Intercept) | 20.784 | 50.172 | 0.41425 | 0.68027 | 60 | 0.349 |
| | Section | -0.24718 | 0.046876 | -5.273 | 2.23E-06 | | |
| | Gamma | -0.14137 | 1.776 | -0.079602 | 0.93684 | | |
| | Dynheight | 0.045881 | 0.19731 | 0.23254 | 0.81697 | | |
| Omega Ar. | (Intercept) | 74.829 | 8.8833 | 8.4236 | 1.56E-11 | 60 | 0.8 |
| | Section | 0.063384 | 0.0082997 | 7.6369 | 3.07E-10 | | |
| | Gamma | -2.6433 | 0.31445 | -8.4062 | 1.67E-11 | | |
| | Dynheight | -0.47008 | 0.034935 | -13.456 | 3.43E-19 | | |

Table C.1: Multiple linear regression results for WSDW. Model predictors are neutral density (Gamma), dynamic height (Dynheight) and a categorical predictor for DP or A23 (Section). P values for the section predictor which are less than 0.05 are shown in red. The number of observations is recorded in the column labelled 'N'.

LCDW

| Variable | Predictor | Estimate | SE | T-stat | P-value | N | R2 |
|--------------|-------------|-----------|-----------|-----------|------------|------|-------|
| Theta | (Intercept) | 174.66 | 2.1552 | 81.04 | 0 | 1086 | 0.859 |
| | Section | 0.068002 | 0.014982 | 4.5388 | 6.29E-06 | | |
| | Gamma | -6.1618 | 0.076553 | -80.49 | 0 | | |
| | Dynheight | 0.43871 | 0.036226 | 12.11 | 9.50E-32 | | |
| Salinity | (Intercept) | 36.7 | 0.25013 | 146.72 | 0 | 1086 | 0.214 |
| | Section | 0.0077214 | 0.0017388 | 4.4407 | 9.89E-06 | | |
| | Gamma | -0.06927 | 0.0088845 | -7.7967 | 1.49E-14 | | |
| | Dynheight | 0.057321 | 0.0042043 | 13.634 | 3.55E-39 | | |
| Oxygen | (Intercept) | -3180.9 | 92.615 | -34.345 | 2.98E-173 | 1041 | 0.583 |
| | Section | 0.88344 | 0.63003 | 1.4022 | 0.16115 | | |
| | Gamma | 119.65 | 3.2905 | 36.363 | 2.60E-187 | | |
| | Dynheight | -17.385 | 1.5517 | -11.204 | 1.39E-27 | | |
| pCFC12 | (Intercept) | 1111.1 | 772.32 | 1.4387 | 0.15228 | 158 | 0.261 |
| | Section | 1.8074 | 4.3835 | 0.41231 | 0.68069 | | |
| | Gamma | -41.19 | 27.493 | -1.4982 | 0.13613 | | |
| | Dynheight | -81.517 | 11.254 | -7.2435 | 1.96E-11 | | |
| DIC | (Intercept) | 1937.8 | 52.237 | 37.096 | 1.97E-153 | 568 | 0.122 |
| | Section | -0.42254 | 0.35973 | -1.1746 | 0.24065 | | |
| | Gamma | 11.651 | 1.8554 | 6.2795 | 6.79E-10 | | |
| | Dynheight | 5.3494 | 0.87373 | 6.1225 | 1.73E-09 | | |
| TA | (Intercept) | 1565.1 | 77.798 | 20.117 | 3.05E-67 | 532 | 0.315 |
| | Section | 3.3665 | 0.53182 | 6.3302 | 5.24E-10 | | |
| | Gamma | 28.502 | 2.7645 | 10.31 | 7.84E-23 | | |
| | Dynheight | 8.77 | 1.2505 | 7.0133 | 7.16E-12 | | |
| fCO2 | (Intercept) | 7568.6 | 308.24 | 24.554 | 2.23E-79 | 370 | 0.615 |
| | Section | -11.913 | 2.3822 | -5.0008 | 8.88E-07 | | |
| | Gamma | -252.62 | 10.943 | -23.085 | 2.08E-73 | | |
| | Dynheight | -25.193 | 4.9699 | -5.0692 | 6.36E-07 | | |
| pH | (Intercept) | 15.649 | 0.40456 | 38.68 | 2.35E-131 | 370 | 0.637 |
| | Section | 0.014019 | 0.0031266 | 4.4838 | 9.82E-06 | | |
| | Gamma | -0.27988 | 0.014362 | -19.487 | 1.57E-58 | | |
| | Dynheight | -0.10544 | 0.0065229 | -16.165 | 9.69E-45 | | |
| Revelle fac. | (Intercept) | 16.378 | 4.2567 | 3.8475 | 0.00014074 | 370 | 0.139 |
| | Section | -0.21815 | 0.032898 | -6.6313 | 1.20E-10 | | |
| | Gamma | 0.0012476 | 0.15112 | 0.0082558 | 0.99342 | | |
| | Dynheight | -0.15947 | 0.068633 | -2.3235 | 0.020701 | | |
| Omega Ar. | (Intercept) | 48.488 | 1.0909 | 44.446 | 1.44E-149 | 370 | 0.876 |
| | Section | 0.043129 | 0.0084313 | 5.1154 | 5.06E-07 | | |
| | Gamma | -1.7095 | 0.038729 | -44.14 | 1.21E-148 | | |
| | Dynheight | -0.44897 | 0.01759 | -25.525 | 2.84E-83 | | |

Table C.2: Multiple linear regression results for LCDW. Model predictors are neutral density (Gamma), dynamic height (Dynheight) and a categorical predictor for DP or A23 (Section). P values for the section predictor which are less than 0.05 are shown in red. The number of observations is recorded in the column labelled 'N'.

Appendix D

JR299 section plots

Figures D.1 and D.2 show the DIC, TA, oxygen and silicate concentration measured along the DP and A23 sections of JR299. The distributions of these variables are related to the water masses and frontal structure of the ACC in the Scotia Sea. DIC and TA increase with depth, with highest concentrations found in CDW. Silicate also increases with depth across all sections. There is a clear oxygen minimum in UCDW on both sections with oxygen concentrations below $190 \mu\text{mol kg}^{-1}$. At $\sim 56^\circ\text{S}$ in Drake Passage the PF and SAF are evident in these chemical data as, moving northwards, isopycnals deepen and more recently ventilated water with higher oxygen, lower DIC and lower silicate concentrations reaches deeper in the water column. On this occupation of the SR1b section the PF was quite far north and with data of this resolution it is therefore difficult to separate it from the SAF.

South of the South Scotia Ridge on the A23 section, oxygen concentration increases with depth and DIC, TA and silicate concentrations decrease with depth because the deep water in the Weddell Sea has been more recently ventilated than the old, circumpolar deep water overlying it. Further north on the A23 section, at $\sim 58^\circ\text{S}$, the steepening isopycnals and the southward termination of the oxygen-poor UCDW indicate the SACCF region.

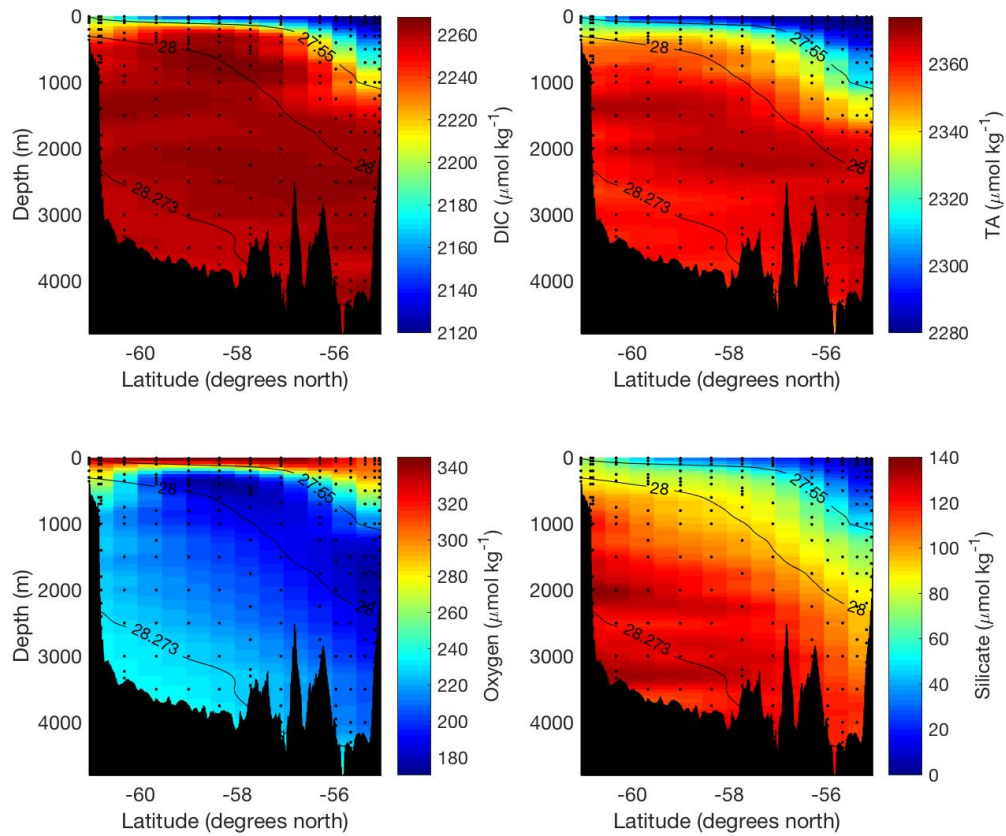


Figure D.1: DIC, TA, oxygen and silicate concentrations along the Drake Passage section of JR299. Neutral density contours pertinent to water mass definition are overlaid (Section 5.2.2). Black dots indicate sample locations. Bathymetry data from Smith and Sandwell (1997).

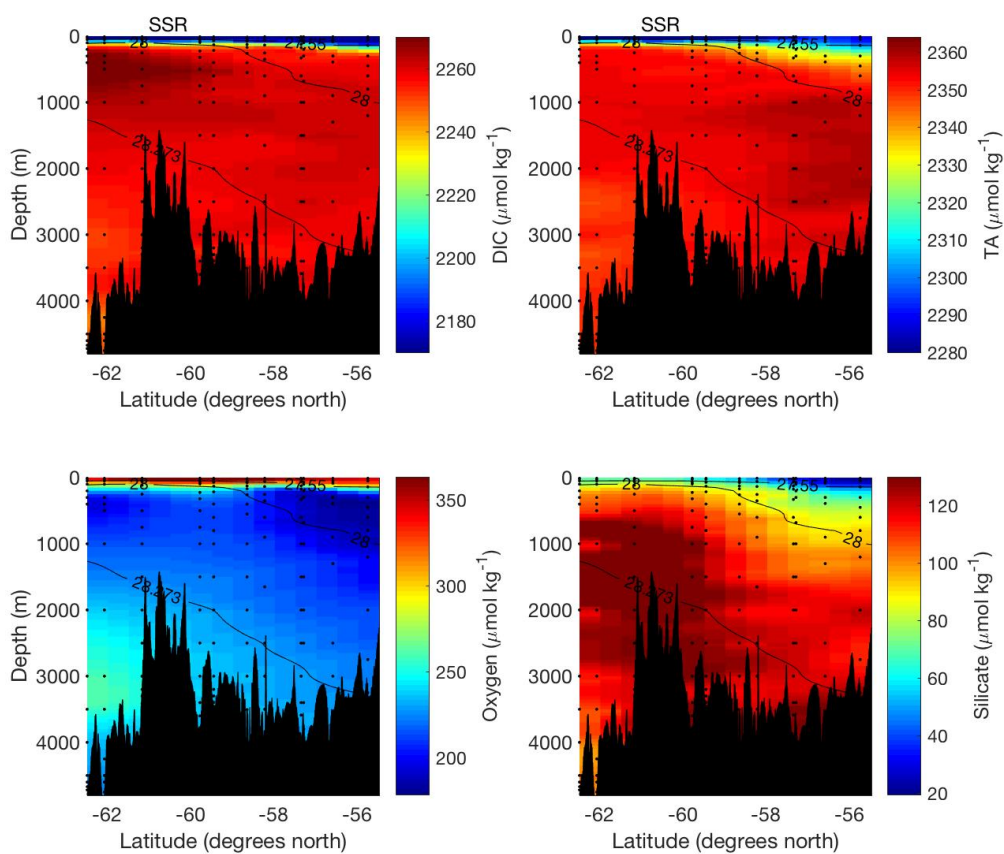


Figure D.2: DIC, TA, oxygen and silicate concentrations along the A23 section of JR299. Neutral density contours pertinent to water mass definition are overlaid (Section 5.2.2). Black dots indicate sample locations. Bathymetry data from Smith and Sandwell (1997). SSR indicates location of the South Scotia Ridge

Appendix E

Pressure effect on pH and Ω

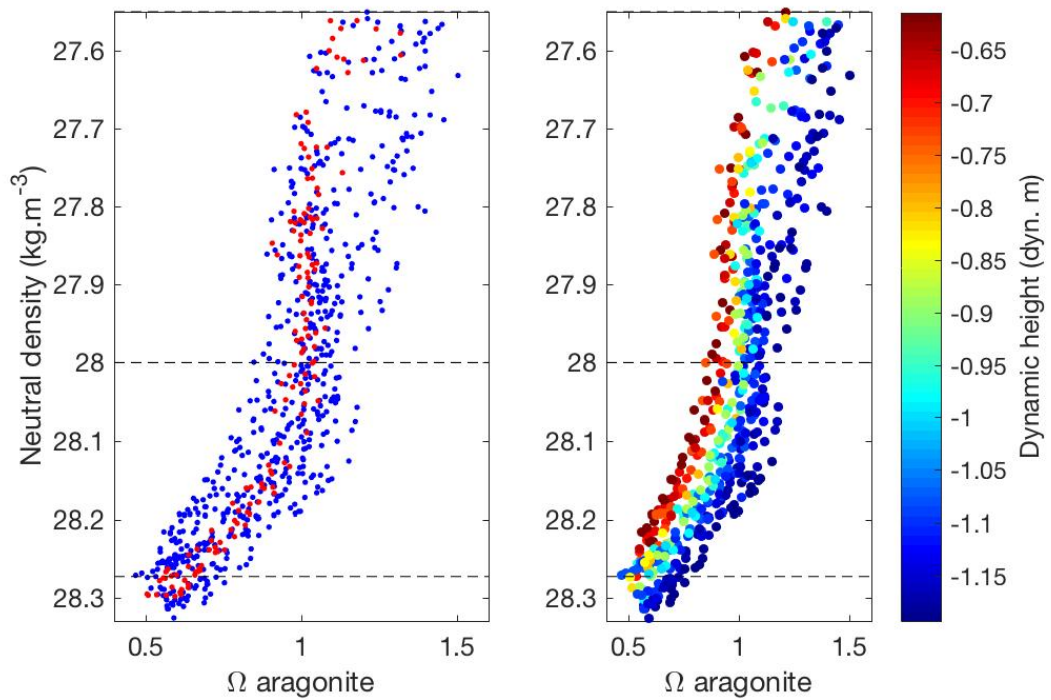


Figure E.1: Left panel: A comparison of DP (blue) and A23 (red) Ω aragonite. Right panel: the DP data coloured by dynamic height. Horizontal dashed lines represent the boundaries between UCDW and LCDW ($\gamma^{\theta} = 28$) and LCDW and WSDW ($\gamma^{\theta} = 28.273$).

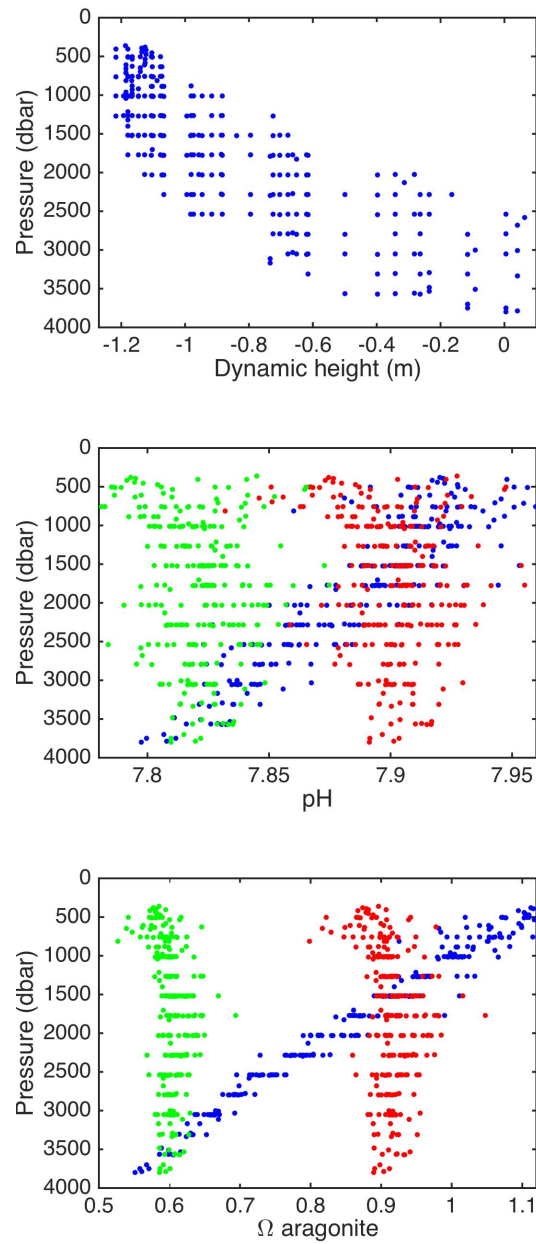


Figure E.2: The shoaling of LCDW in DP from high to low dynamic heights (north to south) (top panel). The influence of pressure on pH (middle panel) and Ω aragonite (bottom panel), both calculated from measured DIC, TA, temperature, salinity, phosphate and silicate. Blue points are calculated using in situ pressure, red points calculated at 1500 dbar, green points calculated at 3500 dbar.

Appendix F

The dynamic height of ACC fronts - circumpolar

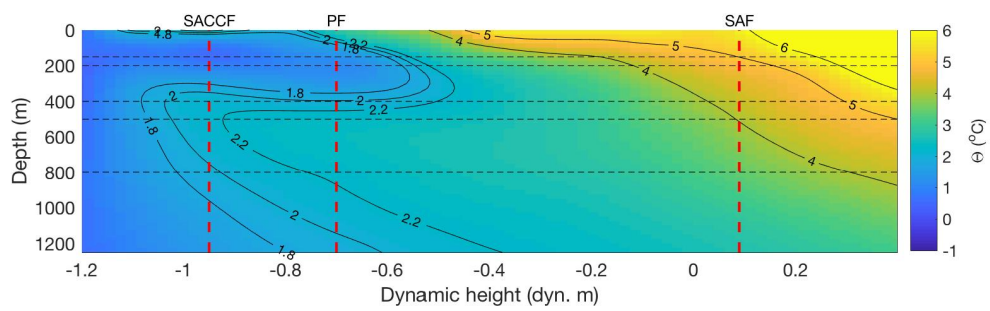


Figure F.1: Validation of circumpolar dynamic height frontal definitions at Drake Passage.

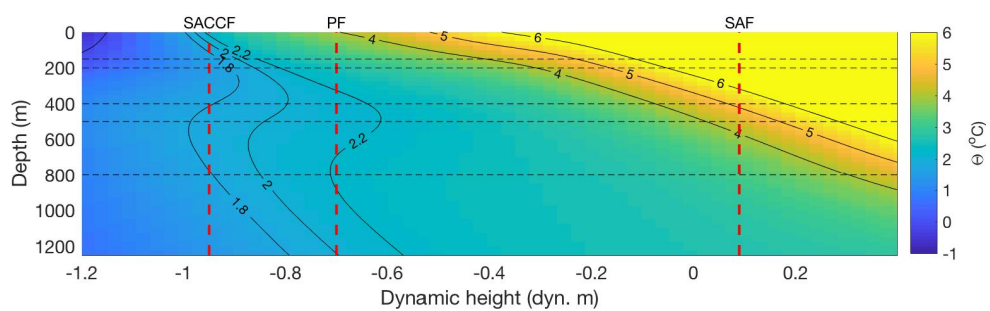


Figure F.2: Validation of circumpolar dynamic height frontal definitions at the prime meridian.

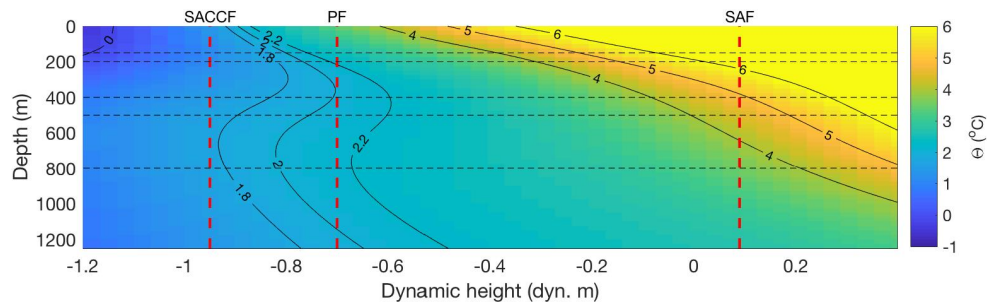


Figure E.3: Validation of circumpolar dynamic height frontal definitions at 115°E .

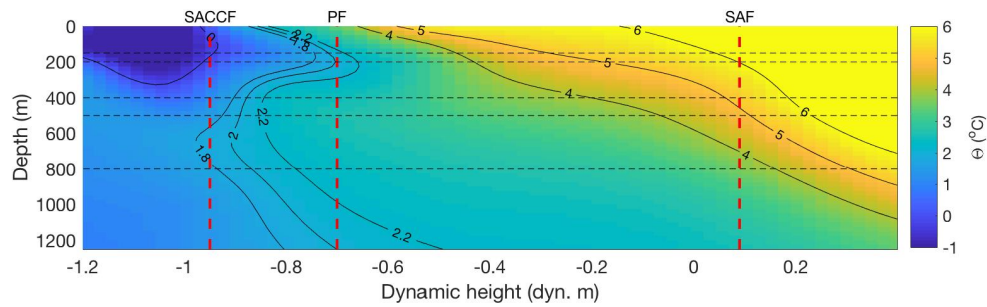


Figure E.4: Validation of circumpolar dynamic height frontal definitions at 150°W .

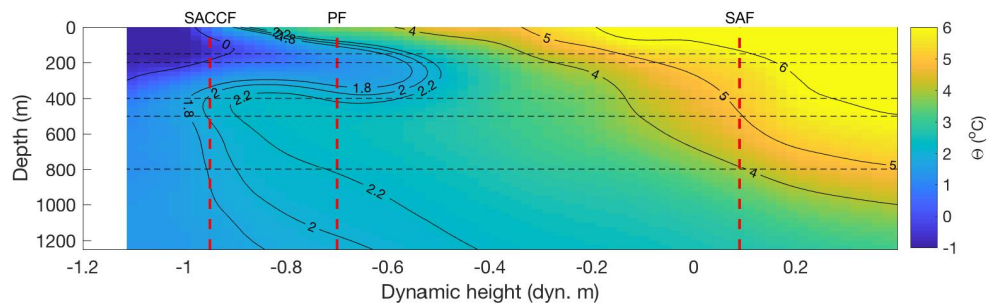


Figure E.5: Validation of circumpolar dynamic height frontal definitions at 103°W .

Appendix G

Circumpolar data distributions

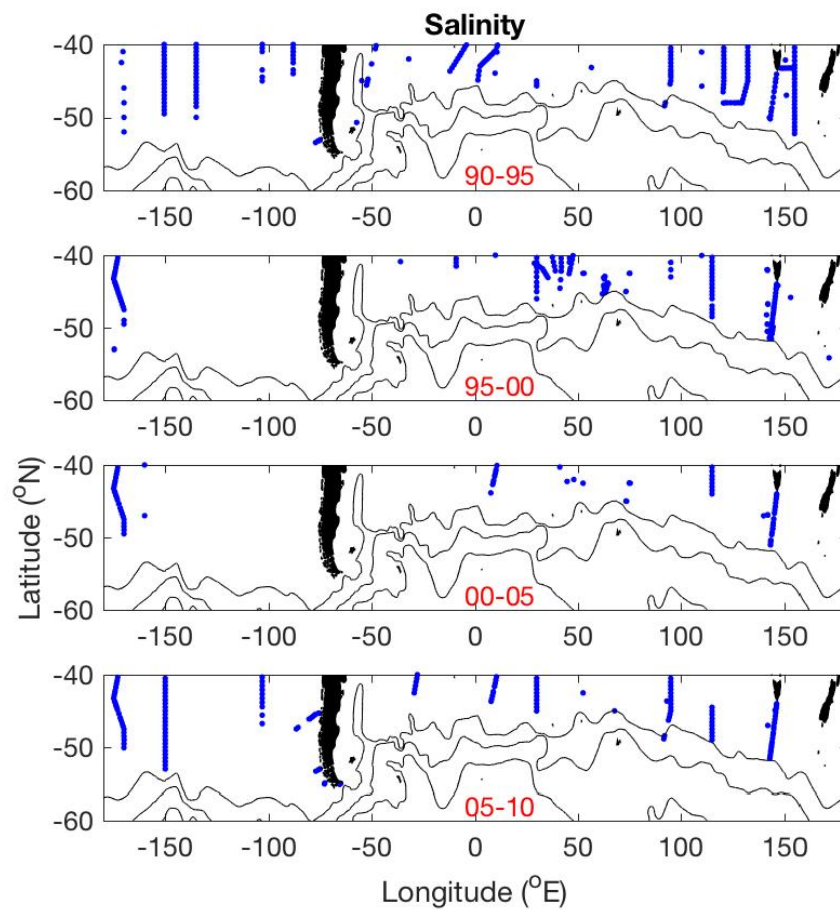


Figure G.1: The circumpolar distribution of salinity data points in SAMW in the GLO-DAPv2 dataset in each of the four pentades (time periods given in red).

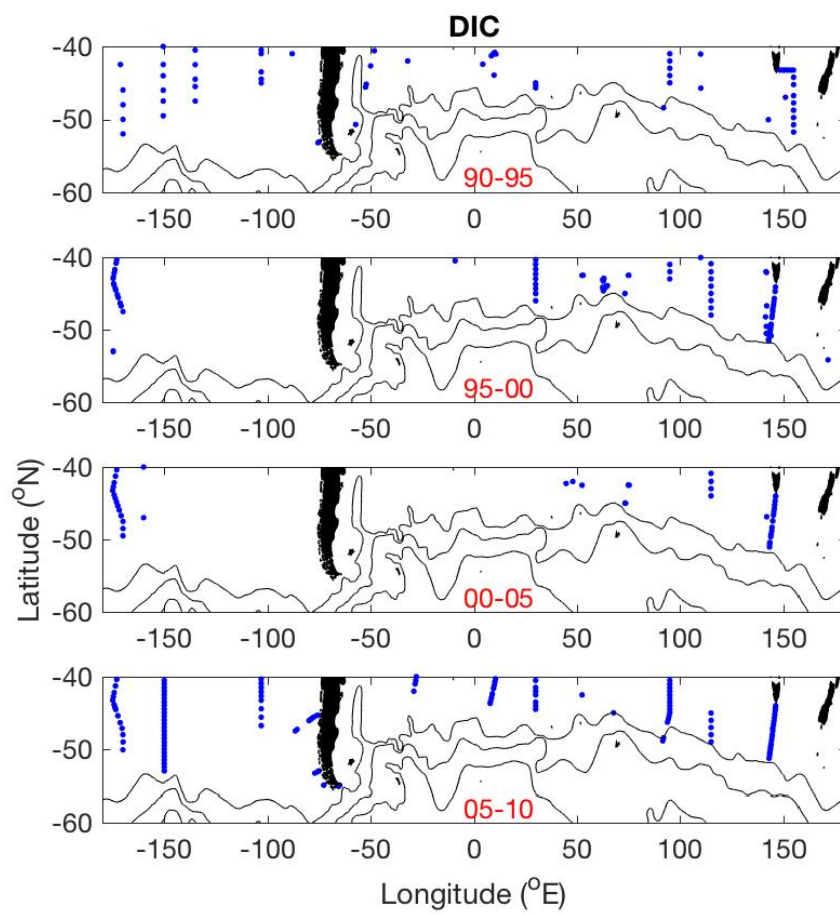


Figure G.2: The circumpolar distribution of DIC data (flagged 'good') in SAMW in the GLODAPv2 dataset in each of the four pentades (time periods given in red).

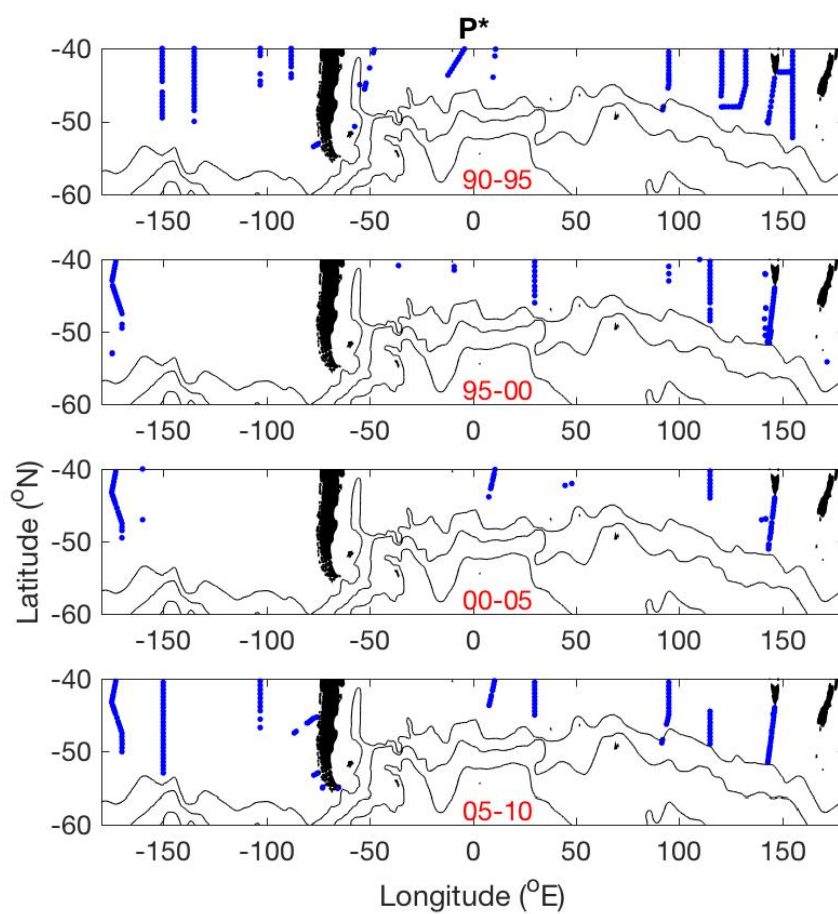


Figure G.3: The circumpolar distribution of data points in SAMW in the GLODAPv2 dataset used for calculating P^* in each of the four pentades (time periods given in red). P^* calculation required data flagged 'good' for oxygen and phosphate.

Appendix H

Abbreviations

AABW Antarctic Bottom Water

AAIW Antarctic Intermediate Water

ACC Antarctic Circumpolar Current

CDW Circumpolar Deep Water

CRM Certified Reference Material

CTD Conductivity Temperature Depth

DIC Dissolved Inorganic Carbon

DP Drake Passage

GLODAP Global Ocean Data Analysis Project

LCDW Lower Circumpolar Deep Water

MLD Mixed Layer Depth

MLR Multiple Linear Regression

MOC Meridional Overturning Circulation

NADW North Atlantic Deep Water

PF Polar Front

RaTS Rothera Biological and Oceanographic Time Series

SACCF Southern Antarctic Circumpolar Current Front

SAF Sub-Antarctic Front

SAM Southern Annular Mode

SAMW Sub-Antarctic Mode Water

SB Southern Boundary

SOCAT Surface Ocean CO₂ Atlas

SOCOM Southern Ocean Carbon and Climate Observation and Modeling

SFZ Shackleton Fracture Zone

SSH Sea Surface Height

TA Total Alkalinity

UCDW Upper Circumpolar Deep Water

VINDTA Versatile Instrument for the Determination of Titration Alkalinity

WAP West Antarctic Peninsula

WOCE World Ocean Circulation Experiment

WSDW Weddell Sea Deep Water

WSBW Weddell Sea Bottom Water

References

- Abernathey, R.P., Cerovecki, I., Holland, P.R., Newsom, E., Mazloff, M., Talley, L.D., 2016. Water-mass transformation by sea ice in the upper branch of the Southern Ocean overturning. *Nature Geoscience* 9, 1–8.
- Adkins, J.F., McIntyre, K., Schrag, D.P., 2002. The Salinity, Temperature, and $\delta^{18}\text{O}$ of the Glacial Deep Ocean. *Science* 298, 1769–1773.
- Álvarez, M., Tanhua, T., Brix, H., Lo Monaco, C., Metzl, N., Mcdonagh, E.L., Bryden, H.L., 2011. Decadal biogeochemical changes in the subtropical Indian Ocean associated with Subantarctic Mode Water. *Journal of Geophysical Research* 116, 1–13.
- Aminot, A., K erouel, R., Coverly, S.C., 2009. Nutrients in Seawater Using Segmented Flow Analysis, in: Wurl, O. (Ed.), *Practical guidelines for the analysis of seawater*. CRC Press, pp. 143–178.
- Anderson, L.G., Holby, O., Lindegren, R., Ohlson, M., 1991. The Transport of Anthropogenic Carbon Dioxide Into the Weddell Sea. *Journal of Geophysical Research* 96, 16679–16687.
- Annett, A.L., Skiba, M., Henley, S.F., Venables, H.J., Meredith, M.P., Statham, P.J., Ganeshram, R.S., 2015. Comparative roles of upwelling and glacial iron sources in Ryder Bay, coastal western Antarctic Peninsula. *Marine Chemistry* 176, 21–33.
- Aoki, S., Bindoff, N.L., Church, J.A., 2005. Interdecadal water mass changes in the Southern Ocean between 30°E and 160°E. *Geophysical Research Letters* 32, 1–5.
- Armstrong, R.A., Lee, C., Hedges, J.I., Honjo, S., Wakeham, S., 2002. A new,

- mechanistic model for organic carbon fluxes in the ocean based on the quantitative association of POC with ballast minerals. *Deep-Sea Research II* 49, 219–236.
- Arrigo, K., Mock, M., Lizotte, M.P., 2010. Primary Producers and Sea Ice, in: Thomas, D.N., Dieckmann, G.S. (Eds.), *Sea Ice*. second ed.. Blackwell Publishing Ltd. chapter 8, pp. 283–326.
- Arrigo, K.R., 2005. Marine microorganisms and global nutrient cycles. *Nature* 437, 349–355.
- Arrigo, K.R., van Dijken, G., Long, M., 2008. Coastal Southern Ocean: A strong anthropogenic CO₂ sink. *Geophysical Research Letters* 35, L21602.
- de Baar, H.J.W., Boyd, P.W., Coale, K.H., Landry, M.R., Tsuda, A., Assmy, P., Bakker, D.C.E., Bozec, Y., Barber, R.T., Brzezinski, M.A., Buesseler, K.O., Boyé, M., Croot, P.L., Gervais, F., Gorbunov, M.Y., Harrison, P.J., Hiscock, W.T., Laan, P., Lancelot, C., Law, C.S., Levasseur, M., Marchetti, A., Millero, F.J., Nishioka, J., Nojiri, Y., van Oijen, T., Riebesell, U., Rijkenberg, M.J.A., Saito, H., Takeda, S., Timmermans, K.R., Veldhuis, M.J.W., Waite, A.M., Wong, C.S., 2005. Synthesis of iron fertilization experiments: From the iron age in the age of enlightenment. *Journal of Geophysical Research C: Oceans* 110, 1–24.
- Bakker, D.C.E., Hoppema, M., Schroder, M., Geibert, W., de Baar, H.J.W., 2008. A rapid transition from ice covered CO₂ rich waters to a biologically mediated CO₂ sink in the eastern Weddell Gyre. *Biogeosciences* 5, 1373–1386.
- Bakker, D.C.E., Pfeil, B., Landa, C.S., Metzl, N., Brien, K.M.O., Olsen, A., Smith, K., Cosca, C., Harasawa, S., Jones, S.D., Nakaoka, S.i., Nojiri, Y., Schuster, U., Steinhoff, T., Sweeney, C., Takahashi, T., Tilbrook, B., Wada, C., Wanninkhof, R., Alin, S.R., Balestrini, C.F., Barbero, L., Bates, N.R., Bianchi, A.A., Bonou, F., Boutin, J., Bozec, Y., Burger, E.F., Cai, W.J., Castle, R.D., Chen, L., Chierici, M., Currie, K., Evans, W., Featherstone, C., Feely, R.A., Fransson, A., Goyet, C., Greenwood, N., Gregor, L., Hankin, S., Hardman-Mountford, N.J., Harlay, J., Hauck, J., Hoppema, M., Humphreys, M.P., Hunt, C., Huss, B.,

- Ibáñez, J.S.P., Johannessen, T., Keeling, R., Kitidis, V., Körtzinger, A., Kozyr, A., Krasakopoulou, E., Kuwata, A., Landschützer, P., Lauvset, S.K., Lefèvre, N., Lo Monaco, C., Manke, A., Mathis, J.T., Merlivat, L., Millero, F.J., Monteiro, P.M.S., Munro, D.R., Murata, A., Newberger, T., Omar, A.M., Ono, T., Paterson, K., Pearce, D., Pierrot, D., Robbins, L.L., Saito, S., Salisbury, J., Schlitzer, R., Schneider, B., Schweitzer, R., Sieger, R., Skjelvan, I., Sullivan, K.F., Sutherland, S.C., Sutton, A.J., Tadokoro, K., Telszewski, M., Tuma, M., van Heuven, S.M.A.C., Vandemark, D., Ward, B., Watson, A.J., Xu, S., 2016. A multi-decade record of high-quality $f\text{CO}_2$ data in version 3 of the Surface Ocean CO_2 Atlas (SOCAT). *Earth System Science Data* 8, 383–413.
- Bakker, D.C.E., Pfeil, B., Smith, K., Hankin, S., Olsen, A., Alin, S.R., Cosca, C., Harasawa, S., Kozyr, A., Nojiri, Y., O'Brien, K.M., Schuster, U., Telszewski, M., Tilbrook, B., Wada, C., Akl, J., Barbero, L., Bates, N.R., Boutin, J., Bozec, Y., Cai, W.J., Castle, R.D., Chavez, F.P., Chen, L., Chierici, M., Currie, K., de Baar, H.J.W., Evans, W., Feely, R.A., Fransson, A., Gao, Z., Hales, B., Hardman-Mountford, N.J., Hoppema, M., Huang, W.J., Hunt, C.W., Huss, B., Ichikawa, T., Johannessen, T., Jones, E.M., Jones, S.D., Jutterström, S., Kitidis, V., Körtzinger, A., Landschützer, P., Lauvset, S.K., Lefèvre, N., Manke, A.B., Mathis, J.T., Merlivat, L., Metzl, N., Murata, A., Newberger, T., Omar, A.M., Ono, T., Park, G.H., Paterson, K., Pierrot, D., Ríos, A.F., Sabine, C.L., Saito, S., Salisbury, J., Sarma, V.V.S.S., Schlitzer, R., Sieger, R., Skjelvan, I., Steinhoff, T., Sullivan, K.F., Sun, H., Sutton, A.J., Suzuki, T., Sweeney, C., Takahashi, T., Tjiputra, J., Tsurushima, N., van Heuven, S.M.A.C., Vandemark, D., Vlahos, P., Wallace, D.W.R., Wanninkhof, R., Watson, A.J., 2014. An update to the Surface Ocean CO_2 Atlas (SOCAT version 2). *Earth System Science Data* 6, 69–90.
- Bates, N.R., Best, M.H.P., Neely, K., Garley, R., Dickson, A.G., Johnson, R.J., 2012. Detecting anthropogenic carbon dioxide uptake and ocean acidification in the North Atlantic Ocean. *Biogeosciences* 9, 2509–2522.
- Bates, N.R., Moran, S.B., Hansell, D.A., Mathis, J.T., 2006. An increasing CO_2

- sink in the Arctic Ocean due to sea-ice loss. *Geophysical Research Letters* 33, L23609.
- Bednaršek, N., Tarling, G.A., Bakker, D.C.E., Fielding, S., Jones, E.M., Venables, H.J., Ward, P., Kuzirian, A., Lézé, B., Feely, R.A., Murphy, E.J., 2012. Extensive dissolution of live pteropods in the Southern Ocean. *Nature Geoscience* 5, 881–885.
- Belkin, I.M., Gordon, A.L., 1996. Southern Ocean fronts from the Greenwich meridian to Tasmania. *Journal of Geophysical Research* 101, 3675–3696.
- Bendschneider, K., Robinson, R.J., 1952. A new spectrophotometric method for the determination of nitrite in sea water. University of Washington Oceanographic Laboratories technical report .
- Bernardello, R., Marinov, I., Palter, J.B., Sarmiento, J.L., Galbraith, E.D., Slater, R.D., 2014. Response of the Ocean Natural Carbon Storage to Projected Twenty-First-Century Climate Change. *Journal of Climate* 27, 2033–2053.
- Berner, E.K., Berner, R.A., 2012. *Global Environment: Water, Air, and Geochemical Cycles*. second ed., Princeton University Press.
- Bindoff, N.L., McDougall, T.J., 1994. Diagnosing climate change and ocean ventilation using hydrographic data. *Journal of Physical Oceanography* 24, 1137–1152.
- Bindoff, N.L., McDougall, T.J., 2000. Decadal Changes along an Indian Ocean Section at 32°S and Their Interpretation. *Journal of Physical Oceanography* 30, 1207–1222.
- Böning, C.W., Dispert, A., Visbeck, M., Rintoul, S.R., Schwarzkopf, F.U., 2008. The response of the Antarctic Circumpolar Current to recent climate change. *Nature Geoscience* 1, 864–869.

- Bozec, Y., Thomas, H., Schiettecatte, L.S., Borges, A.V., Elkalay, K., de Baar, H.J., 2006. Assessment of the processes controlling seasonal variations of dissolved inorganic carbon in the North Sea. *Limnology and Oceanography* 51, 2746–2762.
- Brewer, P.G., 1978. Direct observation of the oceanic CO₂ increase. *Geophysical Research Letters* 5, 997–1000.
- Brewer, P.G., Goldman, J.C., 1976. Alkalinity changes generated by phytoplankton growth. *Limnology and Oceanography* 21, 108–117.
- Brewer, P.G., Riley, J.P., 1966. The automatic determination of silicate-silicon in natural waters with special reference to sea water. *Analytica Chimica Acta* 35, 514–519.
- Broecker, W.S., 1974. "NO", A conservative water-mass tracer. *Earth and Planetary Science Letters* 23, 100–107.
- Brown, K., Miller, L., Davelaar, M., Francois, R., Tortell, P., 2014. Over-determination of the carbonate system in natural sea-ice brine and assessment of carbonic acid dissociation constants under low temperature, high salinity conditions. *Marine Chemistry* 165, 36–45.
- Brown, P.J., Jullion, L., Landschützer, P., Bakker, D.C.E., Naveira Garabato, A.C., Meredith, M.P., Torres-valdés, S., Watson, A.J., Hoppema, M., Loose, B., Telszewski, M., Jones, S.D., Wanninkhof, R.H., 2015. Carbon dynamics of the Weddell Gyre, Southern Ocean. *Global Biogeochemical Cycles* 29, 288–306.
- Brzezinski, M.A., Dickson, M.L., Nelson, D.M., Sambrotto, R., 2003. Ratios of Si, C and N uptake by microplankton in the Southern Ocean. *Deep Sea Research Part II: Topical Studies in Oceanography* 50, 619–633.
- Buesseler, K.O., Antia, A.N., Chen, M., Fowler, S.W., Gardner, W.D., Gustafsson, O., Harada, K., Michaels, A.F., Loeff, M.R.V.D., Sarin, M., Steinberg, D.K., Trull, T., 2007. An assessment of the use of sediment traps for estimating upper ocean particle fluxes. *Journal of Marine Research* 65, 345–416.

- Burke, A., Robinson, L.F., 2012. The Southern Ocean's Role in Carbon Exchange During the Last Deglaciation. *Science* 335, 557–561.
- Butterworth, B.J., Miller, S.D., 2016. Air-sea exchange of carbon dioxide in the Southern Ocean and Antarctic marginal ice zone. *Geophysical Research Letters* 43, 7223–7230.
- Caldeira, K., Wickett, M.E., 2003. Anthropogenic carbon and ocean pH. *Nature* 425, 365.
- Callahan, J.E., 1972. The structure and circulation of deep water in the Antarctic. *Deep Sea Research* 19, 563–575.
- Carrillo, C.J., Smith, R.C., Karl, D.M., 2004. Processes regulating oxygen and carbon dioxide in surface waters west of the Antarctic Peninsula. *Marine Chemistry* 84, 161–179.
- Carter, B.R., Talley, L.D., Dickson, A.G., 2014. Mixing and remineralization in waters detrained from the surface into Subantarctic Mode Water and Antarctic Intermediate Water in the southeastern Pacific. *Journal of Geophysical Research: Oceans* 119, 4001–4028.
- Cerovecki, I., Talley, L.D., Mazloff, M.R., 2011. A Comparison of Southern Ocean Air Sea Buoyancy Flux from an Ocean State Estimate with Five Other Products. *Journal of Climate* 24, 6283–6306.
- Chen, G.T., Millero, F.J., 1979. Gradual increase of oceanic CO₂. *Nature* 277, 205–206.
- Chierici, M., Fransson, A., 2009. Calcium carbonate saturation in the surface water of the Arctic Ocean: undersaturation in freshwater influenced shelves. *Biogeosciences Discussions* 6, 4963–4991.
- Chierici, M., Fransson, A., Lansard, B., Miller, L.A., Mucci, A., Shadwick, E., Thomas, H., Tremblay, J.E., Papakyriakou, T.N., 2011. Impact of biogeochemical

- processes and environmental factors on the calcium carbonate saturation state in the Circumpolar Flaw Lead in the Amundsen Gulf, Arctic Ocean. *Journal of Geophysical Research* 116, C00G09.
- Ciais, P., Sabine, C., Bala, G., Bopp, L., Brovkin, V., Canadell, J., Chhabra, A., DeFries, R., Galloway, J., Heimann, M., Jones, C., Quéré, C.L., Myneni, R.B., Piao, S., Thornton, P., 2013. Carbon and Other Biogeochemical Cycles, in: Stocker, T.F., Qin, G.-K. Plattner, M. Tignor, S.K. Allen, J. Boschung, A. Nauels, Y. Xia, V.B., Midgley, P. (Eds.), *Climate Change 2013: The Physical Science Basis. Contribution of Working Group I to the Fifth Assessment Report of the Intergovernmental Panel on Climate Change*. Cambridge University Press, Cambridge and New York, pp. 465–570.
- Clarke, A., Meredith, M.P., Wallace, M.I., Brandon, M.A., Thomas, D.N., 2008. Seasonal and interannual variability in temperature, chlorophyll and macronutrients in northern Marguerite Bay, Antarctica. *Deep Sea Research Part II: Topical Studies in Oceanography* 55, 1988–2006.
- Comeau, S., Jeffree, R., Teyssié, J.L., Gattuso, J.P., 2010. Response of the Arctic pteropod *Limacina helicina* to projected future environmental conditions. *PloS one* 5, e11362.
- Comiso, J.C., Nishio, F., 2008. Trends in the sea ice cover using enhanced and compatible AMSR-E, SSM/I, and SMMR data. *Journal of Geophysical Research* 113, C02S07.
- Cook, A.J., Fox, A.J., Vaughan, D.G., Ferrigno, J.G., 2005. Retreating glacier fronts on the Antarctic Peninsula over the past half-century. *Science* 308, 541–544.
- Culberson, C., Pytkowicz, R.M., 1968. Effect of pressure on carbonic acid, boric acid and the pH in seawater. *Limnology and Oceanography* 13, 403–417.
- Cunningham, S.A., Alderson, S.G., King, B.A., Brandon, M., 2003. Transport and variability of the Antarctic Circumpolar Current in Drake Passage. *Journal of Geophysical Research* 108, 8084.

- Deacon, G.E.R., 1937. The hydrology of the Southern Ocean - Discovery reports. Cambridge University Press.
- Delille, B., 2006. Inorganic carbon dynamics and air-ice-sea CO₂ fluxes in the open and coastal waters of the Southern Ocean. Ph.D. thesis. Université de Liège.
- Delille, B., Jourdain, B., Borges, A.V., Delille, D., 2007. Biogas (CO₂, O₂, dimethylsulfide) dynamics in spring Antarctic fast ice. *Limnology and Oceanography* 52, 1367–1379.
- Delille, B., Vancoppenolle, M., Geilfus, N.X., Tilbrook, B., Lannuzel, D., Schoemann, V., Becquevort, S., Carnat, G., Delille, D., Lancelot, C., Chou, L., Dieckmann, G.S., Tison, J.L., 2014. Southern Ocean CO₂ sink: The contribution of sea ice. *Journal of Geophysical Research : Oceans* 119, 6340–6355.
- Deppeler, S.L., Davidson, A.T., 2017. Southern Ocean Phytoplankton in a Changing Climate. *Frontiers in Marine Science* 4, 1–28.
- DeVries, T., Holzer, M., Primeau, F., 2017. Recent increase in oceanic carbon uptake driven by weaker upper-ocean overturning. *Nature* 542, 215–218.
- Dickson, A., 2010. The carbon dioxide system in seawater: equilibrium chemistry and measurements, in: Riebesell, U., Fabry, V.J., Hanson, L., Gattuso, J.P. (Eds.), *Guide to best practices for ocean acidification research and data reporting*. Publication Office of the European Union, Luxemburg, pp. 17–52.
- Dickson, A.G., 1981. An exact definition of total alkalinity and a procedure for the estimation of alkalinity and total inorganic carbon from titration data. *Deep Sea Research* 28, 609–623.
- Dickson, A.G., Sabine, C.L., Christian, J.R., 2007. *Guide to best practices for ocean CO₂ measurements*. PICES Special Publication 3. Technical Report.
- Dieckmann, G.S., Nehrke, G., Papadimitriou, S., Göttlischer, J., Steininger, R., Kennedy, H., Wolf-Gladrow, D., Thomas, D.N., 2008. Calcium carbonate as ikaite crystals in Antarctic sea ice. *Geophysical Research Letters* 35, L08501.

- Dierssen, H.M., Smith, R.C., Vernet, M., 2002. Glacial meltwater dynamics in coastal waters west of the Antarctic peninsula. *Proceedings of the National Academy of Sciences of the United States of America* 99, 1790–1795.
- Dlugokencky, E.J., Lang, P.M., Masarie, K.A., Crotwell, A.M., Crotwell, M.J., 2014. Atmospheric Carbon Dioxide Dry Air Mole Fractions from the NOAA ESRL Carbon Cycle Cooperative Global Air Sampling Network, 1968-2013, Version: 2014-06-27.
- Dore, J.E., Houlihan, T., Hebel, D.V., Tien, G., Tupas, L., Karl, D.M., 1996. Freezing as a method of sample preservation for the analysis of dissolved inorganic nutrients in seawater. *Marine Chemistry* 53, 173–185.
- Dore, J.E., Lukas, R., Sadler, D.W., Church, M.J., Karl, D.M., 2009. Physical and biogeochemical modulation of ocean acidification in the central North Pacific. *Proceedings of the National Academy of Sciences of the United States of America* 106, 12235–12240.
- Ducklow, H., Fraser, W., Meredith, M., Stammerjohn, S., Doney, S., Martinson, D., Sailley, S., Schofield, O., Steinberg, D., Venables, H., Amsler, C., 2013. West Antarctic Peninsula: An Ice-Dependent Coastal Marine Ecosystem in Transition. *Oceanography* 26, 190–203.
- Ducklow, H.W., Baker, K., Martinson, D.G., Quetin, L.B., Ross, R.M., Smith, R.C., Stammerjohn, S.E., Vernet, M., Fraser, W., 2007. Marine pelagic ecosystems: the West Antarctic Peninsula. *Philosophical Transactions of the Royal Society B: Biological Sciences* 362, 67–94.
- Egleston, E.S., Sabine, C.L., Morel, F.M.M., 2010. Revelle revisited: Buffer factors that quantify the response of ocean chemistry to changes in DIC and alkalinity. *Global Biogeochemical Cycles* 24, 1–9.
- Evans, G.R., McDonagh, E.L., King, B.A., Bryden, H.L., Bakker, D.C.E., Brown, P.J., Schuster, U., Speer, K.G., Van Heuven, S.M.A.C., 2017. South Atlantic

- interbasin exchanges of mass, heat, salt and anthropogenic carbon. *Progress in Oceanography* 151, 62–82.
- Fairall, C.W., Yang, M., Bariteau, L., Edson, J.B., Helmig, D., McGillis, W., Pezoa, S., Hare, J.E., Huebert, B., Blomquist, B., 2011. Implementation of the Coupled Ocean-Atmosphere Response Experiment flux algorithm with CO₂, dimethyl sulfide, and O₃. *Journal of Geophysical Research* 116, C00F09.
- Feely, R.A., Sabine, C.L., Lee, K., Berelson, W., Kleypas, J., Fabry, V.J., Millero, F.J., 2004. Impact of Anthropogenic CO₂ on the CaCO₃ System in the Oceans. *Science* 305, 362–366.
- Fransson, A., Chierici, M., Miller, L.A., Carnat, G., Shadwick, E., Thomas, H., Pineault, S., Papakyriakou, T.N., 2013. Impact of sea-ice processes on the carbonate system and ocean acidification at the ice-water interface of the Amundsen Gulf, Arctic Ocean. *Journal of Geophysical Research: Oceans* 118, 7001–7023.
- Frolicher, T.L., Sarmiento, J.L., Paynter, D.J., Dunne, J.P., Krasting, J.P., Winton, M., 2015. Dominance of the Southern Ocean in Anthropogenic Carbon and Heat Uptake in CMIP5 Models. *Journal of Climate* 28, 862–886.
- García, H.E., Gordon, L.I., 1992. Oxygen solubility in seawater: Better fitting equations. *Limnology and Oceanography* 37, 1307–1312.
- Geider, R., La Roche, J., 2002. Redfield revisited: variability of C:N:P in marine microalgae and its biochemical basis. *European Journal of Phycology* 37, 1–17.
- Geilfus, N.X., Carnat, G., Dieckmann, G.S., Halden, N., Nehrke, G., Papakyriakou, T., Tison, J.L., Delille, B., 2013. First estimates of the contribution of CaCO₃ precipitation to the release of CO₂ to the atmosphere during young sea ice growth. *Journal of Geophysical Research: Oceans* 118, 244–255.
- Geilfus, N.X., Carnat, G., Papakyriakou, T., Tison, J.L., Else, B., Thomas, H., Shadwick, E., Delille, B., 2012. Dynamics of pCO₂ and related air-ice CO₂ fluxes in

- the Arctic coastal zone (Amundsen Gulf, Beaufort Sea). *Journal of Geophysical Research* 117, C00G10.
- Geilfus, N.X., Galley, R.J., Else, B.G.T., Campbell, K., Papakyriakou, T., Crabeck, O., Lemes, M., Delille, B., Rysgaard, S., 2016. Estimates of ikaite export from sea ice to the underlying seawater in a sea ice-seawater mesocosm. *The Cryosphere* 10, 2173–2189.
- Gent, P.R., 2016. Effects of Southern Hemisphere Wind Changes on the Meridional Overturning Circulation in Ocean Models. *Annual review of marine science* 8, 79–94.
- Gerringa, L.J., Alderkamp, A.C., Laan, P., Thuróczy, C.E., De Baar, H.J., Mills, M.M., van Dijken, G.L., Haren, H.V., Arrigo, K.R., 2012. Iron from melting glaciers fuels the phytoplankton blooms in Amundsen Sea (Southern Ocean): Iron biogeochemistry. *Deep Sea Research Part II: Topical Studies in Oceanography* 71-76, 16–31.
- Gibson, J.A.E., Trull, T.W., 1999. Annual cycle of $f\text{CO}_2$ under sea-ice and in open water in Prydz Bay, East Antarctica. *Marine Chemistry* 66, 187–200.
- Gill, A.E., 1973. Circulation and bottom water production in the Weddell Sea. *Deep Sea Research* 20, 111–140.
- Gille, S.T., 1994. Mean sea surface height of the Antarctic Circumpolar Current from Geosat data: Method and application. *Journal of Geophysical Research: Oceans* 99, 18255–18273.
- Gladyshev, S., Arhan, M., Sokov, A., Speich, S., 2008. A hydrographic section from South Africa to the southern limit of the Antarctic Circumpolar Current at the Greenwich meridian. *Deep Sea Research* 55, 1284–1303.
- Gonzalez-Davila, M., Santana-Casiano, J.M., Fine, R.A., Happell, J., Delille, B., Speich, S., 2011. Carbonate system in the water masses of the Southeast Atlantic

- sector of the Southern Ocean during February and March 2008. *Biogeosciences* 8, 1401–1413.
- Gordon, A.L., Huber, B.A., 1990. Southern Ocean winter mixed layer. *Journal of Geophysical Research* 95, 11655–11672.
- Gordon, A.L., Visbeck, M., Huber, B., 2001. Export of Weddell Sea Deep and Bottom Water. *Journal of Geophysical Research* 106, 9005–9017.
- Gosink, T., Pearson, J., Kelley, J., 1976. Gas movement through sea ice. *Nature* 263, 41–42.
- Goyet, C., Poisson, A., 1989. New determination of carbonic acid dissociation constants in seawater as a function of temperature and salinity. *Deep-Sea Research* 36, 1635–1654.
- Green, S.E., Sambrotto, R.N., 2006. Net community production in terms of C, N, P and Si in the Antarctic Circumpolar Current and its influence on regional water mass characteristics. *Deep-Sea Research Part I: Oceanographic Research Papers* 53, 111–135.
- Gruber, N., Gloor, M., Mikaloff Fletcher, S.E., Doney, S.C., Dutkiewicz, S., Follows, M.J., Gerber, M., Jacobson, A.R., Joos, F., Lindsay, K., Menemenlis, D., Mouchet, A., Müller, S.A., Sarmiento, J.L., Takahashi, T., 2009. Oceanic sources, sinks, and transport of atmospheric CO₂. *Global Biogeochemical Cycles* 23, GB1005.
- Gruber, N., Sarmiento, J.L., Stocker, T.F., 1996. An improved method for detecting anthropogenic CO₂ in the oceans. *Global Biogeochemical Cycles* 10, 809–837.
- Hall, A., Visbeck, M., 2002. Synchronous variability in the Southern Hemisphere atmosphere, sea ice, and ocean resulting from the annular mode. *Journal of Climate* 15, 3043–3057.
- Hall, T., Haine, T., Waugh, D., 2002. Inferring the concentration of anthropogenic carbon in the ocean from tracers. *Global Biogeochemical Cycles* 16, 1–15.

- Hauck, J., Völker, C., 2015. Rising atmospheric CO₂ leads to large impact of biology on Southern Ocean CO₂ uptake via changes of the Revelle factor. *Geophysical Research Letters* 42, 1459–1464.
- Haumann, F.A., Gruber, N., Münnich, M., Frenger, I., Kern, S., 2016. Sea-ice transport driving Southern Ocean salinity and its recent trends. *Nature* 537, 89–92.
- Hauri, C., Doney, S.C., Takahashi, T., Erickson, M., Jiang, G., Ducklow, H.W., 2015. Two decades of inorganic carbon dynamics along the Western Antarctic Peninsula. *Biogeosciences* 12, 6761–6779.
- Heinze, C., Maier-Reimer, E., 1991. Glacial pCO₂ reduction by the world ocean: experiments with the Hamburg carbon cycle model. *Paleoceanography* 6, 395–430.
- Henley, S., Tuerena, R., Annett, A., Fallick, A., Meredith, M., Venables, H., Clarke, A., Ganeshram, R., 2017. Macronutrient supply, uptake and recycling in the coastal ocean of the west Antarctic Peninsula. *Deep Sea Research Part II: Topical Studies in Oceanography* 139, 58–76.
- Heywood, K.J., Naveira Garabato, A.C., Stevens, D.P., 2002. High mixing rates in the abyssal Southern Ocean. *Nature* 415, 1011–1014.
- Ho, D.T., Wanninkhof, R., Schlosser, P., Ullman, D.S., Hebert, D., Sullivan, K.F., 2011. Toward a universal relationship between wind speed and gas exchange: Gas transfer velocities measured with ³He/SF₆ during the Southern Ocean Gas Exchange Experiment. *Journal of Geophysical Research* 116, C00F04.
- Holland, P.R., Kwok, R., 2012. Wind-driven trends in Antarctic sea-ice drift. *Nature Geoscience* 5, 872–875.
- Hoppema, M., de Baar, H.J.W., Bellerby, R.G.J., Fahrbach, E., Bakker, K., 2002a. Annual export production in the interior Weddell Gyre estimated from a chemical mass balance of nutrients. *Deep-Sea Research II* 49, 1675–1689.

- Hoppema, M., de Baar, H.J.W., Fahrbach, E., Bellerby, R.G.J., 2002b. Renewal time and transport of unventilated Central Intermediate Water of the Weddell Sea derived from biogeochemical properties. *Journal of Marine Research* 60, 677–697.
- Hydes, D., Aoyama, M., Aminot, A., Bakker, K., Becker, S., Coverly, S., Daniel, A., Dickson, A.G., Grosso, O., Kerouel, R., van Ooijen, J., Sato, K., Tanhua, T., Woodward, E.M.S., Zhang, J.Z., 2010. Determination of dissolved nutrients (N, P, Si) in seawater with high precision and inter-comparability using gas-segmented continuous flow analysers. The GO-SHIP repeat hydrography manual: a collection of expert reports and guidelines. IOCCP report no.14. Technical Report.
- Ito, T., Bracco, A., Deutsch, C., Frenzel, H., Long, M., Takano, Y., 2015. Sustained growth of the Southern Ocean carbon storage in a warming climate. *Geophysical Research Letters* 42, 4516–4522.
- Ito, T., Follows, M.J., 2005. Preformed phosphate, soft tissue pump and atmospheric CO₂. *Journal of Marine Research* 63, 813–839.
- Ito, T., Follows, M.J., Boyle, E.A., 2004. Is AOU a good measure of respiration in the oceans? *Geophysical Research Letters* 31, 1–4.
- Jackett, D.R., McDougall, T.J., 1997. A Neutral Density Variable for the World's Oceans. *Journal of Physical Oceanography* 27, 237–263.
- Jacobs, S.S., Amos, A.F., Bruchhausen., P.M., 1970. Ross Sea oceanography and Antarctic bottom water formation. *Deep Sea Research* 17, 935–962.
- Jickells, T.D., An, Z.S., Andersen, K.K., Baker, A.R., Bergametti, G., Brooks, N., Cao, J.J., Boyd, P.W., Duce, R.A., Hunter, K.A., Kawahata, H., Kubilay, N., LaRoche, J., Liss, P.S., Mahowald, N., Prospero, J.M., Ridgwell, A.J., Tegen, I., Torres, R., 2005. Global iron connections between desert dust, ocean biogeochemistry, and climate. *Science* 308, 67–71.

- Johnson, K., King, A., Sieburth, J., 1985. Coulometric TCO₂ analyses for marine studies; and introduction. *Marine Chemistry* 16, 61–82.
- Johnson, K.S., Plant, J.N., Coletti, L.J., Jannasch, H.W., Sakamoto, Carole, M., Riser, S.C., Swift, D.D., Williams, N.L., Boss, E., Haëntjens, N., Talley, L.D., Sarmiento, J.L., 2017. Biogeochemical sensor performance in the SOCCOM profiling float array. *Journal of Geophysical Research: Oceans* 122, 1–21.
- Jones, D.C., Meijers, A.J.S., Shuckburgh, E., Sallée, J.B., Haynes, P., McAufield, E.K., Mazloff, M.R., 2016a. How does Subantarctic Mode Water ventilate the Southern Hemisphere subtropics? *Journal of Geophysical Research: Oceans* 121, 6558–6582.
- Jones, E., Fenton, M., Meredith, M., Clargo, N., Ossebaar, S., Ducklow, H.W., Venables, H., de Baar, H., 2017. Ocean acidification and calcium carbonate saturation states in the coastal zone of the West Antarctic Peninsula. *Deep Sea Research Part II: Topical Studies in Oceanography* 139, 181–194.
- Jones, E.M., Bakker, D.C., Venables, H.J., Whitehouse, M.J., Korb, R.E., Watson, A.J., 2010. Rapid changes in surface water carbonate chemistry during Antarctic sea ice melt. *Tellus B* 62B, 621–635.
- Jones, J.M., Gille, S.T., Goosse, H., Abram, N.J., Canziani, P.O., Charman, D.J., Clem, K.R., Crosta, X., de Lavergne, C., Eisenman, I., England, M.H., Fogt, R.L., Frankcombe, L.M., Marshall, G.J., Masson-Delmotte, V., Morrison, A.K., Orsi, A.J., Raphael, M.N., Renwick, J.A., Schneider, D.P., Simpkins, G.R., Steig, E.J., Stenni, B., Swingedouw, D., Vance, T.R., 2016b. Assessing recent trends in high-latitude Southern Hemisphere surface climate. *Nature Climate Change* 6, 917–926.
- Kawaguchi, S., Ishida, A., King, R., Raymond, B., Waller, N., Constable, A., Nicol, S., Wakita, M., Ishimatsu, A., 2013. Risk maps for Antarctic krill under projected Southern Ocean acidification. *Nature Climate Change* 3, 843–847.

- Keeling, C.D., Adams, J.A., Ekdahl, C.A., Guenther, P.R., 1976. Atmospheric Carbon Dioxide Variations at the South Pole. *Tellus* 28, 552–564.
- Keeling, C.D., Piper, S.C., Bacastow, R.B., Wahlen, M., Whorf, T.P., Heimann, M., Meijer, H.A., 2005. Atmospheric CO₂ and ¹³CO₂ exchange with the terrestrial biosphere and oceans from 1978 to 2000: Observations and carbon cycle implications, in: J.R. Ehleringer, Cerling, T.E., Dearing, M.D. (Eds.), *A History of Atmospheric CO₂ and Its Effects on Plants, Animals and Ecosystems*. Springer, New York, pp. 83–113.
- Kessler, A., Tjiputra, J., 2016. The Southern Ocean as a constraint to reduce uncertainty in future ocean carbon sinks. *Earth System Dynamics* 7, 295–312.
- Khatiwala, S., Primeau, F., Hall, T., 2009. Reconstruction of the history of anthropogenic CO₂ concentrations in the ocean. *Nature* 462, 346–9.
- Klaas, C., Archer, D.E., 2002. Association of sinking organic matter with various types of mineral ballast in the deep sea : Implications for the rain ratio. *Global Biogeochemical Cycle* 16, 1116.
- Klatt, O., Roether, W., Hoppema, M., Bultsiewicz, K., Fleischmann, U., Rodehacke, C., Fahrbach, E., Weiss, R.F., Bullister, J.L., 2002. Repeated CFC sections at the Greenwich Meridian in the Weddell Sea. *Journal of Geophysical Research* 107, 3030.
- Kremling, K., Wenck, A., 1986. On the storage of dissolved inorganic phosphate, nitrate and reactive silicate in Atlantic Ocean water samples. *Meeresforschung* 31, 69–74.
- Landschützer, P., Gruber, N., Bakker, D.C.E., Schuster, U., 2014. Recent variability of the global ocean carbon sink. *Global Biogeochemical Cycles* 28, 927–949.
- Landschützer, P., Gruber, N., Bakker, D.C.E., Schuster, U., Nakaoka, S., Payne, M.R., Sasse, T.P., Zeng, J., 2013. A neural network-based estimate of the seasonal

- to inter-annual variability of the Atlantic Ocean carbon sink. *Biogeosciences* 10, 7793–7815.
- Landschützer, P., Gruber, N., Haumann, F.A., Rödenbeck, C., Bakker, D.C.E., van Heuven, S., Hoppema, M., Metzl, N., Sweeney, C., Takahashi, T., Tilbrook, B., Wanninkhof, R., 2015. The reinvigoration of the Southern Ocean carbon sink. *Science* 349, 1221–1224.
- Lannuzel, D., Schoemann, V., de Jong, J., Tison, J.L., Chou, L., 2007. Distribution and biogeochemical behaviour of iron in the East Antarctic sea ice. *Marine Chemistry* 106, 18–32.
- Lauderdale, J.M., Naveira Garabato, A.C., Oliver, K.I.C., Follows, M.J., Williams, R.G., 2013. Wind-driven changes in Southern Ocean residual circulation, ocean carbon reservoirs and atmospheric CO₂. *Climate Dynamics* 41, 2145–2164.
- Lauvset, S.K., Gruber, N., Landschützer, P., Olsen, A., Tjiputra, J., 2015. Trends and drivers in global surface ocean pH over the past 3 decades. *Biogeosciences* 12, 1285–1298.
- Laws, E.A., 1991. Photosynthetic quotients, new production and net community production in the open ocean. *Deep Sea Research Part A. Oceanographic Research Papers* 38, 143–167.
- Le Quéré, C., Andrew, R.M., Canadell, J.G., Sitch, S., Korsbakken, J.I., Peters, G.P., Manning, A.C., Boden, T.A., Tans, P.P., Houghton, R.A., Keeling, R.F., Alin, S., Andrews, O.D., Anthoni, P., Barbero, L., Bopp, L., Chevallier, F., Chini, L.P., Ciais, P., Currie, K., Delire, C., Doney, S.C., Friedlingstein, P., Gkritzalis, T., Harris, I., Hauck, J., Haverd, V., Hoppema, M., Goldewijk, K.K., Jain, A.K., Kato, E., Körtzinger, A., Landschützer, P., Lefèvre, N., Lenton, A., Lienert, S., Lombardozzi, D., Melton, J.R., Metzl, N., Millero, F., Monteiro, P.M.S., Munro, D.R., Nabel, J.E.M.S., Nakaoka, S.i., O'Brien, K., Olsen, A., Omar, A.M., Ono, T., Pierrot, D., Poulter, B., Rödenbeck, C., Salisbury, J., Schuster, U., Jörg, S., Séférian, R., Skjelvan, I., Stocker, B.D., Sutton, A.J., Takahashi, T., Tian, H.,

- Tilbrook, B., van der Laan-Luijkx, I.T., van der Werf, G.R., Viovy, N., Walker, A.P., Wiltshire, A.J., Zaehle, S., 2016. Global Carbon Budget 2016. *Earth System Science Data* 8, 605–649.
- Le Quéré, C., Rödenbeck, C., Buitenhuis, E.T., Conway, T.J., Langenfelds, R., Gomez, A., Labuschagne, C., Ramonet, M., Nakazawa, T., Metzl, N., Gillett, N., Heimann, M., 2007. Saturation of the Southern Ocean CO₂ Sink Due to Recent Climate Change. *Science* 316, 1735–1738.
- Lee, C., Wakeham, S., Arnosti, C., 2004. Particulate Organic Matter in the Sea: The Composition Conundrum. *Ambio* 33, 565–575.
- Legge, O.J., Bakker, D.C.E., Johnson, M.T., Meredith, M.P., Venables, H.J., Brown, P.J., Lee, G.A., 2015. The seasonal cycle of ocean-atmosphere CO₂ flux in Ryder Bay, west Antarctic Peninsula. *Geophysical Research Letters* 42, 2934–2942.
- Legge, O.J., Bakker, D.C.E., Meredith, M.P., Venables, H.J., Brown, P.J., Jones, E.M., Johnson, M.T., 2017. The seasonal cycle of carbonate system processes in Ryder Bay, West Antarctic Peninsula. *Deep-Sea Research Part II* 139, 167–180.
- Lenn, Y.D., Chereskin, T.K., Sprintall, J., 2008. Improving Estimates of the Antarctic Circumpolar Current Streamlines in Drake Passage. *Journal of Physical Oceanography* 38, 1000–1010.
- Lenton, A., Matear, R.J., 2007. Role of the Southern Annular Mode (SAM) in Southern Ocean CO₂ uptake. *Global Biogeochemical Cycles* 21, GB2016.
- Lenton, A., Tilbrook, B., Law, R., Bakker, D., Doney, S., Gruber, N., Ishii, M., Hoppema, M., Lovenduski, N.S., Matear, R.J., McNeil, B.I., Metzl, N., Mikaloff Fletcher, S.E., Monteiro, P.M.S., Rodenbeck, C., Sweeney, C., Takahashi, T., 2013. Sea-air CO₂ fluxes in the Southern Ocean for the period 1990-2009. *Biogeosciences* 10, 4037–4054.
- Liss, P.S., Merlivat, L., 1986. Air-sea gas exchange rates: introduction and synthesis, in: Buat-Ménard, P. (Ed.), *The role of air-sea gas exchange in geochemical*

- cycling NATO ASI Series (Series C: Mathematical and Physical Sciences), vol 185. Springer, Dordrecht, pp. 113–127.
- Lizotte, M.P., 2001. The Contributions of Sea Ice Algae to Antarctic Marine Primary Production. *American Zoologist* 41, 57–73.
- Lo Monaco, C., Goyet, C., Metzl, N., Poisson, A., Touratier, F., 2005. Distribution and inventory of anthropogenic CO₂ in the Southern Ocean: Comparison of three data-based methods. *Journal of Geophysical Research C: Oceans* 110, 1–12.
- Locarnini, R.A., Whitworth, T., Nowlin, W.D., 1993. The importance of the Scotia Sea on the outflow of Weddell Sea Deep Water. *Journal of Marine Research* 51, 135–153.
- Loose, B., McGillis, W.R., Perovich, D., Zappa, C.J., Schlosser, P., 2014. A parameter model of gas exchange for the seasonal sea ice zone. *Ocean Science* 10, 1–12.
- Loose, B., Schlosser, P., 2011. Sea ice and its effect on CO₂ flux between the atmosphere and the Southern Ocean interior. *Journal of Geophysical Research* 116, C11019.
- Lovenduski, N.S., 2005. Impact of the Southern Annular Mode on Southern Ocean circulation and biology. *Geophysical Research Letters* 32, L11603.
- Lueker, T.J., Dickson, A.G., Keeling, C.D., 2000. Ocean pCO₂ calculated from dissolved inorganic carbon, alkalinity, and equations for K₁ and K₂: validation based on laboratory measurements of CO₂ in gas and seawater at equilibrium. *Marine Chemistry* 70, 105–119.
- Lumpkin, R., Speer, K., 2007. Global Ocean Meridional Overturning. *Journal of Physical Oceanography* 37, 2550–2562.
- Lüthi, D., Le Floch, M., Bereiter, B., Blunier, T., Barnola, J.M., Siegenthaler, U., Raynaud, D., Jouzel, J., Fischer, H., Kawamura, K., Stocker, T.F., 2008. High-

- resolution carbon dioxide concentration record 650,000-800,000 years before present. *Nature* 453, 379–382.
- Macdonald, R.W., McLaughlin, F.A., Wong, C.S., 1986. The storage of reactive silicate samples by freezing. *Limnology and Oceanography* 31, 1139–1142.
- Manno, C., Morata, N., Primicerio, R., 2012. *Limacina retroversa*'s response to combined effects of ocean acidification and sea water freshening. *Estuarine, Coastal and Shelf Science* 113, 163–171.
- Marrari, M., Daly, K.L., Hu, C., 2008. Spatial and temporal variability of SeaWiFS chlorophyll a distributions west of the Antarctic Peninsula: Implications for krill production. *Deep-Sea Research Part II: Topical Studies in Oceanography* 55, 377–392.
- Marshall, G.J., 2003. Trends in the Southern Annular Mode from Observations and Reanalyses. *Journal of Climate* 16, 4134–4143.
- Marshall, G.J., Orr, A., van Lipzig, N.P.M., King, J.C., 2006. The impact of a changing Southern Hemisphere Annular Mode on Antarctic Peninsula summer temperatures. *Journal of Climate* 19, 5388–5404.
- Marshall, J., Speer, K., 2012. Closure of the meridional overturning circulation through Southern Ocean upwelling. *Nature Geoscience* 5, 171–180.
- Martin, J.H., 1990. Glacial-interglacial CO₂ change: the iron hypothesis. *Paleoceanography* 5, 1–13.
- Martinson, D.G., McKee, D.C., 2012. Transport of warm Upper Circumpolar Deep Water onto the western Antarctic Peninsula continental shelf. *Ocean Science* 8, 433–442.
- Martiny, A.C., Vrugt, J.A., Primeau, F.W., Lomas, M.W., 2013. Regional variation in the particulate organic carbon to nitrogen ratio in the surface ocean. *Global Biogeochemical Cycles* 27, 723–731.

- Mattsdotter Björk, M., Fransson, A., Torstensson, A., Chierici, M., 2014. Ocean acidification state in western Antarctic surface waters: controls and interannual variability. *Biogeosciences* 11, 57–73.
- McCartney, M.S., 1977. Subantarctic Mode Water, in: Angel, M.V. (Ed.), *A voyage of Discovery: George Deacon 70th anniversary volume*. Pergammon Press, Oxford, p. 712.
- McNeil, B.I., Matear, R.J., 2008. Southern Ocean acidification: a tipping point at 450 ppm atmospheric CO₂. *Proceedings of the National Academy of Sciences of the United States of America* 105, 18860–18864.
- McNeil, B.I., Sweeney, C., Gibson, J.A., 2011. Natural seasonal variability of aragonite saturation state within two Antarctic coastal ocean sites. *Antarctic Science* 23, 411–412.
- McNeil, B.I., Tilbrook, B., Matear, R.J., 2001. Accumulation and uptake of anthropogenic CO₂ in the Southern Ocean, south of Australia. *Journal of Geophysical Research* 106, 31431–31445.
- Meijers, A.J.S., 2014. The Southern Ocean in the Coupled Model Intercomparison Project phase 5. *Philosophical transactions of the Royal Society A* 372, 20130296.
- Meijers, A.J.S., Meredith, M.P., Abrahamsen, P.E., Morales Maqueda, M.A., Jones, D.C., Naveira Garabato, A.C., 2016. Wind-driven export of Weddell Sea slope water. *Journal of Geophysical Research: Oceans* 121, 7530–7546.
- Meiners, K.M., Vancoppenolle, M., Thanassekos, S., Dieckmann, G.S., Thomas, D.N., Tison, J.L., Arrigo, K.R., Garrison, D.L., McMinn, A., Lannuzel, D., van der Merwe, P., Swadling, K.M., Smith, W.O., Melnikov, I., Raymond, B., 2012. Chlorophyll a in Antarctic sea ice from historical ice core data. *Geophysical Research Letters* 39, L21602.
- Meredith, M.P., 2013. Replenishing the abyss. *Nature Geoscience* 6, 166–167.

- Meredith, M.P., Brandon, M.A., Wallace, M.I., Clarke, A., Leng, M.J., Renfrew, I.A., van Lipzig, N.P.M., King, J.C., 2008a. Variability in the freshwater balance of northern Marguerite Bay, Antarctic Peninsula: Results from $\delta^{18}\text{O}$. *Deep-Sea Research Part II: Topical Studies in Oceanography* 55, 309–322.
- Meredith, M.P., Brown, P.J., Naveira Garabato, A.C., Jullion, L., Venables, H.J., Messias, M.J., 2013. Dense bottom layers in the Scotia Sea, Southern Ocean: Creation, lifespan, and destruction. *Geophysical Research Letters* 40, 933–936.
- Meredith, M.P., Hughes, C.W., Foden, P.R., 2003. Downslope convection north of Elephant Island, Antarctica: Influence on deep waters and dependence on ENSO. *Geophysical Research Letters* 30, 1462.
- Meredith, M.P., Jullion, L., Brown, P.J., Naveira Garabato, A.C., Couldrey, M.P., 2014. Dense waters of the Weddell and Scotia Seas: recent changes in properties and circulation. *Phil. Trans. R. Soc. A* 372, 20130041.
- Meredith, M.P., King, J.C., 2005. Rapid climate change in the ocean west of the Antarctic Peninsula during the second half of the 20th century. *Geophysical Research Letters* 32, L19604.
- Meredith, M.P., Naveira Garabato, A.C., Gordon, A.L., Johnson, G.C., 2008b. Evolution of the deep and bottom waters of the Scotia Sea, Southern Ocean during 1995–2005. *Journal of Climate* 21, 3327–3343.
- Meredith, M.P., Renfrew, I.A., Clarke, A., King, J.C., Brandon, M.A., 2004. Impact of the 1997/98 ENSO on upper ocean characteristics in Marguerite Bay, western Antarctic Peninsula. *Journal of Geophysical Research* 109, C09013.
- Meredith, M.P., Stammerjohn, S.E., Venables, H.J., Ducklow, H.W., Martinson, D.G., Iannuzzi, R.A., Leng, M.J., Melchior, J., Wessem, V., Reijmer, C.H., Bartrand, N.E., 2017. Changing distributions of sea ice melt and meteoric water west of the Antarctic Peninsula. *Deep-Sea Research Part II* 139, 40–57.

- Meredith, M.P., Wallace, M.I., Stammerjohn, S.E., Renfrew, I.A., Clarke, A., Venables, H.J., Shoosmith, D.R., Souster, T., Leng, M.J., 2010. Changes in the fresh-water composition of the upper ocean west of the Antarctic Peninsula during the first decade of the 21st century. *Progress in Oceanography* 87, 127–143.
- Meredith, M.P., Woodworth, P.L., Chereskin, T.K., Marshall, D.P., Allison, L.C., Bigg, G.R., Donohue, K., Heywood, K.J., Hughes, C.W., Hibbert, A., Hogg, A.M., Johnson, H.L., Jullion, L., King, B.A., Leach, H., Lenn, Y.D., Maqueda, M.A.M., Munday, D.R., Naveira Garabato, A.C., Provost, C., Sallée, J.B., Sprintall, J., 2011. Sustained monitoring of the Southern Ocean at Drake Passage: past achievements and future priorities. *Reviews of Geophysics* 49, 1–36.
- Metzl, N., Tilbrook, B., Poisson, A., 1999. The annual $f\text{CO}_2$ cycle and the air-sea CO_2 flux in the sub-Antarctic Ocean. *Tellus B* 51, 849–861.
- Miller, L.A., Elliott, S., Papakyriakou, T., 2011a. Sea ice biogeochemistry and material transport across the frozen interface. *Oceanography* 24, 202–218.
- Miller, L.A., Papakyriakou, T.N., Collins, R.E., Deming, J.W., Ehn, J.K., Macdonald, R.W., Mucci, A., Owens, O., Raudsepp, M., Sutherland, N., 2011b. Carbon dynamics in sea ice: A winter flux time series. *Journal of Geophysical Research* 116, C02028.
- Millero, F.J., 2007. The marine inorganic carbon cycle. *Chemical reviews* 107, 308–341.
- Mintrop, L., Pérez, F.F., González Dávila, M., Santana Casiano, J.M., Körtzinger, A., 2000. Alkalinity determination by potentiometry: intercalibration using three different methods. *Ciencias Marinas* 26, 23–27.
- Montes-Hugo, M., Doney, S.C., Ducklow, H.W., Fraser, W., Martinson, D., Stammerjohn, S.E., Schofield, O., 2009. Recent changes in phytoplankton communities associated with rapid regional climate change along the western Antarctic Peninsula. *Science* 323, 1470–1473.

- Montes-Hugo, M., Sweeney, C., Doney, S.C., Ducklow, H., Frouin, R., Martinson, D.G., Stammerjohn, S., Schofield, O., 2010. Seasonal forcing of summer dissolved inorganic carbon and chlorophyll a on the western shelf of the Antarctic Peninsula. *Journal of Geophysical Research* 115, C03024.
- Moreau, S., Vancoppenolle, M., Bopp, L., Aumont, O., Madec, G., Delille, B., Tison, J.L., Barriat, P.Y., Goosse, H., 2016. Assessment of the sea-ice carbon pump: Insights from a three-dimensional ocean-sea-ice biogeochemical model (NEMO-LIM-PISCES). *Elementa* 4, 000122.
- Moy, A.D., Howard, W.R., Bray, S.G., Trull, T.W., 2009. Reduced calcification in modern Southern Ocean planktonic foraminifera. *Nature Geoscience* 2, 276–280.
- Mucci, A., Lansard, B., Miller, L.A., Papakyriakou, T.N., 2010. CO₂ fluxes across the air-sea interface in the southeastern Beaufort Sea: Ice-free period. *Journal of Geophysical Research* 115, C04003.
- Munro, D.R., Lovenduski, N.S., Stephens, B.B., Newberger, T., Arrigo, K.R., Takahashi, T., Quay, P.D., Sprintall, J., Freeman, N.M., Sweeney, C., 2015. Estimates of net community production in the Southern Ocean determined from time series observations (2002-2011) of nutrients, dissolved inorganic carbon, and surface ocean pCO₂ in Drake Passage. *Deep Sea Research Part II: Topical Studies in Oceanography* 114, 49–63.
- Murata, A., Kumamoto, Y., Watanabe, S., Fukasawa, M., 2007. Decadal increases of anthropogenic CO₂ in the South Pacific subtropical ocean along 32°S. *Journal of Geophysical Research* 112, 1–11.
- Murphy, J., Riley, J.P., 1962. A modified single solution method for the determination of phosphate in natural waters. *Analytica Chimica Acta* 27, 31–36.
- Naveira Garabato, A.C., Heywood, K.J., Stevens, D.P., 2002a. Modification and pathways of Southern Ocean Deep Waters in the Scotia Sea. *Deep Sea Research Part I: Oceanographic Research Papers* 49, 681–705.

- Naveira Garabato, A.C., Jullion, L., Stevens, D.P., Heywood, K.J., King, B.A., 2009. Variability of Subantarctic Mode Water and Antarctic Intermediate Water in the Drake Passage during the Late-Twentieth and Early-Twenty-First Centuries. *Journal of Climate* 22, 3661–3688.
- Naveira Garabato, A.C., McDonagh, E.L., Stevens, D.P., Heywood, K.J., Sanders, R.J., 2002b. On the export of Antarctic Bottom Water from the Weddell Sea. *Deep Sea Research Part II: Topical Studies in Oceanography* 49, 4715–4742.
- Naveira Garabato, A.C., Stevens, D.P., Heywood, K.J., 2003. Water Mass Conversion, Fluxes, and Mixing in the Scotia Sea Diagnosed by an Inverse Model. *Journal of Physical Oceanography* 33, 2565–2587.
- Nightingale, P.D., Malin, G., Law, C.S., Watson, A.J., Liss, P.S., Liddicoat, M.I., Boutin, J., Upstill-Goddard, R.C., 2000. In situ evaluation of air-sea gas exchange parameterizations using novel conservative and volatile tracers. *Global Biogeochemical Cycles* 14, 373–387.
- Nomura, D., Granskog, M.A., Assmy, P., Simizu, D., Hashida, G., 2013. Arctic and Antarctic sea ice acts as a sink for atmospheric CO₂ during periods of snowmelt and surface flooding. *Journal of Geophysical Research: Oceans* 118, 6511–6524.
- Nowlin, W.D., Whitworth, T., Pillsbury, R.D., 1977. Structure and transport of the Antarctic Circumpolar Current at Drake Passage from short-term measurements. *Journal of Physical Oceanography* 7, 788–802.
- Ohshima, K.I., Fukamachi, Y., Williams, G.D., Nihashi, S., Roquet, F., Kitade, Y., Tamura, T., Hirano, D., Herraiz-Borreguero, L., Field, I., Hindell, M., Aoki, S., Wakatsuchi, M., 2013. Antarctic Bottom Water production by intense sea-ice formation in the Cape Darnley polynya. *Nature Geoscience* 6, 235–240.
- Olsen, A., Key, R.M., van Heuven, S., Lauvset, S.K., Velo, A., Lin, X., Schirnick, C., Kozyr, A., Tanhua, T., Hoppema, M., Jutterström, S., Steinfeldt, R., Jeansson, E., Ishii, M., Perez, F.F., Suzuki, T., 2016. The Global Ocean Data Analysis

- Project version 2 (GLODAPv2) an internally consistent data product for the world ocean. *Earth System Science Data* 8, 297–323.
- Orr, J.C., Fabry, V.J., Aumont, O., Bopp, L., Doney, S.C., Feely, R.A., Gnanadesikan, A., Gruber, N., Ishida, A., Joos, F., Key, R.M., Lindsay, K., Maier-Reimer, E., Matear, R., Monfray, P., Mouchet, A., Najjar, R.G., Plattner, G.K., Rodgers, K.B., Sabine, C.L., Sarmiento, J.L., Schlitzer, R., Slater, R.D., Totterdell, I.J., Weirig, M.F., Yamanaka, Y., Yool, A., 2005. Anthropogenic ocean acidification over the twenty-first century and its impact on calcifying organisms. *Nature* 437, 681–686.
- Orsi, A.H., Johnson, G.C., Bullister, J.L., 1999. Circulation, mixing, and production of Antarctic Bottom Water. *Progress in Oceanography* 43, 55–109.
- Orsi, A.H., Whitworth, T., Nowlin, W.D., 1995. On the meridional extent and fronts of the Antarctic Circumpolar Current. *Deep-Sea Research I* 42, 641–673.
- Papadimitriou, S., Kennedy, H., Kattner, G., Dieckmann, G., Thomas, D., 2004. Experimental evidence for carbonate precipitation and CO₂ degassing during sea ice formation. *Geochimica et Cosmochimica Acta* 68, 1749–1761.
- Pardo, P.C., Pérez, F.F., Khatiwala, S., Ríos, A.F., 2014. Anthropogenic CO₂ estimates in the Southern Ocean: Storage partitioning in the different water masses. *Progress in Oceanography* 120, 230–242.
- Pardo, P.C., Pérez, F.F., Velo, A., Gilcoto, M., 2012. Water masses distribution in the Southern Ocean: Improvement of an extended OMP (eOMP) analysis. *Progress in Oceanography* 103, 92–105.
- Pardo, P.C., Tilbrook, B., Langlais, C., Trull, T.W., Rintoul, S.R., 2017. Carbon uptake and biogeochemical change in the Southern Ocean, south of Tasmania. *Biogeosciences Discussions* , 1–43.
- Parkinson, C.L., Cavalieri, D.J., 2012. Antarctic sea ice variability and trends, 1979-2010. *Cryosphere* 6, 871–880.

- Pérez, F.F., Álvarez, M., Ríos, A.F., 2002. Improvements on the back-calculation technique for estimating anthropogenic CO₂. *Deep-Sea Research I* 49, 859–875.
- Petit, J.R., Jouzel, J., Raynaud, D., Barkov, N.I., Barnola, J.M., Basile, I., Bender, M., Chappellaz, J., Davis, M., Delaygue, G., Delmotte, M., Kotlyakov, V.M., Legrand, M., Lipenkov, V.Y., Lorius, C., Pepin, L., Ritz, C., Saltzman, E., Stievenard, M., 1999. Climate and atmospheric history of the past 420, 000 years from the Vostok ice core, Antarctica. *Nature* 399, 429–436.
- Pierrot, D., Brown, P., Van Heuven, S., Tanhua, T., Schuster, U., Wanninkhof, R., Key, R.M., 2010. CARINA TCO₂ data in the Atlantic Ocean. *Earth System Science Data* 3, 177–187.
- Prézelin, B., Hofmann, E., Moline, M., Klinck, J., 2004. Physical forcing of phytoplankton community structure and primary production in continental shelf waters of the Western Antarctic Peninsula. *Journal of Marine Research* 62, 419–460.
- Provost, C., Renault, A., Barré, N., Sennéchaël, N., Garçon, V., Sudre, J., Huhn, O., 2011. Two repeat crossings of Drake Passage in austral summer 2006: Short-term variations and evidence for considerable ventilation of intermediate and deep waters. *Deep-Sea Research Part II: Topical Studies in Oceanography* 58, 2555–2571.
- Quigg, A., Finkel, Z.V., Irwin, A.J., Rosenthal, Y., Ho, T.Y., Reinfelder, J.R., Schofield, O., Morel, F.M.M., Falkowski, P.G., 2003. Evolutionary inheritance of elemental stoichiometry in phytoplankton. *Nature* 425, 291–294.
- Redfield, A., Ketchum, B.H., Richards, F.A., 1963. The influence of organisms on the composition of sea water, in: Hill, M. (Ed.), *The Sea*. John Wiley and Sons, New York. volume 2, pp. 26–77.
- Revelle, R., Suess, H.E., 1957. Carbon dioxide exchange between atmosphere and ocean and the question of an increase of atmospheric CO₂ during the past decades. *Tellus* 9, 18–27.

- Ridgwell, A., Zeebe, R.E., 2005. The role of the global carbonate cycle in the regulation and evolution of the Earth system. *Earth and Planetary Science Letters* 234, 299–315.
- Rintoul, S.R., 1998. On the Origin and Influence of Adélie Land Bottom Water, in: Jacobs, S.S., Weiss, R.F. (Eds.), *Ocean, Ice, and Atmosphere: Interactions at the Antarctic Continental Margin*. American Geophysical Union, Washington D.C., pp. 151 – 171.
- Rio, M., Hernandez, F., 2004. A mean dynamic topography computed over the world ocean from altimetry, in situ measurements, and a geoid model. *Journal of Geophysical Research* 109, 1–19.
- Ríos, A.F., Vázquez-Rodríguez, M., Padin, X., Pérez, F.F., 2010. Anthropogenic carbon dioxide in the South Atlantic western basin. *Journal of Marine Systems* 83, 38–44.
- Roden, N.P., Shadwick, E.H., Tilbrook, B., Trull, T.W., 2013. Annual cycle of carbonate chemistry and decadal change in coastal Prydz Bay, East Antarctica. *Marine Chemistry* 155, 135–147.
- Roden, N.P., Tilbrook, B., Trull, T.W., Virtue, P., Williams, G.D., 2016. Carbon cycling dynamics in the seasonal sea-ice zone of East Antarctica. *Journal of Geophysical Research: Oceans* 121, 8749–8769.
- Rubin, S., Takahashi, T., Chipman, D., Goddard, J., 1998. Primary productivity and nutrient utilization ratios in the Pacific sector of the Southern Ocean based on seasonal changes in seawater chemistry. *Deep-Sea Research I* 45, 1211–1234.
- Rysgaard, S., Bendtsen, J., Delille, B., Dieckmann, G.S., Glud, R.N., Kennedy, H., Mortensen, J., Papadimitriou, S., Thomas, D.N., Tison, J.L., 2011. Sea ice contribution to the air-sea CO₂ exchange in the Arctic and Southern Oceans. *Tellus B* 63, 823–830.

- Rysgaard, S., Glud, R.N., Lennert, K., Cooper, M., Halden, N., Leakey, R.J.G., Hawthorne, F.C., Barber, D., 2012. Ikaite crystals in melting sea ice - implications for pCO₂ and pH levels in Arctic surface waters. *The Cryosphere* 6, 901–908.
- Rysgaard, S., Glud, R.N., Sejr, M.K., Bendtsen, J., Christensen, P.B., 2007. Inorganic carbon transport during sea ice growth and decay: A carbon pump in polar seas. *Journal of Geophysical Research* 112, C03016.
- Sabine, C.L., Feely, R.A., Gruber, N., Key, R.M., Lee, K., Bullister, J.L., Wanninkhof, R., Wong, C.S., Wallace, D.W.R., Tilbrook, B., Millero, F.J., Peng, T.H., Kozyr, A., 2004. The Oceanic Sink for Anthropogenic CO₂. *Science* 305, 367–371.
- Sabine, C.L., Feely, R.A., Key, R.M., Bullister, J.L., Millero, F.J., Lee, K., Peng, T., Tilbrook, B., Ono, T., Wong, C.S., 2002. Distribution of anthropogenic CO₂ in the Pacific Ocean. *Global Biogeochemical Cycles* 16, 1083.
- Sabine, C.L., Feely, R.A., Millero, F.J., Dickson, A.G., Langdon, C., Mecking, S., Greeley, D., 2008. Decadal changes in Pacific carbon. *Journal of Geophysical Research* 113, C07021.
- Sallée, J.B., Matear, R.J., Rintoul, S.R., Lenton, A., 2012. Localized subduction of anthropogenic carbon dioxide in the Southern Hemisphere oceans. *Nature Geoscience* 5, 579–584.
- Sallée, J.B., Speer, K., Rintoul, S., Wijffels, S., 2010a. Southern Ocean Thermocline Ventilation. *Journal of Physical Oceanography* 40, 509–529.
- Sallée, J.B., Speer, K.G., Rintoul, S.R., 2010b. Zonally asymmetric response of the Southern Ocean mixed-layer depth to the Southern Annular Mode. *Nature Geoscience* 3, 273–279.
- Sambrotto, R.N., Savidge, G., Robinson, C., Boyd, P., Takahashi, T., Karl, D.M.,

- Langdon, C., Chipman, D., Marra, J., Codispoti, L., 1993. Elevated consumption of carbon relative to nitrogen in the surface ocean. *Nature* 363, 248–250.
- Sarmiento, J.L., Gruber, N., 2006. *Ocean biogeochemical dynamics*. Princeton University Press.
- Sarmiento, J.L., Gruber, N., Brzezinski, M.A., Dunne, J.P., 2004. High-latitude controls of thermocline nutrients and low latitude biological productivity. *Nature* 427, 56–60.
- Schuster, U., Watson, A.J., Bakker, D.C.E., De Boer, A.M., Jones, E.M., Lee, G.A., Legge, O., Louwarse, A., Riley, J., Scally, S., 2014. Measurements of total alkalinity and inorganic dissolved carbon in the Atlantic Ocean and adjacent Southern Ocean between 2008 and 2010. *Earth System Science Data* 6, 175–183.
- Sedwick, P.N., Ditullio, R., 1997. Regulation of algal blooms in Antarctic shelf waters by the release of iron from melting sea ice. *Geophysical Research Letters* 24, 2515–2518.
- Semiletov, I., Makshtas, A., Akasofu, S.I., Andreas, E.L., 2004. Atmospheric CO₂ balance: The role of Arctic sea ice. *Geophysical Research Letters* 31, L05121.
- Shadwick, E.H., Thomas, H., Chierici, M., Else, B., Fransson, A., Michel, C., Miller, L.A., Mucci, A., Niemi, A., Papakyriakou, T.N., Tremblay, J.É., 2011. Seasonal variability of the inorganic carbon system in the Amundsen Gulf region of the southeastern Beaufort Sea. *Limnology and Oceanography* 56, 303–322.
- Shadwick, E.H., Tilbrook, B., Williams, G.D., 2014. Carbonate chemistry in the Mertz Polynya (East Antarctica): Biological and physical modification of dense water outflows and the export of anthropogenic CO₂. *Journal of Geophysical Research: Oceans* 119, 1–14.
- Shadwick, E.H., Trull, T.W., Thomas, H., Gibson, J.A.E., 2013. Vulnerability of polar oceans to anthropogenic acidification: comparison of Arctic and Antarctic seasonal cycles. *Scientific reports* 3, 2339.

- Siani, G., Michel, E., Pol-holz, R.D., DeVries, T., Lamy, F., Carel, M., Isguder, G., Dewilde, F., Laurantou, A., 2013. Carbon isotope records reveal precise timing of enhanced Southern Ocean upwelling during the last deglaciation. *Nature Communications* 4, 2758.
- Sievers, H.A., Nowlin, W.D., 1984. The Stratification and Water Masses at Drake Passage. *Journal of Geophysical Research* 89, 10489–10514.
- Sigman, D.M., Hain, M.P., Haug, G.H., 2010. The polar ocean and glacial cycles in atmospheric CO₂ concentration. *Nature* 466, 47–55.
- Skalar, 2009a. Analysis: nitrate+nitrite, Catnr. 461-032 issue 062309/MH/99256750. Technical Report.
- Skalar, 2009b. Analysis: phosphate, Catnr. 503-010 issue 062309/MH/99256750. Technical Report.
- Skalar, 2009c. Analysis: silicate, Catnr. 563-051 issue 062309/MH/99256750. Technical Report.
- Sloyan, B., Rintoul, S.R., 2001a. Circulation, Renewal, and Modification of Antarctic Mode and Intermediate Water. *Journal of Physical Oceanography* 31, 1005–1030.
- Sloyan, B.M., Rintoul, S.R., 2001b. The Southern Ocean Limb of the Global Deep Overturning Circulation. *Journal of Physical Oceanography* 31, 143–173.
- Smith, I.J., Stevens, D.P., Heywood, K.J., Meredith, M.P., 2010a. The flow of the Antarctic Circumpolar Current over the North Scotia Ridge. *Deep Sea Research Part I: Oceanographic Research Papers* 57, 14–28.
- Smith, M.J., Ho, D.T., Law, C.S., McGregor, J., Popinet, S., Schlosser, P., 2010b. Uncertainties in gas exchange parameterization during the SAGE dual-tracer experiment. *Deep Sea Research Part II: Topical Studies in Oceanography* , 869–881.

- Smith, W.H.F., Sandwell, D.T., 1997. Global Sea Floor Topography from Satellite Altimetry and Ship Depth Soundings. *Science* 277, 1956–1962.
- Sokolov, S., Rintoul, S.R., 2002. Structure of Southern Ocean fronts at 140°E. *Journal of Marine Systems* 37, 151–184.
- Sokolov, S., Rintoul, S.R., 2007. Multiple Jets of the Antarctic Circumpolar Current South of Australia. *Journal of Physical Oceanography* 37, 1394–1412.
- Sokolov, S., Rintoul, S.R., 2009. Circumpolar structure and distribution of the Antarctic Circumpolar Current fronts: 1. Mean circumpolar paths. *Journal of Geophysical Research* 114, C11018.
- Speer, K., Rintoul, S.R., Sloyan, B.M., 2000. The Diabatic Deacon Cell. *Journal of Physical Oceanography* 30, 3212–3222.
- Stammerjohn, S.E., Martinson, D.G., Smith, R.C., Yuan, X., Rind, D., 2008. Trends in Antarctic annual sea ice retreat and advance and their relation to El Niño Southern Oscillation and Southern Annular Mode variability. *Journal of Geophysical Research* 113, C03S90.
- Stendardo, I., Gruber, N., Kortzinger, A., 2009. CARINA-Oxygen : a new high-quality oxygen database for the Atlantic Ocean. *Earth System Science Data Discussions* 2, 103–135.
- Stephens, B.B., Keeling, R.F., 2000. The influence of Antarctic sea ice on glacial-interglacial CO₂ variations. *Nature* 404, 171–174.
- Sudre, J., Garçon, V., Provost, C., Sennéchaël, N., Huhn, O., Lacombe, M., 2011. Short-term variations of deep water masses in Drake Passage revealed by a multiparametric analysis of the ANT-XXIII/3 bottle data. *Deep-Sea Research Part II: Topical Studies in Oceanography* 58, 2592–2612.
- Sweeney, C., 2003. The Annual Cycle of Surface Water CO₂ and O₂ in the Ross Sea: A model for Gas Exchange on the Continental Shelves of Antarctica. *Antarctic Research Series* 78, 295–312.

- Sweeney, C., Gloor, E., Jacobson, A.R., Key, R.M., McKinley, G., Sarmiento, J.L., Wanninkhof, R., 2007. Constraining global air-sea gas exchange for CO₂ with recent bomb ¹⁴C measurements. *Global Biogeochemical Cycles* 21, GB2015.
- Takahashi, T., Sutherland, S.C., Wanninkhof, R., Sweeney, C., Feely, R.A., Chipman, D.W., Hales, B., Friederich, G., Chavez, F., Sabine, C., Watson, A., Bakker, D.C.E., Schuster, U., Metzl, N., Yoshikawa-Inoue, H., Steinhoff, T., Ishii, M., Midorikawa, T., Nojiri, Y., Ko, A., Hoppema, M., Olafsson, J., Arnarson, T.S., Tilbrook, B., Johannessen, T., Olsen, A., Bellerby, R., Wong, C.S., Delille, B., Bates, N.R., de Baar, H.J.W., 2009. Climatological mean and decadal change in surface ocean pCO₂, and net sea-air CO₂ flux over the global oceans. *Deep-Sea Research II* 56, 554–577.
- Takahashi, T., Sweeney, C., Hales, B., Chipman, D.W., Newberger, T., Goddard, J.G., Iannuzzi, R.A., Sutherland, S.C., 2012. The changing carbon cycle in the Southern Ocean. *Oceanography* 25, 26–37.
- Takahashi, T., Williams, R.T., Bos, D.L., 1982. Carbonate chemistry, in: Broecker, W.S., Spencer, D.W., Craig, H. (Eds.), *GEOSECS Pacific Expedition, Volume 3, Hydrographic Data 1973-1974*. National Science Foundation, Washington D.C., pp. 77–83.
- Tamsitt, V., Drake, H.F., Morrison, A.K., Talley, L.D., Dufour, C.O., Gray, A.R., Griffies, S.M., Mazloff, M.R., Sarmiento, J.L., Wang, J., Weijer, W., 2017. Spiraling pathways of global deep waters to the surface of the Southern Ocean. *Nature Communications* 8, 1–10.
- Tamsitt, V., Talley, L.D., Mazloff, M.R., Cerovecki, I., 2016. Zonal Variations in the Southern Ocean Heat Budget. *Journal of Climate* 29, 6563–6579.
- Tanhua, T., Brown, P.J., Key, R.M., 2009. CARINA: nutrient data in the Atlantic Ocean. *Earth System Science Data* 2, 63–101.
- Tanhua, T., van Heuven, S., Key, R., Velo, A., Olsen, A., Schirnack, C., 2010.

- Quality control procedures and methods of the CARINA database. *Earth System Science Data* 2, 35–49.
- Tanhua, T., Hoppema, M., Jones, E.M., Stöven, T., Hauck, J., González, M., Santana-Casiano, M., Álvarez, M., Strass, V.H., 2017. Temporal changes in ventilation and the carbonate system in the Atlantic sector of the Southern Ocean. *Deep-Sea Research Part II* 138, 26–38.
- Taylor, J.K., 1987. *Quality assurance of chemical measurements*. CRC Press.
- Thomas, D.N., Dieckmann, G.S., 2002. Antarctic Sea ice - a habitat for extremophiles. *Science* 295, 641–644.
- Thomas, E.R., Marshall, G.J., McConnell, J.R., 2008. A doubling in snow accumulation in the western Antarctic Peninsula since 1850. *Geophysical Research Letters* 35, L01706.
- Thomas, H., Ittekkot, V., Osterroht, C., Schneider, B., 1999. Preferential recycling of nutrients - the ocean's way to increase new production and to pass nutrient limitation? *Limnology and Oceanography* 44, 1999–2004.
- Thompson, A.F., Youngs, M.K., 2013. Surface exchange between the Weddell and Scotia Seas. *Geophysical Research Letters* 40, 5920–5925.
- Thompson, D.W.J., Solomon, S., 2002. Interpretation of Recent Southern Hemisphere Climate Change. *Science* 296, 895–899.
- Thompson, D.W.J., Solomon, S., Kushner, P.J., England, M.H., Grise, K.M., Karoly, D.J., 2011. Signatures of the Antarctic ozone hole in Southern Hemisphere surface climate change. *Nature Geoscience* 4, 741–749.
- Ting, Y.H., Holzer, M., 2017. Decadal changes in Southern Ocean ventilation inferred from deconvolutions of repeat hydrographies. *Geophysical Research Letters* 44, 5655–5664.

- Toggweiler, J.R., Russell, J.L., Carson, S.R., 2006. Midlatitude westerlies, atmospheric CO₂, and climate change during the ice ages. *Paleoceanography* 21, PA2005.
- Toole, J.M., Krishfield, R.A., Timmermans, M.L., Proshutinsky, A., 2011. The Ice-Tethered Profiler: Argo of the Arctic. *Oceanography* 24, 126–135.
- Tortell, P.D., Bittig, H.C., Körtzinger, A., Jones, E.M., Hoppema, M., 2015. Biological and physical controls on N₂, O₂, and CO₂ distributions in contrasting Southern Ocean surface waters. *Global Biogeochemical Cycles* 29, 994–1013.
- Turner, J., Colwell, S.R., Marshall, G.J., Lachlan-Cope, T.A., Carleton, A.M., Jones, P.D., Lagun, V., Reid, P.A., Iagovkina, S., 2005. Antarctic climate change during the last 50 years. *International Journal of Climatology* 25, 279–294.
- Turner, J., Lu, H., White, I., King, J.C., Phillips, T., Hosking, J.S., Bracegirdle, T.J., Marshall, G.J., Mulvaney, R., Deb, P., 2016. Absence of 21st century warming on Antarctic Peninsula consistent with natural variability. *Nature* 535, 411–415.
- Van Caspel, M., 2016. The importance of the western Weddell Sea to Weddell Sea Deep Water formation. Ph.D. thesis. Universitat Bremen.
- Van Heuven, S., Pierrot, D., Rae, J., Lewis, E., Wallace, D., 2011a. MATLAB Program Developed for CO₂ System Calculations, ORNL/CDIAC-105b, Carbon Dioxide Information Analysis Center, Oak Ridge National Laboratory, U.S.Department of Energy, Oak Ridge, Tennessee.
- Van Heuven, S.M.A.C., Hoppema, M., Huhn, O., Slagter, H.A., de Baar, H.J.W., 2011b. Direct observation of increasing CO₂ in the Weddell Gyre along the Prime Meridian during 1973-2008. *Deep-Sea Research Part II: Topical Studies in Oceanography* 58, 2613–2635.
- Vaughan, D.G., Marshall, G.J., Connolley, W.M., Parkinson, C., Mulvaney, R., Hodgson, D.A., King, J.C., Pudsey, C.J., Turner, J., 2003. Recent rapid regional climate warming on the Antarctic Peninsula. *Climatic Change* 60, 243–274.

- Velo, A., Perez, F.F., Brown, P., Tanhua, T., Schuster, U., Key, R.M., 2009. CARINA alkalinity data in the Atlantic Ocean. *Earth System Science Data* 1, 45–61.
- Venables, H., Meredith, M.P., Atkinson, A., Ward, P., 2012. Fronts and habitat zones in the Scotia Sea. *Deep-Sea Research Part II* 59-60, 14–24.
- Venables, H.J., Clarke, A., Meredith, M.P., 2013. Wintertime controls on summer stratification and productivity at the western Antarctic Peninsula. *Limnology and Oceanography* 58, 1035–1047.
- Venables, H.J., Meredith, M.P., 2014. Feedbacks between ice cover, ocean stratification, and heat content in Ryder Bay, West Antarctic Peninsula. *Journal of Geophysical Research: Oceans* 119, 5323–5336.
- Vernet, M., Martinson, D., Iannuzzi, R., Stammerjohn, S., Kozlowski, W., Sines, K., Smith, R., Garibotti, I., 2008. Primary production within the sea-ice zone west of the Antarctic Peninsula: I - Sea ice, summer mixed layer, and irradiance. *Deep Sea Research Part II: Topical Studies in Oceanography* 55, 2068–2085.
- Wallace, D.M.R., Johnson, K.M., 1994. Prediction of total dissolved inorganic carbon on basin scales by simple multiple linear regression. *Eos Transactions* 75.
- Wallace, M.I., 2007. Ocean circulation in Marguerite Bay. PhD thesis, The Open University .
- Wang, L., Huang, J., Luo, Y., Zhao, Z., 2016. Narrowing the spread in CMIP5 model projections of air-sea CO₂ fluxes. *Nature Scientific Reports* 6, 37548.
- Wanninkhof, R., 1992. Relationship Between Wind Speed and Gas Exchange over the ocean. *Journal of Geophysical Research* 97, 7373–7382.
- Wanninkhof, R., 2014. Relationship between wind speed and gas exchange over the ocean revisited. *Limnology and Oceanography: Methods* 12, 351–362.
- Wanninkhof, R., Doney, S.C., 2006. Carbon Dioxide, Hydrographic, and Chemical Data Obtained During the R/V Ronald H. Brown Repeat Hydrography Cruise in

- the Atlantic Ocean: CLIVAR CO₂ Section A16S 2005 (11 January - 24 February, 2005), ed. A. Kozyr, ORNL/CDIAC-151, NDP-087. Technical Report.
- Wanninkhof, R., Johnson, K., Williams, N., Sarmiento, J., Riser, S., Briggs, E., Bushinsky, S., Carter, B., Dickson, A., Feely, R., Gray, A., Juranek, L., Key, R., Talley, L., Russel, J., Verdy, A., 2016. An evaluation of pH and NO₃ sensor data from SOCCOM floats and their utilization to develop ocean inorganic carbon products, SOCCOM Carbon System Working Group white paper. Technical Report.
- Wanninkhof, R., Park, G.H., Takahashi, T., Sweeney, C., Feely, R., Nojiri, Y., Gruber, N., Doney, S.C., McKinley, G.A., Lenton, A., Le Quéré, C., Heinze, C., Schwinger, J., Graven, H., Khatiwala, S., 2013. Global ocean carbon uptake: magnitude, variability and trends. *Biogeosciences* 10, 1983–2000.
- Wanninkhof, R., Peng, T.H., Huss, B., Sabine, C.L., Lee, K., 2003. Comparison of Inorganic Carbon System Parameters Measured in the Atlantic Ocean from 1990 to 1998 and Recommended Adjustments. Technical Report. Carbon Dioxide Information Analysis Center, Oak Ridge, Tennessee.
- Waters, J.F., Millero, F.J., Sabine, C.L., 2011. Changes in South Pacific anthropogenic carbon. *Global Biogeochemical Cycles* 25, 1–11.
- Watson, A.J., Naveira Garabato, A.C., 2006. The role of Southern Ocean mixing and upwelling in glacial-interglacial atmospheric CO₂ change. *Tellus, Series B: Chemical and Physical Meteorology* 58, 73–87.
- Watson, A.J., Vallis, G.K., Nikurashin, M., 2015. Southern Ocean buoyancy forcing of ocean ventilation and glacial atmospheric CO₂. *Nature Geoscience* 8, 861–865.
- Waugh, D.W., Haine, T.W., Hall, T.M., 2004. Transport times and anthropogenic carbon in the subpolar North Atlantic Ocean. *Deep Sea Research Part I: Oceanographic Research Papers* 51, 1475–1491.

- Waugh, D.W., Primeau, F., DeVries, T., Holzer, M., 2013. Recent changes in the ventilation of the southern oceans. *Science* 339, 568–70.
- Weiss, R., 1974. Carbon dioxide in water and seawater: the solubility of a non-ideal gas. *Marine Chemistry* 2, 203–215.
- Weiss, R., Price, B., 1980. Nitrous oxide solubility in water and seawater. *Marine Chemistry* 8, 347–359.
- Weston, K., Jickells, T.D., Carson, D.S., Clarke, A., Meredith, M.P., Brandon, M.A., Wallace, M.I., Ussher, S.J., Hendry, K.R., 2013. Primary production export flux in Marguerite Bay (Antarctic Peninsula): Linking upper water-column production to sediment trap flux. *Deep Sea Research Part I: Oceanographic Research Papers* 75, 52–66.
- Whitworth, T., Nowlin, W.D., 1987. Water Masses and Currents of the Southern Ocean at the Greenwich Meridian. *Journal of Geophysical Research* 92, 6462–6476.
- Whitworth, T., Nowlin, W.D., Orsi, A., Locarnini, R.A., Smith, S.G., 1994. Weddell Sea Shelf Water in the Bransfield Strait and Weddell-Scotia Confluence. *Deep-Sea Research I* 41, 629–641.
- Williams, G.D., Aoki, S., Jacobs, S.S., Rintoul, S.R., Tamura, T., Bindoff, N.L., 2010. Antarctic Bottom Water from the Adélie and George V Land coast, East Antarctica (140 - 149°E). *Journal of Geophysical Research* 115, 1–29.
- Williams, N., Juraneck, L.W., Feely, R.A., Johnson, K.S., Sarmiento, J.L., Talley, L.D., Dickson, A.G., Gray, A.R., Wanninkhof, R., Russell, J.L., Riser, S.C., Takeshita, Y., 2017. Calculating surface ocean pCO₂ from biogeochemical Argo floats equipped with pH: An uncertainty analysis. *Global Biogeochemical Cycles* 31, 591–604.
- Williams, N.L., Feely, R.A., Sabine, C.L., Dickson, A.G., Swift, J.H., Talley, L.D.,

- Russell, J.L., 2015. Quantifying Anthropogenic Carbon Inventory Changes in the Pacific Sector of the Southern Ocean. *Marine Chemistry* 174, 147–160.
- Williams, R.G., Follows, M.J., 2011. *Ocean Dynamics and the Carbon Cycle: Principles and Mechanisms*. Cambridge University Press, Cambridge.
- Wong, A.P.S., Bindoff, N.L., Church, J.A., 1999. Large-scale freshening of intermediate waters in the Pacific and Indian oceans. *Nature* 400, 440–443.
- Yager, P.L., Wallace, D.W.R., Johnson, K.M., Smith, W.O., Minnett, P.J., Deming, J.W., 1995. The Northeast Water Polynya as an atmospheric CO₂ sink: A seasonal rectification hypothesis. *Journal of Geophysical Research* 100, 4389–4398.
- Yamamoto-Kawai, M., McLaughlin, F.A., Carmack, E.C., Nishino, S., Shimada, K., 2009. Aragonite Undersaturation in the Arctic Ocean: Effects of Ocean Acidification and Sea Ice Melt. *Science* 326, 1098–1100.
- Zeebe, R., Wolf-Gladrow, D., 2001. *CO₂ in Seawater: Equilibrium, Kinetics, Isotopes*, Elsevier Oceanography Series, 65. Elsevier, Amsterdam.
- Zemmelink, H.J., Delille, B., Tison, J.L., Hintsa, E.J., Houghton, L., Dacey, J.W.H., 2006. CO₂ deposition over the multi-year ice of the western Weddell Sea. *Geophysical Research Letters* 33, L13606.